

Electronic Thesis and Dissertation Repository

6-12-2024 1:30 PM

Porous Titanium Alloy Constructs for Mandibular Reconstruction

Khaled Marwan Anis Hijazi, *Western University*

Supervisor: Rizkalla, Amin S., *The University of Western Ontario*

A thesis submitted in partial fulfillment of the requirements for the Doctor of Philosophy degree
in Biomedical Engineering

© Khaled Marwan Anis Hijazi 2024

Follow this and additional works at: <https://ir.lib.uwo.ca/etd>



Part of the [Biomedical Devices and Instrumentation Commons](#)

Recommended Citation

Hijazi, Khaled Marwan Anis, "Porous Titanium Alloy Constructs for Mandibular Reconstruction" (2024).
Electronic Thesis and Dissertation Repository. 10292.
<https://ir.lib.uwo.ca/etd/10292>

This Dissertation/Thesis is brought to you for free and open access by Scholarship@Western. It has been accepted for inclusion in Electronic Thesis and Dissertation Repository by an authorized administrator of Scholarship@Western. For more information, please contact wlsadmin@uwo.ca.

Abstract

The goal of this study was to develop and validate finite element analysis (FEA) models to predict static and dynamic mechanical properties of porous titanium 6-aluminum 4-vanadium (Ti6Al4V) constructs. Dumbbell-shaped and square prism porous computer models were created with simple cubic unit cell structures with a size of 1 mm and strut thicknesses varying between 250 and 650 μm . The pore diameters ranged between 350 and 750 μm . Constructs were manufactured using selective laser melting (SLM). These constructs were scanned using computed tomography (CT) and scanning electron microscopy (SEM). These constructs were then tested under tensile and flexural static loading using a screw-type universal testing machine and under dynamic flexural loading using a servo-hydraulic testing machine. The FEA models were designed with mechanical properties calibrated to mimic those of the real-life constructs and omit the structural imperfections. The models' predictions were compared to the real-life mechanical testing results. A novel intraosseous porous implant was designed with numerical models to assess the mechanical properties of the implant under physiological loading conditions. The strength and modulus predictions of the FEA models matched those of the SLM-built constructs within a deviation of $< 11\%$, while the deviation of the fatigue strength from the numerical models was $\approx 10\%$. The larger deviations in the toughness predictions of the computer models from the real-life tests were associated with the diminished plastic strain of the SLM-built constructs, which the structural imperfections of the SLM-built constructs might have caused. In addition, SLM-built Ti6Al4V porous constructs with strut thicknesses ranging between 350 and 450 μm were viable for use in the intraosseous mandibular implant design. The implant was intact when exposed to physiological molar clenching. When the implant was exposed to cyclic masticatory forces ranging between 50 and 100 N, its predicted life expectancy was between 4 years at 100 N and 119 years at 50 N, exceeding the time for healthy bone ingrowth to osseointegrate and stabilize within the constructs. The FEA models can swiftly and accurately predict the static and dynamic mechanical properties of SLM-built constructs within a short period, making them suitable for use in clinical settings.

Keywords

Additive Manufacturing, Bone Ingrowth, Fatigue Loading, Finite Element Analysis, Mandible Biomechanics, Mandibular Reconstruction, Porous Constructs, SLM-built Constructs, Stress Shielding, Titanium Alloy Implants.

Summary for lay audience

This study focused on developing computer models to validate and predict porous titanium alloy constructs' static and dynamic mechanical properties. The aim of using these models was to design intraosseous porous implants that could be used for mandible (jaw) reconstruction. A series of porous models were built with void volumes and sizes to 3D-print porous titanium alloy constructs using selective laser melting (SLM). The microstructural features of these constructs were analyzed using computed tomography (CT) and scanning electron microscopy (SEM). The porous constructs were subjected to pull tensile loading and static and dynamic three-point bending to evaluate their mechanical properties. The results of these tests were used to develop and validate finite element analysis (FEA) models to predict the mechanical behaviour of these constructs. The results of these tests demonstrated a close correlation with real-life SLM-built porous constructs, particularly when a low force was applied. The deviations in the strain values were presumed to be an outcome of the structural imperfections detected within the constructs. Using these computer models, an intraosseous jaw implant was built with a porous structure that followed the stiffness of a dried cadaveric jaw model. The analysis showed that the implant can withstand chewing for up to 119 years of service. The computer models developed in this study can be used to create clinical procedures whereby patient-specific orthopedic implants can be designed, tested, and manufactured for implantation within a short time.

Co-authorship statement

Chapter 1, "Background and Literature Review" was adapted from a review article by Hijazi et al. 2024. Titanium Alloy Implants with Lattice Structures for Mandibular Reconstruction. Materials. K. Hijazi wrote this review article and then edited and reviewed by S. J. Dixon, J. E. Armstrong, and A. S. Rizkalla. The article was published on December 29, 2023. The following is the citation of the publication along with the digital object identifier (DOI) of the review article:

HIJAZI, K. M., DIXON, S. J., ARMSTRONG, J. E. & RIZKALLA, A. S. 2024. Titanium Alloy Implants with Lattice Structures for Mandibular Reconstruction. Materials (Basel), 17, 140. <https://doi.org/10.3390/ma17010140>

Chapter 2, "Summary and objectives of the research," was written by K.M. Hijazi and edited and revised by A. S. Rizkalla.

Chapter 3, entitled "Static mechanical and microstructural properties of porous Ti6Al4V constructs," was adapted from a research article by Hijazi et al., Mechanical and Microstructural Properties of Additively Manufactured Porous Titanium Alloy Constructs for Orthopaedic and Maxillofacial Reconstruction. K. Hijazi wrote this research article, and it was then reviewed by H. Mao, D. Holdsworth, S. J. Dixon, and A. S. Rizkalla. K. Hijazi did experimental work in the laboratory of A. S. Rizkalla.

Chapter 4, entitled "Fatigue properties of SLM-built porous Ti6Al4V," was adapted from a research article by Hijazi et al. 2024. Cyclic flexural fatigue of porous Ti6Al4V constructs for use in mandibular reconstruction. International Journal of Fatigue. K. Hijazi wrote this research article, then edited and reviewed it by H. Mao, D. Holdsworth, S. J. Dixon, and A. S. Rizkalla. Experimental work was done by K. Hijazi and was performed in the laboratory of A. S. Rizkalla. The article was accepted on April 11, 2024. The following is the citation of the publication along with the digital object identifier (DOI) of the article:

HIJAZI, K. M., MAO, H., HOLDSWORTH, D. W., DIXON, S. J. & RIZKALLA, A. S. 2024. Cyclic flexural fatigue of porous Ti6Al4V constructs for use in mandibular reconstruction. International Journal of Fatigue, 185, 108329. <https://doi.org/10.1016/j.ijfatigue.2024.108329>

Chapter 5, entitled “Numerical modelling of porous Ti6Al4V implant for mandibular reconstruction,” was adapted from a research article by Hijazi et al., Prototype design of Porous Ti6Al4V Intraosseous Implant for use in Mandibular Reconstruction. This research article was written by K. Hijazi and then edited and reviewed by H. Mao, D. Holdsworth, S. J. Dixon, and A. S. Rizkalla. Experimental work was done by K. Hijazi and was performed in the laboratory of A. S. Rizkalla.

Chapter 6, “Conclusions and General Discussion,” was written by K.M. Hijazi and edited and revised by A. S. Rizkalla.

Acknowledgments

First and foremost, I would like to express my heartfelt gratitude to my supervisor, Dr. Amin S. Rizkalla, for giving me the opportunity to work under his guidance with continued financial support, consistent encouragement, and understanding patience through thick and thin to achieve my goals. This PhD work is the fruit of a long journey, on a rollercoaster of tremendous successes and humbling challenges. Dr. Rizkalla's continuous advice was extremely valuable in making this process bearable and successful. I am truly fortunate to have had such an exceptional mentor, and I am grateful for the trust and encouragement provided to me.

I extend my heartfelt appreciation to my advisory committee members, including Dr. S. Jeffrey Dixon, Dr. Haojie Mao and Dr. David Holdsworth, for providing constructive input, expert advice, and scholarly contributions that have greatly enriched the quality of my dissertation. Their thoughtful critique and thorough evaluations have been crucial in refining my work's conceptual framework and methodology. I am indebted to them for their time, expertise, and dedication to academic excellence, which has significantly strengthened the overall quality of my research.

A special acknowledgment goes to my colleagues in the Biomaterial Lab at Western University. The collaborative and stimulating environment they cultivated played a pivotal role in my academic and personal development. I am grateful for the camaraderie, shared knowledge, and collective efforts that have made the research journey both enjoyable and rewarding. Their support has been a source of inspiration, and I am proud to have been part of such a dynamic and supportive research community.

Lastly, I would like to express my deepest appreciation to my parents for their unwavering love, encouragement, and understanding throughout this challenging yet rewarding pursuit. Their sacrifices, patience, and belief in my abilities have been my pillars of strength. I am grateful for their constant support, which has been the bedrock of my resilience and determination. This achievement would not have been possible without their steadfast commitment to my dreams and aspirations.

Table of contents

Abstract.....	ii
Summary for lay audience	iv
Co-authorship statement	v
Acknowledgments.....	vii
Table of contents.....	viii
List of tables.....	xii
List of figures	xv
List of appendices	xx
List of abbreviations	xxii
Preface.....	xxix
1 Background and literature review	2
1.1 Summary.....	2
1.2 The anatomy and physiology of the mandible.....	2
1.3 Mandibular reconstruction and fixation plates	5
1.4 Materials and techniques used to fabricate fixation plates	6
1.5 Challenges associated with the use of fixation plates.....	7
1.6 Additive manufacturing	11
1.7 Porous design of titanium alloy constructs	13
1.8 Bone growth into lattice constructs.....	20
1.9 Finite element analysis in the development of lattice constructs.....	23
1.10 Lattice-structured mandibular implants with cage and crib designs.....	27
1.11 Microstructural imperfections in SLM-built Ti6Al4V constructs	31
1.12 Fatigue loading of 3D-printed Ti6Al4V constructs	34
1.13 Fabrication measures to minimize structural imperfections	37
1.14 Post-processing treatments to improve mechanical properties and minimize structural imperfections	38
1.15 Challenges with the clinical application of 3D-printed mandibular implants	41
1.16 Knowledge gaps.....	42

1.17	Conclusions.....	43
1.18	References used in this chapter.....	44
2	Summary and objectives of the research.....	71
2.1	Summary.....	71
2.2	Objectives and hypothesis.....	72
3	Static mechanical and microstructural properties of porous Ti6Al4V constructs	74
3.1	Summary.....	74
3.2	Introduction.....	75
3.3	Methods.....	77
3.3.1	Model design and manufacture of porous constructs	77
3.3.2	Microstructural analysis.....	80
3.3.3	Mechanical testing and simulations.....	83
3.3.4	Statistical analysis.....	89
3.4	Results and Discussion	89
3.4.1	Geometrical analysis.....	89
3.4.2	Structural analysis of SLM-built constructs	90
3.4.3	Tensile and flexural testing.....	95
3.4.4	Von Mises stress distributions in porous and nonporous FEA models ..	103
3.4.5	Matching the mechanical properties of constructs to those of mandibular bone.....	105
3.5	Conclusions.....	106
3.6	References used in this chapter.....	107
4	Fatigue properties of SLM-built porous Ti6Al4V constructs.....	117
4.1	Summary.....	117
4.2	Introduction.....	117
4.3	Methods.....	121
4.3.1	Preparation of porous constructs.....	121
4.3.2	Static and dynamic flexural tests	122
4.3.3	Numerical simulations	123
4.3.4	Light and scanning electron microscopy	128

4.3.5	Statistical analyses	129
4.4	Results.....	130
4.4.1	Static flexural tests	130
4.4.2	Dynamic flexural testing.....	131
4.4.3	Numerical modelling of dynamic flexural loading.....	132
4.4.4	Microscopy of fracture sites.....	134
4.5	Discussion.....	135
4.5.1	Comparison of numerical models with SLM-built constructs.....	135
4.5.2	The effect of bone ingrowth on fatigue strength of porous constructs ...	138
4.5.3	Effect of pore geometry on fatigue properties	138
4.5.4	Potential of application in maxillofacial and orthopedic reconstruction	139
4.5.5	Limitations of numerical modelling of cyclic loading.....	139
4.6	Conclusion	140
4.7	References used in this chapter.....	140
5	Numerical modelling of porous Ti6Al4V implant for mandibular reconstruction	149
5.1	Summary.....	149
5.2	Introduction.....	150
5.3	Material and Methods	152
5.3.1	Creation of the mandible and implant models	152
5.3.2	Material properties	157
5.3.3	Static FEA model simulation	158
5.3.4	Fatigue numerical modelling	161
5.4	Results and discussion	162
5.4.1	Static FEA models	162
5.4.2	Fatigue Numerical Modelling.....	167
5.5	Effect of bone ingrowth on the implant	169
5.6	Conclusions.....	170
5.7	References in this chapter	171
6	Conclusions and general discussion.....	177

6.1	Summary and Conclusions	177
6.1.1	Specific objective 1: Design SLM-built porous Ti6Al4V constructs that could be used in mandibular reconstruction.	177
6.1.2	Specific objective 2: Determine the static mechanical properties of SLM-built porous Ti6Al4V.	178
6.1.3	Specific objective 3: Design and build finite element analysis models that mimic the tensile and flexural mechanical properties of SLM-built porous Ti6Al4V constructs.	178
6.1.4	Specific objective 4: Determine the flexural fatigue properties of SLM-built porous Ti6Al4V.....	179
6.1.5	Specific objective 5: Design and build dynamic numerical models that mimic the fatigue flexural properties of SLM-built porous Ti6Al4V constructs.	180
6.1.6	Specific objective 6: Design and build a static and dynamic FEA model of an intraosseous porous mandibular implant that is compatible with mandibular bone.....	180
6.2	Contributions to the current knowledge.....	181
6.3	Impact and significance of the study	182
6.4	Limitations and future work.....	184
6.5	Closing statement.....	186
6.6	References used in this chapter.....	187
	Appendices.....	194
	Curriculum Vitae	261

List of tables

Table 1-1: Selected studies on the static loading of SLM-built lattice constructs.....	16
Table 1-2: Selected studies on the flexural static loading of additively manufactured lattice constructs.	18
Table 1-3: Selected studies investigating bone growth into lattice titanium and Ti6Al4V constructs.	22
Table 3-1: The chemical composition of Ti6Al4V powder. Information was provided by Renishaw PLC (2017).....	80
Table 3-2: The width and thickness dimensions of the SLM-built tensile specimens compared to those of the CAD models.	89
Table A-3: The width and thickness dimensions of the SLM-built flexural specimens compared to those of the CAD models.	90
Table 4-1: Fatigue parameters applied on the Ti6Al4V component of the FEA model. The methods used to determine the values of the parameters are included.	127
Table A-1: X-ray parameters used to scan each of the constructs.	196
Table A-2: Material properties used in FEA models.	217
Table A-3: The Young's modulus (E_T) values obtained from mechanical tests on non-porous Ti6Al4V specimens.....	217
Table A-4: The elastic limit strength (σ_{PT}) and strain (ϵ_{PT}) values obtained from mechanical tests on non-porous Ti6Al4V specimens.	218
Table A-5: The yield point strength (σ_{TY}) and strain (ϵ_{TY}) values obtained from mechanical tests on non-porous Ti6Al4V specimens.	218
Table A-6: The peak strength (σ_{UTS}) and strain (ϵ_{UTS}) values obtained from mechanical tests on non-porous Ti6Al4V specimens.	218

Table A-7: Equations of the fits of the mechanical properties depending on strut thickness (t).....	221
Table A-8: Mechanical properties of mandibular cortical bones.....	222
Table A-9: The optimal design criteria and limitations for the lattice constructs.	222
Table A-10: The optimal strut thickness of lattice constructs at different mandible bone parts, according to Young’s modulus values of cortical bones.	222
Table A-11: The strength properties of the constructs built with the optimized strut thicknesses as well as the standard strut thicknesses used in the mechanical tests.	223
Table A-12: Tensile testing porous CAD models' geometrical properties.	229
Table A-13: Flexural testing porous CAD models' geometrical properties.....	229
Table A-14: The geometrical dimensions of the CAD models used to build the CT-scanned specimens.....	229
Table A-15: The deviation of the SLM-built strut thickness values from the nominal values in porous constructs and models.	230
Table A-16: The deviation of the SLM-built major axis length values from the nominal values in porous constructs and models.....	230
Table A-17: The deviation of the SLM-built minor axis length values from the nominal values in porous constructs and models.....	230
Table A-18: The deviation of the Young’s modulus values of FEA models from the SLM-built constructs.	230
Table A-19: The deviation of the tensile yield strength values of FEA models from the SLM-built constructs.	231
Table A-20: The deviation of the ultimate tensile strength values of FEA models from the SLM-built constructs.	231

Table A-21: The deviation of the tensile toughness values of FEA models from the SLM-built constructs.	231
Table A-22: The deviation of the flexural modulus values of FEA models from the SLM-built constructs.	231
Table A-23: The deviation of the flexural yield strength values of FEA models from the SLM-built constructs.	232
Table A-24: The deviation of the flexural strength values of FEA models from the SLM-built constructs.	232
Table A-25: The deviation of the relative flexural toughness values of FEA models from the SLM-built constructs.	232
Table B-1: Geometrical dimensions of the constructs and models.	244
Table B-2: ($\sigma_{\max} - N_f$) and ($\sigma_{\max}/\sigma_{FY} - N_f$) curve fits found for each of the tests and simulations conducted in this experiment. Information here was used to determine the average deviations.	244
Table B-3: Deviation of yield-normalized fatigue stress ratio ($\sigma_{\max}/\sigma_{FY}$) between the fits from ST350 numerical models and the cyclic flexural loading of SLM-built ST350 constructs.	244
Table B-4: Deviation of yield-normalized fatigue stress ratio ($\sigma_{\max}/\sigma_{FY}$).	246
Table B-5: The overall average deviation for both models, calculated from the results presented in Table B-3 and B-4.	247
Table B-6: Matching of the K_t factor with the best fitting $\sigma_{\max}/\sigma_{FY}$ ranges.	251

List of figures

Figure 1-1: The human mandible includes the mandibular body (MB), two rami (R), two condyles (C), two coronoid processes (CP), and the alveolar process (AP).....	3
Figure 1-2: The general process of designing and constructing medical and surgical implants using AM technology.....	12
Figure 1-3: Additive manufacturing process using selective laser melting (SLM) as presented by Jahadakbar et al. (2016).....	13
Figure 1-4: Representative unit cell and cell designs used in studies utilizing nonstochastic lattice constructs.....	15
Figure 1-5: The mandibular implant introduced by Shen et al. (2022).	28
Figure 1-6: FEA analysis results of the three implants designed by van Kootwijk et al. (2022) under incisal clenching (INC) and right molar biting (RMB).....	30
Figure 3-1: Representative diagrams showing the geometry of the porous CAD models.	79
Figure 3-2: Representative scatter plots of (A) a parallel strut's vertices in polar coordinates in cross-sectional view and (B) a perpendicular struts' vertices in polar coordinates in cross-sectional view.	82
Figure 3-3: Schematic diagrams showing the tensile and three-point bending test setup.	84
Figure 3-4: Boundary and loading conditions for representative tensile S-section (A) and flexural C-section (B) quadrant models.	86
Figure 3-5: Analysis of strut thickness and shape along with representative CT images of the porous constructs.....	91
Figure 3-6: Surface roughness analysis of the struts	93
Figure 3-7: Representative slices from CT-images after segmentation. (A) 350 and (B) 450 μm strut thickness constructs.	95

Figure 3-8: Bar graphs illustrate the mechanical properties of constructs and FEA models.	96
Figure 3-9: Dependence of tensile mechanical properties on nominal strut thickness (shown on the x axes).	98
Figure 3-10: Dependence of flexural mechanical properties on nominal strut thickness (shown on the x axes).	99
Figure 3-11: Images illustrate von Mises stress contour maps of representative FEA models.	105
Figure 4-1: Porous Ti6Al4V CAD models used in this study	121
Figure 4-2: Three-point bending setup. The L/T ratio was 18:1. Arrows represent the applied force (red) and supports (blue).	122
Figure 4-3: Representative three-point bending FEA model from a front view.	124
Figure 4-4: Flexural yield stress and flexural modulus of SLM-built constructs and FEA models.	131
Figure 4-5: The σ_{\max} - Nf and the $\sigma_{\max}\sigma_{FY}$ - Nf curves from fatigue tests.	132
Figure 4-6: Behaviour of fatigue numerical models compared to that of real-life SLM-built constructs.	132
Figure 4-7: The results of the FE-Safe numerical models with and without bone ingrowth, plotted with the fatigue behaviour of real-life SLM-built constructs.	133
Figure 4-8: Visualisation of the flexural cyclic loading simulation of the (A) ST350 and (B) ST350-Bone models at σ_{\max} = 150 MPa.	134
Figure 4-9: Representative light microscope images and SEM images of fatigue loaded constructs.	135
Figure 5-1: 3D image of the mandible generated from the CT images.	153

Figure 5-2: The process of creating the Mandible and IO-mandible models used in the FEA analysis.....	154
Figure 5-3: The components of the intraosseous implant system.....	156
Figure 5-4: Distribution of the Young’s modulus within the bone structure.....	158
Figure 5-5: Detailed description of the mandible and implant-mandible models’ muscular forces and boundary conditions.	160
Figure 5-6: The von Mises stress contour map of the mandible and implant-mandible models along with their components.	164
Figure 5-7: Contour maps of the implant-mandible model showing the maximum principal strain of the bone adjacent to the implant.....	166
Figure 5-8: Fatigue behaviour of the implant-mandible model.....	167
Figure 5-9: Contour map of fatigue-loaded models.....	168
Figure A-1: A schematic of the setup of the porous specimen in the glass test tube with floral foam.....	195
Figure A-2: (A) An image of the specimen loaded into the μ -CT scanning machine. (B) A schematic diagram is shown describing the parts of the μ -CT scanning machine.	196
Figure A-3: The 3D-CT model split into smaller sub-models.....	197
Figure A-4: Representative frequency of the voxels-CT density (frequency-density) histogram.....	198
Figure A-5: The window levelling process applied on the CT slices.	199
Figure A-6: Frequency-density histogram with the black-white extremes superimposed..	200
Figure A-7: The ROIs segmented out of the sub-models, along with the criteria established in the segmentation process.	200
Figure A-8: Examples of struts from one of the sub-models.....	202

Figure A-9: The strut surface vertices shown in cartesian coordinates.	205
Figure A-10: The vertices of the strut surface shown on a polar plot (green) and the best fit ellipse formed from the polar plot vertices (pink).	207
Figure A-11: The surface of the strut with the polar coordinates shown in rectangular form.	211
Figure A-12: The surface plot after the gaussian filter (S-filter) is applied to the raw surface.	213
Figure A-13: The removed part of the surface plot after applying the S-filter.	213
Figure A-14: The removed form surface from the plot. This surface represents the curvature of the strut shape.	214
Figure A-15: The SF-surface plot. This is the primary surface plot that is used in the surface texture measurements.	215
Figure A-16: The stress-plastic strain plastic behaviour of Ti6Al4V used in the FEA analysis.	219
Figure A-17: The FEA simulation of tensile loading of a non-porous Ti6Al4V model (blue) compared to the results of the tensile tests done on SLM-printed constructs (n=10) (grey).	221
Figure A-18: Schematic diagrams showing the FEA models used to compare the tensile mechanical properties with and without structural imperfections.	224
Figure A-19: The mechanical properties predictions from the FEA models of exposed to tensile loading simulations.	225
Figure A-20: von Mises stress contour maps of the nRnD model (A) and nRD model (B).	226
Figure A-21: von Mises stress contour maps of the RnD model (A) RD model and (B) RD model.	227

Figure A-22: Mesh convergence analysis performed on the flexural FEA models with strut thickness of 250 μm .	233
Figure B-1: $\sigma_{\text{max}} - N_f$ (A and C) and $\sigma_{\text{max}}\sigma_{\text{FY}} - N_f$ (B and D) curves for (A and B) ST350 models and (C and D) ST450 models with different K_t values.	248
Figure B-2: The deviation of the $\sigma_{\text{max}}\sigma_{\text{FY}} - N_f$ from the fatigue models when compared to the real-life fatigue tests.	249
Figure B-3: The comparisons of the deviation of (A) ST350 and (B) ST450 models against the real-life $\sigma_{\text{max}}\sigma_{\text{FY}} - N_f$ curves.	250
Figure B-4: The $\sigma_{\text{max}}\sigma_{\text{FY}} - N_f$ curves of (A) ST350 and (B) ST450 real-life tests, original models and optimized models.	251
Figure B-5: Representative light microscopy images of the ST350 constructs that underwent cyclic loading at $\sigma_{\text{max}}\sigma_{\text{FY}} = 0.4$ (A-C) and $\sigma_{\text{max}}\sigma_{\text{FY}} = 0.8$ (D-F).	252
Figure B-6: Representative light microscopy images of the ST450 constructs that underwent cyclic loading at $\sigma_{\text{max}}\sigma_{\text{FY}} = 0.4$ (A-C) and $\sigma_{\text{max}}\sigma_{\text{FY}} = 0.8$ (D-F).	253
Figure B-7: Representative SEM images of the ST350 constructs that underwent cyclic loading at $\sigma_{\text{max}}\sigma_{\text{FY}} = 0.4$ (A-C) and $\sigma_{\text{max}}\sigma_{\text{FY}} = 0.8$ (D-F).	254
Figure B-8: Representative SEM images of the ST450 constructs that underwent cyclic loading at $\sigma_{\text{max}}\sigma_{\text{FY}} = 0.4$ (A-C) and $\sigma_{\text{max}}\sigma_{\text{FY}} = 0.8$ (D-F).	255

List of appendices

A	Additional information for Chapter 3	195
A.1	Computed tomography (CT).....	195
A.1.1	Preparation of specimens	195
A.1.2	Microstructural analysis of the specimen using μ -CT	197
A.1.3	3D-CT model segmentation and porosity measurements	197
A.1.4	Struts' surface profiles extraction	201
A.2	Strut thickness and surface texture analysis.....	203
A.2.1	Preparation and importing of data.....	203
A.2.2	Initial scatter plot	204
A.2.3	Rotation of the strut (only for perpendicular struts)	205
A.2.4	Strut thickness measurement.....	206
A.2.5	Defining the height, span and radial angle of the vertices of the surface profile.....	207
A.2.6	Creating gridded data.....	208
A.2.7	Generating the surface profile for roughness analysis.....	210
A.2.8	Analysis of the surface texture parameters	215
A.2.9	Roughness analysis of the non-porous constructs	215
A.3	The material properties of Ti6Al4V for use in FEA analysis.....	216
A.3.1	Density and Poisson's ratio.....	217
A.3.2	Young's modulus	217
A.3.3	Plastic properties.....	217
A.3.4	Damage simulation	219
A.4	Determining the appropriate lattice properties for mandibular reconstruction... ..	221
A.5	Comparison between the FEA models with and without structural imperfections	223
A.6	Supplementary tables for Chapter 3.....	229
A.7	Mesh convergence analysis results	233
B	Additional information for Chapter 4	234

B.1	MATLAB: Dynamic flexural loading analysis.....	234
B.1.1	Read Data.....	234
B.1.2	Process and cleaning up of data	235
B.1.3	Convert to Stress-Strain	236
B.1.4	Find Extremes	237
B.1.5	Analyze the Fatigue Data.....	238
B.1.6	Plot final curves and table of results	241
B.2	Supplementary tables for Chapter 4.....	244
B.2.1	Models and constructs nominal geometrical measurements.....	244
B.2.2	Fatigue tests and model fits.....	244
B.3	Determining the optimal K_t factor for use in fatigue modelling.....	247
B.4	Multiple K_t values used in the same model	249
B.5	Additional SEM and light microscopy images	252
C	Permissions	256
C.1	Chapters and figures reused from publications in MDPI.....	256
C.1.1	Relevant parts of the thesis: Chapter 1, Figure 1-3 and Figure 1-5	256
C.1.2	MDPI Open Access information and Policy.....	257
C.2	Chapters and figures reused from publications in Elsevier	258
C.2.1	Relevant parts of the thesis: Chapter 4 and Appendix B	258
C.2.2	Relevant parts of the thesis: Figure 1-6	259
D	References used in the Appendices.....	260

List of abbreviations

3PB	Three-point bending
4PB	Four-point bending
AM	Additive manufacturing
AMT	Additive manufacturing technique
AT	Anterior temporalis
b	Basquin's fatigue strength exponent
BA/TA	Bone area/total area
BCC	Body centric cubic
BV/TV	Bone volume/total volume
c	Coffin-Manson fatigue ductility exponent
C	Compression
CAD	Computer-aided design
CFD	Computational fluid dynamics
Cir	Circular
Cry	Crystal
CT	Computed tomography
D	Cyclic loading-induced damage
d	Displacement

D pyr	Double pyramid
Dia	Diamond
DM	Deep masseter
EBM	Electron beam microscopy
E	Energy density
E_F	Flexural modulus
Equ tri	Equilateral triangle
E_T	Young's modulus
FEA	Finite element analysis
FGP	Functionally graded porosity
FT	Feature thickness
Gyr	Gyroid
H	Hatching spacing
HA	Hydroxyapatite
HC	Honeycomb
Hex	Hexagonal
Hex HC	Hexagonal honeycomb
HIP	Hot isostatic pressure
K'	Cyclic strain hardening coefficient

K_t	Stress concentration factor
MP	Medial pterygoid
MT	Middle temporalis
N_f	Number of cycles at fatigue failure
n'	Cyclic strain hardening exponent
Neov	Neovius
N_f	Number of cycles at failure
nRD	No Roughness and with internal defects
nRnD	No Roughness and no internal defects
OS	Outer skin
OT	Octet truss
P	Laser power
P_a	Arithmetic mean height of surface roughness
P_z	Maximum peak to valley height of surface roughness
Por	Porosity
PS	Pore size
PT	Posterior temporalis
R_a	Arithmetic mean roughness (linear)
RD	With both roughness and internal defects

RDod	Rhombic dodecahedron
RnD	With roughness and no internal defects
ROI	Region of interest
Sand	Sandblasted
SC	Simple cubic
Sch	Schwartz
SEM	Scanning electron microscopy
SLA	Sandblasted and chemically etched
SLM	Selective laser melting
SM	Superficial masseter
S_y	Years of service
t	Strut thickness
T	Layer thickness
Ten	Tensile
T_F	Relative flexural toughness at 1% strain level
Ti	Titanium
Ti6Al4V	Titanium-6 aluminum-4 vanadium
TPMS	Triply periodic minimal surface
T_T	Tensile toughness

UCS	Unit cell size
V	Laser scanning speed
Vor	Voronoi
γ	Shear strain
$\Delta\gamma_{\max}/2$	Shear strain amplitude
$\Delta\epsilon_n/2$	Normal strain amplitude
ϵ	Strain
ϵ_a	Amplitude strain
ϵ'_f	Fatigue ductility coefficient
$\epsilon_{f\max}$	Maximum strain during cyclic loading
$\epsilon_{f\min}$	Minimum strain during cyclic loading
ϵ_{PS}	Strain at proportionality limit
ϵ_{TY}	Strain at tensile yield point
ϵ_{UTS}	Strain at maximum tensile strength
η	Stress triaxiality
ρ_{app}	Apparent density
ρ_{ash}	Ash density
σ	Stress

$\bar{\sigma}$	Mean cyclic stress
$\bar{\sigma}_{\text{failure}}$	In FEA, stress if element damage is not activated
σ_a	Amplitude stress during cyclic loading
σ_F	Flexural strength
σ'_f	Fatigue strength coefficient
σ_{failure}	In FEA, stress where failure of element occurs
σ_{fmax}	Maximum applied stress during cyclic loading
$\sigma_{\text{fmax}}/\sigma_{\text{FY}}$	Yield-normalized fatigue stress ratio
σ_{fmin}	Minimum applied stress during cyclic loading
σ_{FY}	Flexural yield strength
σ_P	Stress at proportionality limit
σ_{TY}	Tensile yield strength
σ_{UTS}	Ultimate tensile strength
σ_v	Von Mises stress
σ_x	Principal stress along x-axis
σ_y	Principal stress along y-axis
σ_z	Principal stress along z-axis
τ_x	Shear stress along x-plane

τ_y	Shear stress along y-plane
τ_z	Shear stress along z-plane

Preface

The field of biomedical engineering continues to advance through the boundaries of innovation to address the intricate challenges posed by medical applications. In the spirit of this endeavor, this thesis delves into the realm of mandibular reconstruction. In this thesis, we explore the development of validated computer models that can predict the mechanical properties of porous titanium alloys built using powder bed additive manufacturing techniques. These porous constructs have a high promise in the promotion of bone growth, while having mechanical properties that mimic those of the mandible bone and can fit into mandibular bones directly without any intra-surgery bending. Implants avoid complications associated with misalignment, such as malunion and non-union of bone, as well as stress shielding, which is associated with the difference in stiffness between metal implants and bones. From an aesthetic perspective, such 3D-printed implants that match the mandibular bone result in a better facial feature when compared to the conventional grafting method used nowadays.

While computational modelling has been adopted by researchers and designers of implants for the last few decades, there is active research in the field of matching material and fatigue properties of computer models with the highly variable and often defective additively manufactured porous constructs. Given the difficulties of obtaining defect free porous constructs, we are left with modelling their mechanical properties, with the goal of being able to optimize their structures and geometries. The modelling process normally involves mimicking the structural features of the defects, which might be expensive both in computational power and processing time. Such time might not be feasible or viable in a clinical setting, and result in long waiting time for patient-specific implant preparation. This study takes a different approach, whereby the mechanical properties of the FEA models are calibrated as to fit those of the real-life SLM-built constructs, while keeping the base FEA model as simple as possible, resulting in shorter processing and analysis time consumption. Unlike previous works, this study takes a comprehensive look into developing and validating FEA models under both static and dynamic (fatigue) loading conditions. The general framework proposed in the development of the implant design

starts from the point of examination clinically, through medical imaging of the mandibular bones, followed by the development of the optimized pore geometry, and consequently building the static and dynamic loading models, and finally manufacturing of the implant design upon amending any points of weakness within the design of the implant.

In Chapter 1, we explore the previous works that dealt with the progress of designing and manufacturing porous titanium alloy constructs. In Chapters 3 and 4, we investigate the process behind the identification of the static and fatigue mechanical properties of the constructs, which were then fed into developed computer models that can predict their mechanical behaviour. In addition, we also describe the validation process that was conducted using in vitro tests on real-life porous constructs. In Chapter 5, we describe a case study, where an intraosseous implant was developed using a porous design, which was derived from the porous constructs that were previously designed and tested in the previous chapters. In the concluding chapter (Chapter 6), the implications of the research are discussed, and recommendations for future work are outlined.

Through the development of these numerical models, we aspire to contribute to the standardization of the design and properties of porous implants built using additive manufacturing. By accurately predicting their mechanical properties, a time and cost saving could be achieved, which in turn will catalyze the development of mandibular and orthopedic patient-specific implants.

Khaled Hijazi

April 6, 2024

London, ON, Canada

Chapter 1

Background and literature review

This chapter was adapted with permission from the article: Hijazi, K.M., Dixon, S.J., Armstrong, J.E., Rizkalla, A.S., 2024. Titanium Alloy Implants with Lattice Structures for Mandibular Reconstruction. *Materials (Basel)* 17, 140. <https://doi.org/10.3390/ma17010140>

Chapter 1

1 Background and literature review

1.1 Summary

In recent years, the field of mandibular reconstruction has made great strides in terms of hardware innovations and their clinical applications. There has been considerable interest in using computer-aided design, finite element modelling, and additive manufacturing techniques to build patient-specific surgical implants. Moreover, lattice implants can mimic mandibular bone's mechanical and structural properties. This article reviews current approaches for mandibular reconstruction, their applications, and their drawbacks. Then, we discuss the potential of mandibular devices with lattice structures, their development and applications, and the challenges for their use in clinical settings.

1.2 The anatomy and physiology of the mandible

The mandible is the lower jawbone and consists of a body and two rami. The alveolar process anchors the lower teeth, while the condylar processes form part of the temporomandibular joints, and the coronoid processes provide muscle attachments (Figure 1-1). The mandibular bone comprises two layers, a dense layer of cortical bone covering a lighter core of trabecular bone. The thickness of mandibular cortical bone can be between 1 and 4 mm depending on the anatomical location (Heibel et al., 2001, Katranji et al., 2007, Schwartz-Dabney and Dechow, 2002, Santos et al., 2023, Khairy and Mahaini, 2015). Within the bone, cells specialized in bone remodelling are present. These cells include osteoclasts, osteoblasts, and osteocytes (Maciel et al., 2023). The mandible's movement depends on several muscle groups attached to the mandible (Wexler, 2015). The major muscles involved in mastication are the masseter, temporalis, lateral pterygoid, and medial pterygoid. All these muscles, aside from the lateral pterygoid, perform the closing of the jaw. The forces arising from the muscles are balanced by reaction forces acting bilaterally

on the temporomandibular joints and teeth (Faulkner et al., 1987). During mastication, forces applied through the teeth and the muscles of mastication cause sagittal bending, transverse bending, and torsion of the mandible (van Eijden, 2000). Under these conditions, the mandible typically experiences a combination of tensile loading of the superior and posterior regions and compression loading of the inferior and anterior regions (Figure 1-1).

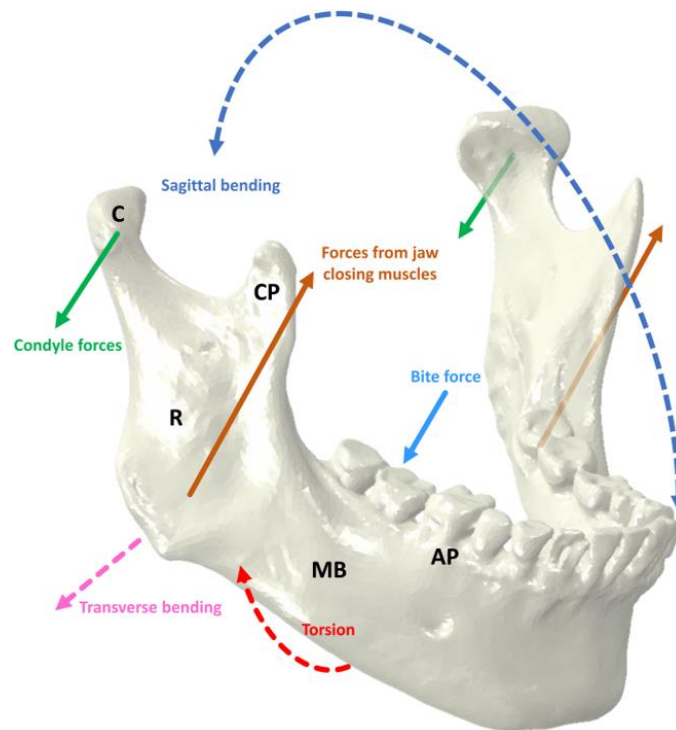


Figure 1-1: The human mandible includes the mandibular body (MB), two rami (R), two condyles (C), two coronoid processes (CP), and the alveolar process (AP).

Solid arrows show loading of the mandible during a unilateral molar bite as described by van Eijden (2000). Distortion of the mandible can be described as a combination of sagittal bending, torsion, and lateral transverse bending, all shown in dashed arrows).

The material properties of the mandible are highly dependent on bone density. Variations in the density of bone can be seen in different locations of the mandible and have been shown to affect mechanical strength and stiffness (Andani et al., 2014, Nagasao et al., 2009, Shapurian et al., 2006, Schwartz-Dabney and Dechow, 2003). Young's modulus values of mandibular cortical bone range between 10 and 31 GPa (Bujtár et al., 2010, Nagasao et al., 2009, Seong et al., 2009) and flexural modulus values range between 4.7 and 21 GPa (Odin et al., 2010). The trabecular bone has Young's modulus values that range between 0.003 and 4.5 GPa (Lakatos et al., 2014, Nagasao et al., 2009, Odin et al., 2010). The Young's

modulus of the whole mandible ranges between 0.07 and 3 GPa (Lakatos et al., 2014, Odin et al., 2010), and the flexural modulus ranges between 3.9 and 5.5 GPa (Odin et al., 2010, Vitins et al., 2003). The flexural strength of combined mandibular cortical and trabecular bones was determined to reach up to 200 MPa (Vitins et al., 2003). As in the case for most bones, mandibular bone is highly anisotropic (Augat et al., 1998).

The static biting forces experienced by mandibles vary according to the location of the applied forces (Ferrario et al., 2004, Pinheiro and Alves, 2015). In vivo studies report that the force applied on the teeth and, consequently, on the mandible reaches a maximum of about 300 N in males and 234 N in females under experimental settings (Ferrario et al., 2004). The stress levels from these forces range between 6.5 MPa and 20 MPa during regular muscular activity and chewing (Gholampour et al., 2019, Peng et al., 2021, Pinheiro and Alves, 2015, Wong et al., 2012). In computer simulations, the stress levels under clenching conditions reach about 60 MPa – and up to 150 MPa during molar clenching – with the highest stresses recorded in the condylar regions (Pinheiro and Alves, 2015). However, it must be noted that the unusually high stress concentration of 150 MPa might be the outcome of oversimplified boundary conditions imposed in computer simulations.

Humans exhibit high variability in the frequency and duration of their chewing activities. Although there have been several attempts to determine the frequency of mastication, only a few studies have examined this parameter in real-life situations. For example, Po et al. (2011) conducted a study that monitored the chewing activity of 21 participants using a portable electromyography detector for three days. The participants recorded 2755 chewing activities, translating to approximately 851 bites per day and 311,000 bites yearly. The study revealed that each chewing episode's mean frequency and duration were 1.5 Hz and 13 s, respectively. Farooq and Sazonov (2016) conducted a study in which they tested a system to detect the number of chews during 120 meals with 30 participants. The study found that participants chewed an average of 660 bites per meal at a frequency of 1.53 Hz, resulting in approximately 723,000 chews per year if we assume a human eats three significant meals per day. Other studies, such as that conducted by Chen (2012), have estimated that humans can chew up to a million times per year. It is worth noting that although the participants consumed various types of food with varying hardness, the

chewing activity was low-force and unlikely to impose excessive stress on the mandible. However, the mandible is consistently stressed due to mastication, swallowing, and, in some cases, parafunctional habits such as clenching and bruxism.

1.3 Mandibular reconstruction and fixation plates

Mandibular reconstruction is a general term encompassing several surgical procedures involved in the repair of the mandible. Mandibular reconstruction is performed when the whole or part of the mandible is destroyed. The goals of mandibular reconstruction are to restore the physical appearance of the lower part of the face, allow for normal eating, optimize speech ability, and allow for normal airflow. Hence, mandibular reconstruction aims to recover the structure of the mandible, provide physical continuity of the mandible, ensure that the reconstructed mandible can withstand masticatory forces, and rehabilitate dental and oral functions (Bak et al., 2010, Batstone, 2018).

Mandibular reconstruction often starts by performing mandibulectomy (Hanasono et al., 2013, Schrom et al., 2019), a surgical procedure to remove defective bone parts. Contemporary mandibular reconstruction commonly involves anchoring and bridging the remaining bones using fixation plates while maintaining occlusal (Bak et al., 2010, Pickrell et al., 2017) function. Grafts are applied within the defect to promote bone healing, with the choice of the graft depending on the size of the defect and the condition of the bone. Generally, a non-vascularized graft is used with less severe mandibular defects (Marechek et al., 2019, Ren et al., 2020, Pogrel, 2021), whereas more extensive and complex defects require autologously extracted vascularized flaps (Hidalgo, 1989, Batstone, 2018, Farwell et al., 2006, Kearns et al., 2018).

Generally, two fracture fixation techniques are applied to mandibular defects during reconstruction (Pickrell et al., 2017). The first is load-bearing fixation, in which the bone is entirely relieved from masticatory loading until healing is complete (Ellis and Miles, 2007). This fixation technique is used when fractures occur in severely atrophic bones or where fractures are comminuted (multiple fractures, which form smaller bone pieces). Load-bearing fixation is typically accomplished by using locking reconstruction plates (Yadav, 2021, Harjani et al., 2012). The second fracture fixation technique is load-sharing, which

allows the load to be distributed between the hardware and the bone at the fracture site. This technique typically works with more minor or superficial fractures, such as non-complex angle and symphyseal fractures (Yadav, 2021, Pickrell et al., 2017). In these cases, the fixation process involves using single miniplates, an arch bar, or lag screw fixation (Bak et al., 2010, Ellis and Miles, 2007, Kreutzer et al., 2022, Yadav, 2021). Fixation plates can be bent to align with the contour of the bone to allow for better facial appearance and for screws to be placed for stabilization (Bak et al., 2010). In the case of secondary reconstructions or in cases of tumors that do not allow local fixation plates, complete maxillo-mandibular fixation or an external fixation bridge may be used to maintain proper alignment of the mandible (Bak et al., 2010, Militsakh et al., 2004, Ung et al., 2002).

1.4 Materials and techniques used to fabricate fixation plates

Mandibular fixation devices are made of metals, with the most used materials being stainless steel, pure titanium, and titanium alloys (Barros et al., 2021, Riviş et al., 2020). The alloy of titanium that is commonly used is titanium-6 aluminum-4 vanadium (Ti6Al4V) (Sidambe, 2014, Warnke et al., 2009). This alloy has a high strength-to-weight ratio (Meier et al., 2023). Ti6Al4V is biologically (Sidambe, 2014) and chemically inert (Tengvall and Lundström, 1992, Jackson et al., 2016), largely passive towards corrosion (Rahman et al., 2014, Schiff et al., 2002), and provides an osteoconductive surface which promotes osseointegration (Albrektsson and Johansson, 2001, Albrektsson et al., 1999, Branemark and Tolman, 1998, Higuchi, 2000, Jayesh and Dhinakarsamy, 2015). Osseointegration is classically defined as the long-term stable fixation of a prosthesis into the adjacent bone tissue (Branemark, 1983, Granstrom, 2007, Jayesh and Dhinakarsamy, 2015).

A combination of formative and subtractive techniques is used conventionally to manufacture surgical implants (Abellán-Nebot et al., 2012, Jackson et al., 2016). Formative manufacturing covers techniques that cause a net change of zero in the mass of bulk materials (DeBoer et al., 2021). Some examples include metal casting and forging. Subtractive manufacturing involves the production of a part by removing mass from bulk

material, entailing a net loss of material, as in the case of milling, turning, and cutting metals (DeBoer et al., 2021). Formative techniques are first used to establish the implant's general shape, followed by machining (subtractive manufacturing) of the part to ensure appropriate detailing and finishing (Abellán-Nebot et al., 2012, DeBoer et al., 2021). Mandibular fixation plates with isotropic and highly controlled material content, geometry, and surface properties can be manufactured using this approach.

1.5 Challenges associated with the use of fixation plates

Although current approaches for mandibular reconstruction are largely successful (Kakarala et al., 2018), Keller et al. (1998), significant issues need to be addressed. Complications may lead to extended surgical procedures, longer hospital stays and recovery processes, and increased risk of surgical revisions (Kakarala et al., 2018, Vignesh et al., 2019).

Malunion and malocclusion are widely acknowledged complications in mandibular reconstruction. Malunion can be defined as a bony union formed at an incorrect position (Perez and Ellis, 2020, Pickrell et al., 2017). Malunion can lead to malocclusions in severe cases, which can cause a loss of occlusal function and facial deformity. Several factors can lead to malunions, including inadequate stabilization, incorrect alignment, inappropriate application or choice of fixation devices, or inadequate bone reduction during surgery (Ellis, 1996, Perez and Ellis, 2020, Pickrell et al., 2017). While malunion defects are detectable early in the healing process, malocclusions are often not recognized until the occlusion is assessed at a late stage (Pickrell et al., 2017). Malunions may require revision surgery.

The non-union of bones is the lack of continuity of bone in a defect post-operation, even after a given healing period has elapsed. High rates of non-union and fibrous union occur in atrophic mandibles with fixation (Ellis, 1996). The non-union of bones can ensue due to poor nutrition, metabolic disturbances, or systemic or localized malignancies and diseases (Mathog et al., 2000, Bochlogyros, 1985). A fibrous union may occur due to fracture instability, infection, or lack of contact between the bone fragments, along with improper

application of fixation devices (Perez and Ellis, 2020). The non-union of bones appears to occur mainly within the angle region and body of the mandible (Bochlogyros, 1985).

Infection is a complication that can arise during mandibular reconstruction, as in any other surgical procedure (Radwan and Mobarak, 2018, Seol et al., 2014). Regardless of the specific treatment approach used, the risk of infection is present due to bacteria in the oral cavity. These bacteria colonize the site of the defect, or the fixation appliances used during reconstruction, leading to infection-related complications. The risk of infection can be exacerbated by fracture instability and disruption in blood flow (Perez and Ellis, 2020).

An ongoing challenge of mandibular implants is healing in patients with bone disorders. For example, patients with osteoradionecrosis due to radiation exposure do not respond well to the current clinical techniques of mandibular reconstruction. Osteoradionecrosis can lead to the loosening of hardware post-implantation and other severe side effects (Buchbinder et al., 1993, Ichimura and Tanaka, 1993, Marx, 1983).

Autologous bone harvesting has been shown to cause anatomical and physiological disruptions in the donor site. Complications related to autologous grafting include the poor appearance of the skin grafts placed on the donor site, weaknesses in the extension and flexion of extremities, and decreased range of motion at the donor site (Daniels et al., 2005, Yim and Wei, 1994), difficulties with surgical operations due to logistical limitations, and variations in the amount of bone stock available for the grafting process (Kakarala et al., 2018, Ling and Peng, 2012, Momoh et al., 2011, Pare et al., 2019). Additionally, complications related to blood flow could occur due to the harvesting of arteries from the donor site to assist with the vascularization of grafts (Bak et al., 2010).

Depending on the fixation method employed, plates are bent to match the desired contour of the bone. A recent clinical study by Zeller et al. (2020) showed that the bending of ready-made fixation plates was more likely to cause fractures in these plates when compared to patient-specific fixation plates. The authors attributed this to the bending process inducing stress concentrations within parts of the plates with sharp angles. Moreover, the bending of plates may not provide a similar contour to that of the mandible and is highly dependent

on the surgeon's skill (van Kootwijk et al., 2022). The bending of fixation plates can also increase the likelihood of fatigue failure.

Another consideration is that current mandibular reconstruction methods do not provide the possibility of matching the mechanical properties of the surgical implants to those of adjacent bone (Jackson et al., 2016). Ti6Al4V is at least three times stiffer than cortical bone. This results in surgical devices and implants bearing a larger portion of the load than adjacent bone, thereby "shielding" the surrounding bone. This mismatch in stiffness results in bones being subjected to inadequate stress levels (Pogrel, 2021). Stress shielding leads to impairment of bone remodelling and reduced bone density, which can lead to loosening of the implant (Sumitomo et al., 2008). Evidence for stress shielding in mandibular implants is primarily derived from animal studies. Kennady et al. (1989b, 1989a) reported significantly lower bone volume in primate bones fixed with rigid plating than those without rigid plating. Some clinical studies attributed mandibular bone atrophy to stress shielding directly or indirectly, whereas other clinical studies point towards alternative reasons for rigid implant failure. There appears to be a consensus that the heavier and larger the reconstruction plate, the more likely it is that stress shielding may occur. Zhou et al. (2010) detected severe bone resorption in patients with mandibular reconstruction using rigid titanium trays. Many researchers looked at bone height loss after implantation as an indicator of the occurrence of stress shielding. Zoumalan et al. (2009) investigated the outcome of fibula free-flap mandibular reconstructions with angular reconstruction plates of 70 patients. These were relatively large reconstruction plates (load-bearing fixation). Zoumalan and coworkers found a marked loss of bone height of approximately 20% about 12 months after implantation. The authors attributed the loss of bone height to stress shielding. Other researchers measured bone height loss after using miniplates. Hidalgo and Pusic (2002) conducted a postsurgical investigation of 20 patients approximately 10 years after undergoing free-flap mandibular reconstruction using miniplates. Hidalgo and coworkers found a postoperative bone height loss of approximately 8%. Miniplates (load-sharing fixation) are generally less stiff than large reconstruction fixation plates (load-bearing fixation), and hence it is possible that the greater bone loss associated with load-bearing fixation is due to stress shielding.

According to the mechanostat theory (Pahr and Reisinger, 2020, Meslier and Shefelbine, 2023, Frost, 1987, Piccinini et al., 2016), bone modelling is influenced by the strain applied on bone. The nature of bone modelling can be matched with four different strain ranges as follows:

- The disuse state occurs when bone strains fall below 800 $\mu\epsilon$, leading to resorption and atrophy (stress shielding).
- The adapted state occurs when bone strain is between 800 $\mu\epsilon$ and 1500 $\mu\epsilon$, and bone is in a state of homeostasis, with a balance between bone formation and resorption.
- The overload state occurs when the bone deformation is between 1500 $\mu\epsilon$ and 7,000 $\mu\epsilon$, and bone modelling and growth occur due to physiologic demand (Biewener, 1993, Shen et al., 2022).
- Yielding occurs at strain levels between 7,000 $\mu\epsilon$ and 15,000 $\mu\epsilon$. At these strain levels, bone accumulates plastic damage that is unrecoverable (Biewener, 1993).
- Pathologic fracture occurs when the strain of bone is beyond 15,000 $\mu\epsilon$ (Shen et al., 2022).

It can thus be seen that an ideal fixation should allow for some strain to occur, ideally between 800 $\mu\epsilon$ and 15,000 $\mu\epsilon$, for homeostasis and growth to occur (Frost, 1987, Frost, 2004, Shen et al., 2022). The use of stiff fixation plates might cause the bone to experience less strain, which in turn would promote bone atrophy (Cilla et al., 2017, Arabnejad et al., 2017).

Design and manufacturing techniques must produce implants with a high level of resolution and sufficient control of geometric and mechanical properties. Conventional manufacturing methods cannot accurately replicate the intricate geometry of human bones (DeBoer et al., 2021). In addition, conventional methods of manufacturing constructs have

further disadvantages, including the significant expenditure of time, material, and energy involved in the fabrication process and the susceptibility to oxidation (Yan et al., 2015). For these reasons, designers in recent years have adopted additive manufacturing to mimic the geometrical and mechanical properties of bone.

1.6 Additive manufacturing

With recent developments in computed tomography, magnetic resonance imaging, and medical image processing, researchers can produce digital images and models that accurately represent the geometrical structure of bones (Vaish and Vaish, 2018). Computer models can be utilized to design implant devices that follow the exact contour and geometry of the original bone structure. Consequently, patient-specific orthopedic implant models can be produced using additive manufacturing (AM) techniques (Eshkalak et al., 2020, Kreutzer et al., 2022, Rehman et al., 2022). Moreover, computer models can be exported into finite element analysis (FEA) programs to perform mechanical loading simulations and prototyping (Geng et al., 2001, Peng et al., 2021, Pinheiro and Alves, 2015, Shen et al., 2022, Chen, 2012). Such approaches have been used to develop patient-specific conventional fixation plates (Kreutzer et al., 2022, Lang et al., 2021, Moiduddin et al., 2020, Zeller et al., 2020), as well as a multitude of other surgical implants (Arabnejad et al., 2017, Xia et al., 2020).

AM, also known as 3D printing, has seen an increase in use by different industries in the past few years, with a global market reaching up to about USD 30 billion in 2022 (Rehman et al., 2022). AM builds constructs layer by layer. It differs from subtractive or formative manufacturing techniques in that the mass change of the construct during manufacturing is positive (Nassehi et al., 2011). AM provides high precision and accuracy for the fabrication of constructs, making possible the creation of intricate and complex implants that would be difficult to produce using subtractive and equivalent manufacturing techniques (Munir et al., 2020, Attar et al., 2017). Moreover, AM techniques reduce material wastage and manufacturing time (Attar et al., 2017). AM is primarily recommended for manufacturing processes where the production volume is low, and design accuracy and intricacy are the main concerns (Bose et al., 2018, Wong and Hernandez, 2012).

While various AM technologies have been developed over the years, the general process involved in producing surgical and medical devices using AM technology remains essentially the same (Figure 1-2). Additive manufacturing requires high levels of precision and computer power to process accurate simulations of FEA models and design intricate prototype models. In addition, the choice of material, input anatomical information accuracy, and output mechanical property requirements are integral to the successful development of (Bose et al., 2018, Wong and Hernandez, 2012) implants using AM.

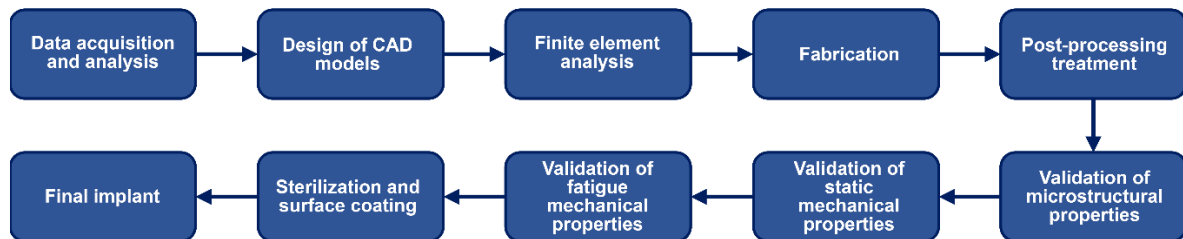


Figure 1-2: The general process of designing and constructing medical and surgical implants using AM technology.

Powder bed fusion techniques, including selective laser melting (SLM), also known as laser powder bed fusion (LPBF), and electron beam melting (EBM), also known as electron powder bed fusion (EPBF), have been of particular interest among researchers (Munir et al., 2020, Popov et al., 2018, Wysocki et al., 2017). SLM uses a laser beam to build highly complex constructs from metal powders (Wehmöller et al., 2005). During SLM manufacturing, a laser beam melts regions of the powder selectively (Wehmöller et al., 2005, Krzyzanowski and Svyetlichnyy, 2021). After the fabrication of each layer, the build plate lowers by one layer, after which the powder is spread to the next layer, and the laser melting process occurs again (Jahadakbar et al., 2018) (Figure 1-3). This process repeats until the construct is wholly manufactured (Jahadakbar et al., 2018).

EBM is a technique like SLM, replacing the laser beam with an intensified electron beam. It should be noted that EBM and SLM might be similar in manufacturing, but their output products could be different in mechanical and microstructural properties (Murr et al., 2012b, Roudnicka et al., 2019).

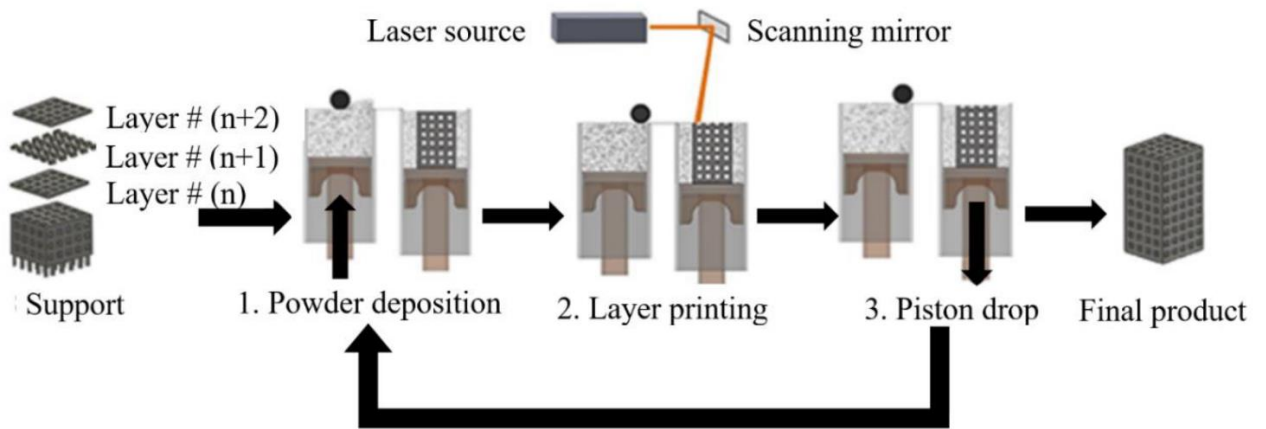


Figure 1-3: Additive manufacturing process using selective laser melting (SLM) as presented by Jahadakbar et al. (2016).

Supports are first built, followed by layer-by-layer fabrication of the constructs. There are two piston-operated chambers, one with the powder and the other where the construct is built. These pistons are shown in brown, while the vertical arrows describe the movement of the parts of the SLM system. (1) The powder is first pushed upward from the powder chamber. The powder is then rolled onto the building chamber using a roller (black circle in the figure). (2) The laser beam is then focused on the powder bed. The layer shape is controlled by managing the laser power and location. (3) Once the layer is completed, the piston in the building chamber is lowered, allowing space for the next layer to be built. This process is repeated until the construct is completed. (This work is licensed under the Creative Commons Attribution 4.0 International License. To view a copy of this license, visit <http://creativecommons.org/licenses/by/4.0/> or send a letter to Creative Commons, P.O. Box 1866, Mountain View, CA 94042, USA).

1.7 Porous design of titanium alloy constructs

As mentioned above, one disadvantage of using titanium and titanium alloy implants is the considerable difference in stiffness compared to bone. Various methods have been proposed to reduce the stiffness of titanium. The method with the most traction among researchers involves introducing pores into titanium alloy constructs.

Two main approaches have been used to introduce pores. The stochastic design is the earlier developed method in which pores are randomly placed without a specific pattern. Metal foaming (Ashby, 2000) and freeze-drying (Qian and Zhang, 2011) have been used to produce stochastic (random) and close-pore structures. Additive manufacturing techniques have also been used to produce stochastic structures made of Ti6Al4V (Al-Ketan et al., 2021). The second strategy is the nonstochastic (controlled) porous design, which produces lattice constructs (Cansizoglu et al., 2008). Nonstochastic porous constructs can only be fabricated using additive manufacturing techniques, as they require a high level of control to produce the periodic patterns of these lattice constructs. Because

the porosity and structural properties of lattice constructs are more amenable to control than in stochastic pore structures, the nonstochastic lattice construction process has been the preferred method to produce bone implants. Lattice constructs can reduce the stiffness of constructs to levels comparable to those of cortical and trabecular bones. The geometric properties of the introduced pores, including porosity (Gibson and Ashby, 1988, Krishna et al., 2007), size (Parthasarathy et al., 2010), and shape (Hedayati et al., 2018, Van Bael et al., 2012), affect the mechanical properties of the lattice constructs.

Nonstochastic constructs consist of unit cells. Unit cell size (UCS) refers to the largest possible diameter of a spherical object that can fit into the unit cell. Features, such as struts or surfaces, are built along the unit cells, with the leftover voids referred to as pores (Seto et al., 2021). Feature thickness (FT) refers to the thickness of the features that make up the boundaries of the unit cells, while pore size (PS) refers to the largest possible diameter of a sphere that can fit into the pore when the features are present. Reporting a pore size for some lattice constructs may be inappropriate, as specific unit cells may have complex design features. In such cases, porosity (P), defined as the volume of the void spaces expressed as a percentage of the overall volume of the structure, can be used. Examples of some types of pore design can be seen in Figure 1-4.

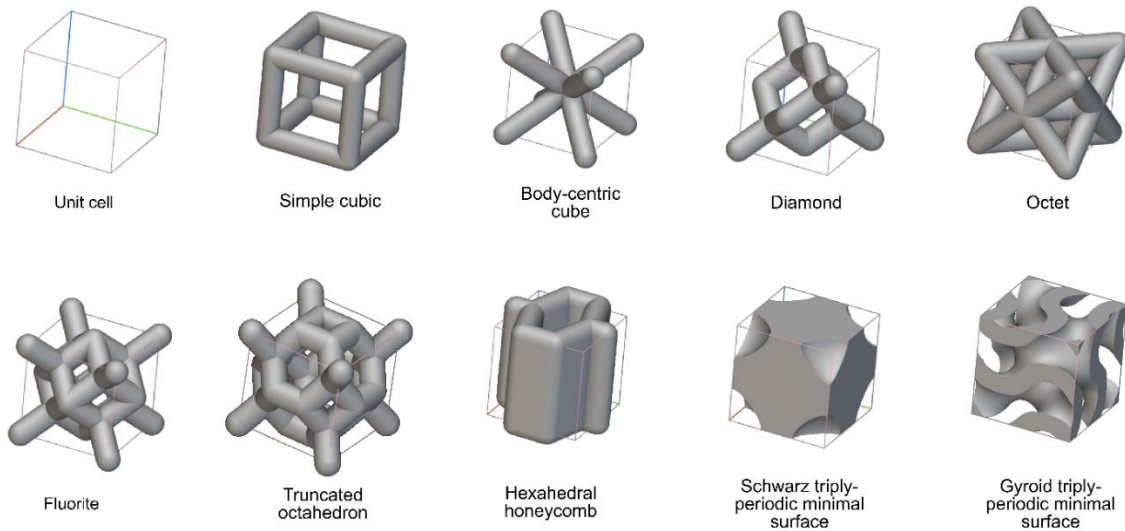


Figure 1-4: Representative unit cell and cell designs used in studies utilizing nonstochastic lattice constructs. The unit cell size in all these examples was kept consistent at 1 mm, while the feature thickness for all the cells was 250 μm . Complex lattice constructs can be designed by combining different cells.

Several recent studies have investigated the mechanical properties of lattice and other porous Ti6Al4V constructs (Table 1-1). Adding pores to constructs decreases their stiffness and their strength. Therefore, it is crucial to ensure that the lattice properties provide sufficient strength to withstand normal mechanical loading. Traditionally, studies of the mechanical properties of lattice constructs have largely involved compression tests. However, mandibles do not experience pure compressive stress. Therefore, researchers have recently tested other loading regimens. Flexural loading tests such as three-point and four-point bending have been performed on lattice constructs. A summary of some of the results of these tests can be seen in Table 1-2.

Table 1-1: Selected studies on the static loading of SLM-built lattice constructs.

Lattice	LT	P (%)	PS (μm)	FT (μm)	UCS (mm)	E (GPa)	σ_U (MPa)	σ_y (MPa)	Reference
SC	T	64	500	300	0.8	42.0	-	-	(Bartolomeu et al., 2021)
		70	600	300	0.9	28.6			
		84	500	150	0.7	22.6			
		88	600	150	0.8	16.1			
		93	600	100	0.7	12.4			
SC	C	93	-	670	4.0	3.0	16	16	(Dallago et al., 2021)
		93		670	4.0	1.8	9	9	
		94		670	4.0	1.8	9	9	
		93		500	3.0	3.0	15	14	
Dia	C	20	-	600	-	11.8	200	-	(El-Sayed et al., 2020)
		26		360		9.6	150		
		44		360		5.0	146		
		51		840		9.3	96		
		56		1000		8.3	228		
		65		840		4.2	69		
		66		600		7.7	185		
		73		840		1.6	82		
		75		600		1.4	52		
		75		600		1.3	47		
		76		600		1.2	49		
		78		600		0.4	26		
		82		840		0.4	19		
		89		200		0.2	10		
		90		600		0.2	8		
		91		360		0.3	9		
93	360	0.1	4						
Dia TPMS	C	-	500	-	1.0	0.6	-	-	(Alabort et al., 2019)
Gyr TPMS		-	200	-	1.0	0.6			
Neov TPMS		-	350	-	1.0	0.6			
Stochastic	C	87	830	210	-	1.7	550	-	(Ghouse et al., 2019)
Dia	C	66	631	283	-	4.7	171	127	(Xiong et al., 2020b)
Hex		67	643	285		3.8	163	110	

Dia-S		51	636	283		10.1	420	350	
Hex-S		53	643	285		11.0	537	424	
Schw TPMS	C	25	138	768	-	58.0	-	520	(Soro et al., 2019)
		42	282	635		44.0		325	
		64	569	552		22.3		160	
Diagonal	C	50	-	1669	5.0	10	200	-	(du Plessis et al., 2018b)
Rhombic				1317		20	200		
Dia	C	80	650	200	-	1.2	36	-	(Zhang et al., 2018)
		76		250		2.0	57		
		73		300		3.0	86		
		68		350		3.8	109		
		66		400		5.2	140		

Abbreviations: BCC—body-centric cubic; C—compression; Dia—diamond; E—modulus; EBM—electron beam melting; FT—feature thickness; Gyr—gyroid; Hex—hexagonal; LT—loading type; σ_y —yield strength; σ_u —ultimate strength; Neov—Neovius; P—porosity; PS—pore size; S—support; SLM—selective laser melting; Sch—Schwarz; SC—simple cubic; T—tensile; TPMS—triple periodic minimal surface; UCS—unit cell size. Note that unavailable modulus and strength values were obtained from published force, displacement, and stiffness values or estimated from the provided graphs.

Table 1-2: Selected studies on the flexural static loading of additively manufactured lattice constructs.

Lattice	AMT	LT	P (%)	FT (μm)	UCS (mm)	E_F (GPa)	σ_{FS} (MPa)	Reference
RDod	EBM	4PB	80	454	3	5.7	60	(Horn et al., 2010)
			70	575	3	7.7	63	
			60	722	3	10.7	84	
			80	905	6	1.7	27	
			70	1153	6	5.6	75	
			60	1408	6	12.5	132	
			80	1361	9	2.4	32	
			70	1732	9	6.6	73	
60	2096	9	14.1	120				
OT	EBM	3PB	-	1000	-	2.5	60	(Di Caprio et al., 2022)
OT (OS)						27.6	376	
OT (OS; SL = 200 mm)	EBM	3PB	-	600	6	18.4	312	(Bellini et al., 2021a, Bellini et al., 2021b)
OT (SL = 120 mm)						12.5	312	
OT (OS; SL = 45 mm)						2.04	237	
FGP-Dia (OS)	SLM	3PB	79	300	1.8–2.2	1.41	100	(Tüzemen et al., 2022)
FGP-Dia (OS)			61	500		2.81	500	
FGP-Dia (OS)			41	700		3.82	780	
FGP-SC (OS)			85	300		0.38	25	
FGP-SC (OS)			75	500		1.15	80	
FGP-SC (OS)			63	700		2.42	270	
FGP-Oct (OS)			84	300		0.66	40	
FGP-Oct (OS)			74	500		1.68	140	
FGP-Oct (OS)			63	700		2.66	320	
FGP-BCC	SLM	3PB		260–810	2	6.4	300	(Song et al., 2021a)
BCC				200		0.8	66	

Abbreviations: 3PB—three-point bending; 4PB—four-point bending; AMT—additive manufacturing technique; BCC—body-centric cubic; C—compression; Dia—diamond; E_F —modulus; EBM—electron beam melting; FGP—functionally graded porosity; FT—feature thickness; LT—loading type; OT—octet truss; OS—outer skin; P—porosity; PS—pore size; RDod—rhombic dodecahedron; SC—simple cubic; SLM—selective laser melting; σ_{FS} —flexural strength; TPMS—triply periodic minimal surface; UCS—unit cell size. Note that unavailable modulus and strength values were obtained from published force, displacement, and stiffness values or estimated from the provided graphs.

Although many studies have investigated lattice constructs with uniform porosity, recent work has focused on lattice constructs with nonuniform pore geometry. For example, functionally graded porous (FGP) constructs have been designed to match the heterogeneous structural or mechanical properties of different locations within bone (Schwartz-Dabney and Dechow, Schwartz-Dabney and Dechow). Porosity gradient FGP designs attempt to match variation in the natural structure of bone (Xu et al., 2023, Mahamood and Akinlabi, 2017, Mahmoud and Elbestawi, 2018). In topology optimized FGP designs, the density of the lattice structure is set to match spatial variation in the mechanical properties of bone (Zhao and Zhang, 2021, Xu et al., 2023). In both cases, the gradient within FGP designs is ideally continuous to simulate the complex features of bone structure and its mechanical properties (Mukherjee et al., 2023).

One approach to produce nonuniform lattice designs is to vary pore geometry by changing the unit cell size or to alter strut thickness without changing the unit cell size. Onal et al. (2018) found that FGP constructs with a pore size ranging from 400 μm on the outside to 800 μm on the inside could provide higher strength than uniform porous constructs with a strut thickness of 600 μm . Shi et al. (2017) and Yang et al. (2019) reported on FGP constructs with compressive moduli similar to the elastic moduli of load-bearing bones. Han et al. (2018) employed a similar technique to develop FGP titanium alloy constructs with a Schwarz triply periodic minimal surface (TPMS) pore structure. Feature thicknesses varied between 483 and 905 μm , producing compressive modulus values ranging between 0.28 and 0.59 GPa. Song et al. (2021b) were able to determine the flexural properties of FGP lattice models, where the density of the porous constructs was adapted to the loading on the construct. The results showed that the FGP constructs had superior performance and strength, while minimizing weight, when compared to uniform lattice constructs.

Another approach for the fabrication of nonuniform lattices is to use biphasic designs, with one phase being a lattice structure and the other being a denser lattice or non-lattice shell or core. This approach has received significant acclaim among researchers due to superior static and fatigue strength when compared to fully lattice design concepts. In this regard, Fousová et al. (2017) produced constructs with a lattice shell and solid core having a Young's modulus equivalent to mandibular bone. SLM-built FGP Ti6AL4V constructs,

with a triply periodic minimal surface design (gyroid or diamond) cellular structure, were investigated for use as bone scaffolds by Liu et al. (2018). They found that both patterns produced compressive moduli comparable to trabecular bone ($\approx 2.1\text{--}3.8$ GPa). Using SLM, Xiong et al. (2020b) built porous constructs with solid cores for potential use in dental implants. The porosities of the constructs ranged between 50 and 70%, and the pore sizes ranged between 420 and 630 μm . The overall compression modulus was between 4 and 11 GPa, within the range of the overall Young's modulus of mandibular bone. Tüzemen et al. (2022) built lattice constructs with functionally graded unit cell sizes and an outer non-lattice skin. These constructs could produce flexural properties comparable to cortical and trabecular bone.

1.8 Bone growth into lattice constructs

Researchers are interested in the potential of lattice SLM-built constructs to allow for bone ingrowth. Bone formation and stabilization around implants have been described in several recent reviews (Wang et al., 2022, Grzeskowiak et al., 2020, Lu et al., 2021, Xiao et al., 2022). Xiao et al. (2022). and (Bai et al., 2021) divided the process of bone-implant integration into five phases: blood clotting, immune response, angiogenesis, osteogenesis, and osseointegration. This process is similar to bone healing following fracture except for the lack of callus formation (Colnot et al., 2007).

Immediately following surgical implantation, blood clots form along the implant and bone boundaries (Xiao et al., 2022, Wang et al., 2022). Immune cells are recruited, and growth factors are released to stimulate the formation of blood vessels (angiogenesis) and bone (osteogenesis) (Sivaraj and Adams, 2016, Xiao et al., 2022, Franchi et al., 2005). Osteogenesis consists of two processes, osteoinduction and osteoconduction. Osteoinduction is the proliferation and differentiation of mesenchymal stem cells to produce preosteoblasts and then osteoblasts (bone-forming cells) (Albrektsson and Johansson, 2001). Osteoconduction is the process by which bone growth is guided along the surface of non-lattice constructs (Albrektsson and Johansson, 2001, Davies, 2003), or the internal surfaces of lattice constructs (Wang et al., 2022). Osseointegration describes the structural and functional integration of the bone and implant along the surfaces in direct

contact (Branemark, 1983, Branemark, 2005). The extent of osseointegration determines the implant's long-term functional loading capability (Jayesh and Dhinakarsamy, 2015).

Parameters, such as pore size, shape, porosity, inter-connectivity, and surface roughness influence cell differentiation, bone ingrowth, and ultimately the osseointegration of lattice constructs (Tan et al., 2017, Wang et al., 2022, Bobbert and Zadpoor, 2017, Van Bael et al., 2012). In vitro studies have investigated osteogenic cell attachment, proliferation, and differentiation on lattice SLM-built constructs (Tan et al., 2017, Wang et al., 2022). These studies established that pore sizes ranging between 500 and 1000 μm (Xue et al., 2007, Van Bael et al., 2012, Rumpler et al., 2008, Warnke et al., 2009) and a porosity of more than 60% (Zhang et al., 2022) are advantageous for osteogenesis. In vivo studies have investigated bone ingrowth into lattice constructs (Tan et al., 2017, Dziaduszezwska and Zielinski, 2021, Wang et al., 2022). A summary of the results from selected in vivo studies can be seen in Table 1-3. Some studies observed bone ingrowth by measuring the volume of bone as a ratio of the total volume of the specimens (BV/TV) using micro-computed tomography (μCT) (Ponader et al., 2010, Tan et al., 2017). Other studies used histological approaches to quantify bone ingrowth (Ponader et al., 2010, Taniguchi et al., 2016). Finally, in some studies, mechanical push-out or pull-out analyses were used to determine the level of integration of the bone and the construct, with higher force applied on the specimen indicating higher levels of integration (Taniguchi et al., 2016, Ponader et al., 2010). In vivo studies indicated that optimal bone ingrowth occurs at pore sizes ranging between 300 and 900 μm , at porosities ranging between 70 and 84%, and with moderate surface roughness (arithmetic mean height between 1 and 2 μm). In addition, biomimetic coatings, such as hydroxyapatite (HA), can promote the integration of SLM-built titanium constructs.

The time taken for bone ingrowth into lattice titanium alloy constructs is also of interest when designing implants. Integration takes between 6 and 12 weeks to occur in some animal models (Zhang et al., 2022, Taniguchi et al., 2016, Watanabe et al., 2023). Moreover, 40% bone growth into the lattice constructs was achieved within 6 months in sheep (Li et al., 2017). Implants with porous (sintered) surfaces were shown to take up to 9 months to fully fuse with human bones (Hofmann et al., 1997).

Table 1-3: Selected studies investigating bone growth into lattice titanium and Ti6Al4V constructs.

Pore	PS (μm)	P (%)	Ra (μm)	Animal	Key Findings	Reference
Rectangular prism pore	450	-	0.08	Pig	BV/TV = 45% at 60 days Bone density lower than original bone	(Ponader et al., 2010)
Equ tri shell	650	-	-	Beagle	HA-coated shell BA/TA = 50% and porous core BA/TA = 40% at 12 weeks HA-coated specimen had the highest push-out strength by 6 weeks of implantation when compared to non-HA-coated porous specimen HA-coated specimen had the highest BA/TA when compared to non-HA-coated porous specimen	(Watanabe et al., 2023)
Equ Tri shell + cir						
Equ Tri shell + cir + HA						
Gyr TPMS	600	-	-	Sheep	The highest push-out force at 12 weeks: SC and Gyr TPMS Highest BV/TV at 12 weeks were found in Gyr, D pyr, and SC Pores with round or quasi-round shape had the largest BV/TV BV/TV at 12 weeks ranged between 60 and 80%	(Kovacs et al., 2023)
SC						
Cir						
Tet						
D pyr						
Vor						
SC	700	40	-	Rats	At the same PS and after 4 weeks, P = 70% and P = 90% had significantly higher BV/TV than P = 40% At the same P and after 4 weeks, BV/TV was highest when the nominal PS = 700 μm	(Zhang et al., 2022)
		70				
		90				
	400	70				
Dia Cry	300	62	-	Rabbits	Mature lamellar bone was detected in all the constructs. At 8 weeks, the deepest penetration was in PS = 600 μm At 8 weeks, the detaching (pull-out) force was highest in PS = 600 μm	(Taniguchi et al., 2016)
	600	66				
	900	64				
SC	700	84	3.33	Rabbits	At 8 weeks, defect bridging was at 80% in all constructs and highest in SLA constructs Mineralized tissue in the original defect was the highest in sandblasted constructs	(de Wild et al., 2013)
SC-Sand			0.94			
SC-SLA			1.16			
Dia	710	68	-	Sheep	CT scans at 3 and 6 months showed significant bone growth.	(Li et al., 2017)

					BV/TV at 6 months reached about 40% Mineralized tissue at 6 months made up 38% of the total volume	
--	--	--	--	--	---	--

Abbreviations: BA/TA—bone area/total area; BV/TV—bone volume/total volume; Cir—circular; Cry—crystal; CT—computed tomography; Dia—diamond; D pyr—double pyramid; Equ tri—equilateral triangle; Gyr TPMS—gyroid TPMS; HA—hydroxyapatite; P—porosity; PS—pore size; Ra—mean arithmetic height of surface roughness; Sand—sandblasted; SC—simple cubic; SLA—sandblasted and chemically etched; Vor—Voronoi. Note: The data reported under key findings were obtained at the maximum time implants were in place. Only in vivo test results are reported.

1.9 Finite element analysis in the development of lattice constructs

The gold standard for determining the mechanical properties of SLM-built constructs is to perform uniaxial or multiaxial testing on multiple specimens. However, this step is both costly and time-consuming. Finite element analysis (FEA) has been widely used in the design of mandibular implants and fixation plates as a precursor to real-life pre-clinical mechanical or clinical trials (Roberts and Pallister, 2012). FEA involves splitting a complex structural model into smaller, less complex parts referred to as finite elements, which can then be resolved through element or nodal analysis (Logan, 2012, Baccouch, 2021). As a computer-based numerical technique, FEA enables calculating the mechanical behaviour of structures under various stress conditions (Ilavarasi and Anburaiyan, 2011). FEA can identify locations of high-stress concentration where implant failure is likely to occur. FEA's accuracy and precision depend highly on the proper assignment of material properties, boundary and loading conditions, and meshing properties, as well as the calculation method used (Plumbridge et al., 2003, Roberts and Pallister, 2012, Logan, 2012, Pidaparti, 2017).

When modelling a lattice construct by FEA, three methods can be used. The first involves modelling lattice constructs as solid elements, which is the most used and precise approach for both lattice and non-lattice models (Di Caprio et al., 2022, Xiong et al., 2021). This method accurately captures the model's geometry, including edge effects such as the intersection of struts. It precisely measures the areas where the lattice model is most vulnerable to stress. Potentially any geometry could be modelled using this method.

However, using solid elements has several drawbacks, and one of the most disadvantageous is the expensive computational power involved. In addition, the results are highly dependent on the meshing properties. The drawbacks of using solid elements have forced researchers, up until recently, to limit the size of tested models (Zhao et al., 2016). However, recent developments in the computational power of processors and the introduction of dedicated graphics processing units have opened the possibility of running simulations using more complex lattice properties through solid element modelling (Di Caprio et al., 2022, Jin et al., 2021). Another approach that can be taken is to optimize the size of the mesh elements, where the regions of interest on the models or regions where stress concentrations could be formed would be assigned a finer mesh size and distribution. In contrast, other regions would be given a coarser mesh.

The second method consists of modelling the struts using beams or cables to represent the lattice elements. By omitting the solid thickness of the struts, the meshing process is simplified, leading to faster simulation. Using beam elements only works with beam-based lattice structures and overlooks stress concentrations and edge effects, making it less accurate than solid elements. This technique was used in recent studies, such as that by Song et al. (2021b). In that study, beam elements were denoted as “virtual” struts that were used to perform the mechanical simulation analysis. Hence, this technique allows for the modelling of FGP lattice models as well as uniform lattice models. An earlier study by Smith et al. (2013) also showed that FEA modelling of constructs using the beam element method produces largely accurate results in models under compression loading.

The third method of modelling lattice constructs in FEA is to use mass and density properties to create representative non-lattice models with the internal density properties associated with lattice models. This technique, known as homogenization, can be used for any lattice and is particularly effective in modelling lattice structures with a high density of pores. However, this method does not assess stress concentration and edge effects, as the exact lattice structure is not provided. Furthermore, this method cannot be used to simulate FGP models. Despite these drawbacks, homogenization may be a good option when the lattice model’s complexity or number of pores makes it impossible to use one of the other two methods. Recent studies, such as the one published by Panettieri et al. (2021),

assessed the accuracy of homogenization techniques when compared to modelling lattice constructs as solid elements. Panettieri and co-workers found that homogenized models have the potential to match solid element modelling. Dias et al. (2014) adopted homogenization techniques to produce lattice scaffold designs.

FEA has been used previously to study the mechanical properties of the mandible (Geng et al., 2001, Vollmer et al., 2000). For example, Koriath and Hannam (1994) identified the levels of forces and deformation experienced by the mandible during a simulated unilateral molar bite. Examples of prototyping using FEA include studies conducted on scaffolds by Luo et al. (2017), who performed mechanical simulations of intercuspal, incisal, and unilateral molar clenching in a mandibular model derived from computed tomography (CT) scans. Other FEA studies have shown that the mandible can experience stress levels ranging between 6.5 and 80 MPa with muscular activity and normal chewing behaviour (Gholampour et al., 2019, Peng et al., 2021, Pinheiro and Alves, 2015, Wong et al., 2012, Yoon et al., 2021).

Ideally, FEA simulations should be validated through mechanical testing of constructs. In this regard, Burton et al. (2019) used FEA and mechanical tests to determine the compressive mechanical properties of porous constructs with variations of TPMS pores and simple cubic pores. Another example is the work conducted by Di Caprio et al. (2022). Di Caprio and co-workers used a combination of FEA and mechanical tests to determine the flexural mechanical properties of lattice constructs. They showed that FEA models have the potential to match real-life testing results when strut thicknesses are modified.

Maxillofacial implants and fixation plates have also been studied using FEA modelling. The formation of stress concentrations in bone adjacent to the fixation devices is critical. One example is a study by Ji et al. (2010) on the effect of miniplate numbers on stress flow through the adjacent mandibular bone. They found that stress shielding escalates with an increasing number of miniplates, which is expected to affect long-term stability of the miniplates. Another measure of the stability of fixation plates relative to the adjacent bone is the strain level of implants and fixation screws during loading, which can also be estimated through FEA. For example, Zhong et al. (2021) conducted a study comparing locking and non-locking, patient-specific mandibular reconstruction plates. The results

showed that locking fixation plates exhibited better strength, flexibility, and general safety, as demonstrated by lower von Mises stress, elastic strain, and deformation, than the non-locking fixation plates. Other studies have determined the effect of geometry and orientation of miniplates on stress concentration, with one example being Jesus et al. (2014). In that study, it was found that lambda-shaped plates displayed a more homogeneous stress distribution than the customarily used straight plates. It was also found that fixation devices with patient-specific properties adapted to the bone surface contour are superior to mass-produced fixation plates.

Discrepancies between CAD models and the resulting geometrical properties of lattice constructs have been reported. Horn et al. (2014) reported that 3D-printed lattice constructs had strut thicknesses and densities that deviated significantly from the original CAD files. In a recently published work, Di Caprio et al. (2022) found that FEA models did not match the flexural properties of their 3D-printed lattice construct counterparts until the strut thickness of the FEA models was reduced by about 20%. These results show that the non-homogeneity of 3D-printed lattice struts and deviations in their geometrical structure should be considered when building FEA models.

Another challenge of FEA analysis is replicating and modelling surface roughness, which is inherent in the 3D printing of Ti6Al4V constructs. Recent attempts to include surface roughness on struts in FEA models are promising. For example, Ghosh et al. (2022) assessed the effects of surface texture on the mechanical properties of 3D-printed steel struts. They first analyzed the surface texture geometry and then incorporated it into an FEA model of the struts. A similar study, conducted by Yáñez et al. (2020), used FEA to analyze the stress concentrations of gyroid TPMS models with different surface roughness levels. Both studies mentioned above showed that stress levels higher than the yield stress of Ti6Al4V can occur due to ridges on the surface. Thus, premature fractures could initiate at the ridges on the surface of the constructs upon application of mechanical loading.

1.10 Lattice-structured mandibular implants with cage and crib designs

Given the benefits of implants with optimized overall geometry and the capability of building lattice structures using additive manufacturing, researchers have been interested in introducing lattice structures into mandibular implants in clinical settings. One design concept that has seen much interest in recent years is the patient-specific intraosseous mandibular implant, with either a cage or a crib structure, to fill the gap formed by mandibular segmentation surgery. This design concept has seen promising clinical results (Kondo et al., 2015, Lee et al., 2019, Malekpour et al., 2014, Mounir et al., 2020, Park et al., 2020). The intraosseous implant design comes with major advantages over the current standard of treatment. While such a design can incorporate bone grafts, it can also function without them, making it a highly versatile option when bone donor site morbidity is a concern. Fatigue fracture risk is reduced as no bending is performed on the implant components during surgery. The technical and surgical complexity is reduced, and the aesthetic outcome is improved due to the matching of implant geometry to the original bone shape (van Kootwijk et al., 2022).

In addition to the previously mentioned advantages, the intraosseous implant is able to restore masticatory functions. For example, Shen et al. (2022) used FEA and in vitro mechanical tests to assess the design of porous intraosseous (cage) mandibular implants with circular or hexagonal pore shapes and pore sizes of 1 or 2 mm (Figure 1-5). Such devices were fixed using two small wing plates that attach the implant to the mandible using screws. The mechanical loading and simulations were performed to emulate loading on the mandible through either molar clenching or group function (molars, premolars, and canine). It was reported that porous Ti6Al4V constructs presented higher stresses than nonporous constructs. However, none exhibited von Mises stresses greater than the yield stress of Ti6Al4V. They also found that pores with circular shapes produced lower stress levels than those with hexagonal shapes, indicating that pores with fewer sharp edges may have higher overall resistance to fracture. When molar clenching was simulated, the FEA model detected strain levels in the surrounding bone (Frost, 1987) that would likely lead to

bone deformation and, consequently, remodelling. The construct built by the researchers incorporated an abutment base fused with the construct, which could then be used to restore occlusal function. The restoration of masticatory and occlusal function has immense importance as a consideration in the design of mandibular implants.



Figure 1-5: The mandibular implant introduced by Shen et al. (2022).

The researchers presented two versions of the implant, the nonporous version of the implant, displayed here from a frontal view (a), and the porous version of the implant, displayed here from a side view (b). (This work is licensed under the Creative Commons Attribution 4.0 International License. To view a copy of this license, visit <http://creativecommons.org/licenses/by/4.0/> or send a letter to Creative Commons, P.O. Box 1866, Mountain View, CA 94042, USA).

Peng et al. (2021) studied another intraosseous (cage) implant concept. The internal structure of the implant consisted of titanium lattice layers with struts connecting the lattice layers. This design allowed for the use of bone grafts. FEA analysis revealed that von Mises stress concentrations were sufficiently low within the implant. The highest stress was concentrated on the screws attaching the implant to the bone (≈ 590 MPa). The researchers showed that the proposed design had a stable stress distribution within itself and the adjacent bone, comparable with that seen in healthy mandibular bone, indicating that the model alleviates stress shielding. Through FEA, the researchers tested the design under different degrees of bone ingrowth to assess the stress and strain experienced by the bone and the implant. This design has enormous potential given the stability and general lack of large stress concentrations in the implants; however, this model was not validated by static

and dynamic mechanical testing. Nevertheless, results from this study demonstrate the ability of porous lattice constructs to overcome stress shielding.

A crib design of an intraosseous mandibular implant was proposed by van Kootwijk et al. (2022). The research group utilized the shape of the mandible to design patient-specific mandibular implants using a semi-automated digital workflow. The design utilizes a basket feature, which means that the implant is open in the superior region, making it compatible with bone grafts. Three designs were tested by the authors, one with a nonporous (solid-implant) design, the second with a complete lattice design (LA-implant), and the third design (TO-implant) consisted of a thick set of bars that were optimized topologically to be lightweight, with a finer lattice filling the spaces between the thick bars (Figure 1-6). Unlike many similar investigations, this study provided both FEA and experimental information to assess the design concept. The researchers also provided a simplified method to experimentally test the mechanical properties of the implant under both static and fatigue loading conditions. The fatigue tests were conducted using constant or incremental cyclic loading within physiological conditions for up to 250,000 cycles at 3 Hz. Results showed that all the implant design models had von Mises stress values that were lower than the yield strength of Ti6Al4V, with stresses concentrated at the angle region of the mandibular implant. All the implants maintained high levels of fatigue strength, with no evidence of failure through the 250,000-cycle loading. The researchers found that the fully lattice design was preferable as it was mechanically compatible with the mandible while maintaining higher porosity and a lower cost of production. This work emphasized the importance of analyzing the mechanical properties of mandibular implants under static and dynamic loading conditions.

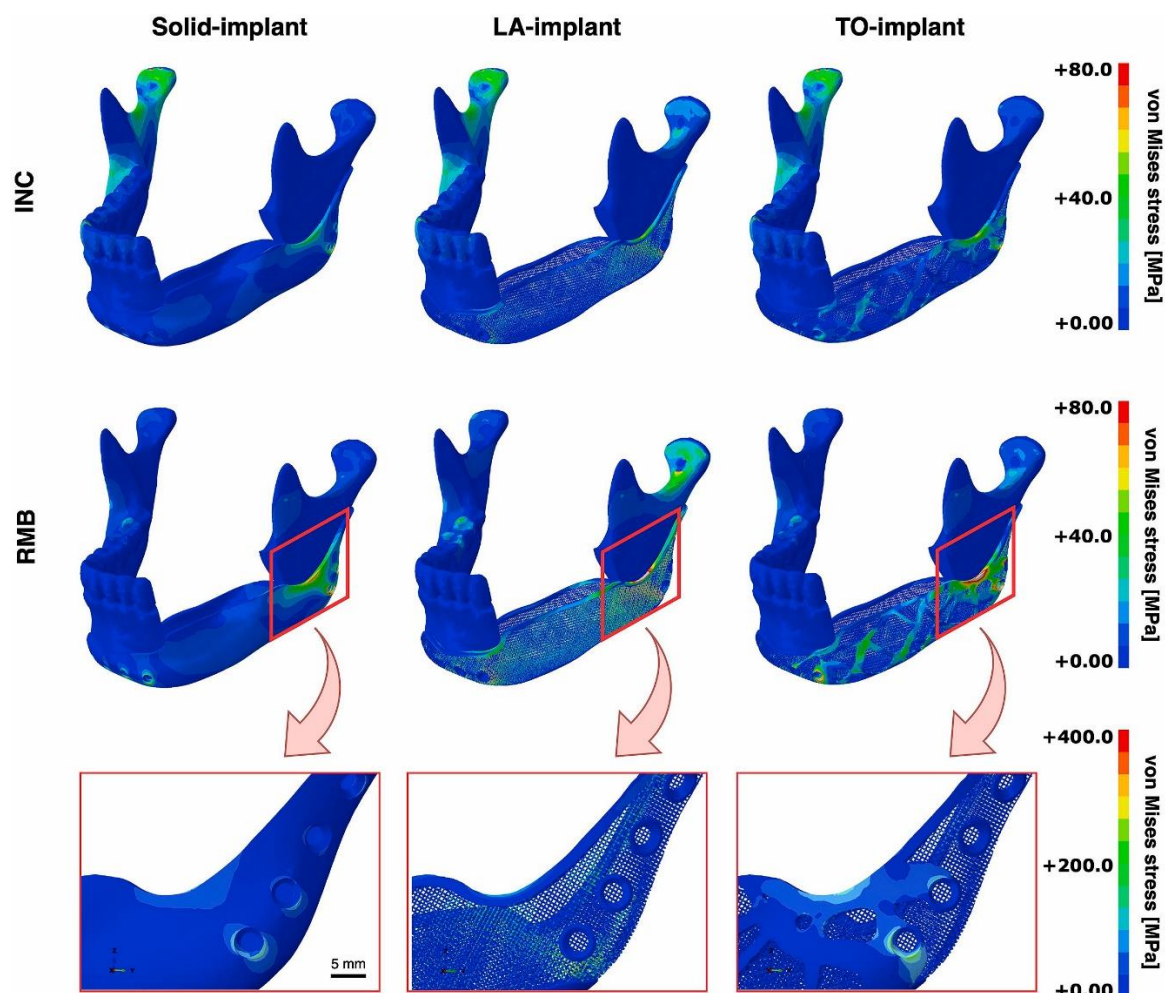


Figure 1-6: FEA analysis results of the three implants designed by van Kootwijk et al. (2022) under incisal clenching (INC) and right molar biting (RMB).

The models were fully non-lattice (solid-implant), fully lattice (LA-implant), and topology optimized (TO-implant) with both lattice and non-lattice parts. The von Mises stresses indicate that no failure is expected within any of the implants, with the highest stress concentrations being located at the angle region of the implant. (This work is licensed under the Creative Commons Attribution by Non-Commercial Non-Derivative 4.0 International License. To view a copy of this license, visit <https://creativecommons.org/licenses/by-nc-nd/4.0/> or send a letter to Creative Commons, P.O. Box 1866, Mountain View, CA 94042, USA).

Another example of an intrasosseous implant was reported by Mommaerts (2016), who used porous implants partially covered with shells to restore mandibular defects at the lower part of the mandibular angle and the lateral mandibular border. The design incorporated pore sizes of 500 μm and diamond-shaped pores. Constructs were implanted in 12 patients with aesthetic and malformation complaints. Most patients were satisfied with the procedure.

However, it should be noted that the patients were only monitored for up to three months following surgery.

These studies show that using SLM to fabricate porous intraosseous mandibular implants is possible. These patient-specific implants attempted to match the mechanical and geometrical properties of the mandibular bone. Future testing of such design concepts should be conducted using both FEA modelling and mechanical loading analyses.

1.11 Microstructural imperfections in SLM-built Ti6Al4V constructs

There is great potential for using 3D printing in fabricating medical implants. However, the application of additive manufacturing faces several operational and functional challenges. These challenges include microstructural issues and internal defects (Snell et al., 2019, Zhang et al., 2017, Khairallah et al., 2016, Kan et al., 2022).

The microstructure of Ti6Al4V is known to have two phases, the hexagonal-shaped α phase, which is stabilized by the aluminum, and the body-centric cubic-shaped β phase, which is stabilized by the vanadium (Park and Lakes, 2007). Ideally, an equiphase $\alpha + \beta$ microstructure, with α grains and a discontinuous β phase, would provide sufficient ductility and strength. In previous studies, different heat treatments and alloy concentrations were used to vary the microstructure, which gave rise to different mechanical properties (Ge et al., 2023, Park and Lakes, 2007, Yan et al., 2019). In SLM-built Ti6Al4V, the microstructure contains prior β grains, within which martensitic α' platelets are present, giving rise to a relatively high yield strength but low ductility (Gong et al., 2015, Murr et al., 2012a, Tan et al., 2017, Yadroitsev et al., 2017). Yan et al. (2019) have shown that lattice Ti6Al4V constructs exposed to hot isostatic pressure (HIP) appear to have both higher compressive strength and higher fracture strain when compared to as-built constructs. HIP involves applying both high temperature and isostatic pressure simultaneously, with the pressure medium being a noble gas like argon. Yan and coworkers also performed microscopic analysis of fracture surfaces in HIP-processed and as-built constructs. They observed a more brittle needle-like α' martensite in as-built constructs and

a more ductile $\alpha + \beta$ lamellar structure in HIP-processed samples. Ge et al. (2023) recently studied SLM-built porous Ti6Al4V constructs. Exposure of these constructs to vacuum annealing converted the microstructure into an equiphase $\alpha + \beta$ structure, which improved ductility. Similar work by Yadroitsev et al. (2017) showed that the ductility of SLM-built Ti6Al4V constructs increased after annealing, which was explained by the formation of an $\alpha + \beta$ structure. Thus, the microstructural texture of SLM-built Ti6Al4V constructs has a direct effect on mechanical properties.

Internal defects are gaps formed within the structure of SLM-built constructs. Such internal defects depend largely on the volumetric energy density applied by the laser on the material (Thijs et al., 2010, Yadroitsev et al., 2015). The equation that governs this process is as follows:

$$E = \frac{P}{VHT} \quad (1-1)$$

where E is energy density, P is laser power, V is laser scanning velocity (speed), H is hatching spacing, and T is layer thickness. To reduce the number and size of internal defects, the energy density should be optimized, which can be achieved by manipulating the parameters described in Equation (1). The optimization of these parameters for additive manufacturing has been described in multiple studies in the last decade (Cunningham et al., 2017, Kan et al., 2022, Montalbano et al., 2021, Snell et al., 2019, Yadroitsev et al., 2015, Zhang et al., 2017).

Identifying and categorizing internal defects is essential to determine their possible effects on mechanical properties (du Plessis et al., 2020b). Defects are typically identified using CT, scanning electron microscopy (SEM), or light microscopy. In general, the three major internal defects that can form on and within SLM constructs are lack-of-fusion, keyhole, and entrapped gas defects (Cunningham et al., 2017, Kan et al., 2022, Snell et al., 2019). When the volumetric energy density is too low, lack-of-fusion defects can occur. These defects can be characterized by their larger size ($>100 \mu\text{m}$) and irregular truncated shape (aspect ratio < 0.5) (Snell et al., 2019, Zhang et al., 2017). Lack of fusion occurs when the low energy density causes insufficient melting and fusion of two consecutive layers in the

additively manufactured constructs. The irregularity in the geometry of these defects is thought to be caused by an erosion of the substrate along different tracks during the SLM process (Khairallah et al., 2016). This would cause the formation of gaps along the hatch distances of the constructs (Kan et al., 2022).

When the volumetric energy density is too high, keyhole defects can occur. These defects are similar in size to the lack-of-fusion defects but have a more regular shape (aspect ratio > 0.5) (Snell et al., 2019, Zhang et al., 2017). Given the high energy density input, evaporation of the metal can occur, which in turn leads to the keyhole formation within the melt pool (Cao et al., 2017, Pal et al., 2020, Kan et al., 2022). The cavity forming the keyhole remains open due to vapor pressure, deepening further due to the scattering of heat from the laser. (Antony and Arivazhagan, 2015, Khairallah et al., 2016, Svenungsson et al., 2015) The keyholes collapse when the laser beam passes, entrapping the vapor into the formed defect.

Gas pores are the smallest internal defects typically seen in SLM constructs. These pores are usually spherical in shape and smaller in size ($<100 \mu\text{m}$) when compared to the other two kinds of internal defects discussed above (Voznesenskaya et al., 2021). Gas pores are known to occur during the evolution of the melt pool, when it is largely unstable and gas from the environment gets entrapped (Ransenigo et al., 2022). It should be noted that gas defects are more likely to occur when the density of the Ti6Al4V powder is low before the 3D-printing process starts (Salem et al., 2019, Zhang et al., 2017).

Internal defects, particularly lack-of-fusion defects, are known to affect the elastic modulus, strength, elongation, and fatigue resistance of SLM-built nonporous Ti6Al4V constructs (Campoli et al., 2013, du Plessis et al., 2020a, du Plessis et al., 2020b, Hu et al., 2020, Leuders et al., 2013, Shipley et al., 2018, Wickmann et al., 2021). In all the cited studies, the defect volume percentage had to be very high for an appreciable effect on material properties to occur. There is general agreement that internal defects of less than 1% in volume percentage and defect sizes of less than $500 \mu\text{m}$ will not cause a marked effect on the mechanical integrity of the constructs (du Plessis et al., 2020b, Gong et al., 2015). In addition, some work has shown that defects forming from low volumetric energy density, such as lack-of-fusion defects, can be more detrimental to the static mechanical

properties than defects forming due to high volumetric energy density, such as keyhole defects (du Plessis et al., 2020a, Gong et al., 2015).

Internal defects take on greater importance when considering lattice-structured porous constructs. This is an active area of investigation among researchers. Salem et al. (2019) Salem et al. performed imaging analysis of a series of lattice Ti6Al4V constructs built using SLM to find a range of laser power and scanning speeds that minimized internal defects. Unlike other studies, Salem et al. (2019) Salem et al. categorized defects forming due to low energy density input into two categories: lack-of-fusion defects that occur due to high scanning speed together with high laser power and “irregular” defects that occur due to high scanning speed together with low or intermediate laser power. While observing the same internal defects seen in nonporous constructs, Salem et al. (2019) Salem et al. indicated that an additional defect, known as sagging, occurs at the junction points of struts in the lattice constructs. These defects occur due to high energy input, which causes excessive molten material to flow downwards under the effect of gravity.

Internal defects in SLM-built Ti6Al4V constructs have been a focus of research over the years. Several methods have been proposed to remove or relieve them. These are further discussed in Sections 1.13 and 1.14 below.

1.12 Fatigue loading of 3D-printed Ti6Al4V constructs

Fatigue properties of 3D-printed Ti6Al4V lattice constructs are critical for their application in clinical settings. The traditional measure of fatigue life in non-lattice Ti6Al4V constructs is the number of cycles that have been applied when the stiffness of the tested construct drops by 90% from its initial stiffness or when the maximum number of cycles (generally between 10^6 and 10^7 cycles) is reached (Ahmadi et al., 2019, Chern et al., 2019, Liu et al., 2020, Zhao et al., 2018). The fatigue life of Ti6Al4V lattice constructs is less than that of non-lattice constructs (Ren et al., 2019, Xiong et al., 2020a). In lattice structures, fatigue strength and resistance are dependent on the composition and microstructure of the construct (Antonysamy et al., 2013, Cao et al., 2017, Kumar et al., 2018, Tong et al., 2016), surface treatment, oxygen content of the surface (Wycisk et al., 2014) (Gao et al., 2017, Moussaoui et al., 2015), and stresses being applied under fatigue loading (Belan et al.,

2019). The fatigue behaviour of lattice constructs, normalized to yield strength, has been described to be dependent mostly on the structure's unit cell shape and surface texture, rather than the density or porosity of the construct (Dallago et al., 2018, Yavari et al., 2015, Zhao et al., 2016).

Several authors have suggested that surface roughness is an important determinant of fatigue properties (As et al., 2008, Deligianni et al., 2001, Palanivel et al., 2016, Yadroitsev et al., 2017, Yáñez et al., 2020). A rough surface texture has been observed in lattice Ti6Al4V constructs produced using powder bed fusion techniques (Ge et al., 2023, Hernández-Nava et al., 2016, Xiao et al., 2020). Roughness can occur in SLM constructs due to the adherence of Ti6Al4V particles to the surface, the staircase effect, and the balling effect. Due to thermal diffusion—an outcome of differences in temperature between loose particles and the solidified material—the particles can be partially melted on the surface of the construct (Alghamdi et al., 2019, Wang et al., 2023). In the staircase effect, SLM is unable to produce smooth curvatures due to the layer thickness being too large to capture the curvature, resulting in a rough surface (Luis Pérez et al., 2001, Pyka et al., 2013, Yan et al., 2019). The balling effect arises from excessive scanning speed and/or low laser power during 3D printing. These lead to instability in the thermal gradient within the melting pool, which would result in Ti6Al4V particles being melted only partially while also compromising integration with the underlying layer. This causes the particles to form spherical agglomerates along the surface (Shipley et al., 2018, Tian et al., 2017, Xiang et al., 2018).

The formation of particles on the surface gives rise to alterations in the general geometry of lattice structures. Tüzemen et al. (2022), Hernández-Nava et al. (2016), and Xiao et al. (2020) reported that struts produced using 3D printing techniques had considerable deviations in geometry and thicknesses, driven by surface waviness and roughness. Adherence of powder onto struts has also been described by Song et al. (2021b), who reported that the thickness of struts in the designed models was less than that in the manufactured constructs. Song and coworkers also found that the FEA models and real-life constructs showed differences in flexural force and displacement values due to

inconsistencies in strut thickness. Thus, surface roughness affects the static and fatigue mechanical behaviour of lattice-structured constructs.

It is believed that mechanical failure is caused by large stress concentrations where surface roughness values are highest (Ahmadi et al., 2018, Hernández-Nava et al., 2016, Oosterbeek and Jeffers, 2022, Xiao et al., 2020, Yáñez et al., 2020). In their review, Cao et al. (2018) and Xiong et al. (2020a) reported that as-built 3D-printed non-lattice Ti6Al4V constructs are not compatible with fatigue-critical applications without significant post-processing treatments, citing surface roughness as the primary factor. Recent studies have found that the shedding of debris can occur during fatigue loading. Despite constructs remaining visibly intact, debris released during repetitive loading must be considered in biomedical applications as it can induce inflammation and bone resorption (Hallab, 2009, Oliveira et al., 2014, Goodman et al., 2020).

The role of internal defects, particularly those formed near the surface of lattice constructs, in fatigue fractures has been debated in the literature. Studies on nonporous constructs, such as those conducted by Kasperovich and Hausmann (2015), showed that internal defects are the initiators of fatigue cracking. Moreover, it was noted that reducing internal defects using hot isostatic pressure produced better fatigue strength. However, this outcome could be attributed to other factors, such as the microstructure becoming closer to the equiphase $\alpha + \beta$ state. Internal defects have been reported to reduce the fatigue life and strength of 3D-printed Ti6Al4V constructs (Leuders et al., 2013, du Plessis et al., 2020a). Nevertheless, a considerable body of work suggests that the cause of fatigue failure is stress concentration along surface ridges. According to Dallago et al. (2018), under the push–pull fatigue loading of lattice Ti6Al4V constructs, cracks originated from surface ridges rather than internal defects. Similarly, Yáñez et al. (2020) showed that, while internal defects were detected, they were of sizes smaller than 50 μm and did not appear to be the source of fatigue cracks. Other studies, such as that by Ahmadi et al. (2019), suggest that internal defects can cause crack initiation at high stresses and low numbers of loading cycles, whereas surface roughness is the main source of crack initiation at low stresses and high numbers of loading cycles.

A solution proposed to improve the fatigue life of Ti6Al4V lattice constructs is to introduce a nonporous core. Xiong et al. (2020a) studied Ti6Al4V lattice constructs with dense cores as dental implants both in vitro and in vivo. In vitro, compression fatigue tests were used to compare completely porous constructs to porous constructs with dense cores. Xiong and co-workers found that a porous Ti6Al4V construct with a dense core of about 1.8 mm in diameter and a porosity of 60% exhibited a fatigue strength of about 265 MPa at 10^6 cycles and an effective fatigue strength of 165 MPa at about 10^5 cycles. The fatigue strength, found by Xiong and co-workers, for the lattice constructs without a solid core was reduced by about 17 times. van Kootwijk et al. (2022) also investigated the effects of using non-lattice parts with porous constructs but found that there were no differences in the mechanical properties. These results were for compressive loading and may not be fully applicable to mandibular implants. Nevertheless, combining nonporous parts in regions of high-stress concentrations within the porous construct could improve the fatigue life of mandibular implants.

1.13 Fabrication measures to minimize structural imperfections

The optimization of SLM parameters is important to reduce the size and quantity of internal defects, whether constructs are lattice or non-lattice. In addition, the optimization of SLM parameters may avoid melt pool instability, which would also reduce the occurrence of surface roughness. Salem et al. (2019) showed that a combination of low laser power and intermediate laser scanning speed produced lattice Ti6Al4V constructs with minimal internal defects. Gong et al. (2015) have shown that lower than optimal energy densities and scan speeds are more likely to lead to the formation of lack-of-fusion defects, whereas higher scan speeds and energy densities may promote the formation of keyhole defects.

Prototyping techniques like FEA can assess different SLM parameters. FEA packages usually include mechanical behaviour analysis, as well as thermal and fluid flow behaviour analysis. The latter analysis is better known as computational fluid dynamics (CFD). Tang et al. (2017) used computer simulations to establish that fusion defects can be avoided by optimizing layer thickness, hatch spacing, and laser scanning speed. Khairallah et al. (2020) also used simulations to show that increasing laser power can reduce the formation

of keyhole pores in 3D-printed metal constructs. Xiang et al. (2018) used computer simulations to assess the formation of lack-of-fusion defects and surface roughness on 3D-printed constructs with different printing parameters, such as beam speed, layer thickness Kasperovich and Hausmann (2015), and hatch spacing. Kasperovich and Hausmann recommended a moderate scanning speed and a larger laser spot size to reduce internal defects. In addition, melting and subsequent cooling rates significantly affected internal defects (Montalbano et al., 2021, Zhang et al., 2017). Entrapped gas defects could be reduced by using a sufficient amount and density of Ti6Al4V powder during the printing process (du Plessis et al., 2018c, Yadroitsev and Smurov, 2011).

Regardless of the fabrication measures taken to minimize internal defects and surface roughness, optimization of SLM parameters cannot completely remove structural imperfections.

1.14 Post-processing treatments to improve mechanical properties and minimize structural imperfections

Post-processing treatments have been employed to reduce structural imperfections and to improve the mechanical properties of Ti6Al4V constructs.

Heat treatments are routinely conducted on constructs post-manufacturing to relieve residual stresses formed during the fabrication process (Shiomi et al., 2004, Matsumoto et al., 1999, Li et al., 2018). One such treatment, better known as annealing, is used to homogenize the microstructure of SLM-built constructs (Matsumoto et al., 1999, Li et al., 2018, Yuan et al., 2018). This approach was reported by Yuan et al. (2018), who tested lattice constructs with simple cubic pore topology and strut thicknesses of around 500 μm . They applied static and dynamic compression loading. They showed that annealing changed the microstructure of the constructs through the formation of coarse α lamellae with a large thickness-to-length ratio. This change increased the ductility of the constructs and, in turn, ramped up fatigue endurance to about 60% of the yield stress, which is well within the endurance limit for dense lattice and non-lattice Ti6Al4V structures.

However, traditional heat treatments do not reduce internal defects or surface roughness. One treatment that addresses the issue of internal defects is hot isostatic pressure (HIP). HIP utilizes both heat (≈ 900 °C) and isostatic pressure (≈ 100 MPa), which causes shrinking and densification of the construct from all directions (Tammas-Williams et al., 2016, Atkinson and Davies, 2000, Guo et al., 2023, Delo and Piehler, 1999). HIP has been shown to relieve Ti6Al4V constructs from internal defects, increasing their strength (Aslan et al., 2021, Liu et al., 2019). In addition, Kasperovich and Hausmann (2015) showed that HIP produces an effect on the microstructure of SLM-built constructs similar to that produced by annealing, with the internal structure becoming an equiphase $\alpha + \beta$ state. Hence, it can be seen that HIP can replace annealing while also reducing internal defects. A solution to deal with sub-surface pores is to apply laser shock peening, which improves the fatigue properties of Ti6Al4V (du Plessis et al., 2019, du Plessis and Rossouw, 2015). It also decreases the roughness of SLM-manufactured Ti6Al4V constructs by about 50% and increases their fatigue life by ten-fold (Aguado-Montero et al., 2022).

There is a wide array of post-processing surface treatments. In general, mandibular implants must exhibit high fatigue strength while maintaining a level of surface roughness that promotes bone cell attachment and proliferation (Jamshidi et al., 2020). A common surface treatment applied to SLM-built constructs is sandblasting or grit-blasting (Jamshidi et al., 2020). In both cases, abrasive particles of sand or grit are applied under high pressure to the surface of the construct, removing irregularities and unmelted particles and thus reducing roughness. However, a disadvantage of this technique is the potential for introducing bacteria into the construct that can hinder bone growth and lead to infection (Cox et al., 2017). Mechanical polishing is the simplest procedure to reduce surface roughness. However, mechanical polishing does not achieve the uniform smoothing of complex structures (Pattabi and Ramakrishna, 2008), making it unsuitable for use in lattice constructs. Other surface treatments for lattice constructs have been considered. These include electropolishing, where the SLM-built construct, as the anode, is immersed in an electrolyte with a cathode and placed under direct current (Dong et al., 2019). Under direct current, a reduction reaction occurs on the SLM-built construct, which uniformly removes surface irregularities (Kuhn, 2004, Rahman et al., 2014, Dong et al., 2019, Zhang et al.,

2019, Tsoeunyane et al., 2022). Another method to reduce surface roughness is chemical etching, which involves the use of acidic etchants to smoothen partially welded powder particles. A major advantage of this technique is that it allows for the removal of surface roughness from within the lattice constructs, unlike most other methods which target only the outer surfaces (Łyczkowska et al., 2014). On the other hand, chemical etching has been shown to be largely nonuniform in its treatment of surface roughness in SLM-built constructs (Hung, 2021).

Given the advantages and disadvantages of post-processing treatments, some researchers advocate for the use of multiple treatments for SLM constructs. For example, Dong et al. (2019) and Pyka et al. (2012) showed that electropolishing can reduce the surface roughness of Ti6Al4V lattice constructs when combined with etching. Another approach that Ahmadi et al. (2018) suggested was a combination of HIP treatment, sandblasting, and a moderate amount of chemical etching to reduce the surface roughness. This combination increased the compression and fatigue strength of lattice constructs as well as their ductility. Similarly, Jamshidi et al. (2020) have shown that a combination of HIP, sandblasting, wet centrifugal polishing, and chemical etching produces non-lattice constructs with enhanced ductility and improved tensile and fatigue strength when compared to as-built constructs. In addition, Jamshidi and coworkers showed that chemical etching, when combined with other treatments, enhances cellular adhesion and proliferation on the surface of SLM-built constructs. It should be noted that there is evidence that HIP can affect other surface roughness treatments, such as grit-blasting (Berger et al., 2020). Hence, any additional surface modifications should be performed after HIP is applied.

Although all these solutions have shown promise in reducing surface roughness and internal defects in lattice constructs, they also come with the disadvantage of decreasing strut thickness or altering the structure of struts. For example, Ahmadi et al. (2018) found that chemical etching can significantly reduce strut thickness. This could be challenging when dealing with lattice structures having small strut thicknesses.

1.15 Challenges with the clinical application of 3D-printed mandibular implants

Several challenges are hindering the introduction of permanent, patient-specific, lattice-structured mandibular implants. One challenge is reconstruction of the mandibular condyle. The condyle is the focus of movement of the mandible, and damage in that region can affect the normal range of motion. Such damage can cause difficulties in mastication and deep breathing, and deficiency in mandibular height (Disa and Cordeiro, 2000). Current treatment choices include using implants made of alloplastic materials (such as copper or titanium alloys) (Shenaq and Klebuc, 1994, Park et al., 2017). Some researchers suggest combining such implants with remodelled autogenous grafts (Mercuri, 2018). However, these options are either prone to complications or not universally suitable for patients. In addition, titanium devices for condylar reconstruction are associated with the risk of erosion (Shenaq and Klebuc, 1994), which would cause implant displacement and pain (Emshoff et al., 2021). In addition, lattice titanium alloys are expected to be highly susceptible to fracture due to friction. Hence, lattice-structured titanium alloy implants are not suitable for condylar reconstruction.

Challenges in the use of lattice titanium alloy implants extend to post-implantation functionality. One issue is the time of healing. There are few clinical studies on the time it takes for bone to grow into porous Ti6Al4V constructs. A few studies reported that porous mandibular implants appeared to be stabilized in patients within three months (Benady et al., 2023, Cordey et al., 2000, Fukuda et al., 2011). In vivo, animal models suggest that this process could take up to 6 months (Li et al., 2017). During bone healing, the issue of septic loosening may arise. Septic loosening is due to infection introduced at the point of implantation or by underlying infections (Bohara and Suthakorn, 2022, Zimmerli et al., 2004). One solution may be to introduce surface coatings onto mandibular implants, containing anti-bacterial agents and/or growth factors to minimize inflammation and stimulate bone ingrowth (Bohara and Suthakorn, 2022).

While several concept designs of intraosseous mandibular implants have been proposed over the years, these devices have not undergone extensive clinical experimentation.

Nevertheless, recent small-scale studies have shown promising outcomes. Xia et al. (2020) studied 10 oncology patients treated with customized Ti6Al4V implants without bone grafts. Results were compared to 10 patients who received vascularized bone grafts and conventional fixation. Compared to patients who underwent conventional treatment, patients from the titanium implant group showed improvements on several fronts, including mandibular contour symmetry, oral and masticatory function, range of mouth opening, and pain related to the temporomandibular joint. The paper did not mention pore topology and properties, but the authors indicated that porosity levels were such that the structural and mechanical properties of the implants matched those of the mandible.

While showing great potential, the use of additive manufacturing in producing clinically viable mandibular implants can be hindered by several challenges. The clinical challenges might require further innovative solutions to these problems, which should be the focus of future research.

1.16 Knowledge gaps

While a great amount of work has been published on designing and manufacturing lattice constructs using 3D printing techniques, this topic is still a subject of active research. Developments in design and testing are needed to ensure that a standardized and methodical workflow is established for the efficient fabrication of safe and effective constructs.

It should be noted that there is a considerable gap in the literature regarding the flexural fatigue properties of Ti6Al4V lattice constructs. This is thought to be due to the complexity of three- and four-point loading regimens used to study fatigue properties (Belan et al., 2019). Most of the studies reported in the literature dealt with compression fatigue testing (Ahmadi et al., 2018, du Plessis et al., 2018a, Xiong et al., 2020a, Yavari et al., 2015). However, during mastication, mandibles are subjected to flexural loading, tensile loading at the inferior border, and compressive loading in the alveolar process (Al-Sukhun et al., 2006, van Eijden, 2000). Mandibular reconstruction plates and implants must endure similar loading conditions. Assessment of the flexural fatigue properties of 3D-printed lattice-structured Ti6Al4V implants would be beneficial for understanding of their failure

mechanism. Flexural loading is more complex than the classically studied compression or push-pull fatigue loading. Flexural loading may be a more appropriate way of investigating mandibular mechanics and the response of lattice Ti6Al4V constructs to static and fatigue loading. Thus, focusing on flexural fatigue properties of lattice constructs should be considered a high priority for future work.

Furthermore, FEA models of lattice Ti6Al4V constructs need to be refined, taking into consideration the presence of internal defects and surface roughness. Although attempts have been made to create such FEA models recently, studies were limited by the computational power available. Improved FEA models would allow for faster and more accurate pre-manufacturing prediction of the mechanical properties of constructs. In addition, if FEA modelling is to become standard for the production of patient-specific implants, then improved FEA models should be available for use without the need for large expenditures of time and computational power.

Further investigation of approaches for alleviating microstructural defects from 3D-printed lattice constructs is required. At this point, there is no standard approach for post-processing heat treatment and surface treatment of lattice constructs. A technique that could be utilized involves computer simulation of 3D-printing parameters using CFD techniques, which have shown potential in determining thermal gradient differences during 3D printing.

The development of lattice structures for oral and maxillofacial applications shows promise for improving aesthetics and mechanical performance. However, an optimal design for mandibular implants that does not require bone grafts would be ideal. Such devices could provide patients with a solution requiring fewer surgical hours and no donor site morbidity. Optimization would require investigation into promoting bone ingrowth and reducing the possibility of postsurgical infection.

1.17 Conclusions

There continues to be considerable interest in the use of 3D-printed Ti6Al4V lattice-structured constructs for mandibular reconstruction. Additive manufacturing techniques

can now be used for the fabrication of Ti-alloy implants. Developing and designing patient-specific mandibular implants would open the door for more efficient mandibular reconstruction. New intraosseous porous implants for bone defects would reduce surgical times and revision surgeries, provide clinicians with additional treatment options, and accelerate healing and restoration of function. Future studies are needed to establish optimal pore geometry for lattice constructs with improved mechanical properties and extended service lives.

1.18 References used in this chapter

- ABELLÁN-NEBOT, J. V., SILLER, H. R., VILA, C. & RODRÍGUEZ, C. A. 2012. An experimental study of process variables in turning operations of Ti-6Al-4V and Cr-Co spherical prostheses. *The International Journal of Advanced Manufacturing Technology*, 63, 887-902.
- AGUADO-MONTERO, S., NAVARRO, C., VÁZQUEZ, J., LASAGNI, F., SLAWIK, S. & DOMÍNGUEZ, J. 2022. Fatigue behaviour of PBF additive manufactured Ti6Al4V alloy after shot and laser peening. *International Journal of Fatigue*, 154.
- AHMADI, S. M., HEDAYATI, R., LI, Y., LIETAERT, K., TÜMER, N., FATEMI, A., RANS, C. D., POURAN, B., WEINANS, H. & ZADPOOR, A. A. 2018. Fatigue performance of additively manufactured meta-biomaterials: The effects of topology and material type. *Acta Biomaterialia*, 65, 292--304.
- AHMADI, S. M., KUMAR, R., BORISOV, E. V., PETROV, R., LEEFLANG, S., LI, Y., TUMER, N., HUIZENGA, R., AYAS, C., ZADPOOR, A. A. & POPOVICH, V. A. 2019. From microstructural design to surface engineering: A tailored approach for improving fatigue life of additively manufactured meta-biomaterials. *Acta Biomaterialia*, 83, 153-166.
- AL-KETAN, O., LEE, D.-W. & ABU AL-RUB, R. K. 2021. Mechanical properties of additively-manufactured sheet-based gyroidal stochastic cellular materials. *Additive Manufacturing*, 48.
- AL-SUKHUN, J., HELENIUS, M., LINDQVIST, C. & KELLEWAY, J. 2006. Biomechanics of the Mandible Part I: Measurement of Mandibular Functional Deformation Using Custom-Fabricated Displacement Transducers. *Journal of Oral and Maxillofacial Surgery*, 64, 1015--1022.
- ALABORT, E., BARBA, D. & REED, R. C. 2019. Design of metallic bone by additive manufacturing. *Scripta Materialia*, 164, 110-114.
- ALBREKTSSON, T. & JOHANSSON, C. 2001. Osteoinduction, osteoconduction and osseointegration. *Eur Spine J*, 10 Suppl 2, S96-101.

- ALBREKTSSON, T., MEREDITH, N., WENNERBERG, A., BRANEMARK, P. I. & TOLMAN, D. E. 1999. *Osseointegration in Craniofacial Reconstruction*, Chicago, Quintessence Publishing Co, Inc.
- ALGHAMDI, A., DOWNING, D., MCMILLAN, M., BRANDT, M., QIAN, M. & LEARY, M. 2019. Experimental and numerical assessment of surface roughness for Ti6Al4V lattice elements in selective laser melting. *The International Journal of Advanced Manufacturing Technology*, 105, 1275-1293.
- ANDANI, M. T., SHAYESTEH MOGHADDAM, N., HABERLAND, C., DEAN, D., MILLER, M. J. & ELAHINIA, M. 2014. Metals for bone implants. Part 1. Powder metallurgy and implant rendering. *Acta Biomater*, 10, 4058-70.
- ANTONY, K. & ARIVAZHAGAN, N. 2015. Studies on energy penetration and Marangoni effect during laser melting process. *Journal of Engineering Science and Technology*, 10, 509 - 525.
- ANTONYSAMY, A. A., MEYER, J. & PRANGNELL, P. B. 2013. Effect of build geometry on the β -grain structure and texture in additive manufacture of Ti6Al4V by selective electron beam melting. *Materials Characterization*, 84, 153-168.
- ARABNEJAD, S., JOHNSTON, B., TANZER, M. & PASINI, D. 2017. Fully porous 3D printed titanium femoral stem to reduce stress-shielding following total hip arthroplasty. *Journal of Orthopaedic Research*, 35, 1774--1783.
- AS, S., SKALLERUD, B. & TVEITEN, B. 2008. Surface roughness characterization for fatigue life predictions using finite element analysis. *International Journal of Fatigue*, 30, 2200-2209.
- ASHBY, M. F. 2000. *Metal Foams : a design guide*, Burlington, MA, United States, Butterworth-Heinemann.
- ASLAN, N., AKSAKAL, B. & FINDIK, F. 2021. Fabrication of porous-Ti6Al4V alloy by using hot pressing technique and Mg space holder for hard-tissue biomedical applications. *J Mater Sci Mater Med*, 32, 80.
- ATKINSON, H. V. & DAVIES, S. 2000. Fundamental aspects of hot isostatic pressing: An overview. *Metallurgical and Materials Transactions A*, 31, 2981-3000.
- ATTAR, H., EHTEMAM-HAGHIGHI, S., KENT, D., WU, X. & DARGUSCH, M. S. 2017. Comparative study of commercially pure titanium produced by laser engineered net shaping, selective laser melting and casting processes. *Materials Science and Engineering: A*, 705, 385-393.
- AUGAT, P., LINK, T., LANG, T. F., LIN, J. C., MAJUMDAR, S. & GENANT, H. K. 1998. Anisotropy of the elastic modulus of trabecular bone specimens from different anatomical locations. *Medical Engineering & Physics*, 20, 124--131.
- BACCOUCH, M. 2021. A Brief Summary of the Finite Element Method for Differential Equations. *Finite Element Methods and Their Applications*. Rijeka: IntechOpen.

- BAI, L., CHEN, P., ZHAO, Y., HANG, R., YAO, X., TANG, B., LIU, C., XIAO, Y. & HANG, R. 2021. A micro/nano-biomimetic coating on titanium orchestrates osteo/angio-genesis and osteoimmunomodulation for advanced osseointegration. *Biomaterials*, 278, 121162.
- BAK, M., JACOBSON, A. S., BUCHBINDER, D. & URKEN, M. L. 2010. Contemporary reconstruction of the mandible. *Oral Oncol*, 46, 71-6.
- BARROS, S. E., VANZ, V., CHIQUETO, K., JANSON, G. & FERREIRA, E. 2021. Mechanical strength of stainless steel and titanium alloy mini-implants with different diameters: an experimental laboratory study. *Prog Orthod*, 22, 9.
- BARTOLOMEU, F., COSTA, M. M., ALVES, N., MIRANDA, G. & SILVA, F. S. 2021. Selective Laser Melting of Ti6Al4V sub-millimetric cellular structures: Prediction of dimensional deviations and mechanical performance. *J Mech Behav Biomed Mater*, 113, 104123.
- BATSTONE, M. D. 2018. Reconstruction of major defects of the jaws. *Aust Dent J*, 63 Suppl 1, S108-S113.
- BELAN, J., KUCHARIKOVÁ, L., TILLOVÁ, E. & CHALUPOVÁ, M. 2019. Three-Point Bending Fatigue Test of Ti6Al6V4 Titanium Alloy at Room Temperature. *Advances in Materials Science and Engineering*, 2019, 1-11.
- BELLINI, C., BORRELLI, R., DI COCCO, V., FRANCHITTI, S., IACOVIELLO, F., MOCANU, L. P. & SORRENTINO, L. 2021a. Failure energy and stiffness of titanium lattice specimens produced by electron beam melting process. *Material Design & Processing Communications*, 3.
- BELLINI, C., BORRELLI, R., DI COCCO, V., FRANCHITTI, S., IACOVIELLO, F. & SORRENTINO, L. 2021b. Damage analysis of Ti6Al4V lattice structures manufactured by electron beam melting process subjected to bending load. *Material Design & Processing Communications*, 3, e223.
- BENADY, A., MEYER, S. J., GOLDEN, E., DADIA, S. & KATARIVAS LEVY, G. 2023. Patient-specific Ti-6Al-4V lattice implants for critical-sized load-bearing bone defects reconstruction. *Materials & Design*, 226, 111605.
- BERGER, M. B., JACOBS, T. W., BOYAN, B. D. & SCHWARTZ, Z. 2020. Hot isostatic pressure treatment of 3D printed Ti6Al4V alters surface modifications and cellular response. *J Biomed Mater Res B Appl Biomater*, 108, 1262-1273.
- BIEWENER, A. A. 1993. Safety factors in bone strength. *Calcif Tissue Int*, 53 Suppl 1, S68-74.
- BOBBERT, F. S. L. & ZADPOOR, A. A. 2017. Effects of bone substitute architecture and surface properties on cell response, angiogenesis, and structure of new bone. *J Mater Chem B*, 5, 6175-6192.
- BOCHLOGYROS, P. N. 1985. Non-union of fractures of the mandible. *J Maxillofac Surg*, 13, 189-93.

- BOHARA, S. & SUTHAKORN, J. 2022. Surface coating of orthopedic implant to enhance the osseointegration and reduction of bacterial colonization: a review. *Biomater Res*, 26, 26.
- BOSE, S., KE, D., SAHASRABUDHE, H. & BANDYOPADHYAY, A. 2018. Additive manufacturing of biomaterials. *Prog Mater Sci*, 93, 45-111.
- BRANEMARK, P.-I. 2005. *The Osseointegration Book - From Calvarium to Calcaneus*, USA, Quintessence Books.
- BRANEMARK, P. I. 1983. Osseointegration and its experimental background. *J Prosthet Dent*, 50, 399-410.
- BRANEMARK, P. I. & TOLMAN, D. E. 1998. *Osseointegration in Craniofacial Reconstruction*. Quintessence Publishing Co.
- BUCHBINDER, D., CURRIVAN, R. B., KAPLAN, A. J. & URKEN, M. L. 1993. Mobilization regimens for the prevention of jaw hypomobility in the radiated patient: a comparison of three techniques. *J Oral Maxillofac Surg*, 51, 863-7.
- BUJTÁR, P., SÁNDOR, G. K. B., BOJTOS, A., SZÚCS, A. & BARABÁS, J. 2010. Finite element analysis of the human mandible at 3 different stages of life. *Oral Surgery, Oral Medicine, Oral Pathology, Oral Radiology, and Endodontology*, 110, 301--309.
- BURTON, H. E., EISENSTEIN, N. M., LAWLESS, B. M., JAMSHIDI, P., SEGARRA, M. A., ADDISON, O., SHEPHERD, D. E. T., ATTALLAH, M. M., GROVER, L. M. & COX, S. C. 2019. The design of additively manufactured lattices to increase the functionality of medical implants. *Mater Sci Eng C Mater Biol Appl*, 94, 901-908.
- CAMPOLI, G., BORLEFFS, M. S., AMIN YAVARI, S., WAUTHLE, R., WEINANS, H. & ZADPOOR, A. A. 2013. Mechanical properties of open-cell metallic biomaterials manufactured using additive manufacturing. *Materials & Design*, 49, 957-965.
- CANSIZOGLU, O., HARRYSSON, O., CORMIER, D., WEST, H. & MAHALE, T. 2008. Properties of Ti-6Al-4V non-stochastic lattice structures fabricated via electron beam melting. *Materials Science and Engineering: A*, 492, 468--474.
- CAO, F., ZHANG, T., RYDER, M. A. & LADOS, D. A. 2018. A Review of the Fatigue Properties of Additively Manufactured Ti-6Al-4V. *The Journal of The Minerals, Metals & Materials Society*, 70, 349--357.
- CAO, S., CHEN, Z., LIM, C. V. S., YANG, K., JIA, Q., JARVIS, T., TOMUS, D. & WU, X. 2017. Defect, Microstructure, and Mechanical Property of Ti-6Al-4V Alloy Fabricated by High-Power Selective Laser Melting. *The Journal of The Minerals, Metals & Materials Society*, 69, 2684-2692.

- CHEN, L. 2012. Finite Element Analysis of the Stress on the Implant-Bone Interface of Dental Implants with Different Structures. *Finite Element Analysis - New Trends and Developments*. Intech.
- CHERN, A. H., NANDWANA, P., YUAN, T., KIRKA, M. M., DEHOFF, R. R., LIAW, P. K. & DUTY, C. E. 2019. A review on the fatigue behavior of Ti-6Al-4V fabricated by electron beam melting additive manufacturing. *International Journal of Fatigue*, 119, 173-184.
- CILLA, M., CHECA, S. & DUDA, G. N. 2017. Strain shielding inspired re-design of proximal femoral stems for total hip arthroplasty. *J Orthop Res*, 35, 2534-2544.
- COLNOT, C., ROMERO, D. M., HUANG, S., RAHMAN, J., CURREY, J. A., NANJI, A., BRUNSKI, J. B. & HELMS, J. A. 2007. Molecular Analysis of Healing at a Bone-Implant Interface. *Journal of Dental Research*, 86, 862-867.
- CORDEY, J., BORGEAUD, M. & PERREN, S. M. 2000. Force transfer between the plate and the bone: relative importance of the bending stiffness of the screws and the friction between plate and bone. *Injury-International Journal of the Care of the Injured*, 31, 21-28.
- COX, S. C., JAMSHIDI, P., EISENSTEIN, N. M., WEBBER, M. A., BURTON, H., MOAKES, R. J. A., ADDISON, O., ATTALLAH, M., SHEPHERD, D. E. T. & GROVER, L. M. 2017. Surface Finish has a Critical Influence on Biofilm Formation and Mammalian Cell Attachment to Additively Manufactured Prosthetics. *ACS Biomater Sci Eng*, 3, 1616-1626.
- CUNNINGHAM, R., NARRA, S. P., MONTGOMERY, C., BEUTH, J. & ROLLETT, A. D. 2017. Synchrotron-Based X-ray Microtomography Characterization of the Effect of Processing Variables on Porosity Formation in Laser Powder-Bed Additive Manufacturing of Ti-6Al-4V. *The Journal of The Minerals, Metals & Materials Society*, 69, 479-484.
- DALLAGO, M., FONTANARI, V., TORRESANI, E., LEONI, M., PEDERZOLLI, C., POTRICH, C. & BENEDETTI, M. 2018. Fatigue and biological properties of Ti-6Al-4V ELI cellular structures with variously arranged cubic cells made by selective laser melting. *J Mech Behav Biomed Mater*, 78, 381-394.
- DALLAGO, M., RAGHAVENDRA, S., LUCHIN, V., ZAPPINI, G., PASINI, D. & BENEDETTI, M. 2021. The role of node fillet, unit-cell size and strut orientation on the fatigue strength of Ti-6Al-4V lattice materials additively manufactured via laser powder bed fusion. *International Journal of Fatigue*, 142.
- DANIELS, T. R., THOMAS, R., BELL, T. H. & NELIGAN, P. C. 2005. Functional Outcome of the Foot and Ankle After Free Fibular Graft. *Foot & Ankle International*, 26, 597-601.
- DAVIES, J. E. 2003. Understanding Peri-Implant Endosseous Healing. *Journal of Dental Education*, 67, 932-949.

- DE WILD, M., SCHUMACHER, R., MAYER, K., SCHKOMMODAU, E., THOMA, D., BREDELL, M., KRUSE GUJER, A., GRATZ, K. W. & WEBER, F. E. 2013. Bone regeneration by the osteoconductivity of porous titanium implants manufactured by selective laser melting: a histological and micro computed tomography study in the rabbit. *Tissue Eng Part A*, 19, 2645-54.
- DEBOER, B., NGUYEN, N., DIBA, F. & HOSSEINI, A. 2021. Additive, subtractive, and formative manufacturing of metal components: a life cycle assessment comparison. *The International Journal of Advanced Manufacturing Technology*, 115.
- DELIGIANNI, D. D., KATSALA, N., LADAS, S., SOTIROPOULOU, D., AMEDEE, J. & MISSIRLIS, Y. F. 2001. Effect of surface roughness of the titanium alloy Ti-6Al-4V on human bone marrow cell response and on protein adsorption. *Biomaterials*, 22, 1241-51.
- DELO, D. P. & PIEHLER, H. R. 1999. Early stage consolidation mechanisms during hot isostatic pressing of Ti-6Al-4V powder compacts. *Acta Materialia*, 47, 2841-52.
- DI CAPRIO, F., FRANCHITTI, S., BORRELLI, R., BELLINI, C., DI COCCO, V. & SORRENTINO, L. 2022. Ti-6Al-4V Octet-Truss Lattice Structures under Bending Load Conditions: Numerical and Experimental Results. *Metals (Basel)*, 12, 410.
- DIAS, M. R., GUEDES, J. M., FLANAGAN, C. L., HOLLISTER, S. J. & FERNANDES, P. R. 2014. Optimization of scaffold design for bone tissue engineering: A computational and experimental study. *Medical Engineering & Physics*, 36, 448--457.
- DISA, J. J. & CORDEIRO, P. G. 2000. Mandible reconstruction with microvascular surgery. *Semin Surg Oncol*, 19, 226-34.
- DONG, G., MARLEAU-FINLEY, J. & ZHAO, Y. F. 2019. Investigation of electrochemical post-processing procedure for Ti-6Al-4V lattice structure manufactured by direct metal laser sintering (DMLS). *The International Journal of Advanced Manufacturing Technology*, 104, 3401-3417.
- DU PLESSIS, A., GLASER, D., MOLLER, H., MATHE, N., TSHABALALA, L., MFUSI, B. & MOSTERT, R. 2019. Pore Closure Effect of Laser Shock Peening of Additively Manufactured AlSi10Mg. *3D Printing and Additive Manufacturing*, 6, 245-252.
- DU PLESSIS, A., RAZAVI, N. & BERTO, F. 2020a. The effects of microporosity in struts of gyroid lattice structures produced by laser powder bed fusion. *Materials & Design*, 194, 108899.
- DU PLESSIS, A. & ROSSOUW, P. 2015. Investigation of Porosity Changes in Cast Ti6Al4V Rods After Hot Isostatic Pressing. *Journal of Materials Engineering and Performance*, 24, 3137-3141.
- DU PLESSIS, A., YADROITSAVA, I., KOUPRIANOFF, D. & YADROITSEV, I. 2018a. Numerical and experimental study of the effect of artificial porosity in a lattice

structure manufactured by laser based powder bed fusion. Solid Freeform Fabrication Symposium – An Additive Manufacturing Conference.

- DU PLESSIS, A., YADROITSAVA, I. & YADROITSEV, I. 2018b. Ti6Al4V lightweight lattice structures manufactured by laser powder bed fusion for load-bearing applications. *Optics & Laser Technology*, 108, 521-528.
- DU PLESSIS, A., YADROITSAVA, I. & YADROITSEV, I. 2020b. Effects of defects on mechanical properties in metal additive manufacturing: A review focusing on X-ray tomography insights. *Materials & Design*, 187, 108385.
- DU PLESSIS, A., YADROITSEV, I., YADROITSAVA, I. & LE ROUX, S. G. 2018c. X-Ray Microcomputed Tomography in Additive Manufacturing: A Review of the Current Technology and Applications. *3D Printing and Additive Manufacturing*, 5, 227-247.
- DZIADUSZEWSKA, M. & ZIELINSKI, A. 2021. Structural and Material Determinants Influencing the Behavior of Porous Ti and Its Alloys Made by Additive Manufacturing Techniques for Biomedical Applications. *Materials (Basel)*, 14.
- EL-SAYED, M. A., ESSA, K., GHAZY, M. & HASSANIN, H. 2020. Design optimization of additively manufactured titanium lattice structures for biomedical implants. *The International Journal of Advanced Manufacturing Technology*, 110, 2257-2268.
- ELLIS, E., 3RD 1996. Complications of rigid internal fixation for mandibular fractures. *J Craniomaxillofac Trauma*, 2, 32-9.
- ELLIS, E., 3RD & MILES, B. A. 2007. Fractures of the mandible: a technical perspective. *Plast Reconstr Surg*, 120, 76S-89S.
- EMSHOFF, R., BERTRAM, A., HUPP, L. & RUDISCH, A. 2021. Condylar erosion is predictive of painful closed lock of the temporomandibular joint: a magnetic resonance imaging study. *Head Face Med*, 17, 40.
- ESHKALAK, S. K., GHOMI, E. R., DAI, Y., CHOUDHURY, D. & RAMAKRISHNA, S. 2020. The role of three-dimensional printing in healthcare and medicine. *Materials & Design*, 194.
- FAROOQ, M. & SAZONOV, E. 2016. Automatic Measurement of Chew Count and Chewing Rate during Food Intake. *Electronics (Basel)*, 5.
- FARWELL, D. G., KEZIRIAN, E. J., HEYDT, J. L., YUEH, B. & FUTRAN, N. D. 2006. Efficacy of small reconstruction plates in vascularized bone graft mandibular reconstruction. *Head Neck*, 28, 573-9.
- FAULKNER, M. G., HATCHER, D. C. & HAY, A. 1987. A three-dimensional investigation of temporomandibular joint loading. *Journal of Biomechanics*, 20, 997-1002.

- FERRARIO, V., SFORZA, C., SERRAO, G., DELLAVIA, C. & TARTAGLIA, G. 2004. Single tooth bite forces in healthy young adults. *Journal of oral rehabilitation*, 31, 18-22.
- FOUSOVA, M., VOJTECH, D., KUBASEK, J., JABLONSKA, E. & FOJT, J. 2017. Promising characteristics of gradient porosity Ti-6Al-4V alloy prepared by SLM process. *J Mech Behav Biomed Mater*, 69, 368-376.
- FRANCHI, M., FINI, M., MARTINI, D., ORSINI, E., LEONARDI, L., RUGGERI, A., GIAVARESI, G. & OTTANI, V. 2005. Biological fixation of endosseous implants. *Micron*, 36, 665-71.
- FROST, H. M. 1987. Bone "mass" and the "mechanostat": a proposal. *Anat Rec*, 219, 1-9.
- FROST, H. M. 2004. A 2003 update of bone physiology and Wolff's Law for clinicians. *Angle Orthod*, 74, 3-15.
- FUKUDA, A., TAKEMOTO, M., SAITO, T., FUJIBAYASHI, S., NEO, M., PATTANAYAK, D. K., MATSUSHITA, T., SASAKI, K., NISHIDA, N., KOKUBO, T. & NAKAMURA, T. 2011. Osteoinduction of porous Ti implants with a channel structure fabricated by selective laser melting. *Acta Biomaterialia*, 7, 2327--2336.
- GAO, H.-J., ZHANG, Y.-D., WU, Q. & SONG, J. 2017. Experimental Investigation on the Fatigue Life of Ti-6Al-4V Treated by Vibratory Stress Relief. *Metals*, 7.
- GE, J., HUANG, Q., WANG, Y., ZHANG, C., LIU, Q., LU, Z. & YIN, S. 2023. Microstructural optimization and mechanical enhancement of SLM Ti6Al4V TPMS scaffolds through vacuum annealing treatment. *Journal of Alloys and Compounds*, 934, 167524.
- GENG, J. P., TAN, K. B. & LIU, G. R. 2001. Application of finite element analysis in implant dentistry: a review of the literature. *J Prosthet Dent*, 85, 585-98.
- GHOLAMPOUR, S., GHOLAMPOUR, H. & KHANMOHAMMADI, H. 2019. Finite element analysis of occlusal splint therapy in patients with bruxism. *BMC Oral Health*, 19, 205.
- GHOSH, A., KUMAR, A., WANG, X., KIETZIG, A.-M. & BROCHU, M. 2022. Analysis of the effect of surface morphology on tensile behavior of LPBF SS316L microstruts. *Materials Science and Engineering: A*, 831.
- GHOUSE, S., REZNIKOV, N., BOUGHTON, O. R., BABU, S., GEOFFREY NG, K. C., BLUNN, G., COBB, J. P., STEVENS, M. M. & JEFFERS, J. R. T. 2019. The Design and In Vivo Testing of a Locally Stiffness-Matched Porous Scaffold. *Appl Mater Today*, 15, 377-388.
- GIBSON, L. J. & ASHBY, M. F. 1988. *Cellular solids: structure & properties*, Oxford [Oxfordshire];Toronto;, Pergamon Press.

- GONG, H., RAFI, K., GU, H., JANAKI RAM, G. D., STARR, T. & STUCKER, B. 2015. Influence of defects on mechanical properties of Ti–6Al–4V components produced by selective laser melting and electron beam melting. *Materials & Design*, 86, 545-554.
- GOODMAN, S. B., GALLO, J., GIBON, E. & TAKAGI, M. 2020. Diagnosis and management of implant debris-associated inflammation. *Expert Review of Medical Devices*, 17, 41-56.
- GRANSTROM, G. 2007. Craniofacial osseointegration. *Oral Dis*, 13, 261-9.
- GRZESKOWIAK, R. M., SCHUMACHER, J., DHAR, M. S., HARPER, D. P., MULON, P. Y. & ANDERSON, D. E. 2020. Bone and Cartilage Interfaces With Orthopedic Implants: A Literature Review. *Front Surg*, 7, 601244.
- GUO, R. P., CHENG, M., ZHANG, C. J., QIAO, J. W., CAI, C., WANG, Q. J., XU, D. S., XU, L., YANG, R., SHI, Y. S. & LIAW, P. K. 2023. Achieving superior fatigue strength in a powder-metallurgy titanium alloy via in-situ globularization during hot isostatic pressing. *Scripta Materialia*, 228.
- HALLAB, N. J. 2009. A review of the biologic effects of spine implant debris: Fact from fiction. *SAS J*, 3, 143-60.
- HAN, C., LI, Y., WANG, Q., WEN, S., WEI, Q., YAN, C., HAO, L., LIU, J. & SHI, Y. 2018. Continuous functionally graded porous titanium scaffolds manufactured by selective laser melting for bone implants. *J Mech Behav Biomed Mater*, 80, 119-127.
- HANASONO, M. M., MILITSAKH, O. N., RICHMON, J. D., ROSENTHAL, E. L. & WAX, M. K. 2013. Mandibulectomy and Free Flap Reconstruction for Bisphosphonate-Related Osteonecrosis of the Jaws. *JAMA Otolaryngology–Head & Neck Surgery*, 139, 1135-1142.
- HARJANI, B., SINGH, R. K., PAL, U. S. & SINGH, G. 2012. Locking v/s non-locking reconstruction plates in mandibular reconstruction. *Natl J Maxillofac Surg*, 3, 159-65.
- HEDAYATI, R., SADIGHI, M., MOHAMMADI-AGHDAM, M. & HOSSEINI-TOUDESHPY, H. 2018. Comparison of elastic properties of open-cell metallic biomaterials with different unit cell types. *J Biomed Mater Res B Appl Biomater*, 106, 386-398.
- HEIBEL, H., ALT, K. W., WACHTER, R. & BAHR, W. 2001. Kortikalisdicke am Unterkiefer unter besonderer Berücksichtigung der Miniplattenosteosynthese Morphometrische Analyse an Sektionsmaterial. *Mund Kiefer Gesichtschir*, 5, 180-5.
- HERNÁNDEZ-NAVA, E., SMITH, C. J., DERGUTI, F., TAMMAS-WILLIAMS, S., LEONARD, F., WITHERS, P. J., TODD, I. & GOODALL, R. 2016. The effect of

- defects on the mechanical response of Ti-6Al-4V cubic lattice structures fabricated by electron beam melting. *Acta Materialia*, 108, 279-292.
- HIDALGO, D. A. 1989. Fibula Free Flap: A new method of Mandible reconstruction. *Plastic and Reconstructive Surgery*, July.
- HIDALGO, D. A. & PUSIC, A. L. 2002. Free-flap mandibular reconstruction: a 10-year follow-up study. *Plast Reconstr Surg*, 110, 438-49; discussion 450-1.
- HIGUCHI, K. W. 2000. Osseointegration or osteointegration? *Oral surgery, oral medicine, oral pathology, oral radiology, and endodontics*, 89, 132.
- HOFMANN, A. A., BLOEBAUM, R. D. & BACHUS, K. N. 1997. Progression of human bone ingrowth into porous-coated implants. Rate of bone ingrowth in humans. *Acta Orthop Scand*, 68, 161-6.
- HORN, T. J., HARRYSSON, O. L. A., LITTLE, J. P., WEST II, H. A. & MARCELLIN-LITTLE, D. J. 2010. Design and manufacturing of bone analog models for the mechanical evaluation of custom medical implants.
- HORN, T. J., HARRYSSON, O. L. A., MARCELLIN-LITTLE, D. J., WEST, H. A., LASCELLES, B. D. X. & AMAN, R. 2014. Flexural properties of Ti6Al4V rhombic dodecahedron open cellular structures fabricated with electron beam melting. *Additive Manufacturing*, 1-4, 2-11.
- HU, Y. N., WU, S. C., WITHERS, P. J., ZHANG, J., BAO, H. Y. X., FU, Y. N. & KANG, G. Z. 2020. The effect of manufacturing defects on the fatigue life of selective laser melted Ti-6Al-4V structures. *Materials & Design*, 192.
- HUNG, W. 2021. Postprocessing of Additively Manufactured Metal Parts. *Journal of Materials Engineering and Performance*, 30, 6439-6460.
- ICHIMURA, K. & TANAKA, T. 1993. Trismus in patients with malignant tumours in the head and neck. *J Laryngol Otol*, 107, 1017-20.
- ILAVARASI, P. U. & ANBURAIAN, M. 2011. Design and Finite Element Analysis of Mandibular Prosthesis. 2011 3rd International Conference on Electronics Computer Technology, 3, 325--329.
- JACKSON, M. J., KOPAC, J., BALAZIC, M., BOMBAC, D., BROJAN, M. & KOSEL, F. 2016. *Titanium and Titanium Alloy Applications in Medicine. Surgical Tools and Medical Devices*. Springer.
- JAHADAKBAR, A., SHAYESTEH MOGHADDAM, N., AMERINATANZI, A., DEAN, D. & ELAHINIA, M. Mechanical evaluation of the SLM fabricated, stiffness-matched, mandibular bone fixation plates. *SPIE Smart Structures and Materials + Nondestructive Evaluation and Health Monitoring*, 2018. SPIE.
- JAHADAKBAR, A., SHAYESTEH MOGHADDAM, N., AMERINATANZI, A., DEAN, D., KARACA, H. E. & ELAHINIA, M. 2016. Finite Element Simulation and

- Additive Manufacturing of Stiffness-Matched NiTi Fixation Hardware for Mandibular Reconstruction Surgery. *Bioengineering (Basel)*, 3, 36.
- JAMSHIDI, P., ARISTIZABAL, M., KONG, W., VILLAPUN, V., COX, S. C., GROVER, L. M. & ATTALLAH, M. M. 2020. Selective Laser Melting of Ti-6Al-4V: The Impact of Post-processing on the Tensile, Fatigue and Biological Properties for Medical Implant Applications. *Materials (Basel)*, 13.
- JAYESH, R. S. & DHINAKARSAMY, V. 2015. Osseointegration. *J Pharm Bioallied Sci*, 7, S226-9.
- JESUS, G. P. D., VAZ, L. G., GABRIELLI, M. F. R., PASSERI, L. A., OLIVEIRA, T. V., NORITOMI, P. Y. & JÜRGENS, P. 2014. Finite element evaluation of three methods of stable fixation of condyle base fractures. *International Journal of Oral and Maxillofacial Surgery*, 43, 1251--1256.
- JI, B., WANG, C., LIU, L., LONG, J., TIAN, W. & WANG, H. 2010. A biomechanical analysis of titanium miniplates used for treatment of mandibular symphyseal fractures with the finite element method. *Oral Surg Oral Med Oral Pathol Oral Radiol Endod*, 109, e21-7.
- JIN, N., YAN, Z., WANG, Y., CHENG, H. & ZHANG, H. 2021. Effects of heat treatment on microstructure and mechanical properties of selective laser melted Ti-6Al-4V lattice materials. *International Journal of Mechanical Sciences*, 190.
- KAKARALA, K., SHNAYDER, Y., TSUE, T. T. & GIROD, D. A. 2018. Mandibular reconstruction. *Oral Oncol*, 77, 111-117.
- KAN, W. H., CHIU, L. N. S., LIM, C. V. S., ZHU, Y., TIAN, Y., JIANG, D. & HUANG, A. 2022. A critical review on the effects of process-induced porosity on the mechanical properties of alloys fabricated by laser powder bed fusion. *Journal of Materials Science*, 57, 9818-9865.
- KASPEROVICH, G. & HAUSMANN, J. 2015. Improvement of fatigue resistance and ductility of TiAl6V4 processed by selective laser melting. *Journal of Materials Processing Technology*, 220, 202--214.
- KATRANJI, A., MISCH, K. & WANG, H. L. 2007. Cortical bone thickness in dentate and edentulous human cadavers. *J Periodontol*, 78, 874-8.
- KEARNS, M., ERMOGENOUS, P., MYERS, S. & GHANEM, A. M. 2018. Osteocutaneous flaps for head and neck reconstruction: A focused evaluation of donor site morbidity and patient reported outcome measures in different reconstruction options. *Arch Plast Surg*, 45, 495-503.
- KELLER, E. E., TOLMAN, D. & ECKERT, S. 1998. Endosseous implant and autogenous bone graft reconstruction of mandibular discontinuity: a 12-year longitudinal study of 31 patients. *Int J Oral Maxillofac Implants*, 13, 767-80.
- KENNADY, M. C., TUCKER, M. R., LESTER, G. E. & BUCKLEY, M. J. 1989a. Histomorphometric evaluation of stress shielding in mandibular continuity defects

- treated with rigid fixation plates and bone grafts. *Int J Oral Maxillofac Surg*, 18, 170-174.
- KENNADY, M. C., TUCKER, M. R., LESTER, G. E. & BUCKLEY, M. J. 1989b. Stress shielding effect of rigid internal fixation plates on mandibular bone grafts. A photon absorption densitometry and quantitative computerized tomographic evaluation. *Int J Oral Maxillofac Surg*, 18, 307-310.
- KHAIRALLAH, S. A., ANDERSON, A. T., RUBENCHIK, A. & KING, W. E. 2016. Laser powder-bed fusion additive manufacturing: Physics of complex melt flow and formation mechanisms of pores, spatter, and denudation zones. *Acta Materialia*, 108, 36-45.
- KHAIRALLAH, S. A., MARTIN, A. A., LEE, J. R. I., GUSS, G., CALTA, N. P., HAMMONS, J. A., NIELSEN, M. H., CHAPUT, K., SCHWALBACH, E., SHAH, M. N., CHAPMAN, M. G., WILLEY, T. M., RUBENCHIK, A. M., ANDERSON, A. T., WANG, Y. M., MATTHEWS, M. J. & KING, W. E. 2020. Controlling interdependent meso-nanosecond dynamics and defect generation in metal 3D printing. *Science*, 368, 660-665.
- KHAIRY, S. G. & MAHAINI, L. 2015. Determination of Buccal Cortical Bone Thickness for Mini-Screws Placement in Horizontal Growth Type Patients by Cone Beam Computed Tomography. *Journal of Dental Health, Oral Disorders & Therapy*, 2.
- KONDO, S., KATSUTA, H., AKIZUKI, A., KURIHARA, Y., KAMATANI, T., YASO, A., NAGASAKI, M., SHIMANE, T. & SHIROTA, T. 2015. Computer-Assisted Surgery for Mandibular Reconstruction Using a Patient-Specific Titanium Mesh Tray and Particulate Cancellous Bone and Marrow. *Case Reports in Clinical Medicine*, 04, 85-92.
- KORIOH, T. W. P. & HANNAM, A. G. 1994. Deformation of the Human Mandible During Simulated Tooth Clenching. *Journal of Dental Research*, 73, 56-66.
- KOVACS, A. E., CSERNATONY, Z., CSAMER, L., MEHES, G., SZABO, D., VERES, M., BRAUN, M., HARANGI, B., SERBAN, N., ZHANG, L., FALK, G., SOOSNE HORVATH, H. & MANO, S. 2023. Comparative Analysis of Bone Ingrowth in 3D-Printed Titanium Lattice Structures with Different Patterns. *Materials (Basel)*, 16, 3861.
- KREUTZER, K., STEFFEN, C., KOERDT, S., DOLL, C., EBKER, T., NAHLES, S., FLUGGE, T., HEILAND, M., BECK-BROICHSITTER, B. & RENDENBACH, C. 2022. Patient-Specific 3D-Printed Miniplates for Free Flap Fixation at the Mandible: A Feasibility Study. *Front Surg*, 9, 778371.
- KRISHNA, B. V., BOSE, S. & BANDYOPADHYAY, A. 2007. Low stiffness porous Ti structures for load-bearing implants. *Acta Biomater*, 3, 997-1006.
- KRZYZANOWSKI, M. & SVYETLICHNYY, D. 2021. A multiphysics simulation approach to selective laser melting modelling based on cellular automata and lattice Boltzmann methods. *Computational Particle Mechanics*, 9, 117-133.

- KUHN, A. 2004. Electropolishing of titanium and its alloys. *Metal Finishing*, 102, 80-86.
- KUMAR, P., PRAKASH, O. & RAMAMURTY, U. 2018. Micro-and meso-structures and their influence on mechanical properties of selectively laser melted Ti-6Al-4V. *Acta Materialia*, 154, 246-260.
- LAKATOS, E., MAGYAR, L. & BOJTAR, I. 2014. Material Properties of the Mandibular Trabecular Bone. *J Med Eng*, 2014, 470539.
- LANG, J. J., BASTIAN, M., FOEHR, P., SEEBACH, M., WEITZ, J., VON DEIMLING, C., SCHWAIGER, B. J., MICHELER, C. M., WILHELM, N. J., GROSSE, C. U., KESTING, M. & BURGKART, R. 2021. Improving mandibular reconstruction by using topology optimization, patient specific design and additive manufacturing?- A biomechanical comparison against miniplates on human specimen. *PLoS One*, 16, e0253002.
- LEE, H., PARK, S. & NOH, G. 2019. Biomechanical analysis of 4 types of short dental implants in a resorbed mandible. *The Journal of Prosthetic Dentistry*, 121, 659--670.
- LEUDERS, S., THÖNE, M., RIEMER, A., NIENDORF, T., TRÖSTER, T., RICHARD, H. A. & MAIER, H. J. 2013. On the mechanical behaviour of titanium alloy TiAl6V4 manufactured by selective laser melting: Fatigue resistance and crack growth performance. *International Journal of Fatigue*, 48, 300--307.
- LI, C., LIU, Z. Y., FANG, X. Y. & GUO, Y. B. Residual Stress in Metal Additive Manufacturing. *Procedia CIRP*, 2018. 348-353.
- LI, S., LI, X., HOU, W., NUNE, K. C., MISRA, R. D. K., CORREA-RODRIGUEZ, V. L., GUO, Z., HAO, Y., YANG, R. & MURR, L. E. 2017. Fabrication of open-cellular (porous) titanium alloy implants: osseointegration, vascularization and preliminary human trials. *Science China Materials*, 61, 525-536.
- LING, X. F. & PENG, X. 2012. What Is the Price to Pay for a Free Fibula Flap? A Systematic Review of Donor-Site Morbidity following Free Fibula Flap Surgery. *Plastic and Reconstructive Surgery*, 129, 657-674.
- LIU, F., ZHANG, D. Z., ZHANG, P., ZHAO, M. & JAFAR, S. 2018. Mechanical Properties of Optimized Diamond Lattice Structure for Bone Scaffolds Fabricated via Selective Laser Melting. *Materials (Basel)*, 11.
- LIU, L., ZHENG, H. & DENG, C. 2019. Influence of HIP Treatment on Mechanical Properties of Ti6Al4V Scaffolds Prepared by L-PBF Process. *Metals*, 9.
- LIU, Y. J., REN, D. C., LI, S. J., WANG, H., ZHANG, L. C. & SERCOMBE, T. B. 2020. Enhanced fatigue characteristics of a topology-optimized porous titanium structure produced by selective laser melting. *Additive Manufacturing*, 32.
- LOGAN, D. L. 2012. Development of the Plane Stress and Plane Strain Stiffness Equations. *A First Course in the Finite Element Method*. Fifth ed. United States: Cengage Learning.

- LU, X., WU, Z., XU, K., WANG, X., WANG, S., QIU, H., LI, X. & CHEN, J. 2021. Multifunctional Coatings of Titanium Implants Toward Promoting Osseointegration and Preventing Infection: Recent Developments. *Front Bioeng Biotechnol*, 9, 783816.
- LUIS PÉREZ, C. J., VIVANCOS CALVET, J. & SEBASTIÁN PÉREZ, M. A. 2001. Geometric roughness analysis in solid free-form manufacturing processes. *Journal of Materials Processing Technology*, 119, 52-57.
- LUO, D., RONG, Q. & CHEN, Q. 2017. Finite-element design and optimization of a three-dimensional tetrahedral porous titanium scaffold for the reconstruction of mandibular defects. *Medical Engineering & Physics*, 47, 176--183.
- ŁYCZKOWSKA, E., SZYMCZYK, P., DYBAŁA, B. & CHLEBUS, E. 2014. Chemical polishing of scaffolds made of Ti-6Al-7Nb alloy by additive manufacturing. *Archives of civil and mechanical engineering.*, 14, 586-594.
- MACIEL, G. B. M., MACIEL, R. M. & DANESI, C. C. 2023. Bone cells and their role in physiological remodeling. *Mol Biol Rep*, 50, 2857-2863.
- MAHAMOOD, R. M. & AKINLABI, E. T. 2017. Types of Functionally Graded Materials and Their Areas of Application. *Functionally Graded Materials*.
- MAHMOUD, D. & ELBESTAWI, M. A. 2018. Selective laser melting of porosity graded lattice structures for bone implants. *The International Journal of Advanced Manufacturing Technology*, 100, 2915-2927.
- MALEKPOUR, Z., SARKARAT, F. & HOOSHANGI, H. 2014. Mandibular Reconstruction Using Custom-Made Titanium Mesh Tray and Autogenous Bone Graft- A Case Report. *Thrita*, 3.
- MARECHEK, A., ALSHARE, A., PACK, S., DEMKO, C., QUERESHY, F. A. & BAUR, D. 2019. Nonvascularized Bone Grafts for Reconstruction of Segmental Mandibular Defects: Is Length of Graft a Factor of Success? *J Oral Maxillofac Surg*, 77, 2557-2566.
- MARX, R. E. 1983. Osteoradionecrosis: a new concept of its pathophysiology. *J Oral Maxillofac Surg*, 41, 283-8.
- MATHOG, R. H., TOMA, V., CLAYMAN, L. & WOLF, S. 2000. Nonunion of the mandible: an analysis of contributing factors. *J Oral Maxillofac Surg*, 58, 746-52; discussion 752-3.
- MATSUMOTO, Y., HASHIMOTO, F. & LAHOTI, G. 1999. Surface Integrity Generated by Precision Hard Turning. *CIRP Annals*, 48, 59-62.
- MEIER, B., WARCHOMICKA, F., PETRUSA, J., KAINDL, R., WALDHAUSER, W. & SOMMITSCH, C. 2023. High Temperature Tensile Strength of Ti6Al4V Processed by L-PBF—Influence of Microstructure and Heat Treatment. *BHM Berg- und Hüttenmännische Monatshefte*, 168, 247-253.

- MERCURI, L. G. 2018. Costochondral Graft Versus Total Alloplastic Joint for Temporomandibular Joint Reconstruction. *Oral and maxillofacial surgery clinics of North America*, 30, 335-342.
- MESLIER, Q. A. & SHEFELBINE, S. J. 2023. Using Finite Element Modeling in Bone Mechanoadaptation. *Curr Osteoporos Rep*, 21, 105-116.
- MILITSAKH, O. N., WALLACE, D. I., KRIET, J. D., GIROD, D. A., OLVERA, M. S. & TSUE, T. T. 2004. Use of the 2.0-mm locking reconstruction plate in primary oromandibular reconstruction after composite resection. *Otolaryngol Head Neck Surg*, 131, 660-5.
- MOIDUDDIN, K., MIAN, S. H., AMEEN, W., ALKINDI, M., RAMALINGAM, S. & ALGHAMDI, O. 2020. Patient-Specific Surgical Implant Using Cavity-Filled Approach for Precise and Functional Mandible Reconstruction. *Applied Sciences*, 10.
- MOMMAERTS, M. Y. 2016. Guidelines for patient-specific jawline definition with titanium implants in esthetic, deformity, and malformation surgery. *Annals of Maxillofacial Surgery*, 6, 287--291.
- MOMOH, A. O., YU, P., SKORACKI, R. J., LIU, S., FENG, L. & HANASONO, M. M. 2011. A Prospective Cohort Study of Fibula Free Flap Donor-Site Morbidity in 157 Consecutive Patients. *Plastic and Reconstructive Surgery*, 128, 714-720.
- MONTALBANO, T., BRIGGS, B. N., WATERMAN, J. L., NIMER, S., PEITSCH, C., SOPCISAK, J., TRIGG, D. & STORCK, S. 2021. Uncovering the coupled impact of defect morphology and microstructure on the tensile behavior of Ti-6Al-4V fabricated via laser powder bed fusion. *Journal of Materials Processing Technology*, 294.
- MOUNIR, M., ABOU-ELFETOUH, A., ELBEIALY, W. & MOUNIR, R. 2020. Patient-specific alloplastic endoprosthesis for reconstruction of the mandible following segmental resection: A case series. *J Craniomaxillofac Surg*, 48, 719-723.
- MOUSSAOUI, K., MOUSSEIGNE, M., SENATORE, J., CHIERAGATTI, R. & LAMESLE, P. 2015. Influence of Milling on the Fatigue Lifetime of a Ti6Al4V Titanium Alloy. *Metals*, 5, 1148-1162.
- MUKHERJEE, S., DHARA, S. & SAHA, P. 2023. Design and Additive Manufacturing of Acetabular Implant with Continuously Graded Porosity. *Bioengineering (Basel)*, 10.
- MUNIR, K., BIESIEKIERSKI, A., WEN, C. & LI, Y. 2020. Selective laser melting in biomedical manufacturing. In: WEN, C. (ed.) *Metallic Biomaterials Processing and Medical Device Manufacturing*. Woodhead Publishing.
- MURR, L. E., GAYTAN, S. M., RAMIREZ, D. A., MARTINEZ, E., HERNANDEZ, J., AMATO, K. N., SHINDO, P. W., MEDINA, F. R. & WICKER, R. B. 2012a. Metal

- Fabrication by Additive Manufacturing Using Laser and Electron Beam Melting Technologies. *Journal of Materials Science & Technology*, 28, 1-14.
- MURR, L. E., MARTINEZ, E., AMATO, K. N., GAYTAN, S. M., HERNANDEZ, J., RAMIREZ, D. A., SHINDO, P. W., MEDINA, F. & WICKER, R. B. 2012b. Fabrication of Metal and Alloy Components by Additive Manufacturing: Examples of 3D Materials Science. *Journal of Materials Research and Technology*, 1, 42-54.
- NAGASAO, T., MIYAMOTO, J. & KAWANA, H. 2009. Biomechanical evaluation of implant placement in the reconstructed mandible. *Int J Oral Maxillofac Implants*, 24, 999-1005.
- NASSEHI, A., NEWMAN, S., DHOKIA, V., ZHU, Z. & ASRAI, I. R. 2011. Using formal methods to model hybrid manufacturing processes. 4th International Conference on Changeable, Agile, Reconfigurable and Virtual Production (CARV2011). Montreal, Canada.
- ODIN, G., SAVOLDELLI, C., BOUCHARD, P. O. & TILLIER, Y. 2010. Determination of Young's modulus of mandibular bone using inverse analysis. *Med Eng Phys*, 32, 630-7.
- OLIVEIRA, L. Y., KUROMOTO, N. K. & SIQUEIRA, C. J. 2014. Treating orthopedic prosthesis with diamond-like carbon: minimizing debris in Ti6Al4V. *J Mater Sci Mater Med*, 25, 2347-55.
- ONAL, E., FRITH, J., JURG, M., WU, X. & MOLOTNIKOV, A. 2018. Mechanical Properties and In Vitro Behavior of Additively Manufactured and Functionally Graded Ti6Al4V Porous Scaffolds. *Metals*, 8, 200.
- OOSTERBEEK, R. N. & JEFFERS, J. R. T. 2022. StrutSurf: A tool for analysis of strut morphology and surface roughness in additively manufactured lattices. *SoftwareX*, 18.
- PAHR, D. H. & REISINGER, A. G. 2020. A Review on Recent Advances in the Constitutive Modeling of Bone Tissue. *Curr Osteoporos Rep*, 18, 696-704.
- PAL, S., GUBELJAK, N., HUDÁK, R., LOJEN, G., RAJŤUKOVÁ, V., BRAJLIH, T. & DRSTVENŠEK, I. 2020. Evolution of the metallurgical properties of Ti-6Al-4V, produced with different laser processing parameters, at constant energy density in selective laser melting. *Results in Physics*, 17.
- PALANIVEL, S., DUTT, A. K., FAIERSON, E. J. & MISHRA, R. S. 2016. Spatially dependent properties in a laser additive manufactured Ti-6Al-4V component. *Materials Science and Engineering: A*, 654, 39-52.
- PANETTIERI, E., BOISSIN, E., MONTEMURRO, M., CATAPANO, A. & JALOCHA, D. 2021. On the accuracy of a homogenized continuum model of lattice structures in modal analyses. *Mechanics of Advanced Materials and Structures*, 1-18.

- PARE, A., BOSSARD, A., LAURE, B., WEISS, P., GAUTHIER, O. & CORRE, P. 2019. Reconstruction of segmental mandibular defects: Current procedures and perspectives. *Laryngoscope Investig Otolaryngol*, 4, 587-596.
- PARK, J. B. & LAKES, R. S. 2007. *Metallic Implant Materials*.
- PARK, J. H., JO, E., CHO, H. & KIM, H. J. 2017. Temporomandibular joint reconstruction with alloplastic prosthesis: the outcomes of four cases. *Maxillofac Plast Reconstr Surg*, 39, 6.
- PARK, J. H., ODKHUU, M., CHO, S., LI, J., PARK, B. Y. & KIM, J. W. 2020. 3D-printed titanium implant with pre-mounted dental implants for mandible reconstruction: a case report. *Maxillofac Plast Reconstr Surg*, 42, 28.
- PARTHASARATHY, J., STARLY, B., RAMAN, S. & CHRISTENSEN, A. 2010. Mechanical evaluation of porous titanium (Ti6Al4V) structures with electron beam melting (EBM). *J Mech Behav Biomed Mater*, 3, 249-59.
- PATTABI, M. & RAMAKRISHNA, K. 2008. Effect of mechanical cutting and polishing on the shape memory transformation behavior of NiTi alloy. *Materials Science and Engineering: A*, 486, 14-18.
- PENG, W. M., CHENG, K. J., LIU, Y. F., NIZZA, M., BAUR, D. A., JIANG, X. F. & DONG, X. T. 2021. Biomechanical and Mechanostat analysis of a titanium layered porous implant for mandibular reconstruction: The effect of the topology optimization design. *Mater Sci Eng C*, 124, 112056.
- PEREZ, D. & ELLIS, E., 3RD 2020. Complications of Mandibular Fracture Repair and Secondary Reconstruction. *Semin Plast Surg*, 34, 225-231.
- PICCININI, M., CUGNONI, J., BOTSIS, J., AMMANN, P. & WISKOTT, A. 2016. Numerical prediction of peri-implant bone adaptation: Comparison of mechanical stimuli and sensitivity to modeling parameters. *Med Eng Phys*, 38, 1348-1359.
- PICKRELL, B. B., SEREBRAKIAN, A. T. & MARICEVICH, R. S. 2017. Mandible Fractures. *Seminars in Plastic Surgery*, 31, 100-107.
- PIDAPARTI, R. M. 2017. *Engineering Finite Element Analysis*, Morgan & Claypool.
- PINHEIRO, M. & ALVES, J. L. 2015. The feasibility of a custom-made endoprosthesis in mandibular reconstruction: Implant design and finite element analysis. *J Craniomaxillofac Surg*, 43, 2116-28.
- PLUMBRIDGE, W. J., MATELA, R. J. & WESTWATER, A. 2003. Finite Element Analysis. In: PLUMBRIDGE, W. J., MATELA, R. J. & WESTWATER, A. (eds.) *Structural Integrity and Reliability in Electronics: Enhancing Performance in a Lead-Free Environment*. Dordrecht: Springer Netherlands.
- PO, J. M., KIESER, J. A., GALLO, L. M., TESENYI, A. J., HERBISON, P. & FARELLA, M. 2011. Time-frequency analysis of chewing activity in the natural environment. *J Dent Res*, 90, 1206-10.

- POGREL, M. A. 2021. The Concept of Stress Shielding in Nonvascularized Bone Grafts of the Mandible-A Review of 2 Cases. *J Oral Maxillofac Surg*, 79, 266.e1-266.e5.
- PONADER, S., WILMOWSKY, C. V., WIDENMAYER, M., LUTZ, R., HEINL, P., KÖRNER, C., SINGER, R. F., NKENKE, E., NEUKAM, F. W. & SCHLEGEL, K. A. 2010. In vivo performance of selective electron beam-melted Ti-6Al-4V structures. *Journal of Biomedical Materials Research Part A*, 92A, 56--62.
- POPOV, V. V., JR., MULLER-KAMSKII, G., KOVALEVSKY, A., DZHENZHERA, G., STROKIN, E., KOLOMIETS, A. & RAMON, J. 2018. Design and 3D-printing of titanium bone implants: brief review of approach and clinical cases. *Biomed Eng Lett*, 8, 337-344.
- PYKA, G., BURAKOWSKI, A., KERCKHOFS, G., MOESEN, M., VAN BAEL, S., SCHROOTEN, J. & WEVERS, M. 2012. Surface Modification of Ti6Al4V Open Porous Structures Produced by Additive Manufacturing. *Advanced Engineering Materials*, 14, 363-370.
- PYKA, G., KERCKHOFS, G., PAPANTONIOU, I., SPEIRS, M., SCHROOTEN, J. & WEVERS, M. 2013. Surface Roughness and Morphology Customization of Additive Manufactured Open Porous Ti6Al4V Structures. *Materials (Basel)*, 6, 4737-4757.
- QIAN, L. & ZHANG, H. 2011. Controlled freezing and freeze drying: A versatile route for porous and micro-/nano-structured materials. *Journal of Chemical Technology and Biotechnology*, 86, 172-184.
- RADWAN, D. & MOBARAK, F. 2018. Plate-related complications after mandibular reconstruction: observational study osteotomy. *Egyptian Journal of Oral and Maxillofacial Surgery*, 9, 22-27.
- RAHMAN, Z. U., POMPA, L. & HAIDER, W. 2014. Influence of Electropolishing and Magneto-electropolishing on Corrosion and Biocompatibility of Titanium Implants. *Journal of Materials Engineering and Performance*, 23, 3907-3915.
- RANSENIGO, C., TOCCI, M., PALO, F., GINESTRA, P., CERETTI, E., GELFI, M. & POLA, A. 2022. Evolution of Melt Pool and Porosity During Laser Powder Bed Fusion of Ti6Al4V Alloy: Numerical Modelling and Experimental Validation. *Lasers in Manufacturing and Materials Processing*, 9, 481-502.
- REHMAN, M., YANEN, W., MUSHTAQ, R. T., ISHFAQ, K., ZAHOOR, S., AHMED, A., KUMAR, M. S., GUEYEE, T., RAHMAN, M. M. & SULTANA, J. 2022. Additive manufacturing for biomedical applications: a review on classification, energy consumption, and its appreciable role since COVID-19 pandemic. *Progress in Additive Manufacturing*.
- REN, D., LI, S., WANG, H., HOU, W., HAO, Y., JIN, W., YANG, R., MISRA, R. D. K. & MURR, L. E. 2019. Fatigue behavior of Ti-6Al-4V cellular structures fabricated by additive manufacturing technique. *Journal of Materials Science & Technology*, 35, 285-294.

- REN, Z. H., FAN, T. F., ZHANG, S. & WU, H. J. 2020. Nonvascularized Iliac Bone Reconstruction for the Mandible Without Maxillofacial Skin Scarring. *J Oral Maxillofac Surg*, 78, 288-294.
- RIVIȘ, M., ROI, C., ROI, A., NICA, D., VĂLEANU, A. & RUSU, L.-C. 2020. The Implications of Titanium Alloys Applied in Maxillofacial Osteosynthesis. *Applied Sciences*, 10.
- ROBERTS, G. L. & PALLISTER, I. 2012. Finite element analysis in trauma & orthopaedics – an introduction to clinically relevant simulation & its limitations. *Orthopaedics and Trauma*, 26, 410-416.
- ROUDNICKA, M., MISURAK, M. & VOJTECH, D. 2019. Differences in the Response of Additively Manufactured Titanium Alloy to Heat Treatment - Comparison between SLM and EBM. *Manufacturing Technology*, 19, 668-673.
- RUMPLER, M., WOESZ, A., DUNLOP, J. W., VAN DONGEN, J. T. & FRATZL, P. 2008. The effect of geometry on three-dimensional tissue growth. *J R Soc Interface*, 5, 1173-80.
- SALEM, H., CARTER, L. N., ATTALLAH, M. M. & SALEM, H. G. 2019. Influence of processing parameters on internal porosity and types of defects formed in Ti6Al4V lattice structure fabricated by selective laser melting. *Materials Science and Engineering A*, 767, 138387.
- SANTOS, I. G., RAMOS DE FARIA, F., DA SILVA CAMPOS, M. J., DE BARROS, B. A. C., RABELO, G. D. & DEVITO, K. L. 2023. Fractal dimension, lacunarity, and cortical thickness in the mandible: Analyzing differences between healthy men and women with cone-beam computed tomography. *Imaging Sci Dent*, 53, 153-159.
- SCHIFF, N., GROSGOGEAT, B., LISSAC, M. & DALARD, F. 2002. Influence of fluoride content and pH on the corrosion resistance of titanium and its alloys. *Biomaterials*, 23, 1995-2002.
- SCHROM, T., BAST, F. & KNIPPING, S. 2019. Partial mandibulectomy without bony reconstruction in patients with oropharyngeal or mouth cancer. *Contemporary Oncology/Współczesna Onkologia*, 23, 146-150.
- SCHWARTZ-DABNEY, C. L. & DECHOW, P. C. 2002. Edentulation Alters Material Properties of Cortical Bone in the Human Mandible. *Journal of Dental Research*, 81, 613--617.
- SCHWARTZ-DABNEY, C. L. & DECHOW, P. C. 2003. Variations in cortical material properties throughout the human dentate mandible. *American Journal of Physical Anthropology*, 120, 252--277.
- SEOL, G.-J., JEON, E.-G., LEE, J.-S., CHOI, S.-Y., KIM, J.-W., KWON, T.-G. & PAENG, J.-Y. 2014. Reconstruction plates used in the surgery for mandibular discontinuity defect. *Journal of the Korean Association of Oral and Maxillofacial Surgeons*, 40, 266--271.

- SEONG, W. J., KIM, U. K., SWIFT, J. Q., HEO, Y. C., HODGES, J. S. & KO, C. C. 2009. Elastic properties and apparent density of human edentulous maxilla and mandible. *Int J Oral Maxillofac Surg*, 38, 1088-93.
- SETO, Y., SHARIF ULLAH, A., KUBO, A., D'ADDONA, D. M. & TETI, R. On the Porous Structuring using Unit Cells. 14th CIRP Conference on Intelligent Computation in Manufacturing Engineering, 2021. *Procedia CIRP* 99, 381–386.
- SHAPURIAN, T., DAMOULIS, P. D., REISER, G. M., GRIFFIN, T. J. & RAND, W. M. 2006. Quantitative Evaluation of Bone Density Using the Hounsfield Index. *INT J ORAL MAXILLOFAC IMPLANTS* 21, 290-7.
- SHEN, Y. W., TSAI, Y. S., HSU, J. T., SHIE, M. Y., HUANG, H. L. & FUH, L. J. 2022. Biomechanical Analyses of Porous Designs of 3D-Printed Titanium Implant for Mandibular Segmental Osteotomy Defects. *Materials (Basel)*, 15, 576.
- SHENAQ, S. M. & KLEBUC, M. J. A. 1994. TMJ reconstruction during vascularized bone graft transfer to the mandible. *Microsurgery*, 15, 299-304.
- SHI, J., YANG, J., LI, Z., ZHU, L., LI, L. & WANG, X. 2017. Design and fabrication of graduated porous Ti-based alloy implants for biomedical applications. *Journal of Alloys and Compounds*, 728, 1043--1048.
- SHIOMI, M., OSAKADA, K., NAKAMURA, K., YAMASHITA, T. & ABE, F. 2004. Residual Stress within Metallic Model Made by Selective Laser Melting Process. *CIRP Annals*, 53, 195-198.
- SHIPLEY, H., MCDONNELL, D., CULLETON, M., COULL, R., LUPOI, R., O'DONNELL, G. & TRIMBLE, D. 2018. Optimisation of process parameters to address fundamental challenges during selective laser melting of Ti-6Al-4V: A review. *International Journal of Machine Tools and Manufacture*, 128, 1-20.
- SIDAMBE, A. T. 2014. Biocompatibility of Advanced Manufactured Titanium Implants- A Review. *Materials (Basel)*, 7, 8168-8188.
- SIVARAJ, K. K. & ADAMS, R. H. 2016. Blood vessel formation and function in bone. *Development*, 143, 2706-15.
- SMITH, M., GUAN, Z. & CANTWELL, W. J. 2013. Finite element modelling of the compressive response of lattice structures manufactured using the selective laser melting technique. *International Journal of Mechanical Sciences*, 67, 28--41.
- SNELL, R., TAMMAS-WILLIAMS, S., CHECHIK, L., LYLE, A., HERNÁNDEZ-NAVA, E., BOIG, C., PANOUTSOS, G. & TODD, I. 2019. Methods for Rapid Pore Classification in Metal Additive Manufacturing. *JOM*, 72, 101-109.
- SONG, J., TANG, Q., FENG, Q., MA, S., GUO, F. & HAN, Q. 2021a. Investigation on the modelling approach for variable-density lattice structures fabricated using selective laser melting. *Materials & Design*, 212.

- SONG, J., TANG, Q., FENG, Q., MA, S., GUO, F. & HAN, Q. 2021b. Investigation on the modelling approach for variable-density lattice structures fabricated using selective laser melting. *Materials & Design*, 212, 110236.
- SORO, N., ATTAR, H., WU, X. & DARGUSCH, M. S. 2019. Investigation of the structure and mechanical properties of additively manufactured Ti-6Al-4V biomedical scaffolds designed with a Schwartz primitive unit-cell. *Materials Science and Engineering: A*, 745, 195-202.
- SUMITOMO, N., NORITAKE, K., HATTORI, T., MORIKAWA, K., NIWA, S., SATO, K. & NIINOMI, M. 2008. Experiment study on fracture fixation with low rigidity titanium alloy. *Journal of Materials Science: Materials in Medicine*, 19, 1581--1586.
- SVENUNGSSON, J., CHOQUET, I. & KAPLAN, A. F. H. 2015. Laser Welding Process – A Review of Keyhole Welding Modelling. *Physics Procedia*, 78, 182-191.
- TAMMAS-WILLIAMS, S., WITHERS, P. J., TODD, I. & PRANGNELL, P. B. 2016. The Effectiveness of Hot Isostatic Pressing for Closing Porosity in Titanium Parts Manufactured by Selective Electron Beam Melting. *Metallurgical and Materials Transactions A*, 47, 1939-1946.
- TAN, X. P., TAN, Y. J., CHOW, C. S. L., TOR, S. B. & YEONG, W. Y. 2017. Metallic powder-bed based 3D printing of cellular scaffolds for orthopaedic implants: A state-of-the-art review on manufacturing, topological design, mechanical properties and biocompatibility. *Mater Sci Eng C* 76, 1328-1343.
- TANG, M., PISTORIUS, P. C. & BEUTH, J. L. 2017. Prediction of lack-of-fusion porosity for powder bed fusion. *Additive Manufacturing*, 14, 39-48.
- TANIGUCHI, N., FUJIBAYASHI, S., TAKEMOTO, M., SASAKI, K., OTSUKI, B., NAKAMURA, T., MATSUSHITA, T., KOKUBO, T. & MATSUDA, S. 2016. Effect of pore size on bone ingrowth into porous titanium implants fabricated by additive manufacturing: An in vivo experiment. *Mater Sci Eng C* 59, 690-701.
- TENGVALL, P. & LUNDSTRÖM, I. 1992. Physico-chemical considerations of titanium as a biomaterial. *Clinical Materials*, 9, 115-134.
- THIJS, L., VERHAEGHE, F., CRAEGHS, T., HUMBEECK, J. V. & KRUTH, J.-P. 2010. A study of the microstructural evolution during selective laser melting of Ti-6Al-4V. *Acta Materialia*, 58, 3303-3312.
- TIAN, Y., TOMUS, D., ROMETSCH, P. & WU, X. 2017. Influences of processing parameters on surface roughness of Hastelloy X produced by selective laser melting. *Additive Manufacturing*, 13, 103-112.
- TONG, J., BOWEN, C. R., PERSSON, J. & PLUMMER, A. 2016. Mechanical properties of titanium-based Ti-6Al-4V alloys manufactured by powder bed additive manufacture. *Materials Science and Technology*, 33, 138-148.

- TSOEUNYANE, G. M., MATHE, N., TSHABALALA, L., MAKHATHA, M. E. & LUO, Z. 2022. Electropolishing of Additively Manufactured Ti-6Al-4V Surfaces in Nontoxic Electrolyte Solution. *Advances in Materials Science and Engineering*, 2022, 1-12.
- TÜZEMEN, M. Ç., SALAMCI, E. & ÜNAL, R. 2022. Investigation of the relationship between flexural modulus of elasticity and functionally graded porous structures manufactured by AM. *Materials Today Communications*, 31, 103592.
- UNG, F., ROCCO, J. W. & DESCHLER, D. G. 2002. Temporary intraoperative external fixation in mandibular reconstruction. *Laryngoscope*, 112, 1569-73.
- VAISH, A. & VAISH, R. 2018. 3D printing and its applications in Orthopedics. *J Clin Orthop Trauma*, 9, S74-S75.
- VAN BAEL, S., CHAI, Y. C., TRUSCELLO, S., MOESEN, M., KERCKHOFS, G., VAN OOSTERWYCK, H., KRUTH, J. P. & SCHROOTEN, J. 2012. The effect of pore geometry on the in vitro biological behavior of human periosteum-derived cells seeded on selective laser-melted Ti6Al4V bone scaffolds. *Acta Biomater*, 8, 2824-34.
- VAN EIJDEN, T. M. 2000. Biomechanics of the mandible. *Critical Reviews in Oral Biology & Medicine*, 11, 123-136.
- VAN KOOTWIJK, A., MOOSABEIKI, V., SALDIVAR, M. C., PAHLAVANI, H., LEEFLANG, M. A., KAZEMIVAND NIAR, S., PELLIKANAN, P., JONKER, B. P., AHMADI, S. M., WOLVIUS, E. B., TUMER, N., MIRZAALI, M. J., ZHOU, J. & ZADPOOR, A. A. 2022. Semi-automated digital workflow to design and evaluate patient-specific mandibular reconstruction implants. *J Mech Behav Biomed Mater*, 132, 105291.
- VIGNESH, U., MEHROTRA, D., HOWLADER, D., SINGH, P. K. & GUPTA, S. 2019. Patient Specific Three-Dimensional Implant for Reconstruction of Complex Mandibular Defect. *Journal of Craniofacial Surgery*, 30, e308-e311.
- VITINS, V., DOBELIS, M., MIDDLETON, J., LIMBERT, G. & KNETS, I. 2003. Flexural and creep properties of human jaw compact bone for FEA studies. *Comput Methods Biomech Biomed Engin*, 6, 299-303.
- VOLLMER, D., MEYER, U., JOOS, U., VEGH, A. & PIFFKO, J. 2000. Experimental and finite element study of a human mandible. *J Craniomaxillofac Surg*, 28, 91-6.
- VOZNESENSKAYA, A. A., ZHDANOV, A. V. & RAZNOSCHIKOV, A. S. 2021. Evolution of porosity depending on SLM mode and subsequent HIP processing. *Journal of Physics: Conference Series*, 2077.
- WANG, D., LV, J., WEI, X., LU, D. & CHEN, C. 2023. Study on Surface Roughness Improvement of Selective Laser Melted Ti6Al4V Alloy. *Crystals (Basel)*, 13, 306.

- WANG, R., NI, S., MA, L. & LI, M. 2022. Porous construction and surface modification of titanium-based materials for osteogenesis: A review. *Front Bioeng Biotechnol*, 10, 973297.
- WARNKE, P. H., DOUGLAS, T., WOLLNY, P., SHERRY, E., STEINER, M., GALONSKA, S., BECKER, S. T., SPRINGER, I. N., WILTFANG, J. & SIVANANTHAN, S. 2009. Rapid prototyping: porous titanium alloy scaffolds produced by selective laser melting for bone tissue engineering. *Tissue Eng Part C Methods*, 15, 115-24.
- WATANABE, R., TAKAHASHI, H., MATSUGAKI, A., UEMUKAI, T., KOGAI, Y., IMAGAMA, T., YUKATA, K., NAKANO, T. & SAKAI, T. 2023. Novel nano-hydroxyapatite coating of additively manufactured three-dimensional porous implants improves bone ingrowth and initial fixation. *J Biomed Mater Res B Appl Biomater*, 111, 453-462.
- WEHMÖLLER, M., WARNKE, P. H., ZILIAN, C. & EUFINGER, H. 2005. Implant design and production—a new approach by selective laser melting. *International Congress Series*, 1281, 690-695.
- WEXLER, A. M. 2015. Anatomy of the Head and Neck. In: TAUB, P. J., PATEL, P. K., BUCHMAN, S. R. & COHEN, M. N. (eds.) *Ferraro's Fundamentals of Maxillofacial Surgery*. Second ed. New York, NY, USA: Springer.
- WICKMANN, C., BENZ, C., HEYER, H., WITTE-BODNAR, K., SCHAFER, J. & SANDER, M. 2021. Internal Crack Initiation and Growth Starting from Artificially Generated Defects in Additively Manufactured Ti6Al4V Specimen in the VHCF Regime. *Materials (Basel)*, 14.
- WONG, K. V. & HERNANDEZ, A. 2012. A Review of Additive Manufacturing. *ISRN Mechanical Engineering*, 2012, 1-10.
- WONG, R. C., TIDEMAN, H., MERKX, M. A., JANSEN, J. & GOH, S. M. 2012. The modular endoprosthesis for mandibular body replacement. Part 1: mechanical testing of the reconstruction. *J Craniomaxillofac Surg*, 40, e479-86.
- WYCISK, E., SOLBACH, A., SIDDIQUE, S., HERZOG, D., WALTHER, F. & EMMELMANN, C. 2014. Effects of Defects in Laser Additive Manufactured Ti-6Al-4V on Fatigue Properties. *Physics Procedia*, 56, 371-378.
- WYSOCKI, B., MAJ, P., SITEK, R., BUHAGIAR, J., KURZYDŁOWSKI, K. & ŚWIĘSZKOWSKI, W. 2017. Laser and Electron Beam Additive Manufacturing Methods of Fabricating Titanium Bone Implants. *Applied Sciences*, 7, 657.
- XIA, Y., FENG, Z. C., LI, C., WU, H., TANG, C., WANG, L. & LI, H. 2020. Application of additive manufacturing in customized titanium mandibular implants for patients with oral tumors. *Oncol Lett*, 20, 51.

- XIANG, Y., ZHANG, S., WEI, Z., LI, J., WEI, P., CHEN, Z., YANG, L. & JIANG, L. 2018. Forming and defect analysis for single track scanning in selective laser melting of Ti6Al4V. *Applied Physics A*, 124, 685.
- XIAO, L., LI, S., SONG, W., XU, X. & GAO, S. 2020. Process-induced geometric defect sensitivity of Ti-6Al-4V lattice structures with different mesoscopic topologies fabricated by electron beam melting. *Materials Science and Engineering A*, 778, 139092.
- XIAO, Y., DING, Y., ZHUANG, J., SUN, R., SUN, H. & BAI, L. 2022. Osteoimmunomodulation role of exosomes derived from immune cells on osseointegration. *Front Bioeng Biotechnol*, 10, 989537.
- XIONG, Y., HAN, Z., QIN, J., DONG, L., ZHANG, H., WANG, Y., CHEN, H. & LI, X. 2021. Effects of porosity gradient pattern on mechanical performance of additive manufactured Ti-6Al-4V functionally graded porous structure. *Materials & Design*, 208, 109911.
- XIONG, Y., WANG, W., GAO, R., ZHANG, H., DONG, L., QIN, J., WANG, B., JIA, W. & LI, X. 2020a. Fatigue behavior and osseointegration of porous Ti-6Al-4V scaffolds with dense core for dental application. *Materials & Design*, 195.
- XIONG, Y. Z., GAO, R. N., ZHANG, H., DONG, L. L., LI, J. T. & LI, X. 2020b. Rationally designed functionally graded porous Ti6Al4V scaffolds with high strength and toughness built via selective laser melting for load-bearing orthopedic applications. *J Mech Behav Biomed Mater*, 104, 103673.
- XU, Y., HAN, G., HUANG, G., LI, T., XIA, J. & GUO, D. 2023. Properties Evaluations of Topology Optimized Functionally Graded Lattice Structures Fabricated by Selective Laser Melting. *Materials (Basel)*, 16.
- XUE, W., KRISHNA, B. V., BANDYOPADHYAY, A. & BOSE, S. 2007. Processing and biocompatibility evaluation of laser processed porous titanium. *Acta Biomater*, 3, 1007-18.
- YADAV, A. 2021. Principles of Internal Fixation in Maxillofacial Surgery. In: BONANTHAYA, K., PANNEERSELVAM, E., MANUEL, S., KUMAR, V. V. & RAI, A. (eds.) *Oral and Maxillofacial Surgery for the Clinician*. Singapore: Springer.
- YADROITSEV, I., KRAKHMALOV, P. & YADROITSAVA, I. 2015. Hierarchical design principles of selective laser melting for high quality metallic objects. *Additive Manufacturing*, 7, 45-56.
- YADROITSEV, I., KRAKHMALOV, P., YADROITSAVA, I. & DU PLESSIS, A. 2017. Qualification of Ti6Al4V ELI Alloy Produced by Laser Powder Bed Fusion for Biomedical Applications. *JOM*, 70, 372-377.
- YADROITSEV, I. & SMUROV, I. 2011. Surface Morphology in Selective Laser Melting of Metal Powders. *Physics Procedia*, 12, 264-270.

- YAN, C., HAO, L., HUSSEIN, A. & YOUNG, P. 2015. Ti-6Al-4V triply periodic minimal surface structures for bone implants fabricated via selective laser melting. *Journal of the Mechanical Behavior of Biomedical Materials*, 51, 61--73.
- YAN, X., LUPOI, R., WU, H., MA, W., LIU, M., O'DONNELL, G. & YIN, S. 2019. Effect of hot isostatic pressing (HIP) treatment on the compressive properties of Ti6Al4V lattice structure fabricated by selective laser melting. *Materials Letters*, 255.
- YÁNEZ, A., FIORUCCI, M. P., CUADRADO, A., MARTEL, O. & MONOPOLI, D. 2020. Surface roughness effects on the fatigue behaviour of gyroid cellular structures obtained by additive manufacturing. *International Journal of Fatigue*, 138, 105702.
- YANG, L., MERTENS, R., FERRUCCI, M., YAN, C., SHI, Y. & YANG, S. 2019. Continuous graded Gyroid cellular structures fabricated by selective laser melting: Design, manufacturing and mechanical properties. *Materials & Design*, 162, 394-404.
- YAVARI, S. A., AHMADI, S. M., WAUTHLE, R., POURAN, B., SCHROOTEN, J., WEINANS, H. & ZADPOOR, A. A. 2015. Relationship between unit cell type and porosity and the fatigue behavior of selective laser melted meta-biomaterials. *Journal of the Mechanical Behavior of Biomedical Materials*, 43, 91--100.
- YIM, K. K. & WEI, F. C. 1994. Fibula osteoseptocutaneous flap for mandible reconstruction. *Microsurgery*, 15, 245-9.
- YOON, Y., KIM, J.-E., JUNG, J., OH, S.-H., NOH, G. & KWON, Y.-D. 2021. Effect of mandibular contouring surgery on the stress distribution during various clenching tasks. *Journal of Computational Design and Engineering*, 8, 570-580.
- YUAN, W., HOU, W., LI, S., HAO, Y., YANG, R., ZHANG, L.-C. & ZHU, Y. 2018. Heat treatment enhancing the compressive fatigue properties of open-cellular Ti-6Al-4V alloy prototypes fabricated by electron beam melting. *Journal of Materials Science & Technology*, 34, 1127-1131.
- ZELLER, A. N., NEUHAUS, M. T., WEISSBACH, L. V. M., RANA, M., DHAWAN, A., ECKSTEIN, F. M., GELLRICH, N. C. & ZIMMERER, R. M. 2020. Patient-Specific Mandibular Reconstruction Plates Increase Accuracy and Long-Term Stability in Immediate Alloplastic Reconstruction of Segmental Mandibular Defects. *J Maxillofac Oral Surg*, 19, 609-615.
- ZHANG, B., LI, Y. & BAI, Q. 2017. Defect Formation Mechanisms in Selective Laser Melting: A Review. *Chinese Journal of Mechanical Engineering*, 30, 515-527.
- ZHANG, B., PEI, X., ZHOU, C., FAN, Y., JIANG, Q., RONCA, A., D'AMORA, U., CHEN, Y., LI, H., SUN, Y. & ZHANG, X. 2018. The biomimetic design and 3D printing of customized mechanical properties porous Ti6Al4V scaffold for load-bearing bone reconstruction. *Materials & Design*, 152, 30--39.

- ZHANG, Y., LI, J., CHE, S. & TIAN, Y. 2019. Electrochemical Polishing of Additively Manufactured Ti-6Al-4V Alloy. *Metals and Materials International*, 26, 783-792.
- ZHANG, Y., SUN, N., ZHU, M., QIU, Q., ZHAO, P., ZHENG, C., BAI, Q., ZENG, Q. & LU, T. 2022. The contribution of pore size and porosity of 3D printed porous titanium scaffolds to osteogenesis. *Biomater Adv*, 133, 112651.
- ZHAO, S., LI, S. J., HOU, W. T., HAO, Y. L., YANG, R. & MISRA, R. D. K. 2016. The influence of cell morphology on the compressive fatigue behavior of Ti-6Al-4V meshes fabricated by electron beam melting. *J Mech Behav Biomed Mater*, 59, 251-264.
- ZHAO, S., LI, S. J., WANG, S. G., HOU, W. T., LI, Y., ZHANG, L. C., HAO, Y. L., YANG, R., MISRA, R. D. K. & MURR, L. E. 2018. Compressive and fatigue behavior of functionally graded Ti-6Al-4V meshes fabricated by electron beam melting. *Acta Materialia*, 150, 1-15.
- ZHAO, Z. & ZHANG, X. S. 2021. Design of graded porous bone-like structures via a multi-material topology optimization approach. *Structural and Multidisciplinary Optimization*, 64, 677-698.
- ZHONG, S., SHI, Q., SUN, Y., YANG, S., VAN DESSEL, J., GU, Y., CHEN, X., LUBBERS, H. T. & POLITIS, C. 2021. Biomechanical comparison of locking and non-locking patient-specific mandibular reconstruction plate using finite element analysis. *J Mech Behav Biomed Mater*, 124, 104849.
- ZHOU, L. B., SHANG, H. T., HE, L. S., BO, B., LIU, G. C., LIU, Y. P. & ZHAO, J. L. 2010. Accurate reconstruction of discontinuous mandible using a reverse engineering/computer-aided design/rapid prototyping technique: a preliminary clinical study. *J Oral Maxillofac Surg*, 68, 2115-21.
- ZIMMERLI, W., TRAMPUZ, A. & OCHSNER, P. E. 2004. Prosthetic-Joint Infections. *New England Journal of Medicine*, 351, 1645-1654.
- ZOUMALAN, R. A., HIRSCH, D. L., LEVINE, J. P. & SAADEH, P. B. 2009. Plating in microvascular reconstruction of the mandible: can fixation be too rigid? *J Craniofac Surg*, 20, 1451-1454.

Chapter 2

Summary and objectives of the research

Chapter 2

2 Summary and objectives of the research

2.1 Summary

While the development of SLM to build porous Ti6Al4V implants has seen widespread interest among researchers, several challenges face the use of this technology in clinical settings. These were discussed in the previous chapter. In the scope of this dissertation, some of these challenges were addressed:

1. Research findings related to the design of SLM-built porous Ti6Al4V do not address the use of fine porous patterns, instead opting for a thin shell design to mimic the cortical bone structure.
2. Current finite element analysis models of porous Ti6Al4V do not reflect the structural and mechanical properties of real-life SLM-built constructs.
3. Lack of numerical models that predict the fatigue strength of SLM-built porous Ti6Al4V constructs.
4. Numerical modeling of whole porous Ti6Al4V implant designs is time and cost-consuming due to the high computational power required.

To address these four above challenges, it is proposed to design and build numerical models, based on finite element analysis (FEA), that can predict the mechanical properties of SLM-built porous Ti6Al4V constructs.

2.2 Objectives and hypothesis

General objective: To design and build static and dynamic numerical models that can predict the static and dynamic mechanical properties of SLM-built porous Ti6Al4V constructs and validate them with real-life mechanical data.

Main hypotheses: Static and dynamic numerical models of porous Ti6Al4V constructs that use adjusted mechanical parameters to account for internal defects and surface roughness can predict their static and dynamic mechanical properties within a deviation $\approx 10\%$ from the real-life mechanical tests.

Specific objective 1: Design SLM-built porous Ti6Al4V constructs that could be used in mandibular reconstruction. This was addressed in chapter 3.

Specific objective 2: Determine the static mechanical properties of SLM-built porous Ti6Al4V. This was addressed in chapter 3.

Specific objective 3: Design and build finite element analysis models that mimic the tensile and flexural mechanical properties of SLM-built porous Ti6Al4V constructs. This was addressed in chapter 3.

Specific objective 4: Determine the flexural fatigue properties of SLM-built porous Ti6Al4V. This was addressed in chapter 4.

Specific objective 5: Design and build dynamic numerical models that mimic the fatigue flexural properties of SLM-built porous Ti6Al4V constructs. This was addressed in chapter 4.

Specific objective 6: Design and build a static and dynamic FEA model of an intraosseous porous mandibular implant that is compatible with mandibular bone. This was addressed in Chapter 5.

Chapter 3

Static mechanical and microstructural properties of porous Ti6Al4V constructs

This chapter was adapted from the manuscript: Hijazi, K. M., Mao, H., Holdsworth, D. W., Dixon, S. J. & Rizkalla, A. S. Mechanical and Microstructural Properties of Additive Manufactured Microporous Titanium Alloy Constructs for Orthopaedic and Maxillofacial Reconstruction [Unpublished results].

Chapter 3

3 Static mechanical and microstructural properties of porous Ti6Al4V constructs

3.1 Summary

Porous intraosseous implants, fabricated from titanium alloy by selective laser melting (SLM), promote osseointegration and decrease stress shielding. Nevertheless, the application of such constructs in surgery has been restricted due to issues with their structural and mechanical properties. In addition, the flexural properties of porous constructs are not well known. Hence, this research aimed to investigate the mechanical and microstructural properties of porous constructs made from Ti6Al4V alloy for applications such as mandibular reconstruction. Computer models were created of dumbbell-shaped and square prism constructs with cubic pore structures. Five strut thicknesses between 250 and 650 μm with a constant 1 mm unit cell size were created, which gave rise to pores of sizes between 350 and 750 μm . Nonporous models were used as controls. Constructs were fabricated from these models using selective laser melting. Computed tomography was used to investigate internal defects and surface roughness. Internal defects made up $< 1.2\%$ of the total volume. Loose and partially melted particles caused a rough surface on the struts, with arithmetic mean height ranging between 2.0 and 9.5 μm . Finite element analysis (FEA) was performed to simulate tensile and flexural loadings and predict locations of mechanical weaknesses. Static tensile and three-point bend tests were performed on SLM-built constructs using an Instron screw-type testing machine. The FEA models incorporated mechanical properties of Ti6Al4V, which were sourced from the stress-strain curves from tensile tests on nonporous constructs produced via selective laser melting. There was a close agreement between the FEA simulations and the actual tensile and flexural strengths and moduli of the constructs (deviation $< 11\%$). The real-life mechanical test and FEA test results demonstrated that the modulus and

strength values strongly correlated with strut thickness ($R^2 > 0.95$). Porous Ti6Al4V constructs with strut thicknesses ranging between 350 and 450 μm were found to have modulus and strength values that matched those of the mandible. This study demonstrated that FEA models can accurately predict the mechanical behaviour of SLM-built porous constructs. This will permit the rapid design of patient-specific porous devices that facilitate bone alignment, vascularization, tissue ingrowth, and skeletal function.

3.2 Introduction

Metal fixation plates are often used in mandibular reconstruction to hold bone grafts in place (Pickrell et al., 2017). Titanium alloys such as titanium 6-aluminum 4-vanadium (Ti6Al4V) have been widely used to build fixation plates due to their superior mechanical properties and demonstrated biocompatibility in orthopedic applications (Sidambe, 2014, Warnke et al., 2009, Liu and Shin, 2019). However, several complications have been found to arise from conventional mandibular reconstruction methods, including malunion or non-union of bone post-plating due to misalignment of bones and plates, limitation in the amount of bone for grafting, damage to the bone donor site, and infection (section 1.5).

In the past few years, endoprostheses designed as a cage or basket have been envisioned by researchers. These designs mimicked both the geometry and the mechanical properties of mandibular bones (Peng et al., 2021, van Kootwijk et al., 2022, Shen et al., 2022). These designs are anticipated to avoid surgical misalignments and produce stable bone segments post-surgery, thereby reducing the possibility of implant failure. A major requirement for the success of metal endoprostheses is to have mechanical properties matching those of bones. The Young's modulus of Ti6Al4V (≈ 100 GPa) is about four-fold greater than that of cortical bone (≈ 25 GPa) (Jackson et al., 2016, Nagasao et al., 2009). The mismatch of stiffness between bone and Ti6Al4V gives rise to stress shielding, where bones adjacent to stiff mandibular implants do not receive sufficient deformation for bone modelling to occur, leading to bone atrophy and eventual loosening and failure of the implant (Pogrel, 2021, Zhou et al., 2010, Zoumalan et al., 2009, Kennady et al., 1989b, Kennady et al., 1989a). The introduction of open cell pores into the constructs reduces their stiffness to levels comparable to those of cortical and trabecular bones (Ge et al., 2023, van Kootwijk

et al., 2022, Di Caprio et al., 2022). In addition, these porous Ti6Al4V constructs permit healthy bone ingrowth (Li et al., 2017, Taniguchi et al., 2016, De Wild et al., 2019).

The advent of powder-bed additive manufacturing techniques, such as selective laser melting (SLM), opened the door to producing constructs with intricate porous structures (Peng et al., 2021, van Kootwijk et al., 2022, Shen et al., 2022). SLM uses a high-intensity laser that melts metal powders to shape constructs out of computer-aided design (CAD) models (Bose et al., 2018, Jahadakbar et al., 2016). Given the time and cost involved in the building and testing of SLM-built porous constructs, computer numerical models that simulate loading using finite element analysis (FEA) have seen wide adoption for the mechanical testing of constructs (Peng et al., 2021, van Kootwijk et al., 2022, Shen et al., 2022). A two-step process – using FEA to optimize the mechanical properties of porous models, followed by building these constructs using SLM – allows the production of patient-specific implants (Oldhoff et al., 2021, van Kootwijk et al., 2022).

The combined use of FEA modelling and SLM to design, test and produce patient-specific mandibular and orthopedic implants is an area of active research. However, a major disadvantage of using SLM is the presence of internal defects within the constructs. These may include lack-of-fusion defects, gas bubbles, microcracks, and keyhole defects (Zhang et al., 2017, Snell et al., 2019, Voznesenskaya et al., 2021, Ransenigo et al., 2022, Salem et al., 2019). In addition to internal defects, rough texture occurs on the surface of SLM-built constructs (Hernández-Nava et al., 2016, Ge et al., 2023, Xiao et al., 2020, Mower and Long, 2016, Yáñez et al., 2020). When in excess, these defects are thought to affect the mechanical properties of porous constructs (Gong et al., 2015, du Plessis et al., 2018b). The microstructure of SLM-built Ti6Al4V constructs contains martensitic α' platelets, giving the constructs high yield strength but low ductility when compared to conventionally made Ti6Al4V constructs (Tan et al., 2017, Gong et al., 2015, Murr et al., 2012). Simulating internal defects and surface roughness by including them in FEA models can be highly expensive both in computational power and processing time (Dong et al., 2017). This could be the reason why most relevant studies have either tested porous construct models with smaller sizes (Zhao et al., 2016), used symmetrical properties to reduce the FEA model size (Song et al., 2021), or modelled porous constructs using

simplified beam elements (Song et al., 2021). Much of the work that was conducted over the past 20 years on SLM-built constructs used compressive tests to characterize their mechanical properties (El-Sayed et al., 2020, Bartolomeu et al., 2021, Ran et al., 2018). However, mandibles are known to predominantly experience flexural deformation through sagittal bending and lateral bending, as well as torsion (van Eijden, 2000). That is why flexural tests are needed to better understand the mechanical behaviour of these constructs for use in mandibular applications. Nevertheless, little work has been reported in the literature that deals with the flexural properties of porous constructs. Previous studies have concentrated on large pore sizes with thick struts and complex pore shapes (sections 1.7 and 1.8). In contrast, in the present investigation, we focused on pores with unit cell size = 1 mm and simple cubic designs. It should be noted that simple cubic pores permit excellent bone ingrowth (Kovacs et al., 2023), and the pore sizes used in the present study are in the range that is optimal for bone ingrowth (Chapter 1).

The main objective of this study is to design FEA models that predict the mechanical properties of SLM-built porous Ti6Al4V constructs and to characterize the mechanical behaviour of these constructs using flexural and tensile static loading.

3.3 Methods

3.3.1 Model design and manufacture of porous constructs

3.3.1.1 Design of unit cells and CAD models

A series of porous and nonporous CAD models were prepared as dumbbell-shaped tokens for tensile testing and square prism models for flexural testing (Figure 3-1). All models were generated by the propagation of unit cells, shaped as simple cubes. These unit cells were built each with a uniform strut thickness ranging between 250 and 650 μm , while maintaining a unit cell size of 1 mm. ASTM standards were implemented, as closely as possible, in the design of the tensile models (ASTM E345-16, E8/E8M-22) and flexural models (ASTM E290-22). Pores were present throughout the flexural models and between the grips in the tensile models. The porous tensile models were similar to those used in other studies (e.g., Bartolomeu et al. (2021) and Naghavi et al. (2022)). The flexural porous

models were designed in line with previous work by Horn et al. (2014) and Di Caprio et al. (2022). Nonporous construct models were used as controls. Initially, struts were designed with square cross-sectional shapes (S-section struts), which are computationally less expensive to use in FEA simulations. However, upon analyzing the strut microstructure in the SLM-built constructs (see section 3.4.2.1 below), a second series of CAD models were built with circular cross-sectional shapes (C-section struts) to better represent the final strut geometry.

Tensile models had a nominal gauge length (L) \times base width (W) \times base thickness (T) of 9 mm \times 3 mm \times 1 mm. Flexural models had a nominal length (L) \times base width (W) \times base thickness (T) of 100 mm \times 4 mm \times 4 mm. To perform microstructural analysis, different square prism porous and nonporous CAD models were built, with the dimensions being 10 mm \times 5 mm \times 5 mm. For detailed dimensions of the CAD models, see Appendix A, section A.6, Table A-12 to Table A-14.

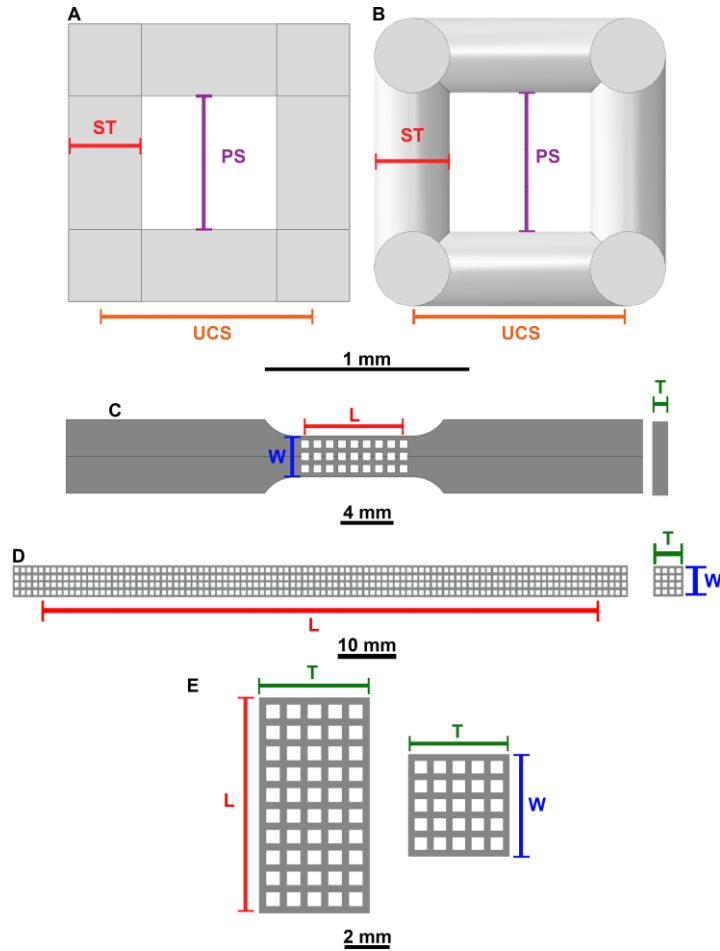


Figure 3-1: Representative diagrams showing the geometry of the porous CAD models.

The unit pore used to build the models had a constant unit cell size ($UCS = 1 \text{ mm}$). The struts had one of two designs, either (A) a square strut cross-section (S-section) or (B) a circular strut cross-section (C-section). For each model, the strut thickness (ST) was varied between $250 \text{ }\mu\text{m}$ and $650 \text{ }\mu\text{m}$, which in turn varied the pore size (PS) between $350 \text{ }\mu\text{m}$ and $750 \text{ }\mu\text{m}$. The models were designed as (C) dumbbell-shaped tokens for tensile tests, (D) square-prism beams for flexural tests or (E) square prisms for microstructural analysis. The gauge length (L), width (W), and thickness (T) are labelled for each of the representative models.

3.3.1.2 Manufacturing of constructs

Ti6Al4V constructs were fabricated from S-section CAD models using SLM. A local company (Additive Design in Surgical Solutions Center, London, Canada) performed the fabrication process, employing a Renishaw AM 400 SLM system (Renishaw PLC, Wotton-under-Edge, United Kingdom). The powder used was Ti6Al4V ELI-0406, with chemical composition described in Table 3-1.

Table 3-1: The chemical composition of Ti6Al4V powder. Information was provided by Renishaw PLC (2017).

Ti	Al	V	Fe	O	C	N	H	Y
> 89%	5.5 – 6.5%	3.5–4.5%	<0.25%	<0.13%	<0.08%	<0.03%	<0.012%	<0.005%

For all the constructs, the laser power ranged between 100 and 200 W. The laser beam diameter was 70 μm , the layer thickness was 30 μm , the laser point diameter was 40 μm , the exposure time per point ranged between 40 and 60 μs , the hatch point distance was 75 μm , and the powder grain diameter ranged between 15 and 45 μm . All the constructs were built with the smallest surface laid on the bed of the SLM, with the length of the constructs along the vertical axis of the building and perpendicular to the wiper direction of the SLM.

Following the SLM process, heat treatment was applied to relieve constructs from internal residual stresses generated during printing. Constructs were first placed in a charging box, followed by purging of the box environment with argon. The box was then heated in a furnace through the following cycle: the specimens were heated to 350°C over a period of 60 min and then kept at that temperature for 30 min. The specimens were then heated to 850°C over a period of 60 min and kept at that temperature for an additional 60 min. Finally, the furnace was cooled slowly to room temperature. Geometric measurements of all tensile and flexural specimens were performed prior to mechanical testing.

Porous specimens (n=120) were built using SLM for the tensile and flexural tests. The sample size for each strut thickness and for nonporous specimens built using SLM was n=10. In addition, 7 nonporous tensile specimens and 6 flexural specimens were prepared from a cast stock of Grade 5-Ti6Al4V (McMaster Carr, Elmhurst, Illinois, United States). For microstructural analysis, two specimens were printed for each strut thickness group.

3.3.2 Microstructural analysis

3.3.2.1 Imaging of constructs using μ -CT

The porous constructs built with SLM were scanned using μ -CT (Nikon Metris μ -CT Scanner, Nikon Metrology, Brighton, MI, United States) at the Sustainable Archaeology lab (Museum of Ontario Archaeology, London, ON, Canada). Details of the CT parameters and steps to perform the imaging process can be found in Appendix A, section A.1. The

voxel size achieved for each scan was set at 7.5 μm except in one construct from the 650 μm strut thickness group, where a malfunction of the $\mu\text{-CT}$ scanner caused a slight drop in the voxel size to 7.1 μm (see Appendix A, section A.1.1, Table A-1).

3.3.2.2 Segmentation of $\mu\text{-CT}$ images

The CT scanning produced a stacked series of images for each specimen, which were reconstructed into a three-dimensional (3D) model using Nikon CT Pro 3D Software (Nikon Corporation) (Appendix A, section A.1.2). These 3D-CT models were segmented and analyzed using Dragonfly software (Dragonfly 2022, Comet Technologies Canada Inc., Montreal, QC, Canada). Segmentation was done using a CT-density thresholding process similar to the one proposed by Otsu (1979). Further details on the segmentation process can be seen in Appendix A, section A.1.3. Each 3D CT model was split into sixteen smaller cubic or rectangular prism sub-models, each with a volume of about 20 mm^3 . Each sub-model's voxels were segmented into four regions of interest (ROIs): the macropores, internal defects, titanium alloy, and outer surface. The voxels occupied by internal defects were marked and used to measure the volume percentage of internal defects from each sub-model. The internal defects were split into separate ROIs and further analyzed to determine their average diameter. This value was determined by finding the average of the maximum and minimum Feret diameters. Feret diameter was defined as the span length of the defect at any given direction (Merkus, 2009).

3.3.2.3 Strut thickness analysis

Two struts were selected randomly from each analyzed sub-model of the porous constructs, one parallel to the building axis (termed parallel struts) and another that was perpendicular to the building axis (termed perpendicular struts) (see Appendix A, section A.2). The surface profiles from these struts were extracted and converted to 3D mesh images, with elements covering the surface and vertices at the surface peaks and valleys. These mesh images were then exported to a custom-made script written using MATLAB (MATLAB R2022b, Natick, MA, United States). The script removed duplicate vertices, and the images were converted from Cartesian coordinates to polar coordinates (Appendix A, section A.1.4). All vertices were put together on 2D polar coordinates, which were then used to

interpolate an ellipse. Then each ellipse was used to calculate the thickness of the individual struts by averaging the length of the major and minor axes (Figure 3-2). The major axis of an ellipse is the longest segment that passes through the center of the ellipse and connects the two widest points on the surface. The minor axis is the shortest segment that passes through the center of the ellipse and connects the two narrowest points on the surface. While the original CAD models had square cross-sectional (S-section) struts, almost all the struts were found to be fitting an elliptical or circular cross-section. Details of the strut thickness measurements can be found in Appendix A, section A.2.

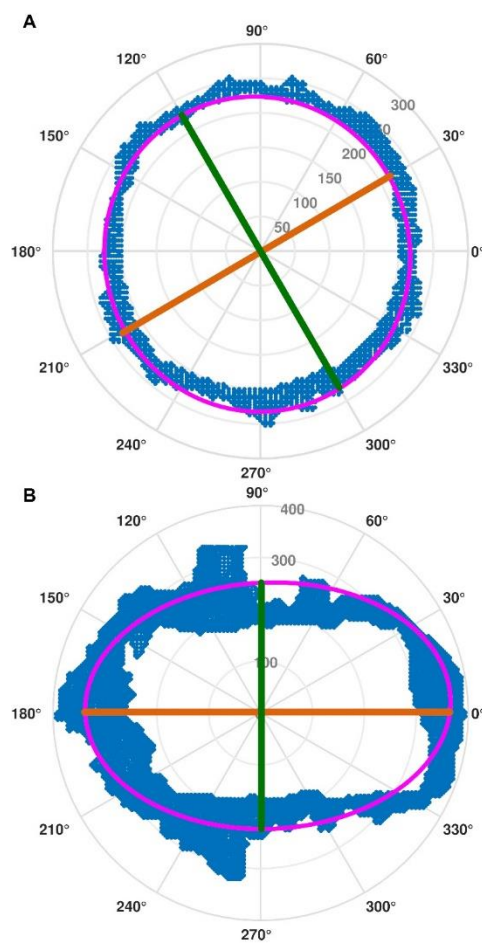


Figure 3-2: Representative scatter plots of (A) a parallel strut's vertices in polar coordinates in cross-sectional view and (B) a perpendicular struts' vertices in polar coordinates in cross-sectional view.

The blue points represent the peak and valley points on the strut surface, which were used to calculate the average best-fit ellipse that represents the cross-section of the strut (pink). The thickness of the strut was determined as the average of the major axis (orange) and minor axis (green) lengths.

3.3.2.4 Surface texture analysis

Using the surface profile polar 3D meshes, the areal surface roughness was estimated using the previously mentioned MATLAB script, which included several iterative digital filtering steps to extract the surface texture parameters (Appendix A, sections A.2). The polar plots were first rolled out into a rectangular plot, where the x-axis was the radial angle (radians), the y-axis was the span length (μm), and the z-axis was the height of the profile (μm). This process produced the raw surface profile extracted directly from the strut's surface. Raw surfaces were post-processed to remove detached elements and noise effects using a median filter. The forming surface was filtered out to remove the waviness associated with the shape of the struts. This process produced the primary surface profile. The nonporous construct surface analysis underwent the same process, except Cartesian plots were used instead of polar plots (Appendix A, sections A.2). The surface texture parameters of interest were arithmetic mean height and the maximum peak-valley height.

3.3.3 Mechanical testing and simulations

3.3.3.1 Tensile and flexural testing

Tensile and flexural tests of 3D-printed constructs were conducted using an Instron universal testing system (Instron 3345, Instron, Norwood, MA, United States). Schematic diagram of the setup of the tensile and flexural tests can be seen in Figure 3-3.

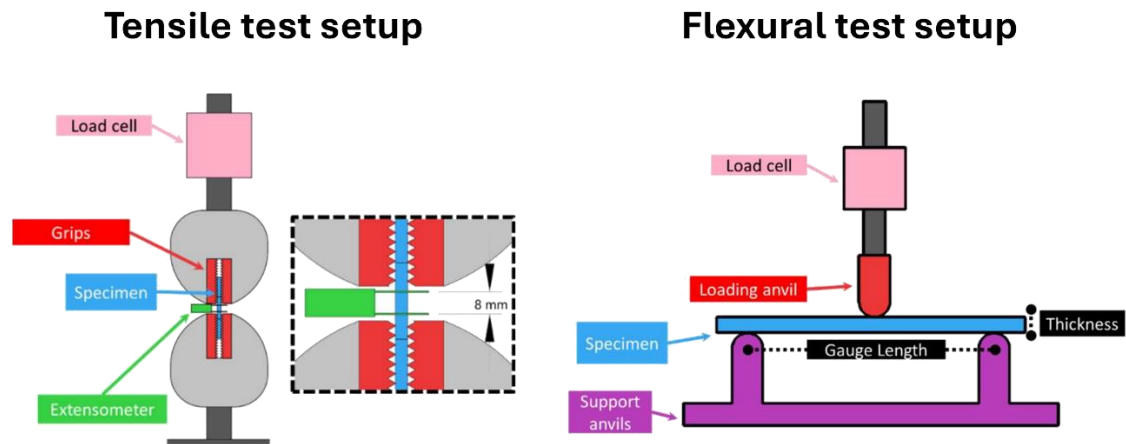


Figure 3-3: Schematic diagrams showing the tensile and three-point bending test setup.

For tensile loading tests, specimens were gripped into the universal testing machine and coupled to an extensometer (Axial Extensometer 3542, Epsilon Tech, Jackson, WY, United States) as per ASTM standards (ASTM E345-16, E8/E8M-21). The extensometer was used to record displacement values during tensile loading. Three-point bending (flexural) tests were done according to ASTM standards (ASTM E290-14). In the tensile tests, the gauge length was set at 8 mm for all the specimens. In the flexural tests, the gauge length-to-thickness ratio was set to be greater than 16:1. A 5 kN Instron 2519 load cell was installed with the Instron system to read the force values. The crosshead speed for all tests was 1 mm/min, with the data recorded at 100 points per second. Loading was applied to all the samples until the force reached 4300 N, the failure of samples, or until the samples slipped out of the supports in the case of flexural tests. In all tests, a cut-off of 10 N was used to remove any slack at the start of the loading process.

3.3.3.2 FEA simulations

Simulia Abaqus 2020 (Dassault Systèmes Simulia Corp, Providence, RI, United States) was used to perform FEA analyses. The first step in this process was to split each model into four quadrants. Since all the models were symmetric in geometry and the struts were uniform, the analysis could be done on only one of the quadrants; this technique has been shown to work well in previous studies (Song et al., 2021). The boundary and loading conditions were set up on the FEA models. Boundary conditions were chosen to mimic the

mechanical testing protocols described in subsection 3.3.3.1 (Figure 3-4). All test models were discretized into linear hexahedral mesh elements (C3D8I) with an average size of 125 μm . The mesh element size was determined by performing mesh convergence analysis. It should be noted all the FEA models used in Chapters 3 and 4 were designed to have the same mesh element size to ensure consistency. In addition, the mesh element size could not exceed the thinnest feature dimension. Mesh convergence analysis was done to determine the optimal mesh element size. This element size is the threshold size at which the stiffness converged into a constant value regardless of how much finer the mesh element size was set while maintaining the lowest possible processing time. The porous flexural model with a strut thickness of 250 μm was used, which had the finest strut thicknesses. The software did not allow running simulations with mesh element sizes that were lower than 75 μm , so FEA simulations were run using mesh element sizes ranging between 75 and 500 μm , and the simulations were stopped when the displacement reached 1 mm. The results showed that flexural modulus converged at about 8.34 GPa when the mesh element size was 125 μm (see Appendix A.7). Therefore, a mesh element size of 125 μm was used to develop models in Chapters 3 and 4. The number of hexahedral elements in the models ranged between 1.2×10^5 and 7.0×10^5 . The anvil models were discretized using 1 mm linear hexahedral elements (C3D8I).

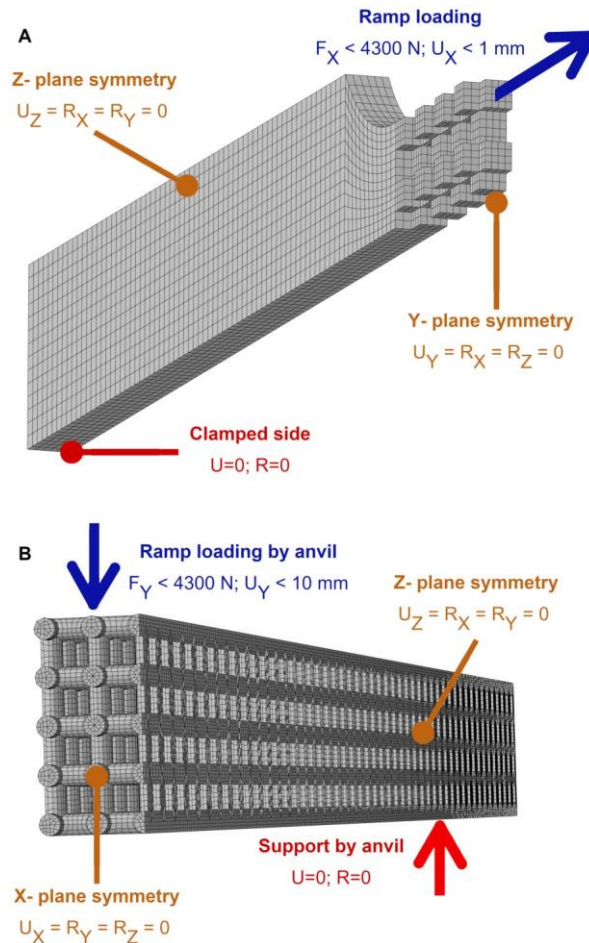


Figure 3-4: Boundary and loading conditions for representative tensile S-section (A) and flexural C-section (B) quadrant models.

Symmetrical boundary conditions were applied to ensure that full-sized models were recognized. Representative S-section and C-section models are shown with their mesh discretization. S-section and C-section models were discretized using 125- μm hexahedral linear elements. U is the displacement along the x-axis (X), y-axis (Y), or z-axis (Z), as indicated. R is the rotation around the x-axis (X), y-axis (Y), or z-axis (Z), as indicated. The blue arrows represent the direction of forces (F) applied on the model, and the red arrows indicate the location of clamping in the tensile model and support in the flexural model. The planes where symmetrical boundary conditions were applied to the model are labelled orange.

The next step was to determine the elastic-plastic material properties of Ti6Al4V for use in the FEA analysis (Appendix A, section A.3). While only the elastic region of loading is crucial for the design of medical implants, the plastic region of loading was also modelled to test the ability of FEA models to predict failure of the porous constructs. In addition, the yield point exists within the plastic region of loading, and hence modelling of the plastic region was deemed necessary to predict yield strength. These material properties were derived from the average stress-strain curves of all the mechanical tests performed on the SLM-built nonporous tensile constructs. The stress and strain values proportionality limit

point, the yield point, and the ultimate tensile strength point were first determined and introduced into an ABAQUS tool that allowed for the calibration of the FEA material. The ABAQUS tool was then used to interpolate the stress-strain relationship between the three points that identified the plastic region of the material within the FEA models. The density was assigned from information provided by Renishaw PLC (2017) Renishaw PLC (2017). Poisson's ratio was taken from a study by Peng et al. (2020). The fracture strain, stress triaxiality, and damage evolution were determined using the methods described by Wagner (2021). These FEA models were then used to perform tensile and three-point bending ramp loading simulations up to 4300 N.

Force-displacement readings were acquired to determine the overall predicted mechanical properties of the models, reflecting the way force and displacement readings are taken in real-life mechanical tests. In the case of tensile models, reaction forces were measured from the clamped side of the grips, while displacement was measured as the deformation within the porous part of the tensile models. In the flexural models, reaction force was read from the support anvil models while deflection was measured from the displacement of the loading anvil.

Contour maps of the FEA models were produced after each simulation, where the von Mises stresses of the elements were analyzed to determine where stress concentrations were predicted to occur. Von Mises stress (σ_v) is a scalar value of stress, which is defined as the uniaxial tensile stress that would create the same distortion levels as that created by the combined applied stresses (Logan, 2012). The von Mises stress is calculated using the following equation:

$$\sigma_v = \left(\frac{1}{\sqrt{2}}\right) \sqrt{(\sigma_x - \sigma_y)^2 + (\sigma_y - \sigma_z)^2 + (\sigma_x - \sigma_z)^2 + 6(\tau_x^2 + \tau_y^2 + \tau_z^2)} \quad (3-1)$$

where σ_v is the von Mises stress value, σ_x , σ_y and σ_z , are normal stresses along the x, y, and z axes, respectively, while τ_x , τ_y , and τ_z are the shear stresses along the x, y, and z planes, respectively.

3.3.3.3 Calculation of the mechanical properties of models and constructs

For all mechanical tests, the specimen dimensions, and the force-displacement (F-d) curves were used to calculate the engineering stress-strain and true stress-strain curves for each specimen. The mechanical properties were calculated using the following equations:

$$\varepsilon_E = \frac{d}{L} \quad (3-2)$$

$$\sigma_E = \frac{F}{WT} \quad (3-3)$$

$$\varepsilon_t = \ln(1 + \varepsilon_E) \quad (3-4)$$

$$\sigma_t = \sigma_E(1 + \varepsilon_E) \quad (3-5)$$

$$\varepsilon_f = \frac{6Td}{L^2} \quad (3-6)$$

$$\sigma_f = \frac{3FL}{2WT^2} \quad (3-7)$$

Where ε_E is the engineering tensile strain, ε_t is true tensile strain, σ_t is true tensile stress, ε_f is flexural strain, σ_f flexural stress, d is displacement, L is the gauge length, T is the thickness, and W is the width. The tensile (σ_{TY}) and flexural yield stress (σ_{FY}) were calculated by finding the point of intersection between the stress-strain curve and a straight line parallel to the elastic region with 0.2% offset. The 0.2% offset method is standard for determining the yield point in metals such as Ti6Al4V, where the elastic-plastic deformation transition point is not clearly defined. The peak stress was measured to find the tensile (σ_{UTS}) and flexural ultimate strength (σ_F), respectively. Young's modulus (E_T) and flexural modulus (E_F) were found by calculating the slope of the elastic region of the stress-strain curve. The tensile (T_T) and flexural toughness (T_F) were found by calculating the area under the stress-strain curve. It should be noted that the stress-strain values calculated in this study are 'apparent' in nature, as both the porous and nonporous constructs were treated as continuum structures, despite that not being the case for porous constructs. This was done to simplify the characterization of the mechanical properties of the complex porous constructs and models.

Relative deviation in mechanical and structural properties between FEA or CAD models and SLM-built constructs were calculated as a percentage using the following equation:

$$\text{Relative deviation} = \left(\frac{|X_{\text{SLM}} - X_{\text{Model}}|}{X_{\text{SLM}}} \right) \times 100 \quad (3-8)$$

where X is the mechanical property or strut dimension being compared.

3.3.4 Statistical analysis

All statistical analyses and curve fittings were conducted using GraphPad Prism 9 (GraphPad Prism, Boston MA, USA) and Tukey's ranked order test at a 0.95 confidence level. Results were placed in the format of mean \pm standard deviation (SD). The surface roughness values were placed in the format of mean \pm standard error of the mean (SEM).

3.4 Results and Discussion

3.4.1 Geometrical analysis

The overall geometrical measurements of the SLM-built specimens can be seen in Table 3-2 and Table 3-3. The struts in all the constructs with strut thickness $\geq 350 \mu\text{m}$ were intact. Struts with a thickness $< 350 \mu\text{m}$ appeared defective when received. All the SLM constructs were slightly thicker than the CAD models. In tensile specimens, the average difference in dimension between CAD models and SLM constructs was $46 \pm 23 \mu\text{m}$ in width and $47 \pm 17 \mu\text{m}$ in thickness. In flexural specimens, the average difference in dimension between CAD models and SLM constructs was $100 \pm 34 \mu\text{m}$ in width and $100 \pm 37 \mu\text{m}$ in thickness.

Table 3-2: The width and thickness dimensions of the SLM-built tensile specimens compared to those of the CAD models.

Model/Constructs Code	SLM Constructs		Difference between CAD and SLM	
	Width (mm)	Thickness (mm)	Width (mm)	Thickness (mm)
TS250	3.27 ± 0.01	1.30 ± 0.06	0.02	0.05
TS350	3.38 ± 0.04	1.38 ± 0.03	0.03	0.03
TS450	3.52 ± 0.06	1.51 ± 0.08	0.07	0.06
TS550	3.54 ± 0.07	1.53 ± 0.07	0.01	0.02
TS650	3.72 ± 0.05	1.72 ± 0.06	0.07	0.07
Nonporous	3.20 ± 0.07	1.20 ± 0.01	0.05	0.05

SLM constructs dimensions are means \pm SD. The differences are the absolute values of the differences between the CAD model dimensions and the means of the dimensions of the SLM-built constructs.

Table A-3: The width and thickness dimensions of the SLM-built flexural specimens compared to those of the CAD models.

Model/Constructs Code	SLM Constructs		Difference between CAD and SLM	
	Width (mm)	Thickness (mm)	Width (mm)	Thickness (mm)
FS250	4.32 ± 0.04	4.31 ± 0.04	0.07	0.06
FS350	4.42 ± 0.03	4.42 ± 0.02	0.07	0.07
FS450	4.52 ± 0.02	4.52 ± 0.02	0.17	0.17
FS550	4.64 ± 0.03	4.63 ± 0.02	0.09	0.08
FS650	4.76 ± 0.03	4.77 ± 0.03	0.11	0.12
Nonporous	5.09 ± 0.03	5.10 ± 0.02	0.09	0.10

SLM constructs dimensions are means ± SD. The differences are the absolute values of the differences between the CAD model dimensions and the means of the dimensions of the SLM-built constructs.

3.4.2 Structural analysis of SLM-built constructs

3.4.2.1 Strut thickness

Overall, the average deviation of the printed strut thickness from the nominal strut thickness was $\approx 6\%$ in the parallel direction, and $\approx 24\%$ in the perpendicular direction (Figure 3-5). In the case of the struts along the perpendicular direction, the thickness was consistently larger than the nominal strut thickness. For both parallel and perpendicular struts, their cross-sectional shape tended to be more circular when their nominal strut thickness was less than $550 \mu\text{m}$, even though the design specified struts with square cross-sections. However, parallel struts with nominal thicknesses of $\geq 550 \mu\text{m}$ had better geometrical conformity with the original design (deviation $< 5\%$). The circular and elliptical cross-sectional shape of the thinner struts could be related to the laser beam diameter being large relative to the strut dimensions.

As mentioned in section 3.3.2.3, an elliptical fit was used to calculate the strut thickness. All the struts along the perpendicular direction exhibited noticeable differences between their major and minor axis lengths, which is consistent with previous studies (Almalki et al., 2023, Vrana et al., 2018). These researchers have analyzed SLM beams built along different inclination angles from the vertical building direction. They found that the closer the inclination angle of the beam is from the vertical axis, the smaller the deviation of the beam thickness. Almalki et al. (2023) defined the effective diameter to be the nominal thickness of an SLM-built strut beyond which it matched the shape and thickness of the

ideal model. In that study, this effective diameter, for Ti6Al4V, was found to be between 500 μm and 1 mm. In the present study, this effective diameter appeared to be within a range of 450 to 550 μm . The difference in the effective diameters between the two studies may be due to the thinner struts used in the present study.

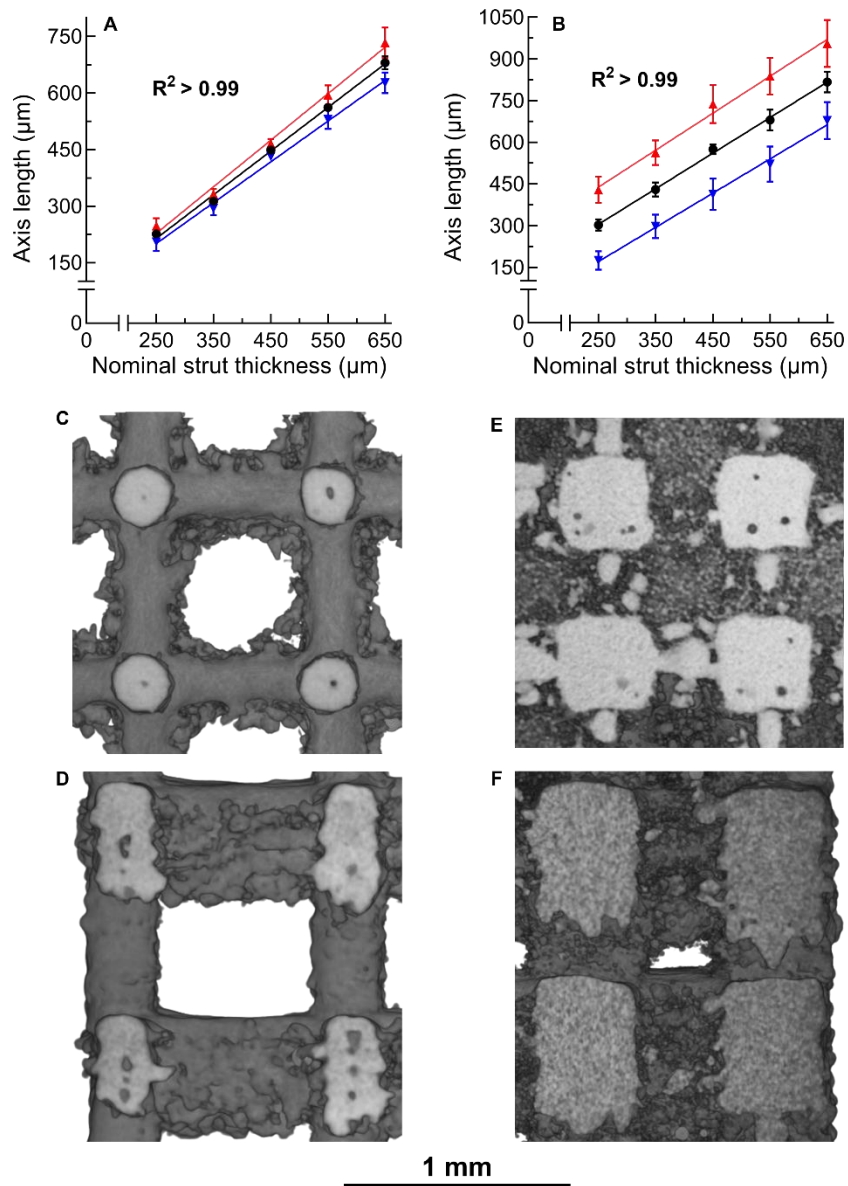


Figure 3-5: Analysis of strut thickness and shape along with representative CT images of the porous constructs.

The regression fits of major axis length (\blacktriangle), minor axis length (\blacktriangledown), and strut thickness (\bullet) of SLM-built struts plotted against nominal strut thickness for (A) parallel struts, which are the struts with length axis along

the vertical build axis, and (B) perpendicular struts, which are the struts with length axis perpendicular to the build axis. Data are means \pm SD, $n = 16$. (C-F) Representative 3D images constructed from CT scans are shown for (C) parallel struts with a nominal thickness of 350 μm , (D) perpendicular struts with a nominal thickness of 350 μm , (E) parallel struts with a nominal thickness of 650 μm , and (F) perpendicular struts with a nominal thickness of 650 μm . The thickness of the parallel struts was more consistent with the nominal strut thickness, while the perpendicular struts' thickness had progressively larger deviations with larger nominal strut thickness. The thinner struts tended to have an elliptical cross-sectional shape despite the original model being the S-section. The data presented in plots A and B are included in Appendix A, sections A.6, Table A-17 – Table A-19

3.4.2.2 Analysis of surface roughness

The surfaces of randomly selected struts were extracted from CT-images and analyzed to determine their surface roughness (Figure 3-6). The roughness of the SLM-built nonporous constructs had a significantly higher arithmetic mean height ($12 \pm 1 \mu\text{m}$) and maximum peak-valley height ($114 \pm 13 \mu\text{m}$) than all the porous specimens ($p < 0.05$) except those with 650 μm strut thickness ($p > 0.05$). There was no significant correlation between strut thickness and surface roughness parameters ($R^2 < 0.50$). Parallel struts of different thicknesses showed no significant difference in the arithmetic mean height (average $\approx 4.3 \mu\text{m}$) or the maximum peak-valley height (average $\approx 61 \mu\text{m}$) ($p > 0.05$). The arithmetic mean height for the perpendicular struts ranged between 2 and 9.5 μm . Furthermore, the roughness of the 350 μm and 450 μm thick perpendicular struts was significantly greater in arithmetic mean height than the other groups ($p < 0.05$). The perpendicular struts of different thicknesses showed no significant differences in maximum peak-valley height of (average $\approx 113 \mu\text{m}$). The results from the arithmetic mean height closely agree with those seen in some other studies of Ti6Al4V porous constructs. Kadirgama et al. (2018) found that the arithmetic surface roughness of SLM-built porous Ti6Al4V (as measured by linear track measurement) was between 8 and 13 μm . These struts were built at an angle of 45° from the building axis, versus 0° and 90° for the struts built in the present study. In accord with our findings, Kadirgama and coworkers also concluded that the nominal strut thickness did not impact surface roughness values.

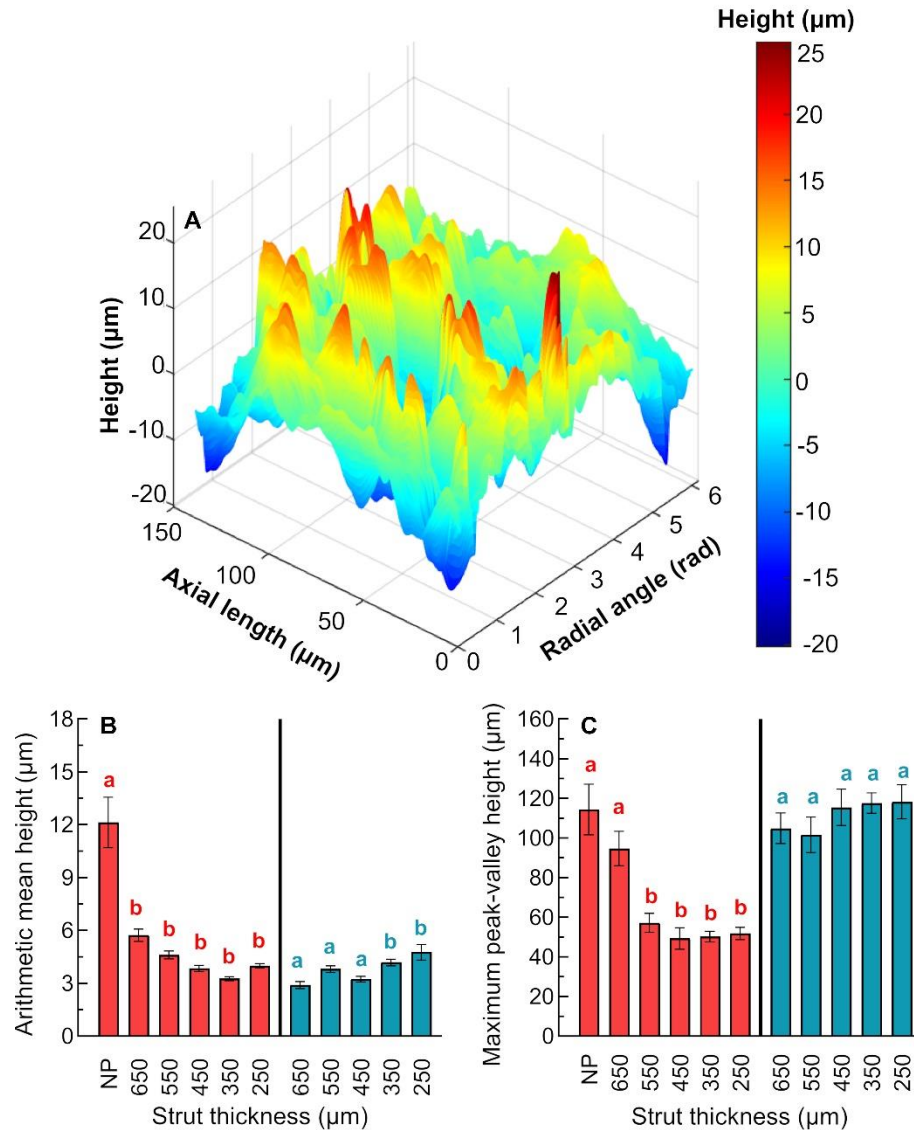


Figure 3-6: (A) Representative profile of the surface of a strut. The color scale bar represents height along the z-axis in μm . Bar graphs represent (B) surface arithmetic mean height and (C) surface peak-valley height for constructs with different strut thicknesses.

NP indicates nonporous constructs. The red bars represent parallel struts, and blue bars represent the perpendicular struts. Data are means \pm SEM, $n = 16$. Within each group of five or six bars, the same lower-case letter indicates no significant difference; different lower-case letters indicate a significant difference.

Surface roughness originates from multiple sources. Small particles could be seen on the surface of the struts, with agglomerates seen particularly on the bottom surface and sides of the perpendicular struts, as well as on the parallel struts located close to the center of the constructs. Parallel struts had both small spherical particles along with a wavy surface. Surface roughness is known to be affected directly by the SLM-printing strategy used, laser

parameters, and heating conditions during the building of constructs. Thermal diffusion, caused by a difference in temperature between loose Ti6Al4V particles and the solidified material, might lead particles to adhere along the edges of the struts (Alghamdi et al., 2019, Wang et al., 2023), which might explain their widespread presence over all the struts. Perpendicular struts might have been affected by a lack of supporting structures along their length, which would cause them to sag while hanging between the two vertical struts on their ends (Piscopo et al., 2019). The roughness seen in the perpendicular struts is thought to be caused by weld deposits, consisting of loose particles, dropping from the melt pool (Vrana et al., 2022), which would explain their irregular structure. Waviness seen prominently in the struts can be explained by the balling phenomenon. Balling occurs when the laser power is too low, or the laser scanning speed is too high. Ti6Al4V particles with larger diameters are not melted sufficiently due to the lower exposure, while the Ti6Al4V particles with smaller diameters melt more readily (Xiang et al., 2018). Due to the heterogeneous heating and high surface tension, the melt pool is prevented from spreading uniformly, causing the formation of spheres (Li and Gu, 2014, Shipley et al., 2018, Xiang et al., 2018).

3.4.2.3 Analysis of internal defects

CT scanning was performed to assess internal defects in 3D-printed Ti6Al4V constructs (Figure 3-7). Internal defects made up less than 1.2% of the total volume of the constructs and the largest of the defects were $< 300 \mu\text{m}$. The volume-percentage of internal defects showed poor correlation with nominal strut thickness ($R^2=0.08$). The largest internal defects were located close to the junctions of the struts and were generally irregular in shape. These internal defects could have occurred for multiple reasons. The small and regular internal defects are most likely due to gas entrapment (Zhang et al., 2017, Salem et al., 2019, Ransenigo et al., 2022). The larger deficiencies with irregular shape could be either keyhole defects (Khairallah et al., 2016, Antony and Arivazhagan, 2015, Svenungsson et al., 2015) or lack-of-fusion defects (Snell et al., 2019). The lack-of-fusion defects are characteristically elongated along the building direction, as seen in the present study. These defects occur due to a combination of incompatible volumetric energy density

– controlled by the laser power and scanning speed – and unstable melt pool (Ransenigo et al., 2022, Yadroitsev et al., 2015, Thijs et al., 2010).

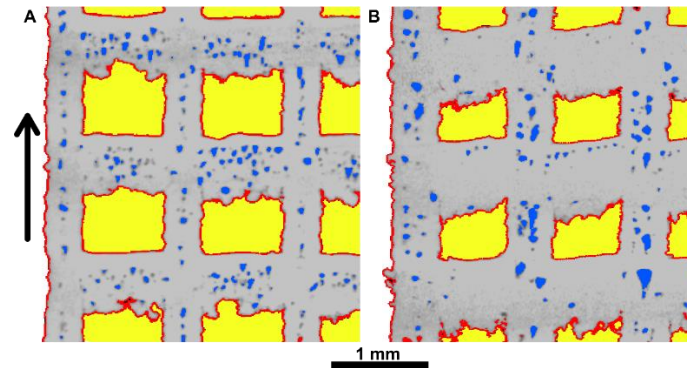


Figure 3-7: Representative slices from CT-images after segmentation. (A) 350 and (B) 450 μm strut thickness constructs.

The segmentation process split images into four ROIs depending on their CT-density values: the macropores (yellow), internal defects (blue), titanium alloy (grey), and outer surface (red). The arrow indicates the direction of SLM building.

3.4.3 Tensile and flexural testing

3.4.3.1 Mechanical properties of nonporous constructs

Mechanical properties of nonporous cast and SLM-printed specimens were compared (Figure 3-8). The tensile properties were not significantly different between cast and SLM-built nonporous constructs except for toughness. FEA simulation of the tensile nonporous model showed mechanical properties like those of the cast and SLM-built constructs except for toughness. None of the cast specimens failed under flexural loading. The flexural toughness for both groups of specimens was measured at 1% strain level. Flexural properties of cast and SLM specimens showed significant differences for all the properties ($p < 0.05$). The cast specimens exhibited significantly lower flexural yield strength, higher relative flexural toughness, higher flexural modulus, and lower flexural strength than the SLM constructs ($p < 0.05$). The flexural behaviour of nonporous FEA simulations was closer to that of the cast specimens. These results are in line with previous observations, which point towards the microstructural characteristics of SLM-built Ti6Al4V constructs giving them enhanced strength properties and deteriorated ductility compared to

conventionally built constructs (Tan et al., 2017, Gong et al., 2015, Murr et al., 2012). However, the difference in strength appears to be limited to flexural rather than tensile strength.

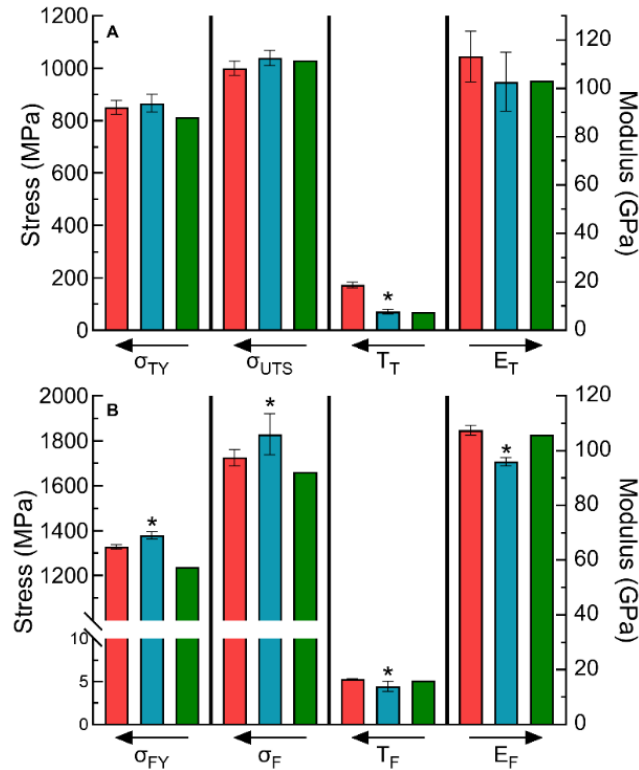


Figure 3-8: Bar graphs illustrate the mechanical properties of nonporous cast (red) and SLM-built constructs (blue), as well as the FEA simulations of the nonporous models (green).

(A) tensile mechanical properties including tensile yield stress (σ_{TY}), ultimate tensile strength (σ_{UTS}), tensile toughness (T_T), and Young's modulus (E_T). (B) flexural mechanical properties including flexural yield strength (σ_{FY}), flexural strength (σ_F), relative flexural toughness (T_F), and flexural modulus (E_F). The arrows indicate whether the y-axis is on the left or the right-hand side. Data are means \pm SD, $n = 6-10$. Asterisks on the blue bars indicate a significant difference from the corresponding red bars.

3.4.3.2 Mechanical properties of porous constructs

The dependence of mechanical properties on strut thickness was assessed in tensile (Figure 3-9) and flexural (Figure 3-10) tests. Most tensile specimens failed close to the center of the gauge, with some failing closer to one of the ends of the gauge length. Tensile stress parameters and Young's modulus exhibited a natural logarithmic relationship with strut thickness ($R^2 > 0.95$). Tensile toughness values exhibited an exponential relationship ($R^2 > 0.95$). Deviations in the mechanical properties of the FEA models from those of the SLM-built porous constructs are provided in Appendix A, sections A.6, Table A-20 – Table A-

27. The deviation of the FEA C-section tensile models compared to SLM-built constructs was 8% in Young's modulus, 3% in tensile yield strength, 3% in ultimate tensile strength, and about 85% in tensile toughness. There was also a natural logarithmic relationship between the thickness of the strut and the flexural properties ($R^2 > 0.95$). The deviation of the FEA C-section flexural models compared to SLM-built constructs was 4% in flexural modulus, 11% in flexural yield strength, 9% in the maximum flexural strength values, and 4% in relative flexural toughness. Fractures within the flexural specimens and FEA models always occurred in the region with maximum tensile stress, which was on the side opposite to the region of contact with the loading anvil. It was found that the C-section FEA models matched better with the mechanical properties of SLM-built constructs than did the S-section FEA models. This can be explained by the circular cross-sectional shape of the SLM-built constructs, with thinner struts better matching the C-section models. Overall, the mechanical properties of the C-section FEA models closely matched the mechanical properties of the SLM-built constructs. Therefore, geometrical discrepancies in the SLM-built constructs appear to have little effect on their strength and modulus properties.

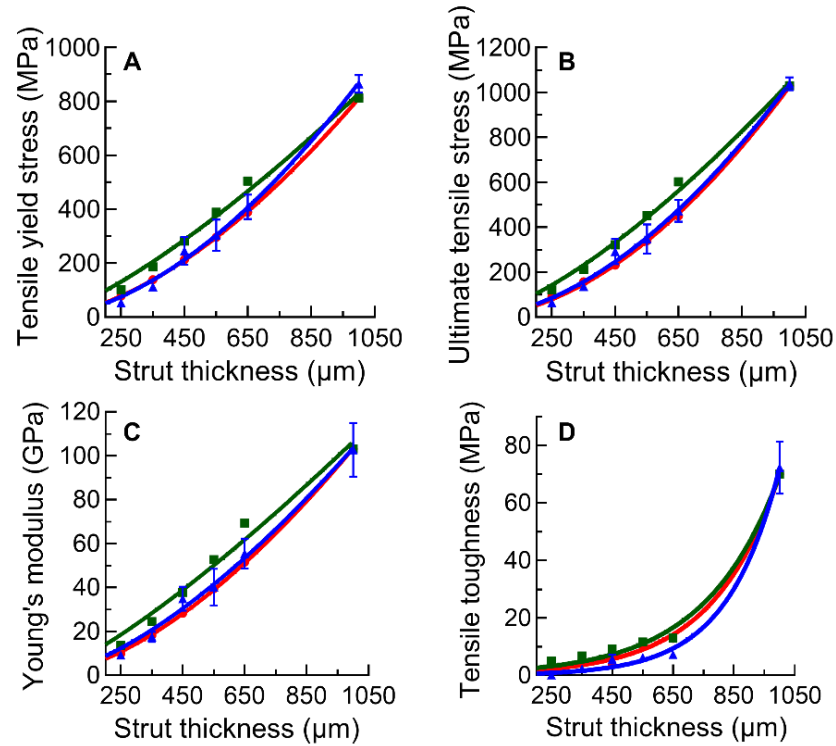


Figure 3-9: Dependence of (A) tensile yield stress, (B) ultimate tensile strength, (C) Young's modulus, and (D) tensile toughness on nominal strut thickness (shown on the x axes).

The data points represent SLM-built constructs (blue), S-section FEA models (green), and C-section FEA models (red). All the fits had a strong natural logarithmic correlation with the strut thickness ($R^2 \geq 0.95$), except the tensile toughness vs. strut thickness. The tensile toughness and strut thickness were well fit with an exponential function ($R^2 \geq 0.95$). 1000- μm strut thickness represents nonporous constructs. Data are means \pm SD, $n = 9-10$. The equations of the fits shown in these plots can be seen in Appendix A, Table A-7. Note that one of the mechanical tensile testing results in the 550 μm strut thickness group was removed as it was an outlier.

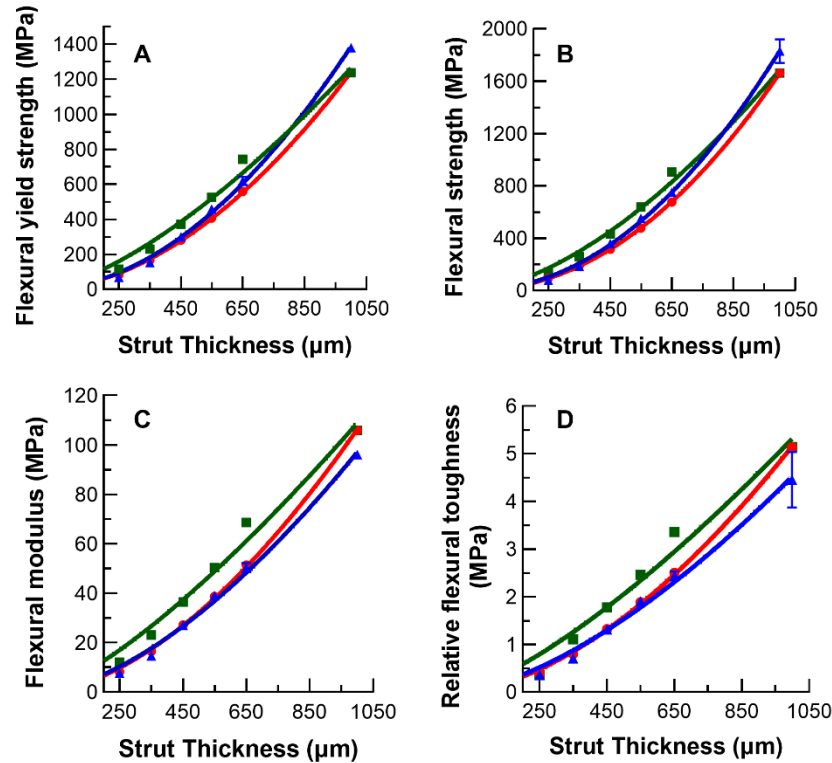


Figure 3-10: Dependence of (A) flexural yield stress, (B) flexural strength, (C) flexural modulus, and (D) relative flexural toughness on nominal strut thickness (shown on the x axes).

The data points represent SLM-built constructs (blue), S-section FEA models (green), and C-section FEA models (red). All the fits had a strong natural logarithmic correlation with the strut thickness ($R^2 \geq 0.95$). 1000- μm strut thickness represents nonporous constructs. Data are means \pm SD, $n = 10$. The equations of the fits shown in these plots can be seen in Appendix A, Table A-7.

In the present study, we tested porous constructs with different strut thicknesses. Our results show that, when pore shape and unit cell size are kept constant, the tensile and flexural properties of SLM-built constructs are dominated by the thickness of the struts and their cross-sectional shape. This aligns with previous studies on porous Ti6Al4V constructs (Tüzemen et al., 2022, Di Caprio et al., 2022, Bellini et al., 2021b). Unlike previous work focusing on flexural loading of porous constructs, the present study focused on pores with a unit cell size of 1 mm and struts that were thinner than 650 μm . In contrast, Horn et al. (2014) used unit cell sizes that ranged between 3 and 9 mm, and strut thicknesses ranging between 450 and 2100 μm . Tüzemen et al. (2022) worked on porous constructs that had a unit cell size ranging between 1.8 and 2.2 mm, with strut thicknesses ranging between 300 and 700 μm . While such dimensions would produce porous constructs with flexural moduli similar to that of trabecular bone, the flexural strength would not be sufficient for use in

cortical bone reconstruction without an outer nonporous skin (Di Caprio et al., 2022, Bellini et al., 2021a, Bellini et al., 2021b). While most previous work has focused on complex pore shapes, such as rhombic dodecahedron (Horn et al., 2014) and octet pores (Di Caprio et al., 2022, Bellini et al., 2021a, Bellini et al., 2021b), those in the present study were simple cubic pores. Importantly, it has recently been shown that simple cubic pores better support bone ingrowth than other more complex pore designs (Kovacs et al., 2023). Moreover, pore sizes in the present study were between 350 and 750 μm , which puts them within the range found previously to be ideal for promoting bone ingrowth (Section 1.8). Finally, one aim of this study was to examine the properties of structures with different pore sizes and strut thicknesses with a constant unit cell size, which in turn could be applied to the design of porous implants. Using this information, patient-specific porous constructs can be designed in a more streamlined fashion. By keeping the unit cell size constant, we will reduce the variables that need adjustment to just one (strut thickness). Changing of strut thickness would allow a spatial gradient of pores sizes to be produced. The pore sizes produced from this base unit cell size and strut thickness range are predicted to allow stable bone ingrowth, with sufficient pore volume to allow osteoinduction and osteoconduction to occur (see section 1.8). Furthermore, by keeping the unit cell size constant at 1 mm, rather than a larger size, we will be better able to reproduce the physiological contours of the bone while avoiding jagged surfaces.

FEA models can be best described as ‘ideal’ because they do not consider thermal history effects on the microstructure of SLM-built constructs or manufacturing-produced irregularities. Nevertheless, in the present study, minimal deviations were observed between the mechanical properties of the FEA models and the SLM-built constructs. Slight differences in the mechanical properties of FEA and SLM-built structures may be related to the variations in the strut thickness, shape, and misalignment, which can be seen even within individual struts (Dallago et al., 2018, Liu et al., 2017). In the present study, the only major deviation between the behaviour of FEA models and SLM-built constructs was seen in their toughness. SLM-built constructs are known to have lower ductility due to their microstructural attributes, which are not reflected in the FEA models. Given that the application of porous constructs designed in this study is limited to the elastic region of

loading, the issue of ductility is not of direct concern. Nevertheless, some studies have shown that treatments such as annealing cause rearrangement of the microstructural build of porous constructs, improving their ductility (Yadroitsev et al., 2017, Ge et al., 2023).

Manufacturing irregularities, such as surface roughness and internal defects, are important considerations when using SLM to manufacture constructs (du Plessis et al., 2022). It is known that surface roughness can be beneficial, as it can promote osteoconductivity of the implant (Deligianni et al., 2001). However, surface roughness may also cause premature failure due to stress concentrations forming at ridges on the surface (Yáñez et al., 2020, Lozanovski et al., 2019). In addition, surface roughness is known to have a dire effect on the fatigue strength of porous constructs (Benedetti et al., 2021). In their review article, du Plessis et al. (2020b) reported that internal defects and surface roughness have a larger effect on the ductility than on the strength of SLM-built constructs. Yadroitsev et al. (2017) reported that elongation to failure of Ti6Al4V SLM-built constructs was lower when the constructs were not annealed. In the present study, the exact effects of surface roughness cannot be conclusively explained, given that surface roughness was not modelled in FEA. Since the mechanical properties of smooth-surfaced FEA porous models did not deviate significantly from those of SLM-built constructs, it is unlikely that surface roughness had a marked effect on strength or stiffness. This conclusion aligns with the results of previous studies, such as Dallago et al. (2018) who found an insignificant effect of surface roughness on the stiffness of SLM-built porous Ti6Al4V constructs.

Several studies have suggested that internal defects might affect the stiffness and strength of SLM-built constructs (Campoli et al., 2013, du Plessis et al., 2020a), driven by the formation of local high-stress concentrations (Shiple et al., 2018, du Plessis et al., 2020b). However, these effects are limited to situations where defects are prevalent. Gong et al. (2015) showed that internal defects did not affect Young's modulus, strength, or elongation of SLM-built nonporous Ti6Al4V constructs at volume-percentage levels < 1%. Moreover, du Plessis et al. (2018a) showed that defects with diameters < 500 μm did not have a significant effect on the strength of SLM-built porous specimens. In addition, some researchers have suggested that keyhole defects have less detrimental effects than lack-of-fusion defects on the static mechanical properties of SLM-built constructs (du Plessis et

al., 2020a, Gong et al., 2015). In the present study, internal defects had a volume percentage close to 1.2 %, and the greatest diameters were $< 300 \mu\text{m}$; thus, it is unlikely that they caused deterioration in the mechanical properties of the SLM-built constructs. This outcome is supported by the fact that FEA models did not show a significant difference in strength when compared to SLM-built constructs.

We next addressed the possible effects of surface roughness and internal defects using the FEA modelling. We assessed the effects of structural imperfections on mechanical properties (details can be found in Appendix A.5). Simplified FEA porous models, with a strut thickness of $350 \mu\text{m}$, were built with or without surface roughness and/or internal defects. These models were put under tensile loading simulations. In the elastic region, only minor differences in Young's modulus and strength were observed (5% and 7% reductions, respectively, in models with both structural imperfections compared to models without structural imperfections). In contrast, in the plastic region, larger differences in ultimate tensile strength and elongation were observed. Ultimate tensile strength in the model with both structural imperfections was reduced by 16% compared to the model without structural imperfections. Elongation at the point of failure in the model with both structural imperfections was reduced by 57% when compared to the model without structural imperfections. The reason for the drop in elongation appears to be the higher concentration of stress around structural imperfections, which in turn would cause localized yielding and premature failure. This test provides evidence that, while strength was not severely affected by the presence of internal defects or surface roughness, these structural imperfections compromised the elongation of the models. This outcome is in keeping with the results of previous works (du Plessis et al., 2020b, Yadroitsev et al., 2017). The models designed for the test had C-section struts. Tensile models showed that perpendicular struts did not incur any large stress concentrations, hence it is presumed that modelling of an elliptically shaped strut was not necessary. It should be noted that this test was not performed on flexural models, where the shape of the perpendicular strut could have a larger effect on the flexural mechanical properties. However, as stated above, the similarity between the mechanical properties of the C-section FEA models (without

structural imperfections) and the SLM-built constructs argue that geometrical discrepancies should have little effect.

3.4.4 Von Mises stress distributions in porous and nonporous FEA models

The contours of von Mises stress distributions were assessed in FEA models (Figure 3-11). In the tensile nonporous model, the stress distribution appeared to be uniform before reaching the yield point. In addition, no elements had von Mises stresses higher than the yield strength of Ti6Al4V (866 MPa). The von Mises stresses reached a maximum value of about 1038 MPa before failure occurred. In the tensile porous models, high von Mises stresses were seen within parallel struts, while the perpendicular struts exhibited lower stresses. All porous tensile models presented uniform von Mises stress distributions. However, it can be noted that the C-section models exhibited lower stresses than the S-section models. This could result from high-stress concentrations forming along sharp edges of the S-section models. None of the models had von Mises stresses > 866 MPa.

Flexural models showed a similar trend to that of tensile models. In the case of the nonporous flexural model, some elements reached von Mises stresses above 866 MPa at the region of contact with the loading anvil. Before reaching the flexural yield point, the von Mises stresses were below Ti6Al4V's yield strength. Failure occurred at the point of contact with the loading anvil, due to the tie constraint between the loading anvil and the rest of the model. However, all porous flexural models exhibited failure within the tensile region.

Regardless of the loading condition tested, the elements that had the highest stress concentrations were the ones closest to the junctions of the struts in the models. This aligns with our observations of SLM-built constructs, where failures occurred at the junctions of the struts. Previous studies (Xiao et al., 2020, Xiong et al., 2021, du Plessis et al., 2018b) showed a similar outcome to the present study for both in FEA simulations and mechanical testing. However, in these previous studies, FEA models were built based on micrographs of porous constructs; in contrast, in the present study, FEA models were built from idealized CAD models with material properties derived from real-life mechanical tests of SLM-built Ti6Al4V. Thus, a major drawback of using a beam-based lattice design is that

stress concentration nodes at the junctions of struts – combined with internal defects (Salem et al., 2019) and high surface roughness (Xiao et al., 2020) – could lead to premature failure. Recent studies have investigated using other pore shapes, such as triply periodic pores, to eliminate the need for sharp-edged junctions as a design feature (Ge et al., 2023). Another solution to avoid stress concentrations along the sharp edges at the junctions of struts is to fill the corners with fillets. Previous studies, such as that done by Raghavendra et al. (2023), have shown that such fillets distribute the von Mises stress more evenly, avoiding high stress concentrations. In turn, this increases both the compressive modulus and compressive yield stress, as well as fatigue strength. Future work should investigate these methods to minimize stress concentrations in porous constructs.

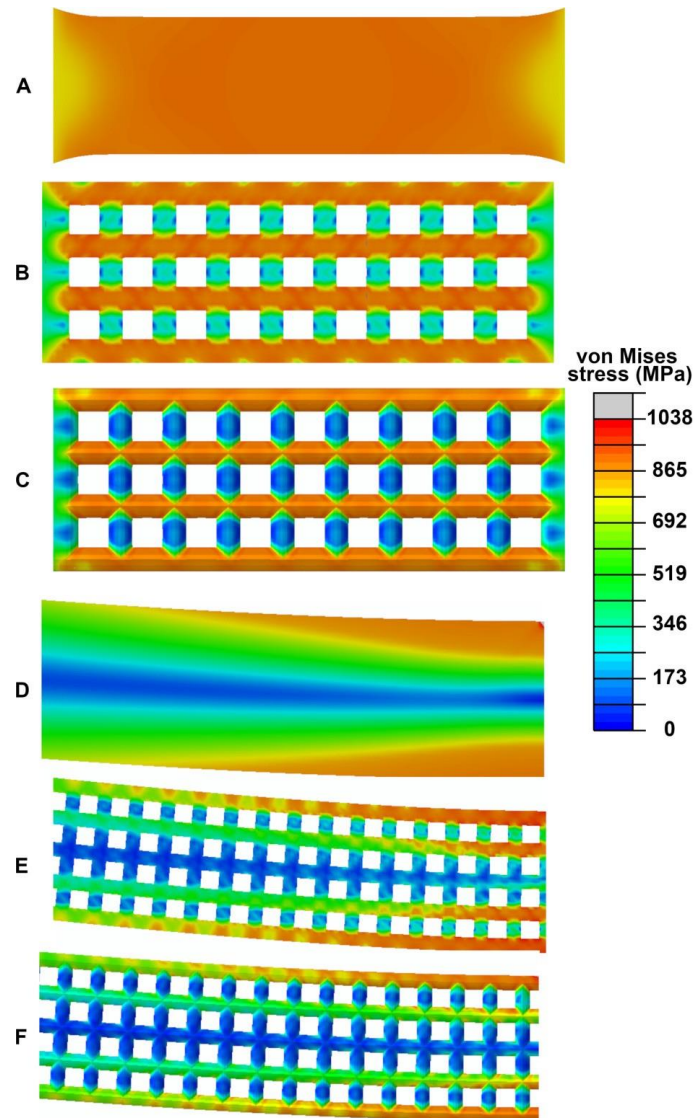


Figure 3-11: Images illustrate von Mises stress contour maps of representative FEA models.

Six FEA models are represented: (A) tensile nonporous, (B) tensile S-section porous, (C) tensile C-section porous, (D) flexural nonporous, (E) flexural S-section porous, and (F) flexural C-section porous. Models are displayed before the yield point. The von Mises stresses were largely uniform along the struts in the direction of loading for tensile models. Whereas stress concentrations were found in the flexural models in struts perpendicular to the loading direction. Elements with stress values > 1038 MPa are coloured grey.

3.4.5 Matching the mechanical properties of constructs to those of mandibular bone

Using the fits observed from the mechanical properties of SLM-built Ti6Al4V constructs (Appendix A.4, Table A-7), a suitable range of strut thickness properties can be chosen for

use in mandibular reconstruction (Appendix A.4). According to Nagasao et al. (2009), Young's modulus of the mandibular cortical bone ranges between 16 and 31 GPa. Thus, it can be deduced that the Young's modulus of porous Ti6Al4V constructs made of simple cubic pores, with strut thicknesses between 300 and 450 μm , match the Young's modulus of mandible cortical bones.

When considering the flexural strength (≤ 120 MPa) (Vitins et al., 2003) and ultimate tensile strength of mandibular cortical bone (≤ 130 MPa) (Nagasao et al., 2009, van Eijden, 2000), it can be seen that the constructs with strut thicknesses ranging between 350 and 450 μm are optimal for use in SLM-built mandibular reconstruction devices. Moreover, constructs built using this strut thickness range were observed in the present study to be structurally intact. Furthermore, constructs with this strut thickness range are expected to have a Young's modulus between 20 and 30 GPa, along with tensile and flexural strengths of more than 138 MPa, making them mechanically compatible with mandibular bone, avoiding issues such as stress shielding. In addition, the pore sizes produced from these strut thicknesses are between 550 μm and 650 μm , which are expected to facilitate bone ingrowth (Taniguchi et al., 2016, Wang et al., 2016, Sing et al., 2016, Perez and Mestres, 2016).

3.5 Conclusions

This study investigated the tensile and flexural mechanical behaviour and microstructural properties of SLM-built porous Ti6Al4V constructs of different strut thicknesses and porosities. FEA models of these porous constructs were produced, and their mechanical properties compared to those of SLM-built specimens. Matching the Young's modulus of implants to that of mandibular bone is expected to minimize stress shielding. Such implants should provide improved mechanical performance and better interaction with the bone for clinical applications in maxillofacial and orthopedic surgery. The following specific conclusions can be drawn from this study.

1. The deviations seen between CAD and SLM-built struts is dependent on their orientation, with less deviation ($\approx 5\%$) seen in parallel struts when compared to the perpendicular struts ($\approx 24\%$).

2. Thinner struts tend to have circular strut cross-section, while thicker struts tend to be more consistent with the nominal square strut cross-sectional shape seen in the CAD models.
3. The mechanical properties of FEA models with struts of circular cross-section show close alignment with the mechanical properties of SLM-built specimens (deviation $\leq 11\%$). In both FEA models and SLM-built constructs, strut thickness is a major factor that affected their mechanical properties.
4. Surface roughness in SLM-built constructs is present on all struts (arithmetic mean height was between 2.0 and 9.5 μm). Minimal internal defects are found within the struts (volume percentage $< 1.2\%$). These structural imperfections do not markedly affect the strength of the constructs but decrease their elongation.
5. Constructs with strut thicknesses between 350 μm and 450 μm are expected to be optimal for use in porous mandibular implant designs.

3.6 References used in this chapter

- ALGHAMDI, A., DOWNING, D., MCMILLAN, M., BRANDT, M., QIAN, M. & LEARY, M. 2019. Experimental and numerical assessment of surface roughness for Ti6Al4V lattice elements in selective laser melting. *The International Journal of Advanced Manufacturing Technology*, 105, 1275-1293.
- ALMALKI, A., DOWNING, D., NORONHA, J., DASH, J., LOZANOVSKI, B., TINO, R., ALGHAMDI, A., KHORASANI, M., QIAN, M., BRANDT, M. & LEARY, M. 2023. The effect of geometric design and materials on section properties of additively manufactured lattice elements. *The International Journal of Advanced Manufacturing Technology*, 126, 3555-3577.
- ANTONY, K. & ARIVAZHAGAN, N. 2015. Studies on energy penetration and Marangoni effect during laser melting process. *Journal of Engineering Science and Technology*, 10, 509 - 525.
- BARTOLOMEU, F., COSTA, M. M., ALVES, N., MIRANDA, G. & SILVA, F. S. 2021. Selective Laser Melting of Ti6Al4V sub-millimetric cellular structures: Prediction of dimensional deviations and mechanical performance. *J Mech Behav Biomed Mater*, 113, 104123.
- BELLINI, C., BORRELLI, R., DI COCCO, V., FRANCHITTI, S., IACOVIELLO, F. & SORRENTINO, L. 2021a. Bending properties of titanium lattice structures

produced by electron beam melting process. *Fatigue & Fracture of Engineering Materials & Structures*, 44, 1961-1970.

- BELLINI, C., BORRELLI, R., DI COCCO, V., FRANCHITTI, S., IACOVIELLO, F. & SORRENTINO, L. 2021b. Damage analysis of Ti6Al4V lattice structures manufactured by electron beam melting process subjected to bending load. *Material Design & Processing Communications*, 3, e223.
- BENEDETTI, M., DU PLESSIS, A., RITCHIE, R. O., DALLAGO, M., RAZAVI, N. & BERTO, F. 2021. Architected cellular materials: A review on their mechanical properties towards fatigue-tolerant design and fabrication. *Materials Science and Engineering: R: Reports*, 144, 100606.
- BOSE, S., KE, D., SAHASRABUDHE, H. & BANDYOPADHYAY, A. 2018. Additive manufacturing of biomaterials. *Prog Mater Sci*, 93, 45-111.
- CAMPOLI, G., BORLEFFS, M. S., AMIN YAVARI, S., WAUTHLE, R., WEINANS, H. & ZADPOOR, A. A. 2013. Mechanical properties of open-cell metallic biomaterials manufactured using additive manufacturing. *Materials & Design*, 49, 957-965.
- DALLAGO, M., FONTANARI, V., TORRESANI, E., LEONI, M., PEDERZOLLI, C., POTRICH, C. & BENEDETTI, M. 2018. Fatigue and biological properties of Ti-6Al-4V ELI cellular structures with variously arranged cubic cells made by selective laser melting. *J Mech Behav Biomed Mater*, 78, 381-394.
- DE WILD, M., GHAYOR, C., ZIMMERMANN, S., RÜEGG, J., NICHOLLS, F., SCHULER, F., CHEN, T.-H. & WEBER, F. E. 2019. Osteoconductive Lattice Microarchitecture for Optimized Bone Regeneration. *3D Printing and Additive Manufacturing*, 6, 40-49.
- DELIGIANNI, D. D., KATSALA, N., LADAS, S., SOTIROPOULOU, D., AMEDEE, J. & MISSIRLIS, Y. F. 2001. Effect of surface roughness of the titanium alloy Ti-6Al-4V on human bone marrow cell response and on protein adsorption. *Biomaterials*, 22, 1241-51.
- DI CAPRIO, F., FRANCHITTI, S., BORRELLI, R., BELLINI, C., DI COCCO, V. & SORRENTINO, L. 2022. Ti-6Al-4V Octet-Truss Lattice Structures under Bending Load Conditions: Numerical and Experimental Results. *Metals (Basel)*, 12, 410.
- DONG, G., TANG, Y. & ZHAO, Y. F. 2017. A Survey of Modeling of Lattice Structures Fabricated by Additive Manufacturing. *Journal of Mechanical Design*, 139, 100906.
- DU PLESSIS, A., RAZAVI, N., BENEDETTI, M., MURCHIO, S., LEARY, M., WATSON, M., BHATE, D. & BERTO, F. 2022. Properties and applications of additively manufactured metallic cellular materials: A review. *Progress in Materials Science*, 125, 100918.

- DU PLESSIS, A., RAZAVI, N. & BERTO, F. 2020a. The effects of microporosity in struts of gyroid lattice structures produced by laser powder bed fusion. *Materials & Design*, 194, 108899.
- DU PLESSIS, A., YADROITSAVA, I., KROUPRIANOFF, D. & YADROITSEV, I. 2018a. Numerical and experimental study of the effect of artificial porosity in a lattice structure manufactured by laser based powder bed fusion. *Solid Freeform Fabrication Symposium – An Additive Manufacturing Conference*.
- DU PLESSIS, A., YADROITSAVA, I. & YADROITSEV, I. 2018b. Ti6Al4V lightweight lattice structures manufactured by laser powder bed fusion for load-bearing applications. *Optics & Laser Technology*, 108, 521-528.
- DU PLESSIS, A., YADROITSAVA, I. & YADROITSEV, I. 2020b. Effects of defects on mechanical properties in metal additive manufacturing: A review focusing on X-ray tomography insights. *Materials & Design*, 187, 108385.
- EL-SAYED, M. A., ESSA, K., GHAZY, M. & HASSANIN, H. 2020. Design optimization of additively manufactured titanium lattice structures for biomedical implants. *The International Journal of Advanced Manufacturing Technology*, 110, 2257-2268.
- GE, J., HUANG, Q., WANG, Y., ZHANG, C., LIU, Q., LU, Z. & YIN, S. 2023. Microstructural optimization and mechanical enhancement of SLM Ti6Al4V TPMS scaffolds through vacuum annealing treatment. *Journal of Alloys and Compounds*, 934, 167524.
- GONG, H., RAFI, K., GU, H., JANAKI RAM, G. D., STARR, T. & STUCKER, B. 2015. Influence of defects on mechanical properties of Ti-6Al-4V components produced by selective laser melting and electron beam melting. *Materials & Design*, 86, 545-554.
- HERNÁNDEZ-NAVA, E., SMITH, C. J., DERGUTI, F., TAMMAS-WILLIAMS, S., LEONARD, F., WITHERS, P. J., TODD, I. & GOODALL, R. 2016. The effect of defects on the mechanical response of Ti-6Al-4V cubic lattice structures fabricated by electron beam melting. *Acta Materialia*, 108, 279-292.
- HORN, T. J., HARRYSSON, O. L. A., MARCELLIN-LITTLE, D. J., WEST, H. A., LASCELLES, B. D. X. & AMAN, R. 2014. Flexural properties of Ti6Al4V rhombic dodecahedron open cellular structures fabricated with electron beam melting. *Additive Manufacturing*, 1-4, 2-11.
- JACKSON, M. J., KOPAC, J., BALAZIC, M., BOMBAC, D., BROJAN, M. & KOSEL, F. 2016. *Titanium and Titanium Alloy Applications in Medicine. Surgical Tools and Medical Devices*. Springer.
- JAHADAKBAR, A., SHAYESTEHE MOGHADDAM, N., AMERINATANZI, A., DEAN, D., KARACA, H. E. & ELAHINIA, M. 2016. Finite Element Simulation and Additive Manufacturing of Stiffness-Matched NiTi Fixation Hardware for Mandibular Reconstruction Surgery. *Bioengineering (Basel)*, 3, 36.

- KADIRGAMA, K., HARUN, W. S. W., TARLOCHAN, F., SAMYKANO, M., RAMASAMY, D., AZIR, M. Z. & MEHBOOB, H. 2018. Statistical and optimize of lattice structures with selective laser melting (SLM) of Ti6AL4V material. *The International Journal of Advanced Manufacturing Technology*, 97, 495-510.
- KENNADY, M. C., TUCKER, M. R., LESTER, G. E. & BUCKLEY, M. J. 1989a. Histomorphometric evaluation of stress shielding in mandibular continuity defects treated with rigid fixation plates and bone grafts. *Int J Oral Maxillofac Surg*, 18, 170-174.
- KENNADY, M. C., TUCKER, M. R., LESTER, G. E. & BUCKLEY, M. J. 1989b. Stress shielding effect of rigid internal fixation plates on mandibular bone grafts. A photon absorption densitometry and quantitative computerized tomographic evaluation. *Int J Oral Maxillofac Surg*, 18, 307-310.
- KHAIRALLAH, S. A., ANDERSON, A. T., RUBENCHIK, A. & KING, W. E. 2016. Laser powder-bed fusion additive manufacturing: Physics of complex melt flow and formation mechanisms of pores, spatter, and denudation zones. *Acta Materialia*, 108, 36-45.
- KOVACS, A. E., CSERNATONY, Z., CSAMER, L., MEHES, G., SZABO, D., VERES, M., BRAUN, M., HARANGI, B., SERBAN, N., ZHANG, L., FALK, G., SOOSNE HORVATH, H. & MANO, S. 2023. Comparative Analysis of Bone Ingrowth in 3D-Printed Titanium Lattice Structures with Different Patterns. *Materials (Basel)*, 16, 3861.
- LI, S., LI, X., HOU, W., NUNE, K. C., MISRA, R. D. K., CORREA-RODRIGUEZ, V. L., GUO, Z., HAO, Y., YANG, R. & MURR, L. E. 2017. Fabrication of open-cellular (porous) titanium alloy implants: osseointegration, vascularization and preliminary human trials. *Science China Materials*, 61, 525-536.
- LI, Y. & GU, D. 2014. Thermal behavior during selective laser melting of commercially pure titanium powder: Numerical simulation and experimental study. *Additive Manufacturing*, 1-4, 99-109.
- LIU, L., KAMM, P., GARCÍA-MORENO, F., BANHART, J. & PASINI, D. 2017. Elastic and failure response of imperfect three-dimensional metallic lattices: the role of geometric defects induced by Selective Laser Melting. *Journal of the Mechanics and Physics of Solids*, 107, 160-184.
- LIU, S. & SHIN, Y. C. 2019. Additive manufacturing of Ti6Al4V alloy: A review. *Materials & Design*, 164, 107552.
- LOGAN, D. L. 2012. Development of the Plane Stress and Plane Strain Stiffness Equations. *A First Course in the Finite Element Method*. Fifth ed. United States: Cengage Learning.
- LOZANOVSKI, B., LEARY, M., TRAN, P., SHIDID, D., QIAN, M., CHOONG, P. & BRANDT, M. 2019. Computational modelling of strut defects in SLM manufactured lattice structures. *Materials & Design*, 171, 107671.

- MERKUS, H. G. 2009. Particle Size, Size Distributions and Shape. Particle Size Measurements Fundamentals, Practice, Quality. Springer.
- MOWER, T. M. & LONG, M. J. 2016. Mechanical behavior of additive manufactured, powder-bed laser-fused materials. *Materials Science and Engineering: A*, 651, 198-213.
- MURR, L. E., GAYTAN, S. M., RAMIREZ, D. A., MARTINEZ, E., HERNANDEZ, J., AMATO, K. N., SHINDO, P. W., MEDINA, F. R. & WICKER, R. B. 2012. Metal Fabrication by Additive Manufacturing Using Laser and Electron Beam Melting Technologies. *Journal of Materials Science & Technology*, 28, 1-14.
- NAGASAO, T., MIYAMOTO, J. & KAWANA, H. 2009. Biomechanical evaluation of implant placement in the reconstructed mandible. *Int J Oral Maxillofac Implants*, 24, 999-1005.
- NAGHAVI, S. A., TAMADDON, M., MARGHOUB, A., WANG, K., BABAMIRI, B. B., HAZELI, K., XU, W., LU, X., SUN, C., WANG, L., MOAZEN, M., WANG, L., LI, D. & LIU, C. 2022. Mechanical Characterisation and Numerical Modelling of TPMS-Based Gyroid and Diamond Ti6Al4V Scaffolds for Bone Implants: An Integrated Approach for Translational Consideration. *Bioengineering (Basel)*, 9, 504.
- OLDHOFF, M. G. E., MIRZAALI, M. J., TUMER, N., ZHOU, J. & ZADPOOR, A. A. 2021. Comparison in clinical performance of surgical guides for mandibular surgery and temporomandibular joint implants fabricated by additive manufacturing techniques. *J Mech Behav Biomed Mater*, 119, 104512.
- OTSU, N. 1979. A Threshold Selection Method from Gray-Level Histograms. *IEEE Transactions on Systems, Man, and Cybernetics*, 9, 62-66.
- PENG, C., TRAN, P., NGUYEN-XUAN, H. & FERREIRA, A. J. M. 2020. Mechanical performance and fatigue life prediction of lattice structures: Parametric computational approach. *Composite Structures*, 235, 111821.
- PENG, W. M., CHENG, K. J., LIU, Y. F., NIZZA, M., BAUR, D. A., JIANG, X. F. & DONG, X. T. 2021. Biomechanical and Mechanostat analysis of a titanium layered porous implant for mandibular reconstruction: The effect of the topology optimization design. *Mater Sci Eng C*, 124, 112056.
- PEREZ, R. A. & MESTRES, G. 2016. Role of pore size and morphology in musculo-skeletal tissue regeneration. *Mater Sci Eng C*, 61, 922-39.
- PICKRELL, B. B., SEREBRAKIAN, A. T. & MARICEVICH, R. S. 2017. Mandible Fractures. *Seminars in Plastic Surgery*, 31, 100-107.
- PISCOPO, G., SALMI, A. & ATZENI, E. 2019. On the quality of unsupported overhangs produced by laser powder bed fusion. *International Journal of Manufacturing Research*, 14.

- POGREL, M. A. 2021. The Concept of Stress Shielding in Nonvascularized Bone Grafts of the Mandible-A Review of 2 Cases. *J Oral Maxillofac Surg*, 79, 266.e1-266.e5.
- RAGHAVENDRA, S., DALLAGO, M., ZANINI, F., CARMIGNATO, S., BERTO, F. & BENEDETTI, M. 2023. A probabilistic average strain energy density approach to assess the fatigue strength of additively manufactured cellular lattice materials. *International Journal of Fatigue*, 172.
- RAN, Q., YANG, W., HU, Y., SHEN, X., YU, Y., XIANG, Y. & CAI, K. 2018. Osteogenesis of 3D printed porous Ti6Al4V implants with different pore sizes. *J Mech Behav Biomed Mater*, 84, 1-11.
- RANSENIGO, C., TOCCI, M., PALO, F., GINESTRA, P., CERETTI, E., GELFI, M. & POLA, A. 2022. Evolution of Melt Pool and Porosity During Laser Powder Bed Fusion of Ti6Al4V Alloy: Numerical Modelling and Experimental Validation. *Lasers in Manufacturing and Materials Processing*, 9, 481-502.
- RENISHAW PLC 2017. Data sheet: Ti6Al4V ELI-0406 powder for additive manufacturing. In: RENISHAW (ed.).
- SALEM, H., CARTER, L. N., ATTALLAH, M. M. & SALEM, H. G. 2019. Influence of processing parameters on internal porosity and types of defects formed in Ti6Al4V lattice structure fabricated by selective laser melting. *Materials Science and Engineering A*, 767, 138387.
- SHEN, Y. W., TSAI, Y. S., HSU, J. T., SHIE, M. Y., HUANG, H. L. & FUH, L. J. 2022. Biomechanical Analyses of Porous Designs of 3D-Printed Titanium Implant for Mandibular Segmental Osteotomy Defects. *Materials (Basel)*, 15, 576.
- SHIPLEY, H., MCDONNELL, D., CULLETON, M., COULL, R., LUPOI, R., O'DONNELL, G. & TRIMBLE, D. 2018. Optimisation of process parameters to address fundamental challenges during selective laser melting of Ti-6Al-4V: A review. *International Journal of Machine Tools and Manufacture*, 128, 1-20.
- SIDAMBE, A. T. 2014. Biocompatibility of Advanced Manufactured Titanium Implants-A Review. *Materials (Basel)*, 7, 8168-8188.
- SING, S. L., AN, J., YEONG, W. Y. & WIRIA, F. E. 2016. Laser and electron-beam powder-bed additive manufacturing of metallic implants: A review on processes, materials and designs. *J Orthop Res*, 34, 369-85.
- SNELL, R., TAMMAS-WILLIAMS, S., CHECHIK, L., LYLE, A., HERNÁNDEZ-NAVA, E., BOIG, C., PANOUTSOS, G. & TODD, I. 2019. Methods for Rapid Pore Classification in Metal Additive Manufacturing. *JOM*, 72, 101-109.
- SONG, J., TANG, Q., FENG, Q., MA, S., GUO, F. & HAN, Q. 2021. Investigation on the modelling approach for variable-density lattice structures fabricated using selective laser melting. *Materials & Design*, 212, 110236.
- SVENUNGSSON, J., CHOQUET, I. & KAPLAN, A. F. H. 2015. Laser Welding Process – A Review of Keyhole Welding Modelling. *Physics Procedia*, 78, 182-191.

- TAN, X. P., TAN, Y. J., CHOW, C. S. L., TOR, S. B. & YEONG, W. Y. 2017. Metallic powder-bed based 3D printing of cellular scaffolds for orthopaedic implants: A state-of-the-art review on manufacturing, topological design, mechanical properties and biocompatibility. *Mater Sci Eng C* 76, 1328-1343.
- TANIGUCHI, N., FUJIBAYASHI, S., TAKEMOTO, M., SASAKI, K., OTSUKI, B., NAKAMURA, T., MATSUSHITA, T., KOKUBO, T. & MATSUDA, S. 2016. Effect of pore size on bone ingrowth into porous titanium implants fabricated by additive manufacturing: An in vivo experiment. *Mater Sci Eng C* 59, 690-701.
- THIJS, L., VERHAEGHE, F., CRAEGHS, T., HUMBEECK, J. V. & KRUTH, J.-P. 2010. A study of the microstructural evolution during selective laser melting of Ti-6Al-4V. *Acta Materialia*, 58, 3303-3312.
- TÜZEMEN, M. Ç., SALAMCI, E. & ÜNAL, R. 2022. Investigation of the relationship between flexural modulus of elasticity and functionally graded porous structures manufactured by AM. *Materials Today Communications*, 31, 103592.
- VAN EIJDEN, T. M. 2000. Biomechanics of the mandible. *Critical Reviews in Oral Biology & Medicine*, 11, 123-136.
- VAN KOOTWIJK, A., MOOSABEIKI, V., SALDIVAR, M. C., PAHLAVANI, H., LEEFLANG, M. A., KAZEMIVAND NIAR, S., PELLIKAAN, P., JONKER, B. P., AHMADI, S. M., WOLVIUS, E. B., TUMER, N., MIRZAALI, M. J., ZHOU, J. & ZADPOOR, A. A. 2022. Semi-automated digital workflow to design and evaluate patient-specific mandibular reconstruction implants. *J Mech Behav Biomed Mater*, 132, 105291.
- VITINS, V., DOBELIS, M., MIDDLETON, J., LIMBERT, G. & KNETS, I. 2003. Flexural and creep properties of human jaw compact bone for FEA studies. *Comput Methods Biomech Biomed Engin*, 6, 299-303.
- VOZNESENSKAYA, A. A., ZHDANOV, A. V. & RAZNOSCHIKOV, A. S. 2021. Evolution of porosity depending on SLM mode and subsequent HIP processing. *Journal of Physics: Conference Series*, 2077.
- VRANA, R., KOUTECKY, T., CERVINEK, O., ZIKMUND, T., PANTELEJEV, L., KAISER, J. & KOUTNY, D. 2022. Deviations of the SLM Produced Lattice Structures and Their Influence on Mechanical Properties. *Materials (Basel)*, 15, 3144.
- VRANA, R., KOUTNY, D., PALOUSEK, D., PANTELEJEV, L., JAROS, J., ZIKMUND, T. & KAISER, J. 2018. Selective Laser Melting Strategy for Fabrication of Thin Struts Usable in Lattice Structures. *Materials (Basel)*, 11, 1763.
- WAGNER, R. 2021. ABAQUS Tutorial: Damage for Ductile Metals - Material Model Explained - Ductile Damage.
- WANG, D., LV, J., WEI, X., LU, D. & CHEN, C. 2023. Study on Surface Roughness Improvement of Selective Laser Melted Ti6Al4V Alloy. *Crystals (Basel)*, 13, 306.

- WANG, X., XU, S., ZHOU, S., XU, W., LEARY, M., CHOONG, P., QIAN, M., BRANDT, M. & XIE, Y. M. 2016. Topological design and additive manufacturing of porous metals for bone scaffolds and orthopaedic implants: A review. *Biomaterials*, 83, 127-41.
- WARNKE, P. H., DOUGLAS, T., WOLLNY, P., SHERRY, E., STEINER, M., GALONSKA, S., BECKER, S. T., SPRINGER, I. N., WILTFANG, J. & SIVANANTHAN, S. 2009. Rapid Prototyping: Porous Titanium Alloy Scaffolds Produced by Selective Laser Melting for Bone Tissue Engineering. *Tissue Engineering Part C: Methods*, 15, 115-124.
- XIANG, Y., ZHANG, S., WEI, Z., LI, J., WEI, P., CHEN, Z., YANG, L. & JIANG, L. 2018. Forming and defect analysis for single track scanning in selective laser melting of Ti6Al4V. *Applied Physics A*, 124, 685.
- XIAO, L., LI, S., SONG, W., XU, X. & GAO, S. 2020. Process-induced geometric defect sensitivity of Ti-6Al-4V lattice structures with different mesoscopic topologies fabricated by electron beam melting. *Materials Science and Engineering A*, 778, 139092.
- XIONG, Y., HAN, Z., QIN, J., DONG, L., ZHANG, H., WANG, Y., CHEN, H. & LI, X. 2021. Effects of porosity gradient pattern on mechanical performance of additive manufactured Ti-6Al-4V functionally graded porous structure. *Materials & Design*, 208, 109911.
- YADROITSEV, I., KRAKHMALOV, P. & YADROITSAVA, I. 2015. Hierarchical design principles of selective laser melting for high quality metallic objects. *Additive Manufacturing*, 7, 45-56.
- YADROITSEV, I., KRAKHMALOV, P., YADROITSAVA, I. & DU PLESSIS, A. 2017. Qualification of Ti6Al4V ELI Alloy Produced by Laser Powder Bed Fusion for Biomedical Applications. *JOM*, 70, 372-377.
- YÁNEZ, A., FIORUCCI, M. P., CUADRADO, A., MARTEL, O. & MONOPOLI, D. 2020. Surface roughness effects on the fatigue behaviour of gyroid cellular structures obtained by additive manufacturing. *International Journal of Fatigue*, 138, 105702.
- ZHANG, B., LI, Y. & BAI, Q. 2017. Defect Formation Mechanisms in Selective Laser Melting: A Review. *Chinese Journal of Mechanical Engineering*, 30, 515-527.
- ZHAO, S., LI, S. J., HOU, W. T., HAO, Y. L., YANG, R. & MISRA, R. D. K. 2016. The influence of cell morphology on the compressive fatigue behavior of Ti-6Al-4V meshes fabricated by electron beam melting. *J Mech Behav Biomed Mater*, 59, 251-264.
- ZHOU, L. B., SHANG, H. T., HE, L. S., BO, B., LIU, G. C., LIU, Y. P. & ZHAO, J. L. 2010. Accurate reconstruction of discontinuous mandible using a reverse engineering/computer-aided design/rapid prototyping technique: a preliminary clinical study. *J Oral Maxillofac Surg*, 68, 2115-21.

ZOUMALAN, R. A., HIRSCH, D. L., LEVINE, J. P. & SAADEH, P. B. 2009. Plating in microvascular reconstruction of the mandible: can fixation be too rigid? *J Craniofac Surg*, 20, 1451-1454.

Chapter 4

Fatigue properties of SLM-built porous Ti6Al4V constructs

This chapter was adapted with permission from the article: Hijazi, K. M., Mao, H., Holdsworth, D. W., Dixon, S. J. & Rizkalla, A. S. 2024. Cyclic flexural fatigue of porous Ti6Al4V constructs for use in mandibular reconstruction. *International Journal of Fatigue*, 185, 108329. <https://doi.org/10.1016/j.ijfatigue.2024.108329>

Chapter 4

4 Fatigue properties of SLM-built porous Ti6Al4V constructs

4.1 Summary

Porous Ti6Al4V constructs have been developed to replace mandibular bone, however the flexural fatigue properties of these constructs must first be assessed. In this study, porous constructs were built by selective laser melting (SLM) and subjected to cyclic flexural loading using a three-point bending setup and a servo-hydraulic Instron machine. Maximum flexural stress was plotted against the number of cycles. Also, numerical models were developed to predict the fatigue strength of porous constructs. These models were validated using experimental test data and extended to account for bone ingrowth. Scanning electron microscopy was used to study the internal and surface structures of dynamically loaded constructs. We found that numerical models of the SLM-built constructs accurately predicted flexural fatigue strength within $\approx 10\%$ deviation. Numerical fatigue models and experimental tests demonstrated that the fatigue strength of constructs was $\approx 30\%$ of their flexural yield strengths. Numerical models with bone ingrowth revealed that fatigue strength was doubled when compared to models without bone ingrowth. This may have been due to a damping effect of bone, resulting in reduction of fatigue failure. Overall, our study demonstrates the effectiveness of using numerical modelling in estimating the fatigue strength of SLM-built constructs intended for mandibular implant designs.

4.2 Introduction

Additive manufacturing techniques, such as selective laser melting (SLM), have revolutionized the design of patient-specific implants and devices with irregular and complex geometries, making them increasingly studied by orthopedic and engineering researchers. This is particularly clear when looking at the work performed by researchers

into designing patient-specific mandibular devices and implants with bone-mimicking geometrical and mechanical properties. SLM has the capability of producing porous titanium – 6 aluminum – 4 vanadium (Ti6Al4V) implants for mandibular reconstruction devices (Sidambe, 2014, Warnke et al., 2009, Taniguchi et al., 2016, Van Bael et al., 2012). The combination of excellent mechanical properties, biocompatibility, and chemical inertness of porous Ti6Al4V makes it a suitable candidate material for building patient-specific implants. Introducing pores into SLM-built Ti6Al4V constructs makes them mechanically compatible with bone and permits bone ingrowth (Zhang and Attar, 2016, Attar et al., 2014). From the work discussed in Chapter 3, we found that porous Ti6Al4V constructs with strut thickness ranging between 350 and 450 μm and a unit cell size of 1 mm exhibited Young's modulus values that matched those of cortical bone within the mandible (Nagasao et al., 2009).

The mandible is subjected to repetitive cyclic loading, making it important to understand the fatigue properties of mandibular reconstruction devices. For example, humans may chew up to one million cycles each year, with the average number of cycles being about 500 thousand (Po et al., 2011, van der Bilt et al., 2006, Chen, 2012, Farooq and Sazonov, 2016). For each chewing activity, the mean frequency is about 1.57 Hz and duration is about 13 s (Po et al., 2011). It has been reported that the force applied on each tooth and, consequently, on the mandible can reach maximum values of ≈ 300 N in males and ≈ 234 N in females (Ferrario et al., 2004). The forces applied during normal mastication range between 50 and 100 N (Waltimo and Könönen, 1993, Sessle, 2014), which in turn could generate stresses ranging between 6.5 and 20 MPa, respectively (Pineiro and Alves, 2015, Peng et al., 2021, Gholampour et al., 2019, Wong et al., 2012). It is well known that mandibles are subjected to flexural loading during the chewing process (Shi et al., 2021, Wong et al., 2016).

Ti6Al4V possesses relatively high resistance towards fatigue loading. It has been reported that the fatigue limit of nonporous constructs ranges between 10^6 and 10^7 cycles (Bathias and Pineau, 2013, Peters and Leyens, 2003), and flexural fatigue strength reaches $\approx 40\%$ of the yield stress (Belan et al., 2019). In two separate studies, Yavari et al. (Yavari et al., 2015, Yavari et al., 2013) reported that the compression fatigue strength of SLM-built

porous constructs depends on the unit cell shape and pore size. Structural imperfections in additively manufactured constructs, such as internal defects (Ahmadi et al., 2019, Wickmann et al., 2021, Leuders et al., 2013, Hu et al., 2020) and surface roughness (Ahmadi et al., 2019, Dallago et al., 2018a, Yáñez et al., 2020), are known to decrease fatigue strength (Section 1.12). However, the origin of fatigue cracks remains under debate in the literature. Some studies assumed that notches along the surface of SLM-built constructs are the main source of fatigue failures. Dallago et al. (2018a) have shown that, when fatigue fracture occurred in additively manufactured porous Ti6Al4V constructs, fatigue cracks initiated on the surface and not along internal defects. Yáñez et al. (2020) presented evidence, both from FEA simulations and fatigue loading on additively manufactured porous Ti6Al4V constructs that suggested that surface roughness, as well as internal defects close to the surface, were sources of fatigue crack formation. On the other hand, some researchers reported that internal defects within porous Ti6Al4V constructs were the origin of fatigue cracks. Leuders et al. (2013) reported that, in additively manufactured Ti6Al4V non-porous constructs, fatigue crack initiation occurs earlier under cyclic loading due to internal defects. In another study, du Plessis et al. (2020a) presented evidence that porous SLM-built Ti6Al4V constructs with internal defects experienced fewer cycles to failure by about 1000 times when compared to constructs without internal defects. Wickmann et al. (2021) reported that internal defects with diameters greater than 200 μm were the source of fatigue cracks. Ahmadi et al. (2018) reported that the site of fatigue crack initiation is dependent on the applied cyclic stress levels, with internal defects being the site of crack initiation under higher stresses while surface roughness is the site of crack initiation during low-stress cyclic loading.

The development of finite element analysis (FEA) and cyclic fatigue loading simulation tools allowed researchers to create accurate numerical models that predict the effect of cyclic loading on porous constructs (Peng et al., 2020, Hitchon, 2022). Peng et al. (2020) found that the fatigue strength of porous Ti6Al4V FEA models was dependent on the unit cell shape and porosity. There is ongoing active research on the modelling of cyclic loading of SLM-built porous constructs. Hitchon (2022) developed numerical models for predicting fatigue strength. These models were calibrated to match the real-life fatigue

properties of SLM-built constructs. These results approximated the fatigue-related mechanical properties of Ti6Al4V, which was conducted through Seeger's approximation method (Bäumel et al., 1990). Surface roughness effects were replicated by including a stress concentration factor (K_t) that reduces the fatigue strength. The rationale behind calibration of the mechanical properties is to consider internal defects within the struts and surface roughness, which have a direct effect on the fatigue strength of the constructs and are not reflected in the FEA models (Hitchon, 2022). This factor has seen recent experimentation to expand its use beyond surface roughness. For example, work by Raghavendra et al. (2023) attempted to create FEA models with modified stress concentration factors (K_t) that reflect the effects of sharp strut junctions and surface roughness. The predicted K_t values in that study were determined from both CT scans and tensile fatigue loading tests on additively manufactured constructs. Understanding the exact parameters that drive differences between real-life and modelling fatigue strength results is important for improving numerical modelling predictions.

To the best of our knowledge, previous studies on fatigue loading of porous SLM-built Ti6Al4V constructs were performed using either compression-compression or push-pull cyclic loading rather than flexural cyclic loading. This is possibly because the research community's interest was primarily concentrated on mimicking the load-bearing bones of the body, which are more likely to experience compressive fatigue loading (Benady et al., 2023). In addition, flexural loading is more complex, which might complicate the interpretation of results (Belan et al., 2019). Nonetheless, in many biomedical applications, such as mandibular loading, flexure is likely more important than pure compression (van Eijden, 2000).

Our main objective in this study was to determine the relationship between the maximum flexural stress and number of cycles for porous Ti6Al4V constructs. We determined the flexural fatigue strength of SLM-built porous Ti6Al4V using cyclic tests for up to 10^6 cycles. This was followed by the development of numerical models to predict the flexural fatigue strength of porous Ti6Al4V constructs. Our study also used microscopy to detect the origin of fatigue cracks. To our knowledge, this is the first study that describes the

flexural fatigue strength of porous Ti6Al4V constructs, using a combined experimental and numerical modelling approach.

4.3 Methods

4.3.1 Preparation of porous constructs

4.3.1.1 Design of porous constructs

Computer-aided design (CAD) modelling was conducted using Simulia Abaqus 2020 (Dassault Systèmes Simulia Corp, Providence, RI, USA). All designs in this study followed ASTM standards (ASTM E290-14) (ASTM, 2014). A series of CAD models were designed as porous beam constructs consisting of repeated simple cubic unit cells throughout the entire beam, with each unit cell having a span length of 1.00 mm. Each model had a uniform strut thickness of either 350 μm (ST350) or 450 μm (ST450). Two different models, made from each strut thickness, were built, each with a different unit cell count along the width \times thickness \times length: the 2 \times 2 layout had 2 \times 2 \times 52-unit cells and the 3 \times 3 layout had 3 \times 3 \times 70-unit cells (Figure 4-1). The nominal dimensions for each of the models are included in Appendix B, Table B-1.

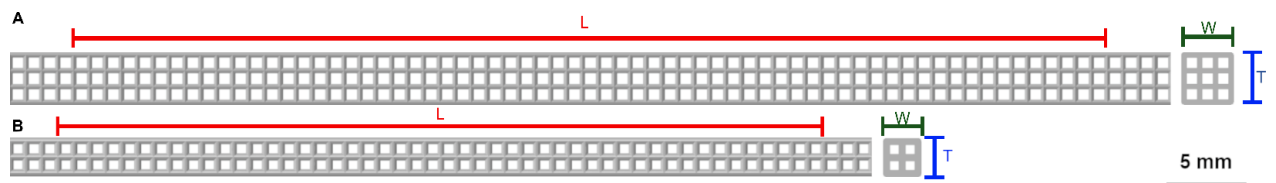


Figure 4-1: Porous Ti6Al4V CAD models used in this study. The strut thicknesses were (A) 350 μm and (B) 450 μm .

L represents the gauge length, W the width, and T the thickness of the model. Gauge length is the distance between the two support anvils used in three-point bending tests. All models had a constant gauge length-to-thickness ratio (L/T) of 18:1.

4.3.1.2 Manufacturing of porous constructs

Ti6Al4V porous constructs were built from CAD models using SLM. This was performed using a Renishaw SLM machine (Renishaw PLC, Wotton-under-Edge, United Kingdom) by Additive Design in Surgical Solutions Center (London, Ontario, Canada). This process was previously described in section 3.3.1.2.

A total of 76 constructs were built from the ST350 and ST450 models. We previously analyzed constructs like those built in this study for surface roughness and internal defects using computed tomography (CT) (Chapter 3). The volume percentage of internal defects was $<1.2\%$, and the arithmetic mean height of the surface roughness was $\approx 4.3 \pm 1.2 \mu\text{m}$.

4.3.2 Static and dynamic flexural tests

4.3.2.1 Static flexural strength testing of SLM-built constructs

Three-point flexural loading tests were conducted on constructs ($n=10$) using a universal Instron machine (Instron 3345, Instron, Norwood, MA, USA) as per ASTM standards (International, 2021, ASTM, 2014). The constructs' dimensions are included in Appendix B, Table B-1. The gauge length-to-T (L/T) ratio was set at 18:1 (Figure 4-2).

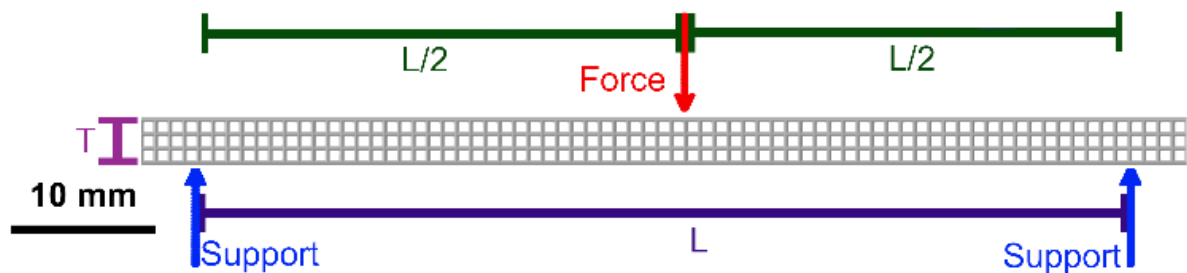


Figure 4-2: Three-point bending setup. The L/T ratio was 18:1. Arrows represent the applied force (red) and supports (blue).

A 500 N load cell was used to record the force values, while displacement readings were recorded from the crosshead location. The applied crosshead speed was 1 mm/min, the data were recorded at a rate of 100 s^{-1} . All force readings were taken after a pre-load of 5 N to remove slack in the readings. Loading was applied until failure. The flexural modulus (E_F), flexural yield stress (σ_{FY}), and flexural strength (σ_{FS}) were calculated from the resultant flexural stress-strain curves. The flexural stress (σ_f) and flexural strain (ϵ_f) were calculated using equations 3-4 and 3-5.

4.3.2.2 Dynamic flexural loading of SLM-built constructs

Flexural cyclic testing was conducted on the porous constructs using a universal Instron servo-hydraulic machine (Instron 8820), interfaced with Wavematrix software (Instron, Norwood, MA, USA) to control the test. A 250 N Dynacell was used to record the cyclic

forces applied on each specimen. The ST350 constructs had a 3×3-unit cell layout while the ST450 had the 2×2-unit cell layout. The initial designs of the ST350 were planned to have similar nominal dimensions as the ST450; however, the ST350 constructs exhibited force levels below the sensitivity of the load cell. Hence the 3×3 layout was used.

The cyclic testing protocol is described as follows. First, the specimens were ramp loaded up to 3 N, a small number of cycles of incrementing stress ranges were then implemented until the minimum pre-set force was reached, then the cyclic loading was initiated using a sinusoidal wave with a frequency of 10 Hz and the ratio between the minimum and maximum stress, known as stress ratio, was set at 0.2. Although the frequency of 10 Hz is much higher than that seen in normal chewing activity (Po et al., 2011), this frequency allowed tests to be completed in a timely manner. In addition, evidence from other studies, such as the one done by Ritchie et al. (1999), suggests that the fatigue behaviour of Ti6Al4V is independent of frequency at frequencies less than 100 Hz. The maximum loading was set in each test between $0.3 \sigma_{FY}$ and $0.9 \sigma_{FY}$ for each of the specimens. The tests were monitored until either 10^6 cycles were reached or until a 75% decrease in force occurred, indicating loss of stiffness. Three specimens ($n=3$) were tested for each of the five stress groups.

Measurements of the force (F), deflection (d), time (t), and cycle count (N) were recorded and fed into a custom MATLAB code included in the Appendix B, Section B.1. The code was used to calculate the maximum (σ_{fmax}) and minimum fatigue stresses (σ_{fmin}), the maximum (ϵ_{fmax}) and minimum fatigue strains (ϵ_{fmin}), the mean stress ($\bar{\sigma}$) and the amplitude stress (σ_a). The ratio between the maximum stress and yield stress ($\sigma_{fmax}/\sigma_{FY}$) was also calculated. This value is called the yield-normalized fatigue stress ratio.

4.3.3 Numerical simulations

4.3.3.1 Static FEA modelling

The numerical simulation process involved two major procedures: static FEA modelling and dynamic loading modelling. CAD models were imported to Simulia Abaqus 2020 (Dassault Systèmes Simulia Corp, Providence, RI, USA) to create FEA computational

models to replicate the static three-point bending tests (Figure 4-3). The material properties of Ti6Al4V, modelling parameters, and boundary conditions that were used in the FEA tests were determined in Chapter 3. The Young's modulus of Ti6Al4V was set at 102 GPa, Poisson's ratio was set to 0.342, the plastic region was interpolated from the results of tensile tests done on non-porous constructs, fracture strain was set at 0.077, and stress triaxiality was set at 0.33. Another CAD model, based on the ST350 and referred to as ST350-Bone, was created with simulated bone placed within the pores. In the ST350-Bone model, a tie constraint was established between the surfaces of the bone and the porous construct to simulate the effect of full osseointegration. The Young's modulus of bone was set at 17 GPa and Poisson's ratio at 0.300, assuming that the bone was mature (Checa et al., 2011).

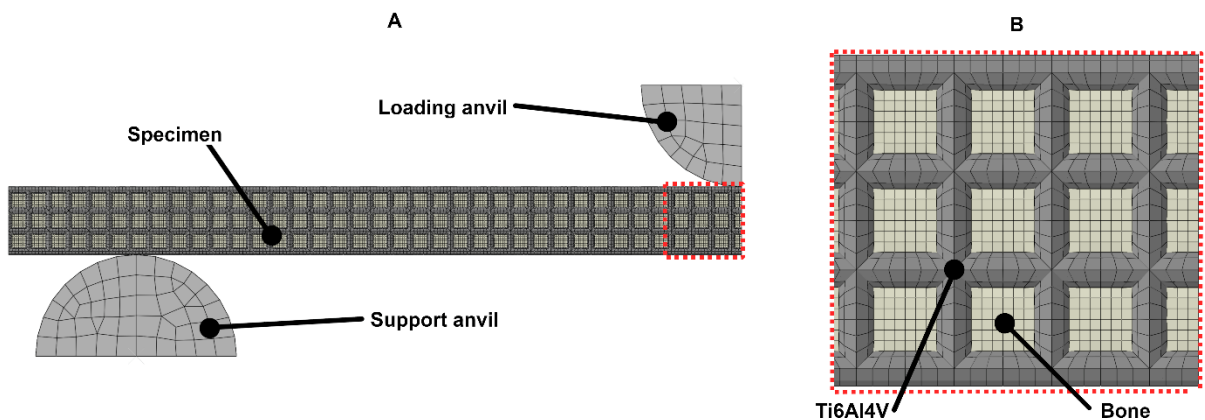


Figure 4-3: Representative three-point bending FEA model from a front view.

The overall assembly (A) consists of 2 cylindrical models, representing the loading and support anvils, and the specimen between them. The specimen is shown in a close-up (B). Two kinds of models were tested, one with porous Ti6Al4V and bone ingrowth, and another with porous Ti6Al4V alone.

All the models were discretized into hexahedral elements (C3D8I), and the global size of these hexahedral meshes was kept at an average of 125 μm . Symmetry constraints were used to simplify the FEA model, as done in previous work (Song et al., 2021) and in Chapter 3. The support and loading anvils were modelled using rigid cylinder models, discretized into 1 mm sized C3D8I elements. All force readings were taken with a cut-off of 5 N. The FEA analysis was conducted by applying ramp loading simulation until failure. The static flexural properties (E_F , σ_{FY} , σ_{FS}) were calculated from the force and displacement

readings following Equations 3-4 and 3-5. The FEA models were captured at the yield point, which was the benchmark used for further analysis.

4.3.3.2 Fatigue numerical modelling

The dynamic loading models were developed using FE-Safe 2020 (Dassault Systèmes Simulia Corp). This software was chosen for its ability to analyze fatigue properties and predict the occurrence of fatigue cracks (As et al., 2008, Peng et al., 2020, Fertig and Kenik, 2011). The fatigue life prediction was based on the Brown-Miller theory with Morrow's correction model, which was found to provide the most realistic method to predict the fatigue life of ductile materials (Peng et al., 2020, Duan et al., 2018a). The Brown-Miller theory assumes that maximum fatigue damage occurs on the plane exhibiting the highest shear strain amplitude (Brown and Miller, 1973). Kandil et al. (1982) developed the function that describes the Brown-Miller theory. Morrow's mean stress correction model was applied to account for the effect of the mean stress when the mean stress was not zero (Morrow, 1968, Ince, 2017). The model predicted the stress amplitude that would occur had the mean stress been zero. The combined Brown-Miller model with Morrow's correction model is as follows (Simulia, 2020):

$$\left(\frac{\Delta\gamma_{\max}}{2}\right) + \left(\frac{\Delta\varepsilon_n}{2}\right) = (1.65)\left(\frac{\sigma'_f - \bar{\sigma}_n}{E_T}\right)(2R)^b + 1.75(\varepsilon'_f)(2R)^c \quad (4-1)$$

where $\left(\frac{\Delta\gamma_{\max}}{2}\right)$ is the shear strain amplitude, and $\left(\frac{\Delta\varepsilon_n}{2}\right)$ is the normal strain amplitude on each plane. σ'_f is the Basquin's fatigue strength coefficient, defined as the true stress corresponding to the fracture of the material in one reversal (R) of a loading cycle (2R) (Morrow, 1968). b is the Basquin's fatigue strength exponent, defined as the slope of the σ_a - N_f curve on a \log_{10} - \log_{10} scale, and describes the rate of increase of the number of cycles to failure when the applied stress decreases (Duan et al., 2018b, Kun et al., 2008, Sabour, 2013). ε'_f is the fatigue ductility coefficient, which is defined as the true strain corresponding to the failure of the material in one reversal. c is the Coffin-Manson fatigue ductility exponent which is defined as the slope of the plastic strain-life curve on a \log_{10} - \log_{10} scale (Chan, 2013), and describes the effect of plastic strain on the fatigue life of the

material (Zhao et al., 2020). E_T represents the Young's modulus of the material that was tested.

Fatigue parameters were applied on the Ti6Al4V component of the FEA model. These parameters include the relevant mechanical properties that are used to predict the $\sigma_a - N_f$ curves of non-porous Ti6Al4V constructs. Since non-porous constructs were not tested in this study, an analytical estimation approach was used to obtain these parameters. The fatigue parameters used in the numerical models are detailed in Table 4-1. In the previous chapter (Chapter 3), we measured the Young's modulus (E_T), tensile yield strength and ultimate tensile strength from tensile loading tests done on non-porous SLM-built Ti6Al4V specimen. The Poisson's ratio used in this study was taken from the literature (Peng et al., 2020). Two of the fatigue parameters, Basquin's fatigue strength exponent (b) and Coffin-Manson fatigue ductility exponent (c) were determined using $\log_{10} \sigma_a - \log_{10} N_f$ and $\log_{10} \epsilon_a - \log_{10} N_f$ curves (Duan et al., 2018b, Simulia, 2020, Chan, 2013). The rest of the fatigue mechanical properties could then be estimated from the previously mentioned mechanical properties (Duan et al., 2018b, Simulia, 2020, Chan, 2013). To simulate the surface roughness properties, a stress concentration factor (K_t) was applied on each of the numerical models. This is a value directly related to the arithmetic mean height of the roughness of the surface being modelled in FEA (Nakhaei et al., 2023, Pilkey, 1997). The actual stress generated in the model was adjusted using the values of K_t and nominal stress evaluated from the FEA analysis as described below in Equation 4-2.

$$\text{Local stress at notch} = K_t(\text{Nominal stress}) \quad (4-2)$$

The arithmetic mean height of the roughness of the constructs built in this study is expected to be like that seen in our previous work (Chapter 3), making the $K_t = 1.3$. Further details on the choice of this K_t value is provided in the Appendix B, section B.3.

Table 4-1: Fatigue parameters applied on the Ti6Al4V component of the FEA model. The methods used to determine the values of the parameters are included.

Parameters	Value	Method of calculation	References
Young's Modulus (E_T)	102.763 GPa	Slope of the linear region of the tensile true σ - ϵ curve.	(Chapter 3)
Poisson's ratio	0.342	Taken directly from reference	(Peng et al., 2020)
Tensile Yield Strength (σ_{TY})	866 MPa	Intercept of 0.2% offset of the elastic true σ - ϵ curve	(Chapter 3)
Ultimate Tensile Strength (σ_{UTS})	1038.98 MPa	Maximum true tensile stress before failure	(Chapter 3)
Basquin's fatigue strength exponent (b)	-0.16	Slope of the $\log_{10} \sigma_a - \log_{10} N_f$ curve	(Duan et al., 2018, Simulia, 2020)
Coffin-Manson fatigue ductility exponent (c)	-0.3	Slope of the plastic region of $\log_{10} \epsilon_a - \log_{10} N_f$ curve	(Duan et al., 2018, Simulia, 2020, Chan, 2013)
Fatigue strength coefficient (σ'_f)	1735.10 MPa	$= 1.67(\sigma_u)$	(Duan et al., 2018, Simulia, 2020)
Cyclic strain hardening exponent (n')	0.533	$= b/c$	(Chan, 2013)
Cyclic strain hardening coefficient (K')	3037.30 MPa	$= \sigma'_f/c^{n'}$	(Chan, 2013)
Fatigue ductility coefficient (ϵ'_f)	0.35	Taken directly from references	(Duan et al., 2018, Simulia, 2020)
Stress concentration factor (K_t)	1.3	The appropriate surface roughness option and σ_{UTS} were chosen in FE-Safe. Roughness values taken from Chapter 3.	(Simulia, 2020)

The FEA models were first exported to the FE-Safe software at the point of yielding. Numerical simulations were conducted by adjusting the force levels between 0.2 and 0.8 of the maximum applied force. To replicate the real-life cyclic loading tests, the stress ratio was kept at 0.2 with a loading frequency of 10 Hz. During each numerical simulation, FE-Safe recorded the nodal stress tensor. The components of the stress tensor were then multiplied by the defined time history of the applied load. This allowed the software to construct time evolutions of the principal stresses. Principal strains were then calculated from the principal stresses. Shear strain amplitude and normal strain amplitude, generated through the loading, were evaluated along the planes of the elements, while fatigue parameters in Table 4-1 were fed into the numerical model. The time histories of the shear strain, normal strain, and normal stress on each plane were then calculated. The software then estimated the number of cycles on each plane within the models using Equation 4-1,

and individual predicted cycles were estimated using the Rainflow counting algorithm (Downing and Socie, 1982). This algorithm converts the uniaxial loading sequence in the numerical simulation of varying stresses into an equivalent set of constant amplitude stress reversals, which are then used to estimate accumulated damage through Palmgren-Miner's rule (Miner, 1945). This rule states that damage (D) caused by cyclic loading at a constant amplitude can be calculated as follows:

$$D = \sum_{n=0}^{N_f} \frac{n}{N_f} \quad (4-3)$$

where D is dimensionless. Its value ranges between 0 and 1, with a value of 1 indicating failure. The number of loading cycles applied on any plane in the model is labeled as n. N_f is the total number of cycles to failure of nonporous Ti6Al4V at the given amplitude stress, which is derived from $\sigma_a - N_f$ curve of Ti6Al4V generated from the mechanical properties listed in Table 2.

The number of cycles to failure was estimated by repeating this workflow until failure was reached, as indicated by the damage calculation. After completing each fatigue simulation, Simulia Abaqus was then used to view where fatigue failure was expected to initiate.

4.3.4 Light and scanning electron microscopy

All microscopic analyses were conducted at the Nanofabrication Facility at Western University (London, ON, Canada). Once the fatigue tests were completed, constructs were examined at the fracture site using a light microscope (Zeiss Axioskop, Carl Zeiss, Oberkochen, Baden-Württemberg, Germany) and scanning electron microscope (SEM) (1540XB FIB/SEM Carl Zeiss). Four specimens were used from both the ST350 and the ST450 construct groups that went under cyclic loading at $0.4 \sigma_{FY}$ and $0.8 \sigma_{FY}$. The SEM was set at a voltage of 5 kV, with scans taken at magnifications ranging between $50\times$ and $750\times$.

4.3.5 Statistical analyses

All statistical analyses were conducted using GraphPad Prism 10 (GraphPad Prism, La Jolla, CA, United States). Mean values were calculated along with their standard deviations. For all the static tests, one-way ANOVA and Tukey's multiple comparison tests were conducted to compare the level of significance between the different groups, with $p < 0.05$ considered as significant.

For each of the construct groups, different curves were plotted using power-series fits to get the σ_{fmax} - N_f and the $\sigma_{fmax}/\sigma_{FY}$ - N_f curves. These equations follow the classical Basquin's model (Basquin, 1910), but use the maximum flexural stress applied on the constructs instead of the amplitude stress (σ_a). The power fit model obtained from the σ_{fmax} - N_f curves could be written as follows:

$$\sigma_{fmax} = X(N_f)^b \quad (4-4)$$

where X is the coefficient of the power series, N_f is the number of cycles at failure, and b is the Basquin's fatigue strength exponent. The power fit model obtained from the $(\sigma_{fmax}/\sigma_{FY})$ - N_f curves could be written as follows:

$$\sigma_{fmax}/\sigma_{FY} = \frac{(X)(N_f)^b}{\sigma_{FY}} \quad (4-5)$$

Percentage deviations of the fatigue numerical models from the real-life, cyclically loaded, SLM-built constructs were calculated from the relative error (R) of the yield-normalized fatigue stress ratio at different N_f values using the equation below:

$$R(N_f) = \frac{|(\sigma_{fmax}/\sigma_{FY})_S - (\sigma_{fmax}/\sigma_{FY})_M|}{(\sigma_{fmax}/\sigma_{FY})_S} \times 100 \quad (4-6)$$

where $R(N_f)$ is the relative deviation at a specific number of cycles N_f , and $(\sigma_{fmax}/\sigma_{FY})_S$ and $(\sigma_{fmax}/\sigma_{FY})_M$ are the yield-normalized fatigue stress ratio values at N_f for the SLM-built constructs and the fatigue numerical models respectively.

4.4 Results

4.4.1 Static flexural tests

The flexural strength and modulus of SLM-built constructs and FEA models showed significant differences when different unit cell layouts were used (Figure 4-4). The flexural yield stress (σ_{FY}) and flexural modulus (E_F) were found to be significantly higher in the 2×2 constructs than in the 3×3 constructs ($p < 0.05$). This is because of the existence of pores at the center line of the longitudinal axis of the 3×3 constructs, as opposed to both other construct layouts, where there were struts built along their transverse axes. In addition, the flexural yield stress (σ_{FY}) values in the FEA models were higher than those seen in the SLM-built constructs. This may have been due to imperfections within the SLM-built constructs (section 3.4.2.2). In addition, the σ_{FY} value for the ST350-Bone model was 466 MPa, indicating that the strength of porous constructs increased when bone ingrowth was present. The FEA model with bone ingrowth exhibited σ_{FY} 2.5 times greater and E_F 1.7 times greater than the FEA model without bone ingrowth.

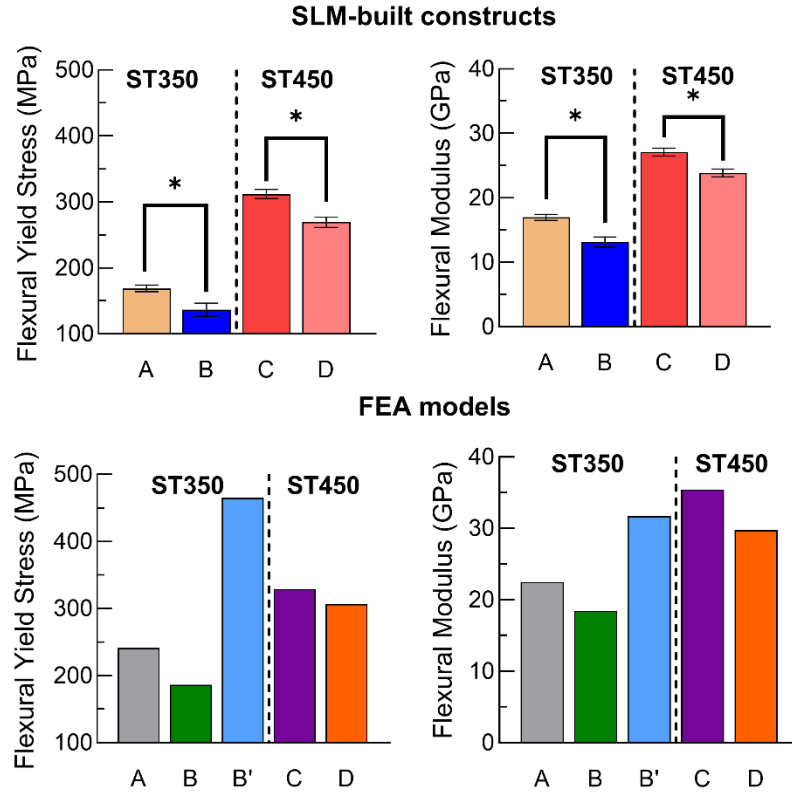


Figure 4-4: Flexural yield stress and flexural modulus of SLM-built constructs and FEA models.

Flexural yield stress and flexural modulus of SLM-built constructs and FEA models. (A) strut thickness 350 μm - 2 \times 2 unit cell width and thickness (ST350-2 \times 2), (B) ST350-3 \times 3, (C) ST450-2 \times 2 (D) ST450-3 \times 3 and (B') ST350-3 \times 3 with bone ingrowth (ST350-3 \times 3-Bone). For SLM-built constructs, data are means \pm SD, n = 10. The flexural yield stress and modulus values of SLM-built constructs were significantly different between the 2 \times 2 and 3 \times 3 arrangements, * $p < 0.05$. The bone ingrowth FEA model (B') exhibited larger flexural yield strength and modulus than the FEA model without bone ingrowth (B).

4.4.2 Dynamic flexural testing

The maximum and yield-normalized fatigue stress values-N curves were determined from the flexural cyclic loading of SLM-built constructs (Figure 4-5). The fatigue results in both groups of constructs followed a power series ($R^2 > 0.89$), which was consistent with Basquin's models (Basquin, 1910). The equations of the fits are included in Appendix B, Table B-1. The values obtained from σ_{fmax} - N_f regression fits of the constructs ST350 and ST450 at 10^6 cycles were found to be 42 MPa and 83 MPa, respectively. The values obtained from the $\sigma_{fmax}/\sigma_{FY}$ - N_f regression fits of the constructs ST350 and ST450 at 10^6 cycles were 0.313 and 0.264 respectively.

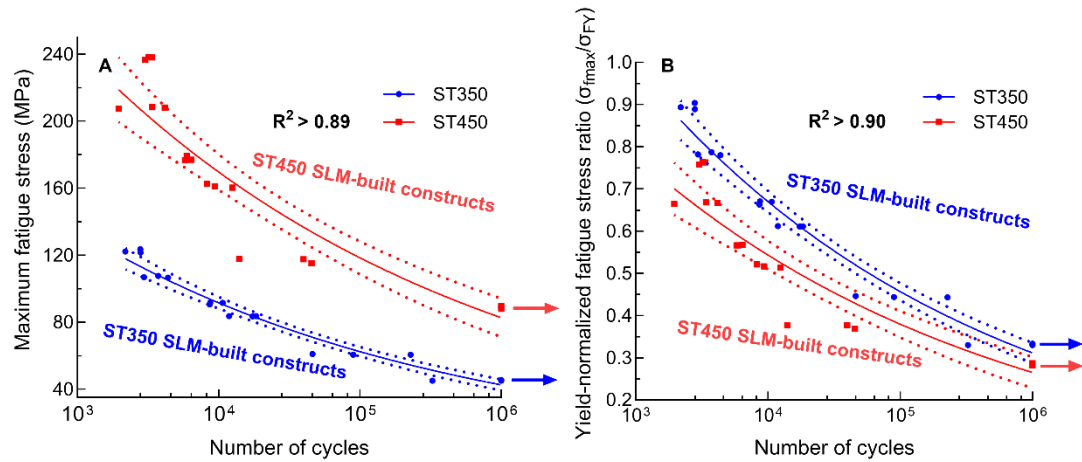


Figure 4-5: The $\sigma_{fmax} - N_f$ and the $\sigma_{fmax}/\sigma_{FY} - N_f$ curves from fatigue tests.

The number of cycles was placed on a logarithmic scale. Curves were fit with power series ($R^2 > 0.89$). The points at 10^6 cycles with arrows represent constructs that did not fail. The dotted curves represent 95% confidence intervals.

4.4.3 Numerical modelling of dynamic flexural loading

Comparisons of the numerical models of cyclic flexural loading with SLM-built constructs were conducted using the $\sigma_{fmax}/\sigma_{FY} - N_f$ curves (Figure 4-6).

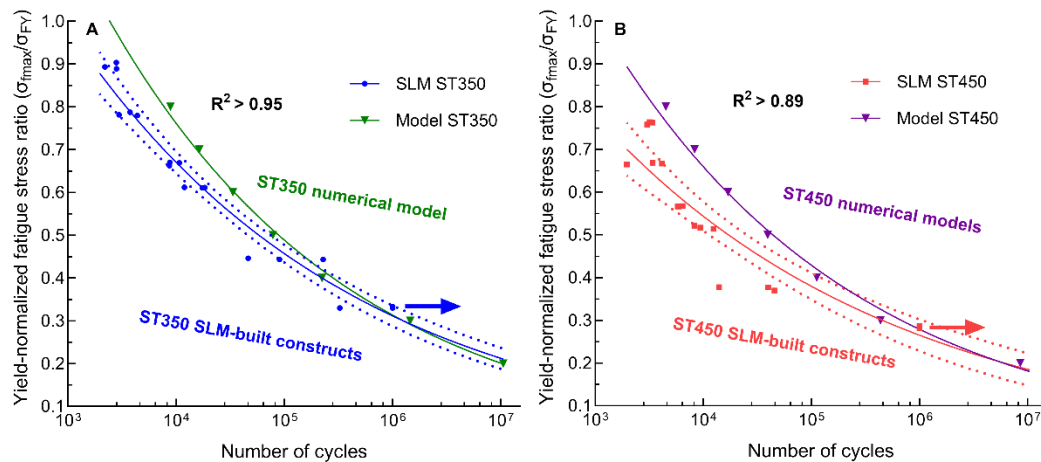


Figure 4-6: Behaviour of fatigue numerical models compared to that of real-life SLM-built constructs.

(A) ST350 constructs and model and (B) ST450 constructs and model. Curves were fit with power series ($R^2 > 0.89$). The curves for the numerical models had an overall average deviation of $\approx 10\%$ when compared to real-life curves. For the SLM-built constructs, the dotted curves represent 95% confidence intervals.

Stress values close to the yield points were chosen as references in the numerical models.

The fatigue numerical models predicted $\sigma_{fmax}/\sigma_{FY} - N_f$ curves that were in close agreement

with the real-life curves. The average deviations of the simulated curves from the real-life curves in both ST350 and ST450 were $\approx 10\%$ over the range of 10^3 to 10^7 cycles, as described in Appendix B, section B.2, Table B-3, B-4, and B-5. It should be noted that the real-life cyclic loading results were extrapolated when the number of cycles was $>10^6$. When looking at the effect of the bone ingrowth in the ST350 model, it was found that its fatigue strength was almost twice that of the model without bone ingrowth (Figure 4-7).

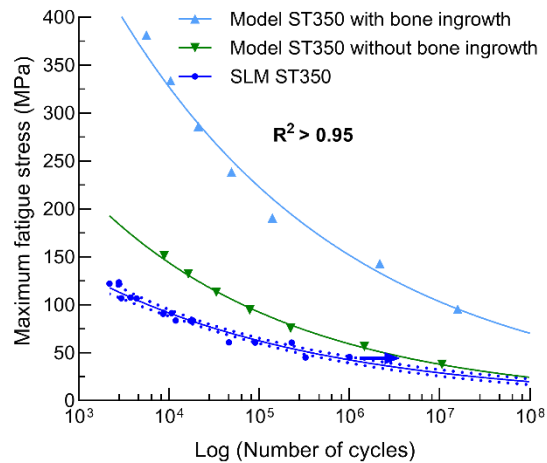


Figure 4-7: The results of the FE-Safe numerical models with and without bone ingrowth, plotted with the fatigue behaviour of real-life SLM-built constructs.

Curves were fit with power series ($R^2 > 0.95$). The porous models with bone ingrowth had almost double the fatigue strength of its counterpart without bone ingrowth. For the SLM-built constructs, the dotted curves represent 95% confidence intervals.

Three-dimensional color-coded stress contour maps, representing the maximum principal stress at different locations along the models, were created from the numerical models (Figure 4-8). The highest stress concentrations were observed at the junctions of the struts. The ST350 models with bone ingrowth (ST350-Bone) exhibited lower stresses compared to ST350 models without bone ingrowth (ST350) at the junctions. Unlike real-life fatigue tests, the numerical models predicted that failure was most likely to occur on the compression side of the porous models. However, this seems to have been driven by the overestimated stress that was associated with the tie constraint created between the loading anvil and the porous construct model.

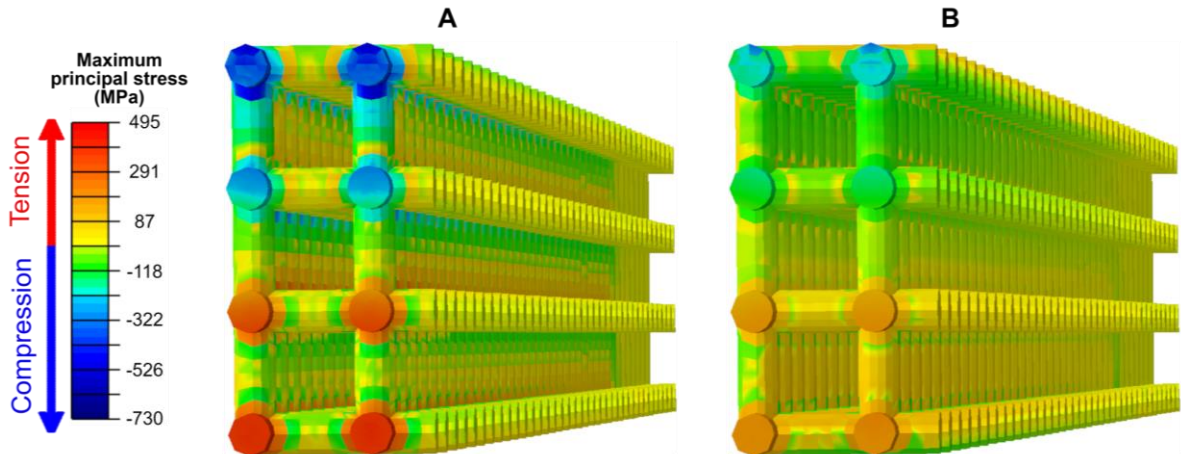


Figure 4-8: Visualisation of the flexural cyclic loading simulation of the (A) ST350 and (B) ST350-Bone models at $\sigma_{fmax} = 150$ MPa.

The colours represent the maximum stress applied on each element during cyclic loading. In all models, failure was expected to occur due to stress concentration at the strut junctions, where the highest stress values were observed. The models with bone ingrowth had lower maximum principal stresses at the junctions, indicating that bone causes a damping effect.

4.4.4 Microscopy of fracture sites

Light microscopic images revealed that fractures occurred near the junctions of the tensile-loaded regions of the constructs (Figure 4-9A & B). Further light microscopy images can be found in Appendix B (Figures B-4 and B-5). When looking at the SEM images of the fractured constructs, the struts were found to exhibit high levels of surface roughness. It was observed that a large amount of partially melted particles was deposited on the strut surfaces; this may have happened because of the balling effect. In addition, the struts exhibited high levels of waviness, which caused variation in their thickness. Fractures could have been initiated either from surface or internal defects (Zhang et al., 2019, Du et al., 2020). However, we observed that fatigue cracks appeared to initiate at the surface of the struts, as displayed in Figure 4-9C & D, as well as in the additional scans provided in Appendix B (Figures B-6 and B-7). Two observations support this notion. The first is the lack of crack formation surrounding any of the internal defects at the sites of fracture. The second is that sites of fracture showed surface damage or fracture plane irregularities suggestive of fracture initiation from the surface.

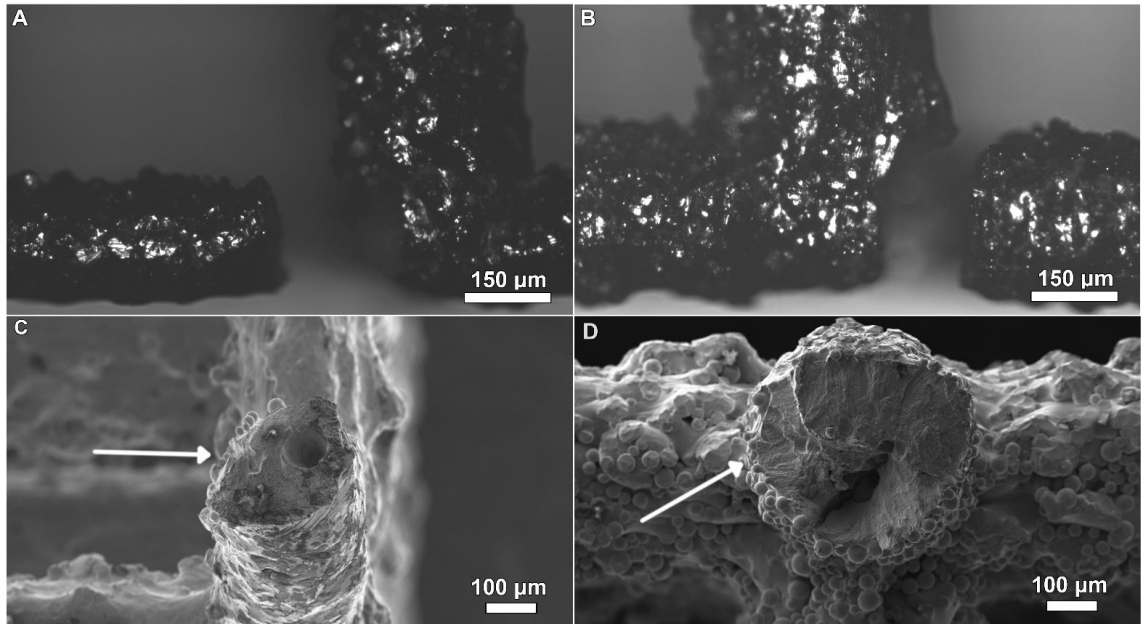


Figure 4-9: Representative light microscope images and SEM images of fatigue loaded constructs.

Representative light microscope images of (A) an ST350 construct tested at $\sigma_{fmax}/\sigma_{FY} = 0.4$ and (B) an ST450 construct at $\sigma_{fmax}/\sigma_{FY} = 0.8$. Representative SEM image of the fracture site of (C) an ST350 construct at $\sigma_{fmax}/\sigma_{FY} = 0.4$ and (D) an ST450 construct at $\sigma_{fmax}/\sigma_{FY} = 0.8$. Fatigue fracture occurred near the junctions of the struts. The struts had a highly rough surface texture, caused by partially melted Ti6Al4V particles, as well as waviness of the structure of the struts. Large internal defects were visible at the fracture sites but did not show evidence of crack initiation. White arrows point to locations of surface damage or fracture plane irregularities.

4.5 Discussion

SLM-built porous Ti6Al4V constructs were tested using cyclic flexural loading. Furthermore, numerical models were developed that predicted the fatigue strength of the Ti6Al4V porous constructs. Thus, this study described the flexural fatigue strength of porous Ti6Al4V constructs, using a combined experimental and numerical approach. In addition, we validated numerical fatigue models that were used to study the effect of bone ingrowth on flexural fatigue loading at $> 10^6$ cycles, which is not feasible to conduct experimentally.

4.5.1 Comparison of numerical models with SLM-built constructs

Our numerical models, with adjusted mechanical parameters, were in close agreement with the $\sigma_{fmax}-N_f$ curves of the SLM-built constructs (Figure 4-6). This helped in the prediction of the fatigue life of constructs with high level of accuracy. In previous work, Hitchon

(2022) produced numerical models of gyroid porous structures, built with Ti6Al4V properties, and validated using experimental static and cyclic loading tests. In that study, however, it was pointed out that numerical models could deviate from real-life testing, particularly in highly porous models. This was assumed to be a direct outcome of internal defects and surface roughness that were not present in numerical models. In the present study, we found that deriving the fatigue strength (b) and fatigue ductility (c) exponents, and the stress concentration factor (K_t) allow prediction of the fatigue strength more accurately. These fatigue parameters were affected by several factors.

The first factor that may have affected the fatigue resistance of SLM-built constructs is associated with its microstructure and post-processing heat treatment. Previous works reported that the microstructure of SLM-built Ti6Al4V is highly anisotropic due to the formation of martensitic structure within the constructs (Shunmugavel et al., 2015), which reduced the ductility (Tan et al., 2017, Gong et al., 2015, Murr et al., 2012). Evidence from the literature suggested that SLM-built Ti6Al4V constructs are negatively affected by their lower ductility (Ahmadi et al., 2019, Heinz and Eifler, 2016, Cao et al., 2018).

The second factor that may have affected the fatigue resistance could be surface roughness. The SEM scans revealed that fracture sites exhibited high surface roughness which was previously observed elsewhere (Chapter 3). due to the balling effect. In addition, the SLM-built Ti6Al4V constructs had internal defects near the surface. The combination of the high stress concentration at the junctions of struts and surface roughness likely promotes fatigue failure (Dallago et al., 2018a, Yáñez et al., 2020).

The third factor that may have affected Ti6Al4V constructs' fatigue strength is internal defects. The SEM images displayed in Figure 4-9 included $\approx 100 \mu\text{m}$ voids at the fracture sites which have been previously observed (section 3.4.2.3). It was shown in studies by Wickmann et al. (2021) and Leuders et al. (2013) that defects within non-porous SLM-built constructs initiated cracking under cyclic loading. Hu et al. (2020) demonstrated that internal pores located close to the surface of non-porous SLM-built constructs were likely to cause failure under cyclic loading.

The results of the present study revealed that cracks in cyclically loaded constructs most likely initiated from the surface and the reduction in ductility accelerated crack propagation. Ahmadi et al. (2019) have also shown that internal defects in porous SLM-built Ti6Al4V constructs were the dominant reason behind fatigue crack initiation at higher stresses and lower number of cycles ($N_f < 10^5$), while crack initiation at lower stresses and higher number of cycles ($N_f > 10^5$) was dominated by surface roughness. The effect of internal defects at high-stress cyclic loading was observed in a study by du Plessis et al. (2020a), who found that removal of internal voids increased the fatigue strength of porous Ti6Al4V constructs by up to 1000 times. Leuders et al. (2013) have demonstrated that residual stresses and martensitic microstructure in titanium alloys result in lower ductility and enhanced crack growth.

The model, derived from the results of cyclic loading of SLM-built constructs, considered the three factors described above. The higher K_t value resulted in lowering the overall fatigue strength of the models, simulating the effect of surface roughness (Figure 4-7). The low fatigue strength exponent (b) for SLM-built constructs resulted in a higher probability of premature failure under higher cyclic amplitudes, due to the existence of internal defects. The higher fatigue ductility exponent (c) was most likely caused by the lower ductility of SLM-constructs. The numerical modelling that incorporated surface roughness, internal defects and reduction in ductility is a more efficient alternative than previous studies using mechanical testing of real-life constructs (Yáñez et al., 2020, Ghosh et al., 2022, du Plessis et al., 2020b).

The models predicted fatigue life with a deviation of $\approx 10\%$. However, the numerical models did show greater deviation at high stresses when compared to low stresses (Appendix B, section B.3). This is thought to be the result of internal defects causing high-stress concentrations leading to failure (Ahmadi et al., 2019). The effects of stress concentrations arising from internal defects could be modelled by introducing a higher K_t value. To test this approach, K_t values were varied between 1.2 and 1.8 on the ST350 and ST450 models (Appendix B, section B.3). The results indicated that, with increasing K_t value, the deviation at higher cyclic stresses decreased significantly, while increasing the deviation at low cyclic stresses. The model with $K_t = 1.3$ was deemed acceptable because

constructs designed using this model are expected to be subjected to lower stresses and high number of cycles (like the stresses encountered during normal chewing action of the mandible). Nevertheless, a further improvement on the fatigue numerical models was tested by applying different K_t values at different stress ranges (as described in Appendix B, section B.4).

4.5.2 The effect of bone ingrowth on fatigue strength of porous constructs

The porous model with bone ingrowth exhibited overall higher fatigue strength when compared to its counterpart without bone ingrowth. This was largely driven by the higher fatigue strength coefficient of the constructs, which was the result of filling the pores with bone. Previous studies demonstrated that porous titanium alloy constructs with fully mature bone ingrowth reduced stress concentrations along the construct (Peng et al., 2021, Gao et al., 2019). Other studies revealed that the time required for full bone ingrowth ranged between 6 and 12 weeks in animal models (Taniguchi et al., 2016, Chen et al., 2019, Deng et al., 2021, Watanabe et al., 2023). However, human studies indicated that the time for complete bone ingrowth in titanium implants with porous surfaces reached up to 9 months (Hofmann et al., 1997). There appears to be a gap of knowledge regarding how long human bone ingrowth would take in fully porous constructs. Hence, it is necessary that porous constructs be durable for a period of at least 9 months.

4.5.3 Effect of pore geometry on fatigue properties

When looking at the $\sigma_{\text{fmax}}/\sigma_{\text{FY}}-N_f$ curves, the fatigue strength of porous constructs at any number of cycles decreased with thinner struts, as expected. This trend agrees with previously reported studies dealing with fatigue loading of porous titanium alloy constructs (Liu et al., 2020, Dallago et al., 2018a, Zhao et al., 2016, Yavari et al., 2015, Yavari et al., 2013, Ahmadi et al., 2019). Unlike other studies, we found that the normalized flexural fatigue strength was also affected by the porosity of the constructs. This is in contrast with results of studies conducted by Yavari, et al. (2013, 2015) and Zhao et al. (2016) where constructs with the same pore shape were found to have the same normalized compression fatigue strength ratio regardless of the porosity or strut thickness.

4.5.4 Potential of application in maxillofacial and orthopedic reconstruction

The porous constructs designed in this study have the potential to endure cyclic loading. However, it should be noted that the number of cycles applied on the constructs was limited to 10^6 cycles, equivalent to about 2 years of mastication loading, assuming that the average yearly number of chewing cycles of an individual is 5×10^5 (Po et al., 2011, van der Bilt et al., 2006, Chen, 2012, Farooq and Sazonov, 2016). The fatigue numerical models that were developed in this study have the potential to predict the behaviour of porous constructs under cyclic loading for a longer period than normally used in real-life tests. This gives the potential for the described numerical models to be used in determining the fatigue strength of SLM-built maxillofacial implants.

4.5.5 Limitations of numerical modelling of cyclic loading

The numerical models used in this study were representative of real-life applications. However, some assumptions might have affected the accuracy of these models. The first assumption was that SLM-built Ti6Al4V constructs were isotropic, which is an oversimplification of what is reported in the literature (Tan et al., 2017, Gong et al., 2015, Murr et al., 2012). The second assumption was that the strut geometry in both SLM-built porous constructs and porous FEA models matched each other. However, SLM-built porous constructs had variations in strut thickness and cross-sectional shapes, when compared to the CAD models used to build these constructs (Vrana et al., 2022). In addition, there were high levels of variability of the density within the struts due to the unavoidable temperature variability within the melt pool during the process of SLM printing (Shiple et al., 2018, Tian et al., 2017, Dallago et al., 2018b). This structural feature was not represented in the FEA models, which assumed a homogenous internal structure within the struts. The third assumption was that of full adhesion at the bone-construct interface. Hence, frictional forces were not considered in the design of the bone-construct model.

4.6 Conclusion

The mechanical properties and fatigue behaviour of porous Ti6Al4V constructs were studied. In addition, numerical models were developed to predict the fatigue strength of constructs manufactured using SLM. These models would allow medical implant designers to effectively and swiftly evaluate the properties of porous constructs intended for use in mandibular reconstruction. The outcomes of the investigation can be summarized as follows:

1. Strut thickness and porosity had a direct effect on both the yield-normalized fatigue stress-versus number of cycles curves and the maximum flexural stress versus -number of cycles curves of porous constructs.
2. Fatigue numerical models utilizing the Brown-Miller theorem with Morrow's correction provided accurate fatigue strength predictions for the flexural cyclic loading of porous SLM-built constructs.
3. Calibrating the fatigue parameters of the numerical models to those of the SLM-built constructs provided an accurate prediction of their fatigue strength (deviation $\approx 10\%$).
4. Fractures of SLM-built porous constructs occurred at strut junctions. They appeared to initiate from the surface of constructs and likely propagated due to the existence of internal defects and reduced ductility.
5. Bone ingrowth eliminated the pores within the constructs, therefore resulted in higher fatigue strength.

4.7 References used in this chapter

- AHMADI, S. M., HEDAYATI, R., LI, Y., LIETAERT, K., TÜMER, N., FATEMI, A., RANS, C. D., POURAN, B., WEINANS, H. & ZADPOOR, A. A. 2018. Fatigue performance of additively manufactured meta-biomaterials: The effects of topology and material type. *Acta Biomaterialia*, 65, 292--304.
- AHMADI, S. M., KUMAR, R., BORISOV, E. V., PETROV, R., LEEFLANG, S., LI, Y., TUMER, N., HUIZENGA, R., AYAS, C., ZADPOOR, A. A. & POPOVICH, V.

- A. 2019. From microstructural design to surface engineering: A tailored approach for improving fatigue life of additively manufactured meta-biomaterials. *Acta Biomaterialia*, 83, 153-166.
- AS, S., SKALLERUD, B. & TVEITEN, B. 2008. Surface roughness characterization for fatigue life predictions using finite element analysis. *International Journal of Fatigue*, 30, 2200-2209.
- ASTM, I. 2014. E290-14: Standard Test Methods for Bend Testing of Material for Ductility. West Conshohocken, PA: ASTM International.
- ATTAR, H., BÖNISCH, M., CALIN, M., ZHANG, L.-C., SCUDINO, S. & ECKERT, J. 2014. Selective laser melting of in situ titanium–titanium boride composites: Processing, microstructure and mechanical properties. *Acta Materialia*, 76, 13--22.
- BASQUIN, O. The exponential law of endurance tests. *Proc Am Soc Test Mater*, 1910. 625-630.
- BATHIAS, C. & PINEAU, A. 2013. *Fatigue of materials and structures: applications to design and damage*, Wiley-Blackwell.
- BÄUMEL, A., SEEGER, T. & BOLLER, C. 1990. *Materials data for cyclic loading*, Amsterdam, Elsevier.
- BELAN, J., KUCHARIKOVÁ, L., TILLOVÁ, E. & CHALUPOVÁ, M. 2019. Three-Point Bending Fatigue Test of TiAl6V4 Titanium Alloy at Room Temperature. *Advances in Materials Science and Engineering*, 2019, 1-11.
- BENADY, A., MEYER, S. J., GOLDEN, E., DADIA, S. & KATARIVAS LEVY, G. 2023. Patient-specific Ti-6Al-4V lattice implants for critical-sized load-bearing bone defects reconstruction. *Materials & Design*, 226, 111605.
- BROWN, M. W. & MILLER, K. J. 1973. A Theory for Fatigue Failure under Multiaxial Stress-Strain Conditions. *Proceedings of the Institution of Mechanical Engineers*, 187, 745-755.
- CAO, X., XU, L., XU, X. & WANG, Q. 2018. Fatigue Fracture Characteristics of Ti6Al4V Subjected to Ultrasonic Nanocrystal Surface Modification. *Metals*, 8.
- CHAN, T. K.-C. 2013. *A Practical Simulation Methodology to Improve Fatigue Life Prediction of Engine Oil Cooler Undergoing Pressure Cycle Testing*. Master of Applied Science, McMaster University.
- CHECA, S., PRENDERGAST, P. J. & DUDA, G. N. 2011. Inter-species investigation of the mechano-regulation of bone healing: comparison of secondary bone healing in sheep and rat. *J Biomech*, 44, 1237-45.
- CHEN, C., HAO, Y., BAI, X., NI, J., CHUNG, S.-M., LIU, F. & LEE, I.-S. 2019. 3D printed porous Ti6Al4V cage: Effects of additive angle on surface properties and biocompatibility; bone ingrowth in Beagle tibia model. *Materials & Design*, 175, 107824.

- CHEN, L. 2012. Finite Element Analysis of the Stress on the Implant-Bone Interface of Dental Implants with Different Structures. *Finite Element Analysis - New Trends and Developments*. Intech.
- DALLAGO, M., FONTANARI, V., TORRESANI, E., LEONI, M., PEDERZOLLI, C., POTRICH, C. & BENEDETTI, M. 2018a. Fatigue and biological properties of Ti-6Al-4V ELI cellular structures with variously arranged cubic cells made by selective laser melting. *J Mech Behav Biomed Mater*, 78, 381-394.
- DALLAGO, M., ZANINI, F., CARMIGNATO, S., PASINI, D. & BENEDETTI, M. Effect of the geometrical defectiveness on the mechanical properties of SLM biomedical Ti6Al4V lattices. ECF22 - Loading and Environmental effects on Structural Integrity, 2018b. *Procedia Structural Integrity*, 161-167.
- DENG, F., LIU, L., LI, Z. & LIU, J. 2021. 3D printed Ti6Al4V bone scaffolds with different pore structure effects on bone ingrowth. *J Biol Eng*, 15, 4.
- DOWNING, S. D. & SOCIE, D. F. 1982. Simple rainflow counting algorithms. *International Journal of Fatigue*, 4, 31-40.
- DU, L., QIAN, G., ZHENG, L. & HONG, Y. 2020. Influence of processing parameters of selective laser melting on high-cycle and very-high-cycle fatigue behaviour of Ti-6Al-4V. *Fatigue & Fracture of Engineering Materials & Structures*, 44, 240-256.
- DU PLESSIS, A., RAZAVI, S. M. J. & BERTO, F. 2020a. The effects of microporosity in struts of gyroid lattice structures produced by laser powder bed fusion. *Materials & Design*, 194.
- DU PLESSIS, A., YADROITSAVA, I. & YADROITSEV, I. 2020b. Effects of defects on mechanical properties in metal additive manufacturing: A review focusing on X-ray tomography insights. *Materials & Design*, 187.
- DUAN, Y., GONZALEZ, J. A., KULKARNI, P. A., NAGY, W. W. & GRIGGS, J. A. 2018. Fatigue lifetime prediction of a reduced-diameter dental implant system: Numerical and experimental study. *Dent Mater*, 34, 1299-1309.
- FAROOQ, M. & SAZONOV, E. 2016. Automatic Measurement of Chew Count and Chewing Rate during Food Intake. *Electronics (Basel)*, 5.
- FERRARIO, V., SFORZA, C., SERRAO, G., DELLAVIA, C. & TARTAGLIA, G. 2004. Single tooth bite forces in healthy young adults. *Journal of oral rehabilitation*, 31, 18-22.
- FERTIG, R. & KENIK, D. 2011. Predicting Composite Fatigue Life Using Constituent-Level Physics. 52nd AIAA/ASME/ASCE/AHS/ASC Structures, Structural Dynamics and Materials Conference. Denver, Colorado.
- GAO, H., LI, X., WANG, C., JI, P. & WANG, C. 2019. Mechanobiologically optimization of a 3D titanium-mesh implant for mandibular large defect: A simulated study. *Mater Sci Eng C Mater Biol Appl*, 104, 109934.

- GHOLAMPOUR, S., GHOLAMPOUR, H. & KHANMOHAMMADI, H. 2019. Finite element analysis of occlusal splint therapy in patients with bruxism. *BMC Oral Health*, 19, 205.
- GHOSH, A., KUMAR, A., WANG, X., KIETZIG, A.-M. & BROCHU, M. 2022. Analysis of the effect of surface morphology on tensile behavior of LPBF SS316L microstruts. *Materials Science and Engineering: A*, 831.
- GONG, H., RAFI, K., GU, H., JANAKI RAM, G. D., STARR, T. & STUCKER, B. 2015. Influence of defects on mechanical properties of Ti-6Al-4V components produced by selective laser melting and electron beam melting. *Materials & Design*, 86, 545-554.
- HEINZ, S. & EIFLER, D. 2016. Crack initiation mechanisms of Ti6Al4V in the very high cycle fatigue regime. *International Journal of Fatigue*, 93, 301-308.
- HITCHON, S. 2022. Mechanical Evaluation of Gyroid Structures to Combat Orthopaedic Implant Infections. Masters Thesis, The University of Western Ontario.
- HOFMANN, A. A., BLOEBAUM, R. D. & BACHUS, K. N. 1997. Progression of human bone ingrowth into porous-coated implants. Rate of bone ingrowth in humans. *Acta Orthop Scand*, 68, 161-6.
- HU, Y. N., WU, S. C., WITHERS, P. J., ZHANG, J., BAO, H. Y. X., FU, Y. N. & KANG, G. Z. 2020. The effect of manufacturing defects on the fatigue life of selective laser melted Ti-6Al-4V structures. *Materials & Design*, 192.
- INCE, A. 2017. A mean stress correction model for tensile and compressive mean stress fatigue loadings. *Fatigue & Fracture of Engineering Materials & Structures*, 40, 939-948.
- INTERNATIONAL, A. 2021. D7264/D7264M-21 Standard Test Method for Flexural Properties of Polymer Matrix Composite Materials. West Conshohocken, PA: ASTM International.
- KANDIL, F. A., BROWN, M. W. & MILLER, K. J. 1982. *Biaxial Low Cycle Fatigue Fracture Of 316 Stainless Steel At Elevated Temperatures*. London, United Kingdom. The Metals Society.
- KUN, F., CARMONA, H. A., ANDRADE, J. S., JR. & HERRMANN, H. J. 2008. Universality behind Basquin's Law of Fatigue. *Phys Rev Lett*, 100, 094301.
- LEUDERS, S., THÖNE, M., RIEMER, A., NIENDORF, T., TRÖSTER, T., RICHARD, H. A. & MAIER, H. J. 2013. On the mechanical behaviour of titanium alloy TiAl6V4 manufactured by selective laser melting: Fatigue resistance and crack growth performance. *International Journal of Fatigue*, 48, 300--307.

- LIU, Y. J., REN, D. C., LI, S. J., WANG, H., ZHANG, L. C. & SERCOMBE, T. B. 2020. Enhanced fatigue characteristics of a topology-optimized porous titanium structure produced by selective laser melting. *Additive Manufacturing*, 32.
- MINER, M. A. 1945. Cumulative Damage in Fatigue. *Journal of Applied Mechanics*, 12, A159-A164.
- MORROW, J. D. 1968. Fatigue properties of metals. In: HALFORD, G. R. & GALLAGHER, J. P. (eds.) *Fatigue Design Handbook*. Warrendale, PA, United States: SAE.
- MURR, L. E., GAYTAN, S. M., RAMIREZ, D. A., MARTINEZ, E., HERNANDEZ, J., AMATO, K. N., SHINDO, P. W., MEDINA, F. R. & WICKER, R. B. 2012. Metal Fabrication by Additive Manufacturing Using Laser and Electron Beam Melting Technologies. *Journal of Materials Science & Technology*, 28, 1-14.
- NAGASAO, T., MIYAMOTO, J. & KAWANA, H. 2009. Biomechanical evaluation of implant placement in the reconstructed mandible. *Int J Oral Maxillofac Implants*, 24, 999-1005.
- NAKHAEI, M., STERBA, M., FOLETTI, J. M., BADIH, L. & BEHR, M. 2023. Experimental analysis and numerical fatigue life prediction of 3D-Printed osteosynthesis plates. *Front Bioeng Biotechnol*, 11, 1133869.
- PENG, C., TRAN, P., NGUYEN-XUAN, H. & FERREIRA, A. J. M. 2020. Mechanical performance and fatigue life prediction of lattice structures: Parametric computational approach. *Composite Structures*, 235, 111821.
- PENG, W. M., CHENG, K. J., LIU, Y. F., NIZZA, M., BAUR, D. A., JIANG, X. F. & DONG, X. T. 2021. Biomechanical and Mechanostat analysis of a titanium layered porous implant for mandibular reconstruction: The effect of the topology optimization design. *Mater Sci Eng C*, 124, 112056.
- PETERS, M. & LEYENS, C. 2003. *Titanium Alloys: Fundamentals and Applications*, Weinheim, Germany, WILEY-VCH Verlag GmbH & Co. KGaA.
- PILKEY, W. D. 1997. *Peterson's stress concentration factors*, John Wiley & Sons, INC.
- PINHEIRO, M. & ALVES, J. L. 2015. The feasibility of a custom-made endoprosthesis in mandibular reconstruction: Implant design and finite element analysis. *J Craniomaxillofac Surg*, 43, 2116-28.
- PO, J. M., KIESER, J. A., GALLO, L. M., TESENYI, A. J., HERBISON, P. & FARELLA, M. 2011. Time-frequency analysis of chewing activity in the natural environment. *J Dent Res*, 90, 1206-10.
- RAGHAVENDRA, S., DALLAGO, M., ZANINI, F., CARMIGNATO, S., BERTO, F. & BENEDETTI, M. 2023. A probabilistic average strain energy density approach to assess the fatigue strength of additively manufactured cellular lattice materials. *International Journal of Fatigue*, 172.

- RITCHIE, R. O., DAVIDSON, D. L., BOYCE, B. L., CAMPBELL, J. P. & RODER, O. 1999. High-cycle fatigue of Ti-6Al-4V. *Fatigue & Fracture of Engineering Materials & Structures*, 22, 621-631.
- SABOUR, M. H. 2013. Fatigue. In: WANG, Q. J. & CHUNG, Y.-W. (eds.) *Encyclopedia of Tribology*. Boston, MA: Springer US.
- SESSLE, B. J. 2014. Neural Basis of Oral and Facial Function. Reference Module in Biomedical Sciences. Elsevier.
- SHI, Q., SUN, Y., YANG, S., VAN DESSEL, J., LÜBBERS, H.-T., ZHONG, S., GU, Y., BILA, M., DORMAAR, T., SCHOENAERS, J. & POLITIS, C. 2021. Failure analysis of an in-vivo fractured patient-specific Ti6Al4V mandible reconstruction plate fabricated by selective laser melting. *Engineering Failure Analysis*, 124.
- SHIPLEY, H., MCDONNELL, D., CULLETON, M., COULL, R., LUPOI, R., O'DONNELL, G. & TRIMBLE, D. 2018. Optimisation of process parameters to address fundamental challenges during selective laser melting of Ti-6Al-4V: A review. *International Journal of Machine Tools and Manufacture*, 128, 1-20.
- SHUNMUGAVEL, M., POLISHETTY, A. & LITTLEFAIR, G. 2015. Microstructure and Mechanical Properties of Wrought and Additive Manufactured Ti-6Al-4V Cylindrical Bars. *Procedia Technology*, 20, 231-236.
- SIDAMBE, A. T. 2014. Biocompatibility of Advanced Manufactured Titanium Implants- A Review. *Materials (Basel)*, 7, 8168-8188.
- SIMULIA 2020. Simulia FE-Safe 2020: Fatigue Theory Reference, Daussault Systemes,.
- SONG, J., TANG, Q., FENG, Q., MA, S., GUO, F. & HAN, Q. 2021. Investigation on the modelling approach for variable-density lattice structures fabricated using selective laser melting. *Materials & Design*, 212, 110236.
- TAN, X. P., TAN, Y. J., CHOW, C. S. L., TOR, S. B. & YEONG, W. Y. 2017. Metallic powder-bed based 3D printing of cellular scaffolds for orthopaedic implants: A state-of-the-art review on manufacturing, topological design, mechanical properties and biocompatibility. *Mater Sci Eng C* 76, 1328-1343.
- TANIGUCHI, N., FUJIBAYASHI, S., TAKEMOTO, M., SASAKI, K., OTSUKI, B., NAKAMURA, T., MATSUSHITA, T., KOKUBO, T. & MATSUDA, S. 2016. Effect of pore size on bone ingrowth into porous titanium implants fabricated by additive manufacturing: An in vivo experiment. *Mater Sci Eng C* 59, 690-701.
- TIAN, Y., TOMUS, D., ROMETSCH, P. & WU, X. 2017. Influences of processing parameters on surface roughness of Hastelloy X produced by selective laser melting. *Additive Manufacturing*, 13, 103-112.
- VAN BAELE, S., CHAI, Y. C., TRUSCELLO, S., MOESEN, M., KERCKHOFS, G., VAN OOSTERWYCK, H., KRUTH, J. P. & SCHROOTEN, J. 2012. The effect of pore geometry on the in vitro biological behavior of human periosteum-derived cells

- seeded on selective laser-melted Ti6Al4V bone scaffolds. *Acta Biomater*, 8, 2824-34.
- VAN DER BILT, A., ENGELEN, L., PEREIRA, L. J. & VAN DER GLAS, H. W. 2006. Chewing performance before and after rehabilitation of complete dentures. *Journal of Dental Research*, 85, 613-7.
- VAN EIJDEN, T. M. 2000. Biomechanics of the mandible. *Critical Reviews in Oral Biology & Medicine*, 11, 123-136.
- VRANA, R., KOUTECKY, T., CERVINEK, O., ZIKMUND, T., PANTELEJEV, L., KAISER, J. & KOUTNY, D. 2022. Deviations of the SLM Produced Lattice Structures and Their Influence on Mechanical Properties. *Materials (Basel)*, 15, 3144.
- WALTIMO, A. & KÖNÖNEN, M. 1993. A novel bite force recorder and maximal isometric bite force values for healthy young adults. *Scand J Dent Res*, 101, 171-5.
- WARNKE, P. H., DOUGLAS, T., WOLLNY, P., SHERRY, E., STEINER, M., GALONSKA, S., BECKER, S. T., SPRINGER, I. N., WILTFANG, J. & SIVANANTHAN, S. 2009. Rapid prototyping: porous titanium alloy scaffolds produced by selective laser melting for bone tissue engineering. *Tissue Eng Part C Methods*, 15, 115-24.
- WATANABE, R., TAKAHASHI, H., MATSUGAKI, A., UEMUKAI, T., KOGAI, Y., IMAGAMA, T., YUKATA, K., NAKANO, T. & SAKAI, T. 2023. Novel nano-hydroxyapatite coating of additively manufactured three-dimensional porous implants improves bone ingrowth and initial fixation. *J Biomed Mater Res B Appl Biomater*, 111, 453-462.
- WICKMANN, C., BENZ, C., HEYER, H., WITTE-BODNAR, K., SCHAFER, J. & SANDER, M. 2021. Internal Crack Initiation and Growth Starting from Artificially Generated Defects in Additively Manufactured Ti6Al4V Specimen in the VHCF Regime. *Materials (Basel)*, 14.
- WONG, R. C., TIDEMAN, H., MERKX, M. A., JANSEN, J. & GOH, S. M. 2012. The modular endoprosthesis for mandibular body replacement. Part 1: mechanical testing of the reconstruction. *J Craniomaxillofac Surg*, 40, e479-86.
- WONG, R. C. W., LOH, J. S. P. & ISLAM, I. 2016. The Role of Finite Element Analysis in Studying Potential Failure of Mandibular Reconstruction Methods. *Perusal of the Finite Element Method*.
- YÁNEZ, A., FIORUCCI, M. P., CUADRADO, A., MARTEL, O. & MONOPOLI, D. 2020. Surface roughness effects on the fatigue behaviour of gyroid cellular structures obtained by additive manufacturing. *International Journal of Fatigue*, 138, 105702.
- YAVARI, S. A., AHMADI, S. M., WAUTHLE, R., POURAN, B., SCHROOTEN, J., WEINANS, H. & ZADPOOR, A. A. 2015. Relationship between unit cell type and

porosity and the fatigue behavior of selective laser melted meta-biomaterials. *Journal of the Mechanical Behavior of Biomedical Materials*, 43, 91--100.

- YAVARI, S. A., WAUTHLE, R., STOK, J. V. D., RIEMSLAG, A. C., JANSSEN, M., MULIER, M., KRUTH, J. P., SCHROOTEN, J., WEINANS, H. & ZADPOOR, A. A. 2013. Fatigue behavior of porous biomaterials manufactured using selective laser melting. *Materials Science and Engineering: C*, 33, 4849--4858.
- ZHANG, L.-C. & ATTAR, H. 2016. Selective Laser Melting of Titanium Alloys and Titanium Matrix Composites for Biomedical Applications: A Review *Advanced Engineering Materials*, 18, 463-475.
- ZHANG, P., HE, A. N., LIU, F., ZHANG, K., JIANG, J. & ZHANG, D. Z. 2019. Evaluation of Low Cycle Fatigue Performance of Selective Laser Melted Titanium Alloy Ti-6Al-4V. *Metals*, 9.
- ZHAO, E., ZHOU, Q., QU, W. & WANG, W. 2020. Fatigue Properties Estimation and Life Prediction for Steels under Axial, Torsional, and In-Phase Loading. *Advances in Materials Science and Engineering*, 2020, 1-8.
- ZHAO, S., LI, S. J., HOU, W. T., HAO, Y. L., YANG, R. & MISRA, R. D. K. 2016. The influence of cell morphology on the compressive fatigue behavior of Ti-6Al-4V meshes fabricated by electron beam melting. *J Mech Behav Biomed Mater*, 59, 251-264.

Chapter 5

Numerical modelling of porous Ti6Al4V implant for mandibular reconstruction

This chapter was adapted from the manuscript: Hijazi, K. M., Mao, H., Holdsworth, D. W., Dixon, S. J., Armstrong, J. E. & Rizkalla, A. S. Prototype Design of Porous Ti6Al4V Intraosseous Implant for Use in Mandibular Reconstruction [Unpublished results].

Chapter 5

5 Numerical modelling of porous Ti6Al4V implant for mandibular reconstruction

5.1 Summary

The design of patient-specific implants often requires the utilization of computer simulations for the characterization of mechanical properties before manufacturing. This step is of great significance when considering the mechanical properties and structural imperfections of additively manufactured implants. We have previously developed numerical models to predict the static and dynamic mechanical properties of porous Ti6Al4V constructs built using selective laser melting (SLM). In the present study, we developed a patient-specific intraosseous mandibular implant based on the models and techniques described in our previous research. The implant model used a simple cubic porous design with an average unit cell size of 1 mm and strut thicknesses ranging between 350 and 450 μm . The overall design of the implant was based on a human mandible model. Finite element analysis was used to simulate right molar clenching on the mandible with and without the implant, under static and dynamic loading conditions. The simulation study showed that the designed implant would remain intact during right molar clenching and should not cause stress shielding. The fatigue numerical models predicted that the implant would be able to remain functional under cyclic masticatory forces (50 - 100 N) for a period ranging between 4 and 119 years. Given that, within a year, bone ingrowth and osseointegration is complete, the implant is predicted to remain intact long-term under physiological loading conditions. The findings of this study demonstrate the potential of computational modelling in developing designs for porous implants built through SLM.

5.2 Introduction

Mandibular reconstruction often involves resecting defective parts of the bone and bridging the gap using a graft (Batstone, 2018). Mandibular grafts are usually fixed in place with metal plates, often made of titanium/aluminum/vanadium alloy (90% titanium, 6% aluminum, and 4% vanadium; abbreviated Ti6Al4V). The plates are then screwed into the remaining mandibular bone (Smolka et al., 2008). This procedure has been highly successful, according to different studies (Kakarala et al., 2018, Keller et al., 1998). However, they are associated with multiple problems. These include incorrect utilization, deployment, or selection of fixation devices, leading to non-union (Perez and Ellis, 2020) or malunions (Pickrell et al., 2017) of bones. Moreover, pre-operative manual bending of the implant, which is normally done to fit the bone contour, has been shown can exacerbate fatigue failures (van Kootwijk et al., 2022, Zeller et al., 2020). Other complications can include poor shape post-surgery, collateral damage, loss of physiological function at the donor site, infection, and compromised vascularization at the donor site as well as at the mandible (Chapter 1). Finally, the use of stiff fixation devices may reduce the stress applied on the bone. Given that bone growth and remodelling are triggered by loading, this may lead to the loss of bone density (Frost, 1987), which in turn may cause the loosening and failure of the fixation devices. This phenomenon is known as stress shielding (Kennady et al., 1989b, Kennady et al., 1989a, Zoumalan et al., 2009, Zhou et al., 2010).

A modern alternative to bone grafting and fixation involves the patient-specific porous intraosseous implants consisting of either a crib or a cage design with fixation elements (Peng et al., 2021, van Kootwijk et al., 2022). The design process of these implants often involves medical imaging, usually computed tomography (CT), of the mandibular bone (van Kootwijk et al., 2022, Peng et al., 2021). Mirror reconstruction is used to rebuild the defective part of the bone from the unaffected side of the mandible (Moiduddin et al., 2019). Metal powder-bed fusion additive manufacturing techniques, such as selective laser melting (SLM) can then be used to build these implants (Eshkalak et al., 2020). Introducing pores with optimized size, shape, and strut thickness permit matching the stiffness of the SLM-built constructs to that of bone (van Kootwijk et al., 2022, Zeller et al., 2020). In

addition, matching the shape of the implant to that of the missing bone might help avoid misalignment that can lead to non-union or malunion of the bone.

Finite element analysis (FEA) was utilized in the creation of computer simulation models to test the structural integrity of implants (Peng et al., 2021, van Kootwijk et al., 2022). This is a very important step in the design and development of implants as it allows determination of flaws in the design prior to manufacturing. In a previous work, we built a series of porous constructs, using SLM, with different strut thicknesses and then applied flexural and tensile loading to these constructs. It was determined that Ti6Al4V constructs with strut thicknesses ranging between 350 and 450 μm and unit cell size of 1 mm have mechanical properties that match those of cortical bone (Chapter 3). The corresponding pore size (ranging between 550 and 650 μm) and simple cubic pore shape are known to be ideal for bone ingrowth (Kovacs et al., 2023, Taniguchi et al., 2016). In addition, the material properties of Ti6Al4V were measured from tensile tests on non-porous Ti6Al4V and used to build FEA-based static numerical models of the porous constructs. These models were found to match the strength and stiffness of the elastic region of SLM-built porous constructs (deviation $< 11\%$). In summary, we showed that, within the elastic region of loading, our FEA-based static numerical models were highly accurate in predicting the mechanical properties of SLM-built porous constructs.

It should be noted that static mechanical tests do not tell the whole story, as mandibles experience repetitive force application of approximately 500,000 times per year (Farooq and Sazonov, 2016, Po et al., 2011). Others have shown that porous SLM-built Ti6Al4V constructs are prone to fatigue failure due to inherent low strength, internal defects, surface roughness, and residual stresses (Liu et al., 2020, Ahmadi et al., 2019). Until recently, most measurements of the fatigue strength of SLM-built porous constructs were performed using compression or push-pull loading conditions. Recently, we applied flexural (three-point bending) cyclic loading to SLM-built porous constructs with either 350 or 450 μm strut thickness and unit cell size of 1 mm (Chapter 4). This was done since mandibles also experience bending deformation during mastication (van Eijden, 2000). Because of the long time and expense in testing these constructs, we also developed FEA-based dynamic numerical models to predict the flexural cyclic loading behaviour of porous Ti6Al4V

constructs. Instead of introducing the structural defects seen in SLM-built constructs, we adjusted fatigue parameters to simulate the effect of defects on the cyclic flexural behaviour of the models (Chapter 3). Our dynamic numerical models accurately predicted the fatigue behaviour of SLM-built porous constructs with average deviation $\approx 10\%$.

Hence, it can be seen from both our previous studies (Chapters 3 and 4) that FEA-based static and dynamic numerical models can produce accurate predictions of the mechanical properties of SLM-built porous constructs. These models can be developed quickly using conventional desktop computers. These advances have the potential to expediate the design of novel patient-specific implants that could then be built within a short period of time using SLM. The present study extends this work to demonstrate how our FEA-based numerical modelling methods can be used to design a novel intraosseous porous implant. Its static and dynamic mechanical properties, structural integrity, and fatigue life were determined using the FEA numerical models.

5.3 Material and Methods

5.3.1 Creation of the mandible and implant models

5.3.1.1 CT imaging and segmentation

Computed tomography (CT) images of a dried adult mandible in transverse planes were acquired from Robarts Research Institute (London, ON, Canada). The thickness of the slices used in the imaging process was 0.156 mm. The density of the voxels was recorded in Hounsfield units (HU). The HU scale is dimensionless, and used to denote radiodensity readings, where water at standard temperature and pressure is set at 0 HU, and air is set at -1000 HU (DenOtter and Schubert, 2022). The CT images were exported to the ORS Dragonfly software package (Object Research Systems, Montreal, QC, Canada), where a 3D image of the mandible was created from the CT images. Two ROIs were segmented and stored from the model of the mandible: the enamel region and the bone/dentine region. These ROIs were discretized where the bone, dentine and marrow spaces were defined as $HU < 3300$ and dental enamel as $HU > 3300$ (Figure 5-1). The mandibular model was converted into stereolithography (STL) mesh models.

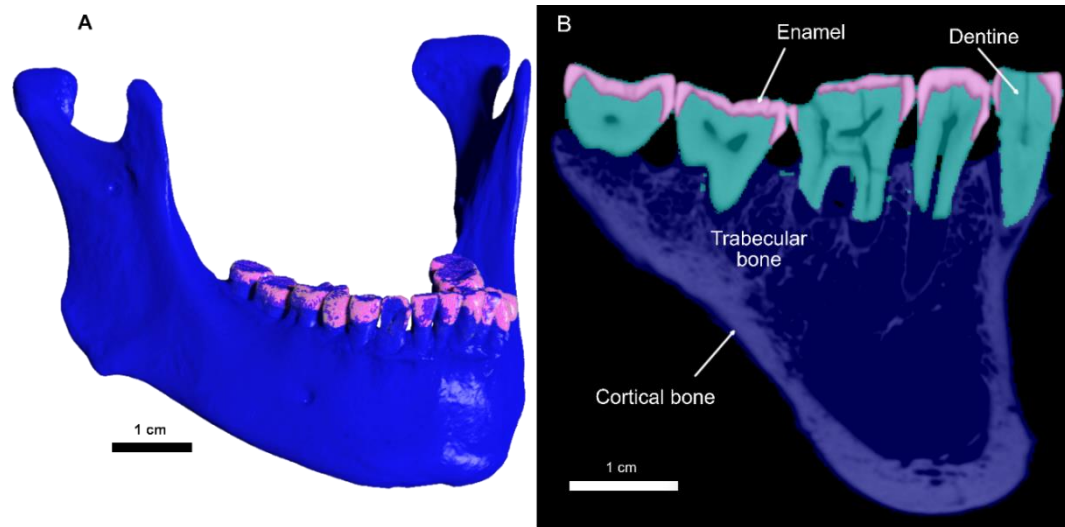


Figure 5-1: 3D image of the mandible generated from the CT images.

(A) 3D reconstruction of the mandible generated from the CT images. The mandibular bone and dentine are pseudocoloured blue, and the enamel is coloured pink. (B) An oblique CT section through the mandibular body. The bone is coloured light blue, the dentine is coloured green, and the enamel is coloured pink.

5.3.1.2 CAD models of the mandible and the intraosseous implant in the mandible

The STL mandibular model, created from CT images, was imported into the CAD software nTop 4.8 (nTop Inc., New York, NY, USA). This software allowed us to create FEA models. A systematic process of multiple steps was used to create the FEA models (Figure 5-2). A Gaussian image filter, with a domain of 0.125 mm in span length, was applied to the mandibular model to remove small artifacts and irregularities. The ROIs found in the image segmentation process were used to identify and designate the elements that represented enamel and bone/dentine in the FEA model. These parts were combined into the mandibular model, which was the first model used in the FEA analysis.

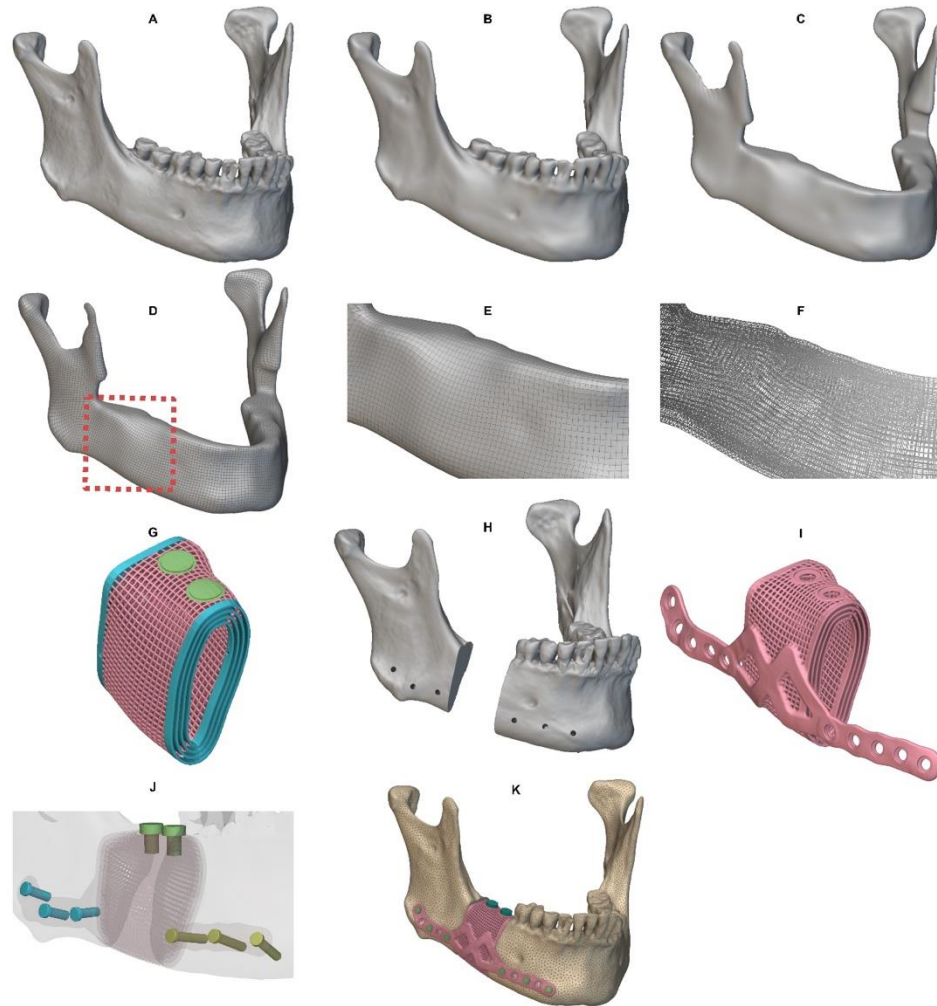


Figure 5-2: The process of creating the Mandible and IO-mandible models used in the FEA analysis.

The initial mandible model created from CT images was imported to nTop (A). The model is then smoothed using a Gaussian image filter (B). This model represents the mandible model, which is then discretized and stored. The crowns of the teeth and the superior aspect of the alveolar process were then removed, followed by another round of image filtering (C). A quadratic surface mesh, with unit cell size ≈ 1 mm, was created along the model (D). The hashed orange box represents the region shown in greater detail in (E). This surface mesh was used as the basis to create grid map that followed the surface mesh and was offset inwards by 3 mm, with each layer being 1 mm away from the other (F). The grid map was then used as to create the porous body of the intraosseous implant (G) The porous model consists of the pores (pink), the connector between the bone and the porous model (blue) and placeholders for the dental implants (green on superior surface). At the same time, a segment of the bone was removed from the right side of the mandibular body, representing the surgical osteotomy (H). Holes were also created in the bone to replicate the surgical drill holes. The porous part from step G was then fused with a fixation bar and holes were created to place the dental implants on the intraosseous implant (I). Dental implant and screw models were then created and placed into the bone model from step I (J). Holes are created within the implant and bones to fit

the screws and dental implant models. Finally, the model is discretized into elements and saved as the implant-mandible model (K).

Using the mandible model, the intraosseous implant was created with the same contour as that of the original bone (Figure 5-2). The intraosseous implant system consisted of a porous body, fixation plate, fixation screws, and dental implants (Figure 5-3). The crowns of the teeth and the superior aspect of the alveolar process were removed from the mandible (Figure 5-2 A-C). The resulting bone model was smoothed, and a square grid map was created on the surface of the mandible, with each square grid having a target span length of 1 mm (Figure 5-2 D-E). This grid map was then offset inwards three times, creating a 3 mm thick cubic grid cells with each layer being 1 mm away from the other (Figure 5-2 F). These cubic grid cells were converted to porous models with simple cubic cell shapes by thickening the edges of the grid with a gradient between 350 μm in the inner struts and 450 μm in the outer struts.

To simulate surgical mandibular resection, a portion of the bone was removed and replaced with the porous model (Figure 5-2 H). A similarly sized piece of the porous model was extracted and fused with the fixation plate, which was designed to follow the contour of the buccal inferior region of the mandible (Figure 5-2 I). This porous model had some open-ended struts, which are not ideal. To correct this issue, all the open-ended struts at the ends of porous model were removed. The gap between the porous model and the bone was then replaced with three concentric plates that were nested 1 mm away from each other (indicated in blue in Figure 5-2 G). These plates had a thickness equal to that of the adjacent struts. This part of the model is the connector between the porous model and the adjacent bones. The porous model was then fixed using six unthreaded bicortical screw models that were placed in the holes created along the fixation plate and the mandibular bone (Figure 5-2 J). Note that the screws were unthreaded for simplicity. Dental implant models were created on the top of the porous model at sites where the molar teeth were originally located, and holes were created in the porous model to accommodate them.

All the models were discretized into quadratic tetrahedral meshes (C3D10). The implant-mandible model had a maximum element size of 0.35 mm, the screw and dental implant

models had a maximum element size of 0.25 mm each, and the bone/dentine/enamel region had a maximum element size of 0.5 mm (Figure 5-3).

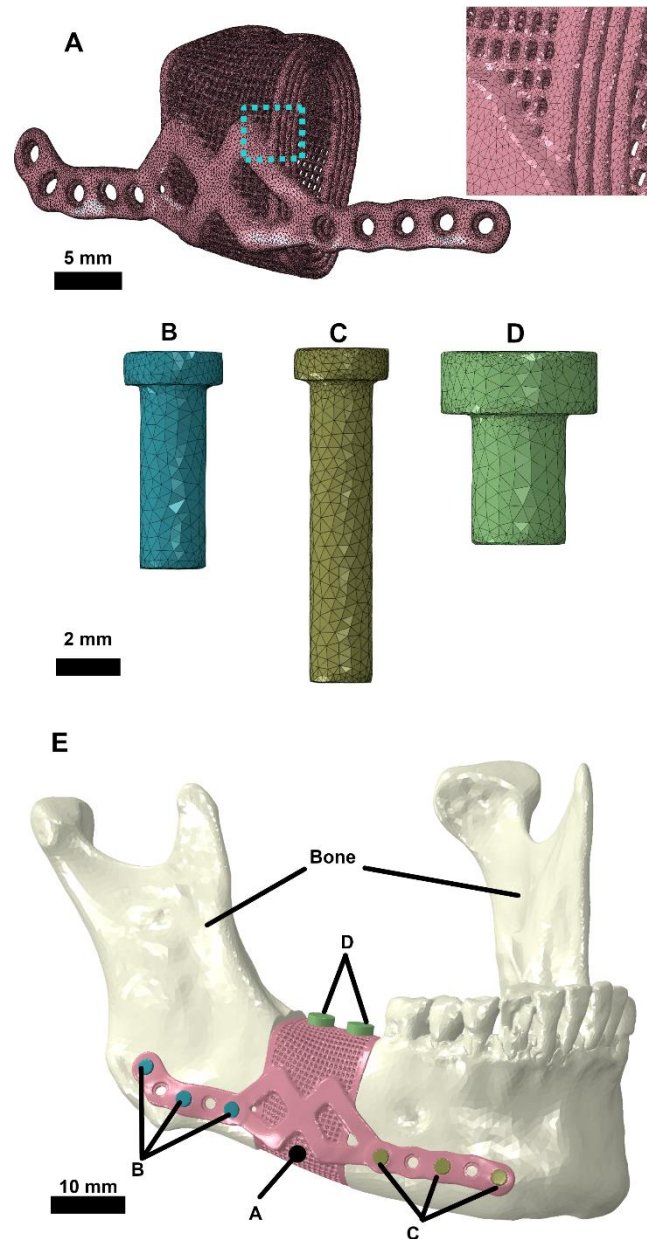


Figure 5-3: The components of the intraosseous implant system.

All the models are discretized using quadratic tetrahedral (C3D10) mesh elements. (A) The intraosseous implant is shown from the oblique view. The region outlined by dashed lines is shown enlarged at the right. This region includes pores, a portion of the concentric plates, and part of the fixation bar. The surface mesh elements are shown, with finer elements along the struts, intermediate elements along the concentric plates, and larger elements along the fixation bar. Two kinds of fixation bicortical screws were modelled, each with

different lengths and the same diameter of 2 mm, the first (B) have a total length of 6 mm and are placed in the posterior portion of the implant, and the second (C) have a total length of 10 mm and are placed in the anterior portion of the implant. (D) The dental implants in the intraosseous implant system were modelled with length of 6 mm and shaft diameter of 3 mm. (E) The assembly of the implant-mandible model is shown with all the parts labeled.

5.3.2 Material properties

The bone and dentine material properties were analyzed as follows. A custom-designed script was used to match the elements of the mandible model with relevant HU radiodensity. This matching was done according to the location of the elements. Each of the HU density values was then converted to ash density (ρ_{ash}) using the following linear relationship:

$$\rho_{\text{ash}} = 0.0003 \text{ HU} + 0.34 \quad -1000 \leq \text{HU} \leq 3300 \quad (5-1)$$

Ash density is the density of the mineralized and inorganic part of the bone, namely the hydroxyapatite ash, (Knowles et al., 2016, Schileo et al., 2008). The ash density was set at a maximum of 1.1 g/cm³ following previous work published by Sabo et al. (2009). On the other hand, the minimum ρ_{ash} was set at 0 g/cm³ and was associated with the minimum HU value found in the CT scans. The minimum HU value was set at -1000 since the scanned mandible was dry. The ρ_{ash} was then converted to apparent density (ρ_{app}), which is defined as the density of the mineralized and organic components of bone (Knowles et al., 2016, Schileo et al., 2008). Previous works have established a linear relationship between ρ_{ash} and ρ_{app} (Schileo et al., 2008, Hangartner and Short, 2007). ρ_{app} was estimated using the equation previously reported by Schileo et al. (2008):

$$\rho_{\text{ash}} = 0.6 \rho_{\text{app}} \quad (5-2)$$

Finally, the ρ_{app} was converted to Young's modulus (E_T) using a model previously developed for ulnar bone by Austman et al. (2009). The following equation describes this conversion:

$$E = 8346 \rho_{\text{app}}^{1.5} \text{ (MPa)} \quad (5-3)$$

This produced bone and dentine material properties that were heterogenous. Equations 5-1 to 5-3 were applied to every bone element in the mandible and IO-mandible models (Figure 5-4).

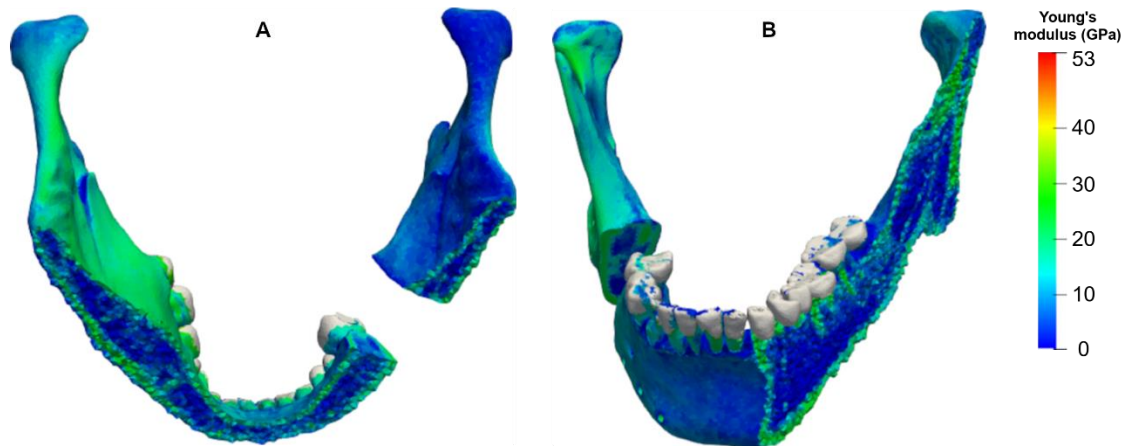


Figure 5-4: Distribution of the Young's modulus within the bone structure.

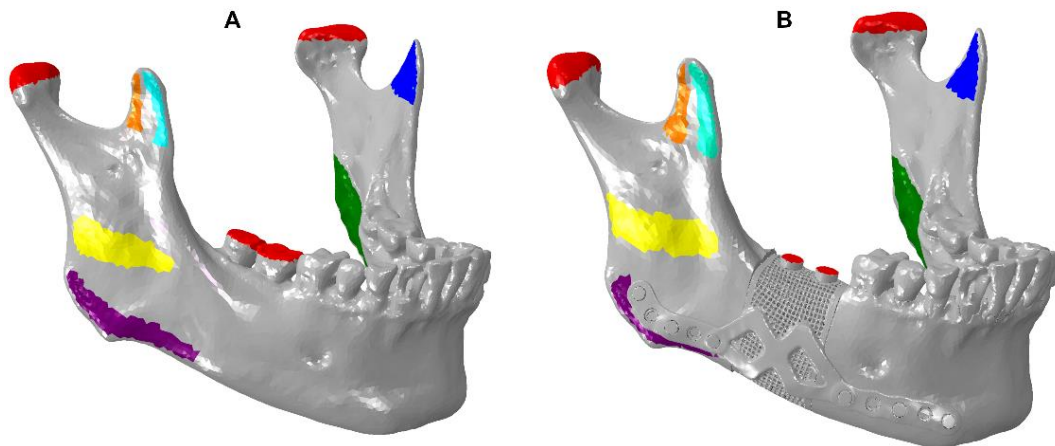
Distribution of the Young's modulus within the bone structure, presented here in its STL mesh form. The gap on the right side of the mandibular body represents the surgical osteotomy. (A) Posterior-inferior oblique view with the mandible sectioned in a horizontal plane close to the inferior border of the ramus and body. (B) Anterior-superior oblique view with the mandible sectioned in an oblique vertical plane through the body and ramus. Elements are shown both along the surface of the mandible model as well as within it. The heat map shows the assigned Young's modulus value for each of the elements. The enamel, shown in the model as light grey coloured, was given a constant Young's modulus of 80 GPa.

A summary of the material properties implemented in the FEA static and fatigue numerical models is listed in Appendix A, Table A-2 and section 4.3.3, Table 4-1. Ti6Al4V material properties were determined from static tensile tests, surface roughness analysis, and cyclic flexural loading tests conducted on porous Ti6Al4V SLM-built constructs (Chapters 3 and 4). The enamel region was assigned Young's modulus value of 80 GPa and Poisson's ratio of 0.3. These parameters were taken from the findings of work done by Rees and Jacobsen (1993) and Craig et al. (1961). Given that the bone and dentine region might include voids within it, the minimum E_T was set at 0 GPa, the maximum E_T that was set for bone and dentine was 53 GPa.

5.3.3 Static FEA model simulation

The models, with their material properties, were exported to Abaqus 2020 (Dassault Systèmes Simulia Corp., Providence, RI, United States). The mesh element quality was analyzed upon importing the models to ABAQUS. Elements that had an aspect ratio

exceeding 5 were considered to be of poor quality. The total number of elements all over the assembly was about 3240835 elements, and of these elements, only 191 elements were found to have a low quality (0.006%). The majority of these poor-quality elements were located within the bone parts of the assembly (158 elements). Hence it was determined that the model elements were of sufficient quality for further analysis procedures. Muscular forces were simulated to replicate the effect of right molar clenching. The magnitude and direction of these muscular forces and constraints followed the properties described by Yoon et al. (2021) and Koriath and Hannam (1994) (Figure 5-5). Koriath and Hannam (1990) determined the muscle force magnitudes and directions using biomechanical analysis.



Muscle attachments		F_x (N)	F_y (N)	F_z (N)
■ Superficial masseter	Right	-28.4	-121.2	-57.4
	Left	23.6	-101.0	-47.9
■ Deep masseter	Right	-32.1	-44.5	21.0
	Left	26.7	-37.1	17.5
■ Medial pterygoid	Right	71.4	-116.1	-54.8
	Left	-51.0	-83.0	-39.1
■ Anterior temporalis	Right	-17.2	-114.0	-5.1
	Left	13.7	-90.5	-4.0
■ Middle temporalis	Right	-14.0	-52.8	31.5
	Left	14.2	-53.6	32.0
■ Posterior temporalis	Right	-9.3	-21.1	38.1
	Left	6.1	-14.0	25.2

Figure 5-5: Detailed description of the mandible and implant-mandible models' muscular forces and boundary conditions.

(A) The mandible model and (B) the implant-mandible model with the approximate locations of muscle attachments and biting forces. These were used to indicate the locations where the loading and boundary conditions were applied in the FE models. The Table shows the muscular force components, previously described by Yoon et al. (2021) for right molar clenching. The red parts in A and B represent regions of reaction forces, either on the right molars (A) or on the dental implants (B) and the condyles in both A and B. These regions were clamped.

FEA modelling was achieved by simulating the distributed forces at locations of major muscle attachments on the mandible. At the same time, two boundary conditions were applied to the models at the condyle regions and on the two molar teeth and dental implants. It should be noted that, in the case of the implant-mandible model, muscle forces were

applied at locations around the fixation plate. The muscle attachments were assumed to recover fully post-healing. The interface between all the intraosseous implant components and the bone, as well as between the dental implant and the intraosseous implant had tie constraints. This bonding represented a fully locked fixation of the intraosseous implant into the bone models. The maximum forces applied during clenching were measured as the maximum reaction force value on the right molar teeth in the mandible model and on the dental implants in the implant-mandible model.

From the FEA simulations, the von Mises stress readings were measured within the Ti6Al4V and bone parts. Von Mises stress (σ_v) is a scalar value of stress, which is defined as the uniaxial tensile stress that would create the same distortion levels as that created by the combined applied stresses (Logan, 2012). The equation used to calculate the von Mises stress can be seen in Equation in Appendix.

Failure of the implant is defined when yielding occurs, which was observed when the von Mises stress exceeded the yield strength of Ti6Al4V (≈ 866 MPa) (Chapter 3) or cortical bone (≈ 140 MPa) (Peng et al., 2021). The force and displacement readings for the models were also recorded and used in fatigue modelling. Finally, the maximum principal strain values of the bone elements were recorded and checked to ensure that they lie within the optimal strain range. The optimal strain range for bone is between 800 and 15,000 $\mu\epsilon$, which would put the bone either in adapted (homeostasis) state (between 800 and 1500 $\mu\epsilon$) or in overload state (between 1500 $\mu\epsilon$ and 15,000 $\mu\epsilon$), which would lead to remodelling. This optimal strain range avoids stress shielding (from insufficient strain) or fracture (from excessive strain) (Frost, 1987, Shen et al., 2022). For each node, the maximum principal strain refers to the value of the principal strain with the highest absolute value.

5.3.4 Fatigue numerical modelling

The implant-mandible FEA model was imported to FE-Safe 2020 (SIMULIA, Inc., Providence, USA) to conduct cyclic loading simulations. The FEA model has multiple increments with increasing reaction forces applied on the intraosseous implant. The increment with the maximum reaction force (F_{max}) on the intraosseous implant was imported. Numerical simulations of cyclic loading were conducted with the applied forces

ranging between a maximum force (0.05 to 1.00 F_{\max}) and a minimum force (0 N). The assumption was made that the average number of chewing cycles of an individual per year is 5×10^5 (Farooq and Sazonov, 2016, Po et al., 2011). The loading frequency was kept at 0.02 Hz. This frequency was determined by dividing the assumed number of cycles by the number of seconds per year. Fatigue strength calculations were based on the Brown-Miller theory with Morrow correction (Morrow, 1968, Kandil et al., 1982). Details of this technique have been described in Chapter 4 and can be further seen in section 4.3.2. The cyclic loading-induced damage on each plane of the model was calculated through Palmgren-Miner's rule (Miner, 1945). Details of this technique have been described in section 4.3.2.4.

From the numerical models, a force-number of cycles to failure (F- N_f) curve and force-number of years of service (F- S_y) curve were generated. The number of years of service was estimated under The following equation was used to convert the number of cycles to the number of years of service (S_y):

$$S_y = \frac{N_f}{500,000} \text{ (Years of service)} \quad (5-4)$$

where N_f is the number of cycles at failure and S_y is the years of service. Using both F- N_f and F- S_y curves, the forces applied in real-life chewing, ranging between 50 and 100 N (Waltimo and Könönen, 1993, Sessle, 2014), were matched with their corresponding predicted number of cycles and years of service.

5.4 Results and discussion

5.4.1 Static FEA models

The von Mises stress (σ_v) contour maps were generated for the maximum force applied during molar clenching (Figure 5-6). In the mandible model, the maximum force was ≈ 535 N, comparable to the maximum force found in the implant-mandible model of ≈ 441

N¹. The bone of the mandible model had $\sigma_v \leq 122$ MPa. For the implant-mandible model, most of the elements of the implant had $\sigma_v < 866$ MPa. Given that for Ti6Al4V the yield stress is 866 MPa, this finding indicates that no yielding is predicted to occur within the implant. However, a handful of elements showed evidence of yielding ($\sigma_v > 866$ MPa). These were limited to the bone-implant interface with sharp angles formed from coarse meshing. Given that the porous construct is very complex, a relatively coarse mesh was chosen due to the limitation of computational power. This coarse mesh caused the unintended effect of forming sharp edges that could have led to high stress concentrations along these regions. Such high-stress concentration regions are not significant to the overall performance of the implant. The von Mises stresses in screws and dental implants did not show evidence of yielding ($\sigma_v < 866$ MPa). The intraosseous implant designed in this study withstood the right molar clenching simulation with most of the elements not yielding.

It must be noted that mesh convergence analysis was not possible in the current study given the limitations on the number of elements that could be used in the model. We chose the finest elements possible to discretize the model parts. Nevertheless, some coarse mesh elements were still formed. Further development of the modelling process would focus on the refining of the element mesh sizes.

¹ The maximum force was less than that in the mandible model, presumably due to the partial loss of attachment of the superficial masseter arising from the placement of the fixation bar.

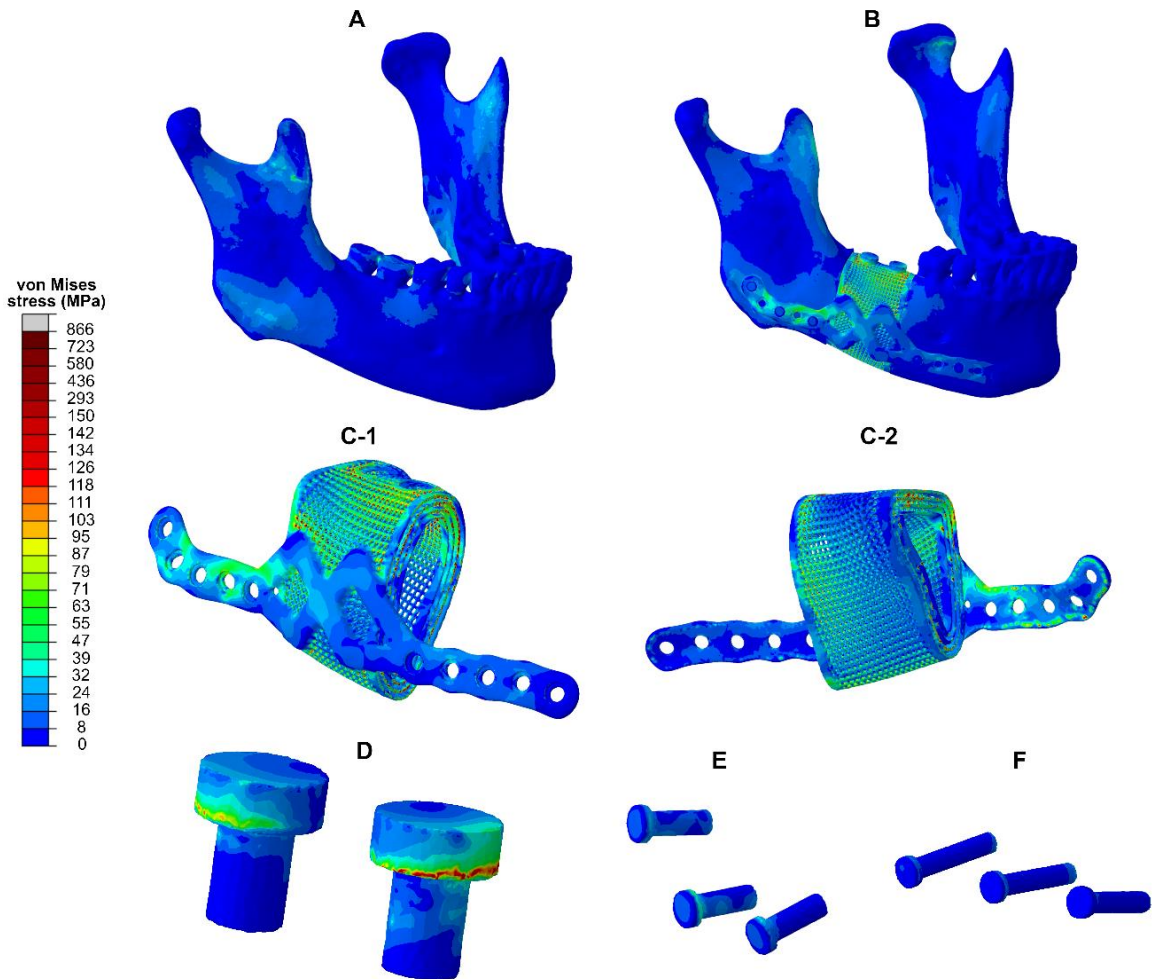


Figure 5-6: The von Mises stress contour map of the mandible and implant-mandible models along with their components.

(A) mandible model and (B) implant-mandible model under right molar clenching. Individual parts of the implant-mandible model are shown as follows: (C) intraosseous implant from (C-1) anterior-oblique view and (C-2) posterior-oblique view. (D) Dental implants, (E) posterior fixation screws, and (F) anterior fixation screws are shown from an anterior-oblique view. The results indicated that the components of the intraosseous implant would remain intact despite being exposed to forces ($F \approx 441$ N) four times as large as those seen in normal chewing activity ($F < 100$ N). The color scale is linear between 0 and 150 MPa (lower 19 blocks) and linear between 150 and 866 MPa (upper 5 blocks).

Our results align with previous works on porous intraosseous implant designs. Shen et al. (2022) used von Mises stress readings from FEA models to show that a shell design intraosseous implant with holes along the shell of diameters of 1 or 2 mm remains intact under right molar clenching simulation similar to the one described in the present study. van Kootwijk et al. (2022) designed a porous intraosseous implant with dodecahedron pores, with strut thickness of 210 μm , pore size of 460 μm and porosity of $\approx 87.5\%$. Their work showed that, with maximum force on the implant of ≈ 600 N, the implant struts

experienced von Mises stresses < 400 MPa. Peng et al. (2021) designed a three-layered porous intraosseous implant and was put under incisal biting FEA simulation. The results from that work indicated that the von Mises stress values were < 600 MPa and the adjacent bones had von Mises stress values < 126 MPa. Unlike these works, the intraosseous implant designed in the present study had a gradient structure, with the inner layer struts being thinner than the outer layers. This gradient strut thickness design allowed the outer shell of the intraosseous implant to absorb the stress from mastication. Previous work has shown that such gradient designs can improve the strength of porous constructs while lowering their stiffness to match that of bone (Onal et al. 2018, Shi et al. 2017, Yang et al. 2019). In the present study, the von Mises stress levels in the majority of bone elements adjacent to the implant reached a maximum of 100 MPa, which is less than the fracture limit of bone (130 MPa). However, some regions along the bone-implant surface experienced higher stress. These were limited to a few elements, which are not deemed to be detrimental in real-life application.

The strain levels in bone induced by right molar clenching on the implant-mandible model was illustrated using contour maps (Figure 5-7). Few points experienced strain value $>15000 \mu\epsilon$, while most of the bone experienced strains that are between 800 and 5000 $\mu\epsilon$. These findings indicate that the implant would not be expected to cause bone damage. There would be little risk of bone fracture, with only handful of elements having strain levels exceeding 15,000 $\mu\epsilon$, the level known to lead to bone fracture (Shen et al., 2022). According to the mechanostat theory, homeostasis and growth of bone can be maintained when the strain value ranges between 800 and 15,000 $\mu\epsilon$ (Shen et al., 2022, Frost, 1987, Frost, 2004). The strain levels indicate that the bone would be largely in a state of homeostasis, with the parts of the bone closer to the implant experiencing overload levels of strain, which are predicted to trigger bone remodelling. This might promote the ingrowth of bone into the porous structure of the implant. The strain levels seen in bone adjacent to the implant proved that the porous implant with its spatially variable stiffness had overall mechanical properties that prevented stress shielding.

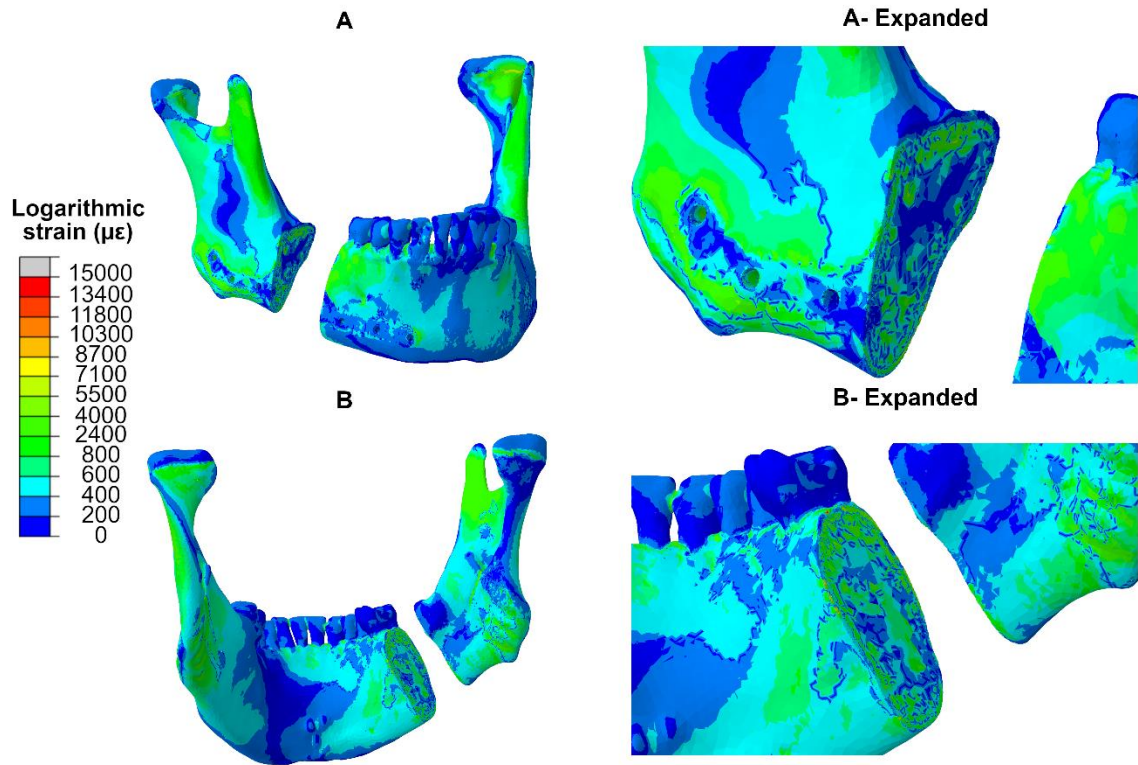


Figure 5-7: Contour maps of the implant-mandible model showing the maximum principal strain of the bone adjacent to the implant from (A) an anterior-oblique view and (B) a posterior-oblique view.

Expanded views are shown at right. The intraosseous implant was removed to show strains in the adjacent bones. The maximum principal strain is defined as the maximum absolute value of the logarithmic (true) strain of the element, which could be either positive if it was tensile strain or negative if it was compressive strain. Bone adjacent to the implant appear to have strains that reach to about 5000 $\mu\epsilon$, with small regions reaching up to 15000 $\mu\epsilon$. Some elements show strains that are higher than 15000 $\mu\epsilon$ but are limited to few elements along the edges of the bone.

When the implant-mandible model was under right molar clenching simulation, the adjacent bone experiences stress levels comparable to those seen in the mandible model without the intraosseous implant, as well as strain levels that are within the optimal range to maintain homeostasis or promote bone remodelling. These results highlight the ability of the intraosseous implant to allow stress transmission to adjacent bones, hence avoiding stress shielding. The outcomes of this experiment are similar to those seen in previous studies. For example, Shen et al. (2022) presented an intraosseous mandibular implant with a cage design made of a hexagonal lattice and tested using FEA under molar clenching conditions. Shen and coworkers showed that such a design allowed bone strain levels within the overload state, which promotes bone remodelling. However, unlike the design

concept proposed in the present study, the design proposed by Shen and coworkers provides a less robust scaffold for bone ingrowth without the use of a bone graft. In work done by Peng et al. (2021), the growth of bone into the porous implant was modelled at different stages. The principal strain levels within the growing bone during incisal biting was between 871 and 2865 $\mu\epsilon$, which is within the same range found in the present study and is optimal for bone homeostasis and remodelling.

5.4.2 Fatigue Numerical Modelling

F- N_f and F- S_y curves were generated using the implant-mandible model to examine fatigue strength (Figure 5-8). For masticatory forces on the mandible ranging between 50 and 100 N, the number of cycles to failure is predicted to range between 4 years ($N_f = 2.3 \times 10^6$ cycles) and 119 years ($N_f = 5.6 \times 10^7$ cycles).

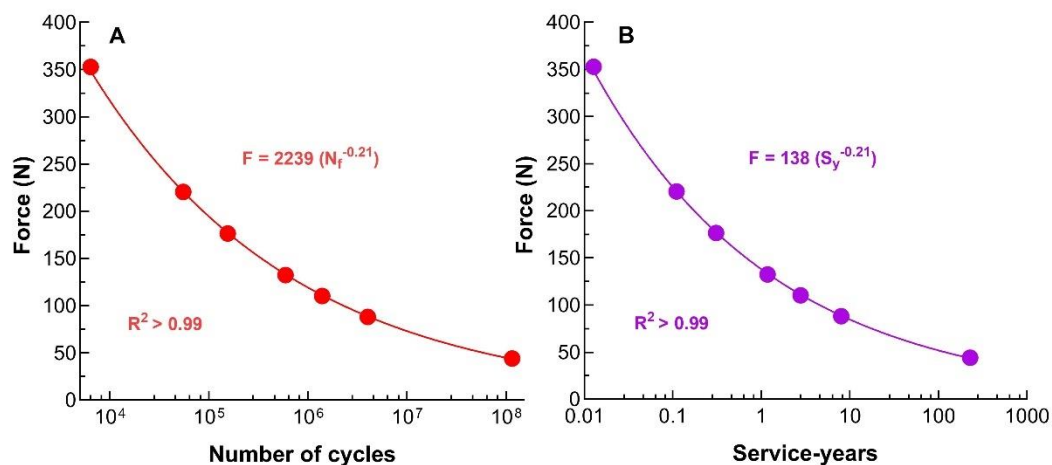


Figure 5-8: Fatigue behaviour of the implant-mandible model. (A) Force (F) vs. number of cycles (N_f), and (B) F vs. number of service-years (S_y) predicted by the numerical fatigue models.

For clarity, the number of cycles is presented on a logarithmic scale, while the service-years is presented on antilogarithmic scale. If the mandible experiences force levels ranging between 50 and 100 N, then the intrasosseous implant would be expected to endure chewing cycles ranging between 4 to 119 years.

Numerical modelling contour maps (at force/maximum force = 80%) revealed the predicted site of fatigue failure at the edge of the intrasosseous implant (Figure 5-9). This was the site of the highest applied stress on the intrasosseous implant. The location where failure occurred had the highest stress-to-yield stress ratio (≈ 1.3). Interestingly, none of the struts within the porous model failed due the fatigue loading, with the maximum stress to

yield stress ratio < 0.05 . The numerical model was directly affected by the coarse mesh used in building of intraosseous implant model, with small regions of high stress concentrations found along the edges of coarse mesh elements. Nevertheless, the model predicted that the porous implant could withstand cyclic loading while remaining intact.

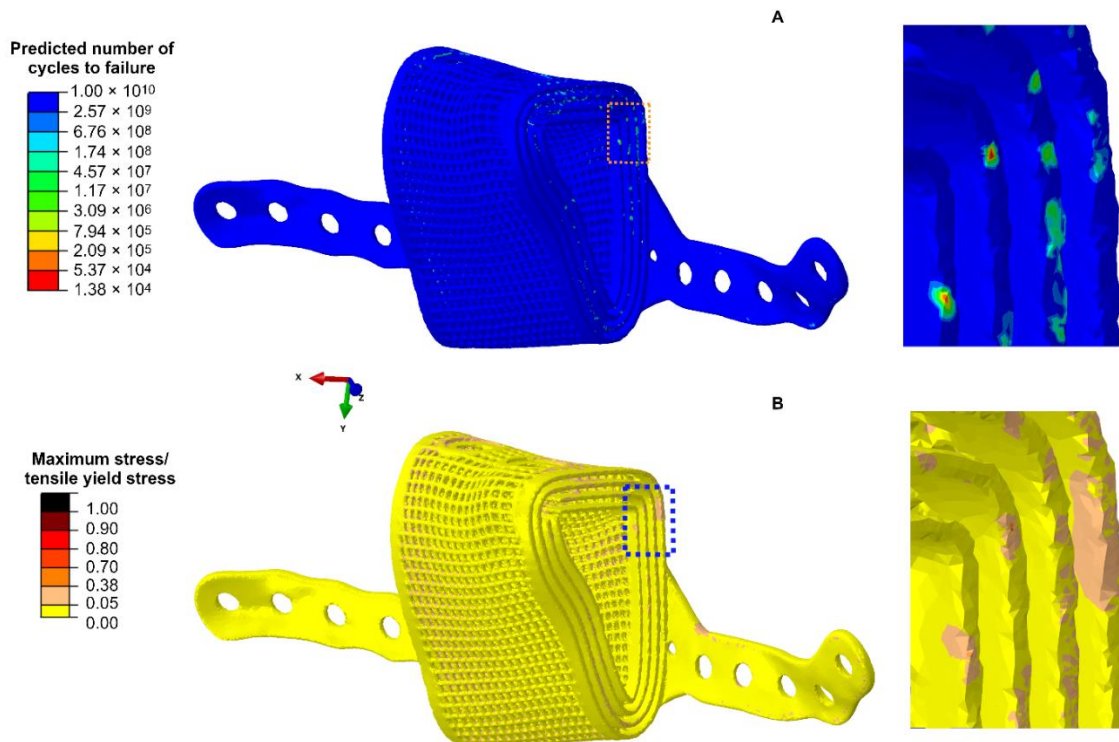


Figure 5-9: Contour map of fatigue-loaded models.

Contour map of (A) predicted number of cycles to failure and (B) maximum stress to tensile yield stress ratio of intraosseous implant models at force/maximum force = 80%. Regions outlined by dashed lines are shown enlarged at the right. Fatigue failure sites (i.e. sites with the lowest predicted number of cycles and the highest stress to tensile yield stress ratio) were found at the edge of the intraosseous implant, in direct contact with the bone. Locations having mesh elements that were rough or had sharp edges appeared as sites of potential failure. However, these were likely artifacts due to coarse meshing. The struts experienced low stress concentrations and were predicted to remain intact.

In our previous work, we validated numerical models in terms of stress, strain, and fatigue responses (Chapters 3 and 4). Future work on mandibular implants will require validation of these models using static and dynamic real-life testing of SLM-built implants. Cyclic loading tests on SLM-built porous constructs are the 'golden standard' for validating their fatigue properties. However, real-life fatigue tests can be very expensive, in addition, they are insufficient in determining the specific locations of weaknesses in these porous constructs. In the present study, a numerical modelling process was developed to predict

the number of years of service using the numerical model validated in Chapter 4. A real-life fatigue study was conducted by van Kootwijk et al. (2022), which showed that porous intraosseous implants with a higher porosity than those used in the current study can withstand cyclic loading up to at least 250,000 cycles of a maximum load of 340 N and minimum load of 30 N (amplitude force = 310 N). Cyclic loading of our models with the same force amplitude of 310 N would cause early failure of the implant designed in the current study ($N_f=16,000$ cycles). However, it should be noted that the intraosseous implant designed by van Kootwijk et al. was not completely porous.

It should be kept in mind that cyclic loading tests for mandibular implants should be conducted for at least 10^6 cycles, as implants are expected to experience at least 500,000 cycles per year in vivo (Farooq and Sazonov, 2016, Po et al., 2011). An advantage of FEA-based fatigue models, such as the one developed in the present study, is that they can predict fatigue for an unlimited number of cycles.

5.5 Effect of bone ingrowth on the implant

It should be noted that the pore sizes used to build our intraosseous implant were chosen with bone ingrowth capability in mind. The size of the pores in our implant were between 550 and 650 μm , which is within the optimal range for healthy bone ingrowth and revascularization (Ponader et al., 2010, Watanabe et al., 2023, Kovacs et al., 2023, Zhang et al., 2022). It was not possible to include bone growth into the intraosseous implant in our model due to the large number of elements that would be involved in the simulation. In previous work where bone ingrowth was included in intraosseous implant FEA models (Peng et al., 2021), larger pores were used resulting in less complex structures.

Previous studies have indicated that the presence of bone growth within porous Ti6Al4V structures provides additional strength and stiffness, which in turn increases the overall fatigue strength of the constructs (Chapter 4). In previous animal studies, it took between 6 and 12 weeks for osseointegration to occur (Taniguchi et al., 2016, Chen et al., 2019, Deng et al., 2021, Watanabe et al., 2023), while human bone took up to 9 months to fully grow and osseointegrate on Ti6Al4V surface (Hofmann et al., 1997). Fatigue strength predictions done on our implant-mandible models indicated that, for the period of 9

months, intraosseous implants withstood masticatory forces of up to 146 N without experiencing fatigue failure. This indicates that during the first 9 months following implant placement, no biting forces should exceed 150 N. Fortunately, the minimum predicted service-years (4 years) for our implant design is enough to allow complete bone ingrowth, after which the healed implant is predicted to survive cyclic loading indefinitely.

The implant design used in this study was built to omit the need for bone grafts; this approach has the potential to reduce invasive procedures involved in mandibular reconstruction. This would lead to a reduction in the risk of infection and the elimination of donor-site bone morbidity issues (see section 1.5). However, the ultimate success of the implant in clinical applications may require appropriate post-processing treatments that would allow the implants to support and promote bone ingrowth. This might include loading the porous implant with biodegradable gels containing bone growth factors and antibacterial agents.

5.6 Conclusions

This study applied our static and dynamic numerical models for the design of SLM-built porous mandibular implants. The use of computer-based numerical models to determine the mechanical properties of porous implant designs can reduce both the time and cost of prototyping and validation of implant designs. This will permit the rapid design and fabrication of patient-specific implants for clinical use. The results of the static numerical models indicate that the designed porous implant, with strut thicknesses ranging between 350 and 450 μm remains intact through right molar clenching. Numerical modelling of cyclic loading predicted that the implant remains intact when subjected to masticatory forces for a period between 4 and 119 years. Given that, within a year, bone ingrowth and osseointegration are complete, the implant is predicted to remain intact long-term under physiological loading conditions. Results from this study show that the static and dynamic numerical models presented in this study can be used to test SLM-built intraosseous mandibular implant designs prior to their fabrication.

5.7 References in this chapter

- AHMADI, S. M., KUMAR, R., BORISOV, E. V., PETROV, R., LEEFLANG, S., LI, Y., TUMER, N., HUIZENGA, R., AYAS, C., ZADPOOR, A. A. & POPOVICH, V. A. 2019. From microstructural design to surface engineering: A tailored approach for improving fatigue life of additively manufactured meta-biomaterials. *Acta Biomaterialia*, 83, 153-166.
- AUSTMAN, R. L., MILNER, J. S., HOLDSWORTH, D. W. & DUNNING, C. E. 2009. Development of a customized density-modulus relationship for use in subject-specific finite element models of the ulna. *Proc Inst Mech Eng H*, 223, 787-94.
- BATSTONE, M. D. 2018. Reconstruction of major defects of the jaws. *Aust Dent J*, 63 Suppl 1, S108-S113.
- BIEWENER, A. A. 1993. Safety factors in bone strength. *Calcif Tissue Int*, 53 Suppl 1, S68-74.
- CHEN, C., HAO, Y., BAI, X., NI, J., CHUNG, S.-M., LIU, F. & LEE, I.-S. 2019. 3D printed porous Ti6Al4V cage: Effects of additive angle on surface properties and biocompatibility; bone ingrowth in Beagle tibia model. *Materials & Design*, 175, 107824.
- CRAIG, R. G., PEYTON, F. A. & JOHNSON, D. W. 1961. Compressive Properties of Enamel, Dental Cements, and Gold. *Journal of Dental Research*, 40, 936 - 945.
- DENG, F., LIU, L., LI, Z. & LIU, J. 2021. 3D printed Ti6Al4V bone scaffolds with different pore structure effects on bone ingrowth. *J Biol Eng*, 15, 4.
- DENOTTER, T. D. & SCHUBERT, J. 2022. Hounsfield Unit, StatPearls Publishing, Treasure Island (FL).
- ESHKALAK, S. K., GHOMI, E. R., DAI, Y., CHOUDHURY, D. & RAMAKRISHNA, S. 2020. The role of three-dimensional printing in healthcare and medicine. *Materials & Design*, 194.
- FAROOQ, M. & SAZONOV, E. 2016. Automatic Measurement of Chew Count and Chewing Rate during Food Intake. *Electronics (Basel)*, 5.
- FROST, H. M. 1987. Bone "mass" and the "mechanostat": a proposal. *Anat Rec*, 219, 1-9.
- FROST, H. M. 2004. A 2003 update of bone physiology and Wolff's Law for clinicians. *Angle Orthod*, 74, 3-15.
- HANGARTNER, T. N. & SHORT, D. F. 2007. Accurate quantification of width and density of bone structures by computed tomography. *Medical Physics*, 34, 3777-3784.
- HOFMANN, A. A., BLOEBAUM, R. D. & BACHUS, K. N. 1997. Progression of human bone ingrowth into porous-coated implants. Rate of bone ingrowth in humans. *Acta Orthop Scand*, 68, 161-6.

- KAKARALA, K., SHNAYDER, Y., TSUE, T. T. & GIROD, D. A. 2018. Mandibular reconstruction. *Oral Oncol*, 77, 111-117.
- KANDIL, F. A., BROWN, M. W. & MILLER, K. J. 1982. *Biaxial Low Cycle Fatigue Fracture Of 316 Stainless Steel At Elevated Temperatures*. London, United Kingdom. The Metals Society.
- KELLER, E. E., TOLMAN, D. & ECKERT, S. 1998. Endosseous implant and autogenous bone graft reconstruction of mandibular discontinuity: a 12-year longitudinal study of 31 patients. *Int J Oral Maxillofac Implants*, 13, 767-80.
- KENNADY, M. C., TUCKER, M. R., LESTER, G. E. & BUCKLEY, M. J. 1989a. Histomorphometric evaluation of stress shielding in mandibular continuity defects treated with rigid fixation plates and bone grafts. *Int J Oral Maxillofac Surg*, 18, 170-174.
- KENNADY, M. C., TUCKER, M. R., LESTER, G. E. & BUCKLEY, M. J. 1989b. Stress shielding effect of rigid internal fixation plates on mandibular bone grafts. A photon absorption densitometry and quantitative computerized tomographic evaluation. *Int J Oral Maxillofac Surg*, 18, 307-310.
- KNOWLES, N. K., REEVES, J. M. & FERREIRA, L. M. 2016. Quantitative Computed Tomography (QCT) derived Bone Mineral Density (BMD) in finite element studies: a review of the literature. *J Exp Orthop*, 3, 36.
- KORIOOTH, T. W. & HANNAM, A. G. 1990. Effect of bilateral asymmetric tooth clenching on load distribution at the mandibular condyles. *J Prosthet Dent*, 64, 62-73.
- KORIOOTH, T. W. & HANNAM, A. G. 1994. Mandibular forces during simulated tooth clenching. *J Orofac Pain*, 8, 178-89.
- KOVACS, A. E., CSERNATONY, Z., CSAMER, L., MEHES, G., SZABO, D., VERES, M., BRAUN, M., HARANGI, B., SERBAN, N., ZHANG, L., FALK, G., SOOSNE HORVATH, H. & MANO, S. 2023. Comparative Analysis of Bone Ingrowth in 3D-Printed Titanium Lattice Structures with Different Patterns. *Materials (Basel)*, 16, 3861.
- LIU, Y. J., REN, D. C., LI, S. J., WANG, H., ZHANG, L. C. & SERCOMBE, T. B. 2020. Enhanced fatigue characteristics of a topology-optimized porous titanium structure produced by selective laser melting. *Additive Manufacturing*, 32.
- LOGAN, D. L. 2012. *Development of the Plane Stress and Plane Strain Stiffness Equations. A First Course in the Finite Element Method*. Fifth ed. United States: Cengage Learning.
- MINER, M. A. 1945. Cumulative Damage in Fatigue. *Journal of Applied Mechanics*, 12, A159-A164.

- MOIDUDDIN, K., MIAN, S. H., ALKHALEFAH, H. & UMER, U. 2019. Digital Design, Analysis and 3D Printing of Prosthesis Scaffolds for Mandibular Reconstruction. *Metals*, 9, 569.
- MORROW, J. D. 1968. Fatigue properties of metals. In: HALFORD, G. R. & GALLAGHER, J. P. (eds.) *Fatigue Design Handbook*. Warrendale, PA, United States: SAE.
- ONAL, E., FRITH, J., JURG, M., WU, X. & MOLOTNIKOV, A. 2018. Mechanical Properties and In Vitro Behavior of Additively Manufactured and Functionally Graded Ti6Al4V Porous Scaffolds. *Metals*, 8, 200.
- PENG, W. M., CHENG, K. J., LIU, Y. F., NIZZA, M., BAUR, D. A., JIANG, X. F. & DONG, X. T. 2021. Biomechanical and Mechanostat analysis of a titanium layered porous implant for mandibular reconstruction: The effect of the topology optimization design. *Mater Sci Eng C*, 124, 112056.
- PEREZ, D. & ELLIS, E., 3RD 2020. Complications of Mandibular Fracture Repair and Secondary Reconstruction. *Semin Plast Surg*, 34, 225-231.
- PICKRELL, B. B., SEREBRAKIAN, A. T. & MARICEVICH, R. S. 2017. Mandible Fractures. *Seminars in Plastic Surgery*, 31, 100-107.
- PO, J. M., KIESER, J. A., GALLO, L. M., TESENYI, A. J., HERBISON, P. & FARELLA, M. 2011. Time-frequency analysis of chewing activity in the natural environment. *J Dent Res*, 90, 1206-10.
- PONADER, S., WILMOWSKY, C. V., WIDENMAYER, M., LUTZ, R., HEINL, P., KÖRNER, C., SINGER, R. F., NKENKE, E., NEUKAM, F. W. & SCHLEGEL, K. A. 2010. In vivo performance of selective electron beam-melted Ti-6Al-4V structures. *Journal of Biomedical Materials Research Part A*, 92A, 56--62.
- REES, J. S. & JACOBSEN, P. H. 1993. The elastic moduli of enamel and dentine. *Clinical Materials*, 14, 35-39.
- SABO, M. T., POLLMANN, S. I., GURR, K. R., BAILEY, C. S. & HOLDSWORTH, D. W. 2009. Use of co-registered high-resolution computed tomography scans before and after screw insertion as a novel technique for bone mineral density determination along screw trajectory. *Bone*, 44, 1163-8.
- SCHILEO, E., DALL'ARA, E., TADDEI, F., MALANDRINO, A., SCHOTKAMP, T., BALEANI, M. & VICECONTI, M. 2008. An accurate estimation of bone density improves the accuracy of subject-specific finite element models. *J Biomech*, 41, 2483-91.
- SESSLE, B. J. 2014. *Neural Basis of Oral and Facial Function*. Reference Module in Biomedical Sciences. Elsevier.
- SHEN, Y. W., TSAI, Y. S., HSU, J. T., SHIE, M. Y., HUANG, H. L. & FUH, L. J. 2022. Biomechanical Analyses of Porous Designs of 3D-Printed Titanium Implant for Mandibular Segmental Osteotomy Defects. *Materials (Basel)*, 15, 576.

- SHI, J., YANG, J., LI, Z., ZHU, L., LI, L. & WANG, X. 2017. Design and fabrication of graduated porous Ti-based alloy implants for biomedical applications. *Journal of Alloys and Compounds*, 728, 1043-1048.
- SMOLKA, K., KRAEHEBUEHL, M., EGGENSPERGER, N., HALLERMANN, W., THOREN, H., IIZUKA, T. & SMOLKA, W. 2008. Fibula free flap reconstruction of the mandible in cancer patients: evaluation of a combined surgical and prosthodontic treatment concept. *Oral Oncol*, 44, 571-81.
- TANIGUCHI, N., FUJIBAYASHI, S., TAKEMOTO, M., SASAKI, K., OTSUKI, B., NAKAMURA, T., MATSUSHITA, T., KOKUBO, T. & MATSUDA, S. 2016. Effect of pore size on bone ingrowth into porous titanium implants fabricated by additive manufacturing: An in vivo experiment. *Mater Sci Eng C* 59, 690-701.
- VAN EIJDEN, T. M. 2000. Biomechanics of the mandible. *Critical Reviews in Oral Biology & Medicine*, 11, 123-136.
- VAN KOOTWIJK, A., MOOSABEIKI, V., SALDIVAR, M. C., PAHLAVANI, H., LEEFLANG, M. A., KAZEMIVAND NIAR, S., PELLIKAAN, P., JONKER, B. P., AHMADI, S. M., WOLVIUS, E. B., TUMER, N., MIRZAALI, M. J., ZHOU, J. & ZADPOOR, A. A. 2022. Semi-automated digital workflow to design and evaluate patient-specific mandibular reconstruction implants. *J Mech Behav Biomed Mater*, 132, 105291.
- WALTIMO, A. & KÖNÖNEN, M. 1993. A novel bite force recorder and maximal isometric bite force values for healthy young adults. *Scand J Dent Res*, 101, 171-5.
- WATANABE, R., TAKAHASHI, H., MATSUGAKI, A., UEMUKAI, T., KOGAI, Y., IMAGAMA, T., YUKATA, K., NAKANO, T. & SAKAI, T. 2023. Novel nano-hydroxyapatite coating of additively manufactured three-dimensional porous implants improves bone ingrowth and initial fixation. *J Biomed Mater Res B Appl Biomater*, 111, 453-462.
- YANG, L., MERTENS, R., FERRUCCI, M., YAN, C., SHI, Y. & YANG, S. 2019. Continuous graded Gyroid cellular structures fabricated by selective laser melting: Design, manufacturing and mechanical properties. *Materials & Design*, 162, 394-404.
- YOON, Y., KIM, J.-E., JUNG, J., OH, S.-H., NOH, G. & KWON, Y.-D. 2021. Effect of mandibular contouring surgery on the stress distribution during various clenching tasks. *Journal of Computational Design and Engineering*, 8, 570-580.
- ZELLER, A. N., NEUHAUS, M. T., WEISSBACH, L. V. M., RANA, M., DHAWAN, A., ECKSTEIN, F. M., GELLRICH, N. C. & ZIMMERER, R. M. 2020. Patient-Specific Mandibular Reconstruction Plates Increase Accuracy and Long-Term Stability in Immediate Alloplastic Reconstruction of Segmental Mandibular Defects. *J Maxillofac Oral Surg*, 19, 609-615.

- ZHANG, Y., SUN, N., ZHU, M., QIU, Q., ZHAO, P., ZHENG, C., BAI, Q., ZENG, Q. & LU, T. 2022. The contribution of pore size and porosity of 3D printed porous titanium scaffolds to osteogenesis. *Biomater Adv*, 133, 112651.
- ZHOU, L. B., SHANG, H. T., HE, L. S., BO, B., LIU, G. C., LIU, Y. P. & ZHAO, J. L. 2010. Accurate reconstruction of discontinuous mandible using a reverse engineering/computer-aided design/rapid prototyping technique: a preliminary clinical study. *J Oral Maxillofac Surg*, 68, 2115-21.
- ZOUMALAN, R. A., HIRSCH, D. L., LEVINE, J. P. & SAADEH, P. B. 2009. Plating in Microvascular Reconstruction of the Mandible. *Journal of Craniofacial Surgery*, 20, 1451--1454.

Chapter 6

Conclusions and General Discussion

Chapter 6

6 Conclusions and general discussion

6.1 Summary and Conclusions

6.1.1 Specific objective 1: Design SLM-built porous Ti6Al4V constructs that could be used in mandibular reconstruction.

6.1.1.1 Summary

CAD models were designed of constructs with simple cubic pores having unit cell size of 1 mm, and strut thicknesses ranging between 250 μm and 650 μm . Nonporous models were also designed. These models were used to build constructs using SLM. Nonporous models were also built through casting. These constructs were put through morphological analysis using CT scanning.

6.1.1.2 Conclusions

- Morphological analysis revealed that the deviations seen between CAD and SLM-built struts is dependent on their orientation, with less deviation ($\approx 5\%$) seen in parallel struts when compared to the perpendicular struts ($\approx 24\%$).
- Thinner struts tend to have circular strut cross-section, while thicker struts tend to be more consistent with the nominal square strut cross-sectional shape seen in the CAD models.
- Surface roughness in SLM-built constructs is present on all struts (arithmetic mean height was between 2.0 and 9.5 μm). Minimal internal defects are found within the struts (volume percentage $< 1.2\%$).

6.1.2 Specific objective 2: Determine the static mechanical properties of SLM-built porous Ti6Al4V.

6.1.2.1 Summary

All constructs were put through either static tensile or flexural ramp loading until failure. Stress-strain curves were generated and used to determine the mechanical properties of the constructs. These mechanical properties were then matched to mandible cortical bone properties to determine the optimal strut thickness range that could be used for mandibular reconstruction.

6.1.2.2 Conclusions

- SLM-built nonporous constructs had strength and modulus values that were similar to those built using casting. Toughness values were significantly different due to higher elongation in cast constructs.
- The strength and modulus of porous constructs were found to increase logarithmically with increasing strut thickness. No correlation was found between strain readings and strut thickness.
- Constructs with strut thicknesses between 350 μm and 450 μm are expected to be optimal for use in porous mandibular implant designs.

6.1.3 Specific objective 3: Design and build finite element analysis models that mimic the tensile and flexural mechanical properties of SLM-built porous Ti6Al4V constructs.

6.1.3.1 Summary

FEA models were built to replicate the mechanical tests done on the porous constructs. The material properties of SLM-built Ti6Al4V nonporous constructs were fed into these models.

6.1.3.2 Conclusions

- The mechanical properties of FEA models with struts of circular cross-section show close alignment with the mechanical properties of SLM-built specimens (deviation $\leq 11\%$).
- The FEA models' toughness readings deviated from those of SLM-built constructs. This was most likely related to the presence of structural imperfections in the SLM-built constructs, which decreased their plastic elongation.

6.1.4 Specific objective 4: Determine the flexural fatigue properties of SLM-built porous Ti6Al4V.

6.1.4.1 Summary

We designed CAD models of porous Ti6Al4V constructs that had strut thickness of either 350 or 450 μm . We then proceeded to build those constructs using SLM. These constructs were put through cyclic flexural loading to determine their stress-life behaviour.

6.1.4.2 Conclusions

- Strut thickness and porosity directly affected the yield-normalized fatigue stress-versus number of cycles to failure curves and the maximum flexural stress versus-number of cycles curves of porous constructs.
- Fractures of SLM-built porous constructs occurred at strut junctions. They appeared to initiate from the surface of constructs and likely propagated due to the existence of internal defects and reduced ductility.

6.1.5 Specific objective 5: Design and build dynamic numerical models that mimic the fatigue flexural properties of SLM-built porous Ti6Al4V constructs.

6.1.5.1 Summary

Numerical models were built to match the fatigue behaviour of the constructs. The fatigue numerical models simulated the effects of structural imperfections (internal defects, surface roughness, and strut thickness inaccuracies) by introducing fatigue parameters derived from the cyclic loading tests conducted in real life.

6.1.5.2 Conclusions

- Calibrating the fatigue parameters of the numerical models to those of the SLM-built constructs provided an accurate prediction of their fatigue strength (deviation $\approx 10\%$).
- Bone ingrowth eliminated the pores within the models, therefore resulted in higher fatigue strength.

6.1.6 Specific objective 6: Design and build a static and dynamic FEA model of an intraosseous porous mandibular implant that is compatible with mandibular bone.

6.1.6.1 Summary

An intraosseous mandibular implant with porous structure was designed as a CAD model. The geometry of the implant was based on CT-images of a cadaveric mandibular bone. The model had varied strut thicknesses ranging from 350 to 450 μm . Numerical models of the mandible with the implant were subjected to simulated right molar clenching and cyclic masticatory loading conditions. The settings of the numerical models were based on those validated in the work described previously in the thesis.

6.1.6.2 Conclusions

- Numerical modelling of cyclic loading predicted that the implant remains intact when subjected to masticatory forces for a period between 4 and 119 years.

6.2 Contributions to the current knowledge

This work is one of the first attempts to comprehensively and simultaneously study the static and dynamic flexural properties of fully porous SLM-built Ti6Al4V constructs' mechanical properties. Previous researchers have investigated either static (Ahmadi et al., 2018, du Plessis et al., 2018a, Xiong et al., 2020a, Yavari et al., 2015) or fatigue compression loading (Yavari et al., 2013, Zhao et al., 2016, Dallago et al., 2018a, de Krijger et al., 2017, Yáñez et al., 2020, Ahmadi et al., 2019) on SLM-built porous Ti6Al4V constructs. In this study, the investigation was focused on flexural loading given its high importance in the context of mandibular biomechanics. Mandible experience high levels of flexural deformation (Al-Sukhun et al., 2006, van Eijden, 2000). As such, implants located within the mandible are expected to experience similar loading conditions, and hence it was deemed crucial to understand the mechanical behaviour and vulnerabilities under flexural loading. While some studies were recently published on the static flexural loading of porous Ti6Al4V constructs (Horn et al., 2014, Di Caprio et al., 2022, Bellini et al., 2021a, Bellini et al., 2021b, Tüzemen et al., 2022, Song et al., 2021), none of them investigated highly intricate and fine porous structures with small unit cell sizes and thin struts as was conducted in this work. On the other hand, to the knowledge of the author, no previous work has investigated the dynamic flexural fatigue properties of SLM-built porous Ti6Al4V. Given that mandibles in humans experience repetitive loading cycles over their lifetimes, the understanding of the constructs' behaviour under cyclic loading is of utmost importance.

FEA has been used previously in the design of maxillofacial implants (Ji et al., 2010, Zhong et al., 2021, Jesus et al., 2014), as well as porous Ti6Al4V mandibular implants (Shen et al., 2022, Peng et al., 2021, van Kootwijk et al., 2022). However, no previous work attempted to build FEA-based dynamic models of SLM-built porous constructs or

mandibular implants with a structure that reflects structural imperfections. While producing models with structural imperfections can be a challenging task due to limitations in computer power and the time consumption it takes for such simulations to run. The amendments to the mechanical properties and fatigue parameters of the FEA models to reflect these changes have been shown to be a suitable option, as this allowed the accurate calibration of the models, while avoiding the use of actual structural imperfections, which reduced the time and computational cost.

6.3 Impact and significance of the study

When discussing the impact of this work on the development in the high end, patient-specific implant designs, there are three principal domains that could be discussed: the optimization of the pore designs for mandibular reconstruction, the integration of fatigue simulations tailored to evaluate SLM-built constructs, and the feasibility of modification of the procedures for other applications.

The strategy behind the use of the pore designs in this study aimed to reduce the number of variables involved in the optimization of the porous structure for mandibular reconstruction. Firstly, the choice of using simple cubic pores stemmed from the excellent bone ingrowth capability of this pore shape (Kovacs et al., 2023). Secondly, the chosen pore geometrical dimensions (pore size, strut thickness and unit cell size) allowed for ideal bone ingrowth conditions (Chapter 1). The strut thickness and pore orientation were the only parameters that required tuning for each patient-specific mandibular implant. This approach allowed easier implant development, as both parameters could be adjusted following the available medical imaging data provided by patients.

The computer models developed in this study were major additions to currently established workflows of building patient-specific implants (Shen et al., 2022, van Kootwijk et al., 2022, Peng et al., 2021). The comprehensive approach taken in the development of the FEA-based static and dynamic numerical models not only complemented earlier developments but provided accurate predictions tailored to the specific characteristics of SLM-built porous Ti6Al4V constructs. Considering the results from this study, fatigue computational modelling can be seen as an alternative to real-life fatigue analysis when it

comes to the development of patient-specific additively manufactured implants. This can be deduced due to multiple reasons: Firstly, the financial and time costs incurred by the static and fatigue mechanical testing of multiple prototypes of each patient-specific implant are extremely prohibitive. Secondly, real-life tests require advanced specialized material testing equipment that may not be available in most hospitals and even in prominent research and development institutions. With the use of the static and dynamic computer models that were developed in this study, accurate predictions of the mechanical properties of novel mandibular implant designs can be done within a short amount of time, with limited computational power usage, and with little overall cost, given that this process would occur ahead of building the implants.

The cutting of time and cost of analysis, while maintaining high levels of accuracy in computational models, makes the design and implementation of patient-specific implants faster and more efficient. This in turn would allow clinical experts to provide patients with implants that could be designed, tested, and implemented within a matter of a few days, with reduced risk of misalignment, stress shielding, and fatigue failure, all of which necessitate revision surgical procedures. In many cases, patients undergoing these procedures may not be able to go under multiple surgical procedures, due to high morbidity risks. In addition, patients would benefit from the reduced time to implement surgical implants as it would allow targeting their conditions that may be too urgent to delay. Given that there would be no need to use autologous bone grafts with the proposed patient-specific implant designs, patients could enjoy the benefits of bone reconstruction without compromising other deficiencies. Finally, patient-specific implants, with accurate contouring of the original bone shape, would have a superior aesthetic outcome when compared to the current bone grafting techniques.

The methods of designing and analyzing the novel implants described in this study should not be seen as being limited only to the mandible. This process could be expanded to designing implants to replace any bone within the human skeletal system. In addition, the pore geometry could be further modified with relative ease according to the specific conditions and requirements of each patient.

6.4 Limitations and future work

The thesis work was not without limitations. Some of these limitations were related to the testing procedure, while others were connected to the capabilities of the SLM and FEA techniques.

Constructs built using SLM have been found to deviate in shape and thickness from the original CAD models. It has been often cited that this deviation occurred due to uncalibrated SLM-parameters, such as stock powder morphology and quantity (Salem et al., 2019, Zhang et al., 2017), laser power and scanning speed (Cunningham et al., 2017, Kan et al., 2022, Montalbano et al., 2021, Snell et al., 2019, Yadroitsev et al., 2015, Zhang et al., 2017), and orientation of the construct during fabrication (Piscopo et al., 2019, Vrana et al., 2022). In addition, the strut thicknesses achieved in this study might have been too small for currently established SLM parameters to achieve shapes and thicknesses close to the nominal ones determined by the CAD models. Optimization of these parameters in a construct-specific design fashion could decrease the chance of these structural deviations to occur (Almalki et al., 2023, Vrana et al., 2018).

Structural imperfections, such as surface roughness and internal defects were present in the tested SLM-built constructs, despite using heat treatment and grit-blasting to reduce them. This could have occurred because the grit blasting process removed partially molten particles along the outer struts of the constructs but not within the inner struts. In addition, neither heat treatment nor grit-blasting targeted the internal defects. Previous studies have suggested that treatments such as HIP and laser shock peening could be suitable to reduce the internal defects (du Plessis et al., du Plessis and Rossouw, Aguado-Montero et al., 2022), while chemical etching and electropolishing were previously suggested to reduce the surface roughness. One or more of these treatments could be applied on the constructs (Ahmadi et al., 2019, Ahmadi et al., 2018, du Plessis et al., du Plessis and Rossouw, Aguado-Montero et al., 2022). However, these treatments have the potential to damage and cause the thinning of the struts (Ahmadi et al., 2019, Ahmadi et al., 2018). Further research is needed to determine the optimal treatments to be used on the intricate porous construct designs used in this study.

The FEA models, particularly those used in the static mechanical loading simulations, did not reflect the effects of lower ductility, internal defects, or surface roughness. Multiple methods have been proposed previously to include structural imperfections. One method that was investigated was the building of FEA models from CT-scanned images of SLM-built porous construct models (Yáñez et al., 2020, du Plessis et al., 2018b). Such a method could be used when studying the specific effects of porous constructs with these structural imperfections or when attempting to predict the mechanical properties of a specific SLM-built implant. However, the disadvantage of this approach is that it cannot be used to predict the static and dynamic mechanical properties of implants before fabrication. Other researchers attempted to build models with customized surface roughness (Ghosh et al., 2022) or internal defect features (du Plessis et al., 2018a). While such investigations produced results that are valuable in understanding the effects of structural imperfections in SLM-built constructs, they were limited to structures with limited complexities, have a geometrically smaller size, or are discretized into a smaller number of mesh elements. As part of this work, an attempt was made to determine the effect of structural imperfections using FEA models under tensile loading. These models have shown that strain at failure dropped significantly when surface roughness and internal defects were present. However, given that this attempt was preliminary, further work is needed to perform similar analyses on a variation of strut thicknesses, as well as structural imperfections such as void percentage and surface roughness parameters. Given the results of this proposed test, a plastic strain reduction factor could be applied to the material properties to account for structural imperfections in the SLM-built constructs. Such solution would allow developers to better reflect the real-life SLM-built constructs even if large models such as the mandible implant model developed in this study.

In addition, while only simple cubic pores of a unit cell size = 1 mm were used in this work, other pore shapes could potentially be used in the design of the implants. While these geometric parameters were chosen for their permittance of bone ingrowth, other pore designs might be preferable due to their higher strength potential (Tüzemen et al., 2022). Fortunately, the techniques used in this study can be repurposed to other pore shapes and

unit cell sizes. Future work would focus on the use modelling techniques discussed in this study on other pore geometries.

The three-point bending method, which was used in the flexural testing process focuses the force on the central region of the specimens which is directly loaded. While three-point bending is viable to determine flexural properties, other methods of applying bending, such as four-point bending, might be better suited for this purpose. That is because four-point bending distributes the applied forces over a larger portion of the specimen, better representing the loading seen in mandibular implants. Another drawback of the flexural testing process in Chapters 3 and 4 was that the ends of the specimen were not clamped. In real-life implant designs, such as that described in Chapter 5, the implant ends are expected to be fixed. Hence, both three- and four-point bending may not fully represent the bending process occurring in the implant. Future work building on the present study should involve testing the specimens while clamping the ends. Furthermore, the implant design proposed in Chapter 5 needs to be validated in appropriate animal models.

Another drawback is that this work was focused on the effects of tensile and flexural loading on porous constructs, which leaves out the effect of torsion. Torsion should be tested in future work.

The techniques used to build the intraosseous implant models could be expanded for use in other maxillofacial and orthopedic applications.

6.5 Closing statement

The results and outcomes of this study prove that numerical modelling techniques described in this study can predict both static and fatigue properties of SLM-built porous Ti6Al4V constructs with high accuracy. In addition, these techniques can provide accurate predictions within a short period of time, allowing researchers and designers to design porous implant that are compliant with bones, particularly in the case of the mandible.

6.6 References used in this chapter

- AGUADO-MONTERO, S., NAVARRO, C., VÁZQUEZ, J., LASAGNI, F., SLAWIK, S. & DOMÍNGUEZ, J. 2022. Fatigue behaviour of PBF additive manufactured Ti6Al4V alloy after shot and laser peening. *International Journal of Fatigue*, 154.
- AHMADI, S. M., HEDAYATI, R., LI, Y., LIETAERT, K., TÜMER, N., FATEMI, A., RANS, C. D., POURAN, B., WEINANS, H. & ZADPOOR, A. A. 2018. Fatigue performance of additively manufactured meta-biomaterials: The effects of topology and material type. *Acta Biomaterialia*, 65, 292--304.
- AHMADI, S. M., KUMAR, R., BORISOV, E. V., PETROV, R., LEEFLANG, S., LI, Y., TUMER, N., HUIZENGA, R., AYAS, C., ZADPOOR, A. A. & POPOVICH, V. A. 2019. From microstructural design to surface engineering: A tailored approach for improving fatigue life of additively manufactured meta-biomaterials. *Acta Biomaterialia*, 83, 153-166.
- AL-SUKHUN, J., HELENIUS, M., LINDQVIST, C. & KELLEWAY, J. 2006. Biomechanics of the Mandible Part I: Measurement of Mandibular Functional Deformation Using Custom-Fabricated Displacement Transducers. *Journal of Oral and Maxillofacial Surgery*, 64, 1015--1022.
- ALABORT, E., BARBA, D. & REED, R. C. 2019. Design of metallic bone by additive manufacturing. *Scripta Materialia*, 164, 110-114.
- ALMALKI, A., DOWNING, D., NORONHA, J., DASH, J., LOZANOVSKI, B., TINO, R., ALGHAMDI, A., KHORASANI, M., QIAN, M., BRANDT, M. & LEARY, M. 2023. The effect of geometric design and materials on section properties of additively manufactured lattice elements. *The International Journal of Advanced Manufacturing Technology*, 126, 3555-3577.
- BARTOLOMEU, F., COSTA, M. M., ALVES, N., MIRANDA, G. & SILVA, F. S. 2021. Selective Laser Melting of Ti6Al4V sub-millimetric cellular structures: Prediction of dimensional deviations and mechanical performance. *J Mech Behav Biomed Mater*, 113, 104123.
- BELLINI, C., BORRELLI, R., DI COCCO, V., FRANCHITTI, S., IACOVIELLO, F., MOCANU, L. P. & SORRENTINO, L. 2021a. Failure energy and stiffness of titanium lattice specimens produced by electron beam melting process. *Material Design & Processing Communications*, 3.
- BELLINI, C., BORRELLI, R., DI COCCO, V., FRANCHITTI, S., IACOVIELLO, F. & SORRENTINO, L. 2021b. Damage analysis of Ti6Al4V lattice structures manufactured by electron beam melting process subjected to bending load. *Material Design & Processing Communications*, 3, e223.
- BIEWENER, A. A. 1993. Safety factors in bone strength. *Calcif Tissue Int*, 53 Suppl 1, S68-74.

- BUJTÁR, P., SÁNDOR, G. K. B., BOJTOS, A., SZÚCS, A. & BARABÁS, J. 2010. Finite element analysis of the human mandible at 3 different stages of life. *Oral Surgery, Oral Medicine, Oral Pathology, Oral Radiology, and Endodontology*, 110, 301--309.
- CUNNINGHAM, R., NARRA, S. P., MONTGOMERY, C., BEUTH, J. & ROLLETT, A. D. 2017. Synchrotron-Based X-ray Microtomography Characterization of the Effect of Processing Variables on Porosity Formation in Laser Power-Bed Additive Manufacturing of Ti-6Al-4V. *The Journal of The Minerals, Metals & Materials Society*, 69, 479-484.
- DALLAGO, M., FONTANARI, V., TORRESANI, E., LEONI, M., PEDERZOLLI, C., POTRICH, C. & BENEDETTI, M. 2018a. Fatigue and biological properties of Ti-6Al-4V ELI cellular structures with variously arranged cubic cells made by selective laser melting. *J Mech Behav Biomed Mater*, 78, 381-394.
- DALLAGO, M., ZANINI, F., CARMIGNATO, S., PASINI, D. & BENEDETTI, M. Effect of the geometrical defectiveness on the mechanical properties of SLM biomedical Ti6Al4V lattices. ECF22 - Loading and Environmental effects on Structural Integrity, 2018b. *Procedia Structural Integrity*, 161-167.
- DE KRIJGER, J., RANS, C., HOOREWEDER, B. V., LIETAERT, K., POURAN, B. & ZADPOOR, A. A. 2017. Effects of applied stress ratio on the fatigue behavior of additively manufactured porous biomaterials under compressive loading. *Journal of the Mechanical Behavior of Biomedical Materials*, 70, 7--16.
- DE WILD, M., SCHUMACHER, R., MAYER, K., SCHKOMMODAU, E., THOMA, D., BREDELL, M., KRUSE GUJER, A., GRATZ, K. W. & WEBER, F. E. 2013. Bone regeneration by the osteoconductivity of porous titanium implants manufactured by selective laser melting: a histological and micro computed tomography study in the rabbit. *Tissue Eng Part A*, 19, 2645-54.
- DI CAPRIO, F., FRANCHITTI, S., BORRELLI, R., BELLINI, C., DI COCCO, V. & SORRENTINO, L. 2022. Ti-6Al-4V Octet-Truss Lattice Structures under Bending Load Conditions: Numerical and Experimental Results. *Metals (Basel)*, 12, 410.
- DU PLESSIS, A., GLASER, D., MOLLER, H., MATHE, N., TSHABALALA, L., MFUSI, B. & MOSTERT, R. 2019. Pore Closure Effect of Laser Shock Peening of Additively Manufactured AlSi10Mg. *3D Printing and Additive Manufacturing*, 6, 245-252.
- DU PLESSIS, A., RAZAVI, N. & BERTO, F. 2020. The effects of microporosity in struts of gyroid lattice structures produced by laser powder bed fusion. *Materials & Design*, 194, 108899.
- DU PLESSIS, A. & ROSSOUW, P. 2015. Investigation of Porosity Changes in Cast Ti6Al4V Rods After Hot Isostatic Pressing. *Journal of Materials Engineering and Performance*, 24, 3137-3141.

- DU PLESSIS, A., YADROITSAVA, I., KROUPRIANOFF, D. & YADROITSEV, I. 2018a. Numerical and experimental study of the effect of artificial porosity in a lattice structure manufactured by laser based powder bed fusion. Solid Freeform Fabrication Symposium – An Additive Manufacturing Conference.
- DU PLESSIS, A., YADROITSAVA, I. & YADROITSEV, I. 2018b. Ti6Al4V lightweight lattice structures manufactured by laser powder bed fusion for load-bearing applications. *Optics & Laser Technology*, 108, 521-528.
- EL-SAYED, M. A., ESSA, K., GHAZY, M. & HASSANIN, H. 2020. Design optimization of additively manufactured titanium lattice structures for biomedical implants. *The International Journal of Advanced Manufacturing Technology*, 110, 2257-2268.
- FROST, H. M. 1987. Bone "mass" and the "mechanostat": a proposal. *Anat Rec*, 219, 1-9.
- FROST, H. M. 2004. A 2003 update of bone physiology and Wolff's Law for clinicians. *Angle Orthod*, 74, 3-15.
- GHOSH, A., KUMAR, A., WANG, X., KIETZIG, A.-M. & BROCHU, M. 2022. Analysis of the effect of surface morphology on tensile behavior of LPBF SS316L microstruts. *Materials Science and Engineering: A*, 831.
- GHOUSE, S., REZNIKOV, N., BOUGHTON, O. R., BABU, S., GEOFFREY NG, K. C., BLUNN, G., COBB, J. P., STEVENS, M. M. & JEFFERS, J. R. T. 2019. The Design and In Vivo Testing of a Locally Stiffness-Matched Porous Scaffold. *Appl Mater Today*, 15, 377-388.
- GONG, H., RAFI, K., GU, H., JANAKI RAM, G. D., STARR, T. & STUCKER, B. 2015. Influence of defects on mechanical properties of Ti-6Al-4V components produced by selective laser melting and electron beam melting. *Materials & Design*, 86, 545-554.
- HARA, T., TAKIZAWA, M., SATO, T. & IDE, Y. 1998. Mechanical properties of buccal compact bone of the mandibular ramus in human adults and children: relationship of the elastic modulus to the direction of the osteon and the porosity ratio. *Bull Tokyo Dent Coll*, 39, 47-55.
- HOFMANN, A. A., BLOEBAUM, R. D. & BACHUS, K. N. 1997. Progression of human bone ingrowth into porous-coated implants. Rate of bone ingrowth in humans. *Acta Orthop Scand*, 68, 161-6.
- HORN, T. J., HARRYSSON, O. L. A., MARCELLIN-LITTLE, D. J., WEST, H. A., LASCELLES, B. D. X. & AMAN, R. 2014. Flexural properties of Ti6Al4V rhombic dodecahedron open cellular structures fabricated with electron beam melting. *Additive Manufacturing*, 1-4, 2-11.
- JESUS, G. P. D., VAZ, L. G., GABRIELLI, M. F. R., PASSERI, L. A., OLIVEIRA, T. V., NORITOMI, P. Y. & JÜRGENS, P. 2014. Finite element evaluation of three methods of stable fixation of condyle base fractures. *International Journal of Oral and Maxillofacial Surgery*, 43, 1251--1256.

- JI, B., WANG, C., LIU, L., LONG, J., TIAN, W. & WANG, H. 2010. A biomechanical analysis of titanium miniplates used for treatment of mandibular symphyseal fractures with the finite element method. *Oral Surg Oral Med Oral Pathol Oral Radiol Endod*, 109, e21-7.
- KAN, W. H., CHIU, L. N. S., LIM, C. V. S., ZHU, Y., TIAN, Y., JIANG, D. & HUANG, A. 2022. A critical review on the effects of process-induced porosity on the mechanical properties of alloys fabricated by laser powder bed fusion. *Journal of Materials Science*, 57, 9818-9865.
- KOVACS, A. E., CSERNATONY, Z., CSAMER, L., MEHES, G., SZABO, D., VERES, M., BRAUN, M., HARANGI, B., SERBAN, N., ZHANG, L., FALK, G., SOOSNE HORVATH, H. & MANO, S. 2023. Comparative Analysis of Bone Ingrowth in 3D-Printed Titanium Lattice Structures with Different Patterns. *Materials (Basel)*, 16, 3861.
- LETTRY, S., SEEDHOM, B. B., BERRY, E. & CUPPONE, M. 2003. Quality assessment of the cortical bone of the human mandible. *Bone*, 32, 35-44.
- LI, S., LI, X., HOU, W., NUNE, K. C., MISRA, R. D. K., CORREA-RODRIGUEZ, V. L., GUO, Z., HAO, Y., YANG, R. & MURR, L. E. 2017. Fabrication of open-cellular (porous) titanium alloy implants: osseointegration, vascularization and preliminary human trials. *Science China Materials*, 61, 525-536.
- MONTALBANO, T., BRIGGS, B. N., WATERMAN, J. L., NIMER, S., PEITSCH, C., SOPCISAK, J., TRIGG, D. & STORCK, S. 2021. Uncovering the coupled impact of defect morphology and microstructure on the tensile behavior of Ti-6Al-4V fabricated via laser powder bed fusion. *Journal of Materials Processing Technology*, 294.
- MURR, L. E., GAYTAN, S. M., RAMIREZ, D. A., MARTINEZ, E., HERNANDEZ, J., AMATO, K. N., SHINDO, P. W., MEDINA, F. R. & WICKER, R. B. 2012. Metal Fabrication by Additive Manufacturing Using Laser and Electron Beam Melting Technologies. *Journal of Materials Science & Technology*, 28, 1-14.
- NAGASAO, T., MIYAMOTO, J. & KAWANA, H. 2009. Biomechanical evaluation of implant placement in the reconstructed mandible. *Int J Oral Maxillofac Implants*, 24, 999-1005.
- ODIN, G., SAVOLDELLI, C., BOUCHARD, P. O. & TILLIER, Y. 2010. Determination of Young's modulus of mandibular bone using inverse analysis. *Med Eng Phys*, 32, 630-7.
- PENG, W. M., CHENG, K. J., LIU, Y. F., NIZZA, M., BAUR, D. A., JIANG, X. F. & DONG, X. T. 2021. Biomechanical and Mechanostat analysis of a titanium layered porous implant for mandibular reconstruction: The effect of the topology optimization design. *Mater Sci Eng C*, 124, 112056.

- PISCOPO, G., SALMI, A. & ATZENI, E. 2019. On the quality of unsupported overhangs produced by laser powder bed fusion. *International Journal of Manufacturing Research*, 14.
- PONADER, S., WILMOWSKY, C. V., WIDENMAYER, M., LUTZ, R., HEINL, P., KÖRNER, C., SINGER, R. F., NKENKE, E., NEUKAM, F. W. & SCHLEGEL, K. A. 2010. In vivo performance of selective electron beam-melted Ti-6Al-4V structures. *Journal of Biomedical Materials Research Part A*, 92A, 56--62.
- SALEM, H., CARTER, L. N., ATTALLAH, M. M. & SALEM, H. G. 2019. Influence of processing parameters on internal porosity and types of defects formed in Ti6Al4V lattice structure fabricated by selective laser melting. *Materials Science and Engineering A*, 767, 138387.
- SEONG, W. J., KIM, U. K., SWIFT, J. Q., HEO, Y. C., HODGES, J. S. & KO, C. C. 2009. Elastic properties and apparent density of human edentulous maxilla and mandible. *Int J Oral Maxillofac Surg*, 38, 1088-93.
- SESSLE, B. J. 2014. *Neural Basis of Oral and Facial Function*. Reference Module in Biomedical Sciences. Elsevier.
- SHEN, Y. W., TSAI, Y. S., HSU, J. T., SHIE, M. Y., HUANG, H. L. & FUH, L. J. 2022. Biomechanical Analyses of Porous Designs of 3D-Printed Titanium Implant for Mandibular Segmental Osteotomy Defects. *Materials (Basel)*, 15, 576.
- SNELL, R., TAMMAS-WILLIAMS, S., CHECHIK, L., LYLE, A., HERNÁNDEZ-NAVA, E., BOIG, C., PANOUTSOS, G. & TODD, I. 2019. Methods for Rapid Pore Classification in Metal Additive Manufacturing. *JOM*, 72, 101-109.
- SONG, J., TANG, Q., FENG, Q., MA, S., GUO, F. & HAN, Q. 2021. Investigation on the modelling approach for variable-density lattice structures fabricated using selective laser melting. *Materials & Design*, 212, 110236.
- SORO, N., ATTAR, H., WU, X. & DARGUSCH, M. S. 2019. Investigation of the structure and mechanical properties of additively manufactured Ti-6Al-4V biomedical scaffolds designed with a Schwartz primitive unit-cell. *Materials Science and Engineering: A*, 745, 195-202.
- TAMATSU, Y., KAIMOTO, K., ARAI, M. & IDE, Y. 1996. Properties of the elastic modulus from buccal compact bone of human mandible. *Bull Tokyo Dent Coll*, 37, 93-101.
- TAN, X. P., TAN, Y. J., CHOW, C. S. L., TOR, S. B. & YEONG, W. Y. 2017. Metallic powder-bed based 3D printing of cellular scaffolds for orthopaedic implants: A state-of-the-art review on manufacturing, topological design, mechanical properties and biocompatibility. *Mater Sci Eng C* 76, 1328-1343.
- TANIGUCHI, N., FUJIBAYASHI, S., TAKEMOTO, M., SASAKI, K., OTSUKI, B., NAKAMURA, T., MATSUSHITA, T., KOKUBO, T. & MATSUDA, S. 2016.

Effect of pore size on bone ingrowth into porous titanium implants fabricated by additive manufacturing: An in vivo experiment. *Mater Sci Eng C* 59, 690-701.

- TÜZEMEN, M. Ç., SALAMCI, E. & ÜNAL, R. 2022. Investigation of the relationship between flexural modulus of elasticity and functionally graded porous structures manufactured by AM. *Materials Today Communications*, 31, 103592.
- VAN EIJDEN, T. M. 2000. Biomechanics of the mandible. *Critical Reviews in Oral Biology & Medicine*, 11, 123-136.
- VAN KOOTWIJK, A., MOOSABEIKI, V., SALDIVAR, M. C., PAHLAVANI, H., LEEFLANG, M. A., KAZEMIVAND NIAR, S., PELLIKAN, P., JONKER, B. P., AHMADI, S. M., WOLVIUS, E. B., TUMER, N., MIRZAALI, M. J., ZHOU, J. & ZADPOOR, A. A. 2022. Semi-automated digital workflow to design and evaluate patient-specific mandibular reconstruction implants. *J Mech Behav Biomed Mater*, 132, 105291.
- VITINS, V., DOBELIS, M., MIDDLETON, J., LIMBERT, G. & KNETS, I. 2003. Flexural and creep properties of human jaw compact bone for FEA studies. *Comput Methods Biomech Biomed Engin*, 6, 299-303.
- VRANA, R., KOUTECKY, T., CERVINEK, O., ZIKMUND, T., PANTELEJEV, L., KAISER, J. & KOUTNY, D. 2022. Deviations of the SLM Produced Lattice Structures and Their Influence on Mechanical Properties. *Materials (Basel)*, 15, 3144.
- VRANA, R., KOUTNY, D., PALOUSEK, D., PANTELEJEV, L., JAROS, J., ZIKMUND, T. & KAISER, J. 2018. Selective Laser Melting Strategy for Fabrication of Thin Struts Usable in Lattice Structures. *Materials (Basel)*, 11, 1763.
- WALTIMO, A. & KÖNÖNEN, M. 1993. A novel bite force recorder and maximal isometric bite force values for healthy young adults. *Scand J Dent Res*, 101, 171-5.
- XIONG, Y., WANG, W., GAO, R., ZHANG, H., DONG, L., QIN, J., WANG, B., JIA, W. & LI, X. 2020a. Fatigue behavior and osseointegration of porous Ti-6Al-4V scaffolds with dense core for dental application. *Materials & Design*, 195.
- XIONG, Y. Z., GAO, R. N., ZHANG, H., DONG, L. L., LI, J. T. & LI, X. 2020b. Rationally designed functionally graded porous Ti6Al4V scaffolds with high strength and toughness built via selective laser melting for load-bearing orthopedic applications. *J Mech Behav Biomed Mater*, 104, 103673.
- YADROITSEV, I., KRAKHMALEV, P. & YADROITSAVA, I. 2015. Hierarchical design principles of selective laser melting for high quality metallic objects. *Additive Manufacturing*, 7, 45-56.
- YÁNEZ, A., FIORUCCI, M. P., CUADRADO, A., MARTEL, O. & MONOPOLI, D. 2020. Surface roughness effects on the fatigue behaviour of gyroid cellular structures obtained by additive manufacturing. *International Journal of Fatigue*, 138, 105702.

- YAVARI, S. A., AHMADI, S. M., WAUTHLE, R., POURAN, B., SCHROOTEN, J., WEINANS, H. & ZADPOOR, A. A. 2015. Relationship between unit cell type and porosity and the fatigue behavior of selective laser melted meta-biomaterials. *Journal of the Mechanical Behavior of Biomedical Materials*, 43, 91--100.
- YAVARI, S. A., WAUTHLE, R., STOK, J. V. D., RIEMSLAG, A. C., JANSSEN, M., MULIER, M., KRUTH, J. P., SCHROOTEN, J., WEINANS, H. & ZADPOOR, A. A. 2013. Fatigue behavior of porous biomaterials manufactured using selective laser melting. *Materials Science and Engineering: C*, 33, 4849--4858.
- ZHANG, B., LI, Y. & BAI, Q. 2017. Defect Formation Mechanisms in Selective Laser Melting: A Review. *Chinese Journal of Mechanical Engineering*, 30, 515-527.
- ZHANG, B., PEI, X., ZHOU, C., FAN, Y., JIANG, Q., RONCA, A., D'AMORA, U., CHEN, Y., LI, H., SUN, Y. & ZHANG, X. 2018. The biomimetic design and 3D printing of customized mechanical properties porous Ti6Al4V scaffold for load-bearing bone reconstruction. *Materials & Design*, 152, 30--39.
- ZHANG, Y., SUN, N., ZHU, M., QIU, Q., ZHAO, P., ZHENG, C., BAI, Q., ZENG, Q. & LU, T. 2022. The contribution of pore size and porosity of 3D printed porous titanium scaffolds to osteogenesis. *Biomater Adv*, 133, 112651.
- ZHAO, S., LI, S. J., HOU, W. T., HAO, Y. L., YANG, R. & MISRA, R. D. K. 2016. The influence of cell morphology on the compressive fatigue behavior of Ti-6Al-4V meshes fabricated by electron beam melting. *J Mech Behav Biomed Mater*, 59, 251-264.
- ZHONG, S., SHI, Q., SUN, Y., YANG, S., VAN DESSEL, J., GU, Y., CHEN, X., LUBBERS, H. T. & POLITIS, C. 2021. Biomechanical comparison of locking and non-locking patient-specific mandibular reconstruction plate using finite element analysis. *J Mech Behav Biomed Mater*, 124, 104849.

Appendices

Appendix A

A Additional information for Chapter 3

A.1 Computed tomography (CT)

A.1.1 Preparation of specimens

Each specimen was wrapped using a thick floral foam, which is made of synthetic plastic, a material that is X-ray blind. The foam and the specimen were placed in a glass test tube (Figure A-1). An effort was made to ensure the specimen was placed upright within the floral foam. Nonporous specimens were installed on a stand without the test tube or floral foam.

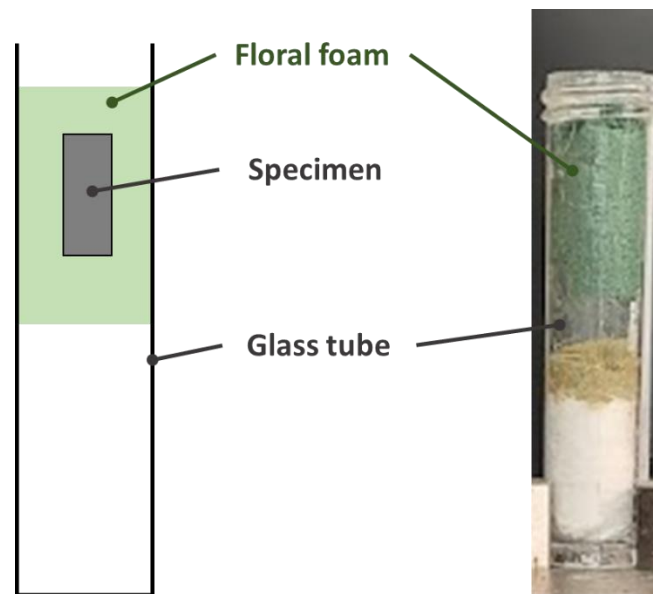


Figure A-1: A schematic of the setup of the porous specimen in the glass test tube with floral foam.

The imaging of the specimen was done using Nikon micro-computed tomography (μ -CT) machine (Nikon Metrology, Brighton, MI, United States) (Figure). Each testing tube was first clamped into a rotating testing stand, which moved the stand in a counterclockwise rotation while exposed to X-ray. A 1.5 mm thick aluminum filter was used to scan the porous constructs. A 0.25 mm copper filter was used to scan the non-porous constructs.

These filters were used to eliminate the effects of beam hardening in the CT images (Barrett and Keat, 2004). A molybdenum target was used for all the scans.

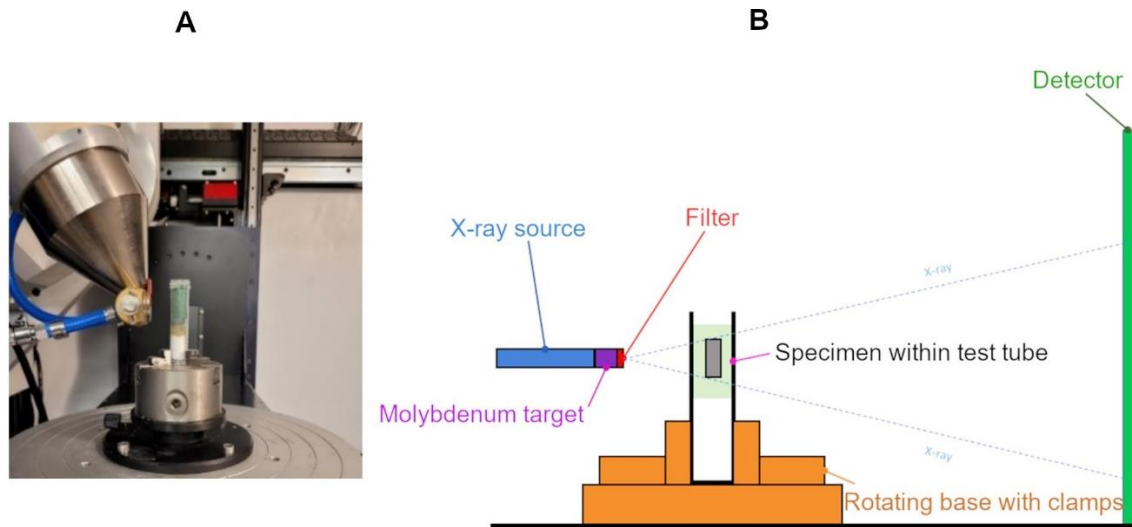


Figure A-2: (A) An image of the specimen loaded into the μ -CT scanning machine. (B) A schematic diagram is shown describing the parts of the μ -CT scanning machine.

X-ray parameters were kept as consistent as possible (Table A-1). However, changes had to be applied as the CT scanner had technical maintenance applied during the experiment, hence why a change in the parameters was necessary. The scanning time was kept the same for each construct at 52 minutes, with an exposure time of one second. Two frames per projection were used, and the total number of projections for each scan was 1570.

Table A-1: X-ray parameters used to scan each of the constructs.

Model Code	Magnification	Filter	Beam Power (kV)	Beam Current (μ A)	Watts (W)
S250-1	33.69	1.5 mm Al	90	140	12.6
S250-2	33.69	1.5 mm Al	90	125	11.3
S350-1	33.69	1.5 mm Al	90	140	12.6
S350-2	33.69	1.5 mm Al	90	125	11.3
S450-1	33.69	1.5 mm Al	90	140	12.6
S450-2	33.69	1.5 mm Al	90	125	11.3
S550-1	33.69	1.5 mm Al	90	140	12.6
S550-2	33.69	1.5 mm Al	90	125	11.3
S650-1	39.52	1.5 mm Al	102	140	17.1
S650-2	33.69	1.5 mm Al	90	125	11.3
SSolid-1	33.69	0.25 mm Cu	115	140	16.1
SSolid-2	33.69	0.25 mm Cu	115	140	16.1

Al – Aluminum; Cu – Copper

A.1.2 Microstructural analysis of the specimen using μ -CT

The CT scanning produced a stacked series of CT images for each specimen, which were reconstructed into three-dimensional (3D) models using CT Pro 3D Software (Nikon Corporation, Minato City, Tokyo, Japan). The CT scanned images were imported into CT Pro 3D software, which produced an initial three-dimensional model from the CT images. The images in the file were then checked to ensure no significant motion occurred during the scanning session. This was done by visually assessing the model to ensure the images were stacked properly and did not show motion evidence. The center of rotation was then determined through manual operation, first by coarse evaluation and subsequently moving into finer evaluations. The center of rotation is finally determined as a set of pixels on the produced model top and bottom. The images were then masked to include the specimen alone. The software reconstructed the CT images.

A.1.3 3D-CT model segmentation and porosity measurements

The segmentation process on the reconstructed 3D-CT model was done using Dragonfly image analysis software (Dragonfly 2022, ORS, Canada). The process of the segmentation was done as follows: 3D-CT models were created from the reconstructed CT images, and each was segmented into 16 smaller rectangular prism sub-models. Each with a volume of about 20 mm^3 (Figure).

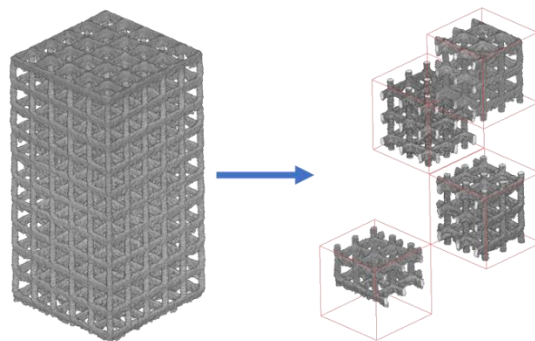


Figure A-3: The 3D-CT model split into smaller sub-models.

A mask rectangular prism shape was used to envelop the sub-model. Everything outside of this mask was removed from the model. The sub-model was then adjusted to be oriented upright, z-axis along the length of the sub-model, with the sagging along the perpendicular

struts facing downwards. The frequency of the voxels-CT density (frequency-density) histogram was then inspected (Figure). Since the only two materials in the sub-model are titanium and air, there were two humps in the histogram, each representing voxels with CT intensities associated with each material.

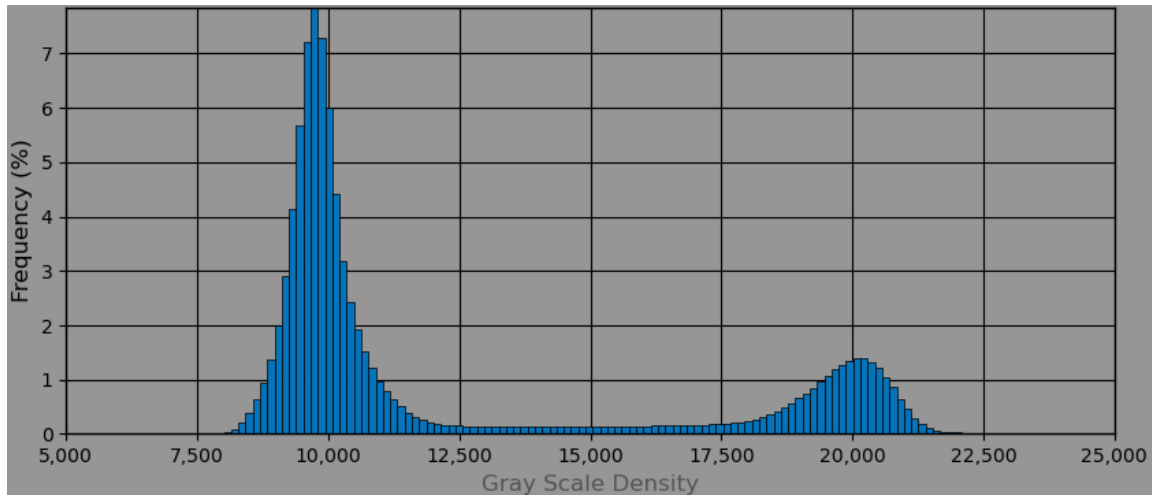


Figure A-4: Representative frequency of the voxels-CT density (frequency-density) histogram. The left hump represents the air voxels, while the right hump represents the titanium alloy voxels.

A contrast window levelling process was then applied, which corrected the white and black coloration in the images by reducing the whites' threshold density and increasing the blacks' threshold density (Figure A-5 A). This would make any voxel with a lower density than the lowest threshold black, while any voxel with a density higher than the highest threshold white. Voxels with densities in between those two thresholds would fall on a grayscale. The histogram is used as a guide to get the appropriate contrast to show as much of the sub-model as possible (Figure A-5 B).

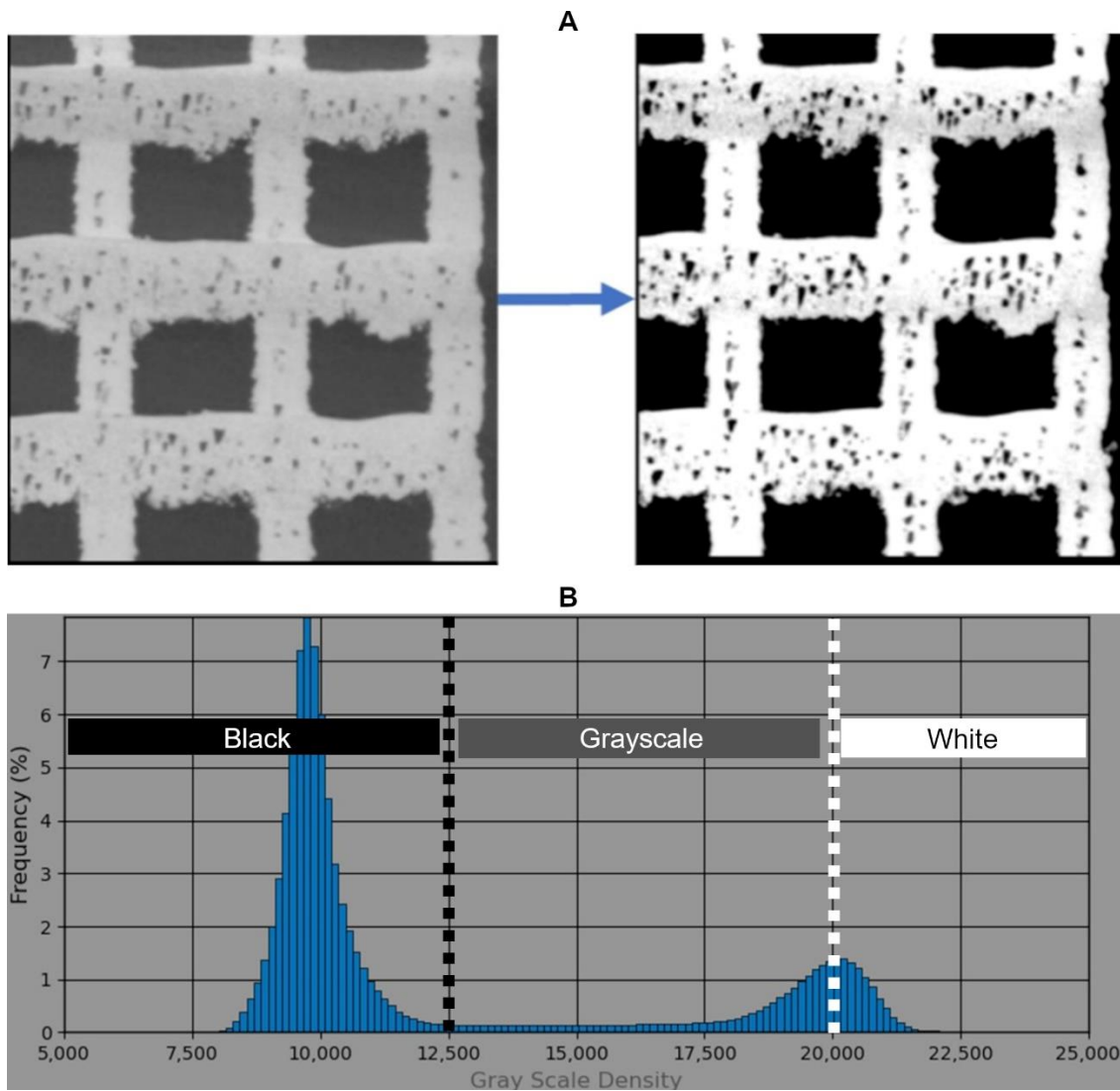


Figure A-5: The window leveling process applied on the CT slices.

(A) Representative 2D slice of a porous Ti6Al4V construct before and after the window leveling process. (B) Frequency-density histogram with the coloration borders superimposed on the histogram.

A calibration of the CT-density values was then applied (Figure A-6). This calibration converts the density values so that the low threshold density chosen is given a value of 0% and the high threshold density chosen is given a value of 100%.

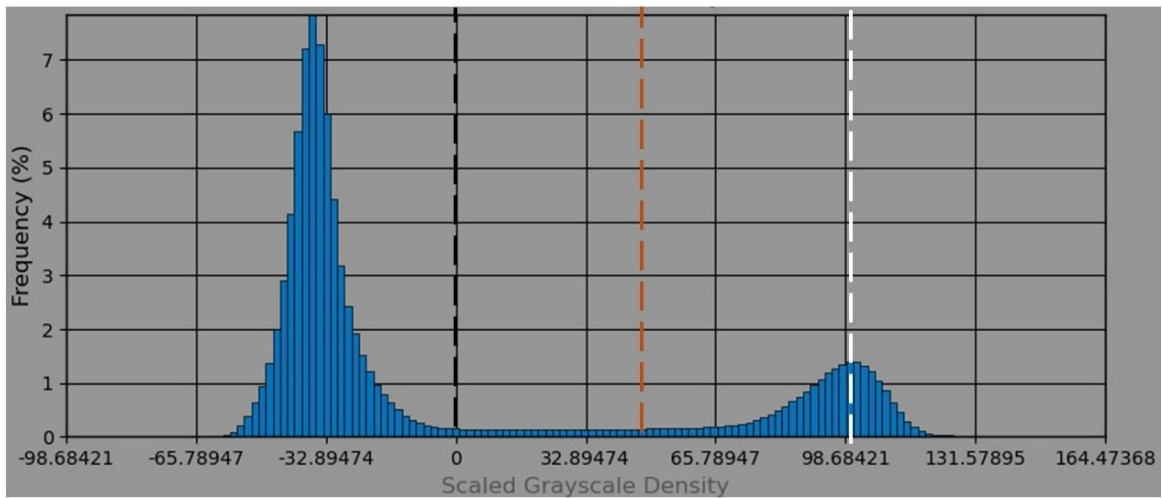


Figure A-6: Frequency-density histogram with the black-white extremes superimposed. A red line represents the 50% calibrated density, the borderline between low and high density.

The segmentation was then done to mark the voxels into regions of interest (ROIs) (Figure A-7).

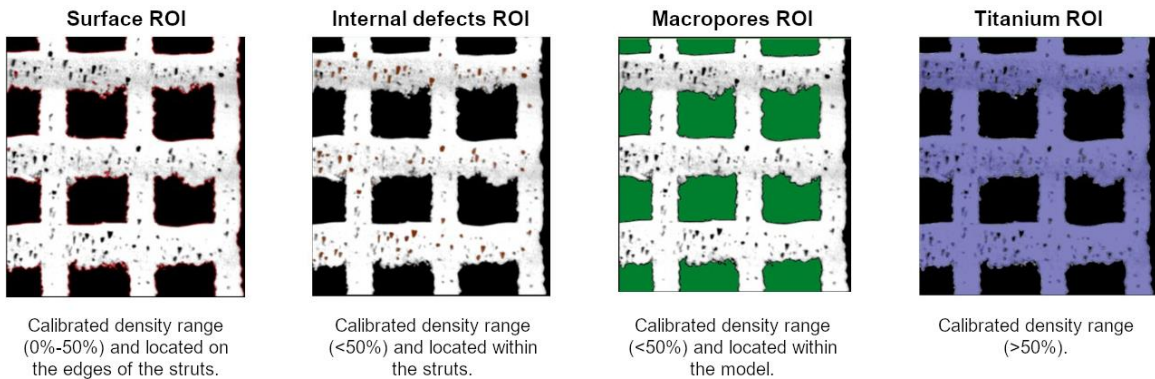


Figure A-7: The ROIs segmented out of the sub-models, along with the criteria established in the segmentation process.

All the ROIs went through the following morphological operations:

- 1) Dilation: expands ROI into neighboring voxels, Kernel size=3, shape=circle
- 2) Closure: expands ROI into neighboring voxels and then takes off any voxels at the edges which have lower densities than indicated range, kernel size=3, shape=circle
- 3) Smooth: takes off voxels from the ROI to ensure no protruding voxels on the edges remain, kernel size = 3, shape = circle.
- 4) Fill inner areas: any voxels within the ROI that are not included are then included.

- 5) Boolean subtraction: used to separate the different ROIs in the event of intersections.
- 6) Remove islands: islands refer to any groups of <7 voxels. These islands are removed using this operation. This step ensures that no artifacts are accidentally included in the ROIs.

The internal defects ROI is further split into smaller ROIs, each representing one of the defects. These ROIs were grouped into a multiple-ROI category to analyze the defects individually. The total volume of each ROI is then measured and compared to the total volume of each sub-model. In addition, the internal defects were then analyzed individually to find their diameters to determine their size values and shapes.

A.1.4 Struts' surface profiles extraction

The struts' surface profiles were extracted from the sub-models using Dragonfly image analysis software (Dragonfly 2022, ORS, Canada). Unless indicated, the following applies to both porous and non-porous constructs.

From each sub-model, two different struts were chosen randomly, one from the struts parallel to the building axis (referred to as parallel struts) and the other from the struts perpendicular to the building axis (referred to as perpendicular struts). In the case of the non-porous CT models, only surfaces that are on the rectangular sides of the constructs were used. Two random surfaces from each sub-model were chosen for the analysis. The surfaces were previously assumed to be located along voxels with 50% scaled density values, so a new surface ROI was created, including all the voxels in the sub-model with 50% scaled density. The desired struts were then masked, and all the other parts of the ROI were excluded. These strut models were converted into STL mesh files (Figure A-8). STL mesh files contain vertices, coordinate points in cartesian format, and faces, which are the elements that form the surface. Both vertices and faces determine the shape of the mesh.

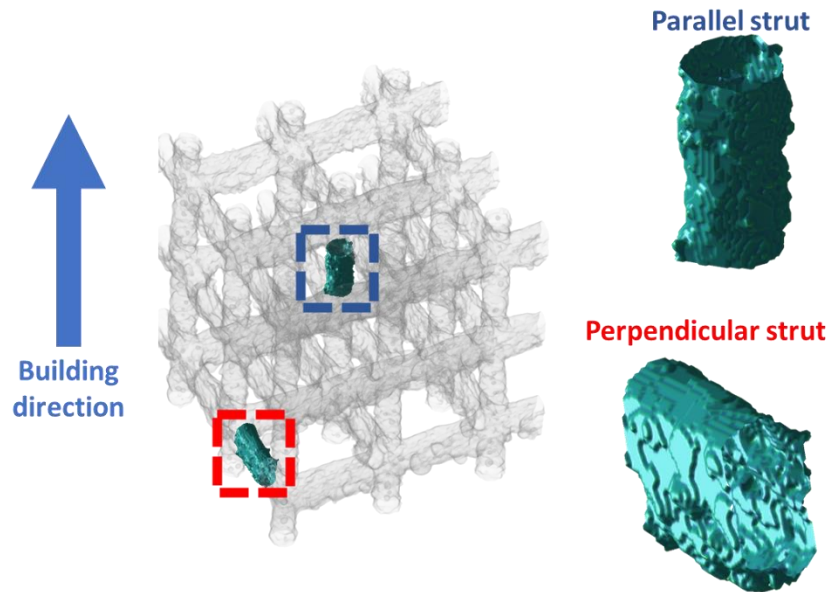


Figure A-8: Examples of struts from one of the sub-models.

The vertices were extracted into Excel files containing the cartesian coordinates of these vertices. In Microsoft Excel software, the coordinates were observed, and vertices pointing to internal defects were deleted. Each Excel file with the coordinate points was then saved for further analysis. A specific specimen code was given to each file in the format 'specimen name'-'orientation,' where orientation is either Z for parallel or XY for perpendicular struts.

A.2 Strut thickness and surface texture analysis

All further analysis of the strut thickness and surface analysis was done using a custom-made MATLAB script. This section explains each step, followed by relevant script commands used to perform these steps.

A.2.1 Preparation and importing of data.

This part of the code cleared all previously recorded data, which avoided overloading the memory space.

```
close all;
clearvars;
```

Specimen information was then provided. This information included the variable name 'Tname'. The Soption variable referred to the orientation of the struts being analyzed. This option was first set as Z for parallel struts, and then switched to XY when analyzing perpendicular struts.

```
Tname=input('Enter specimen name.\n','s');
Soption='Z'; %option can either be Z or XY
```

MATLAB was then prompted to read the Excel file containing the specimen information. The script imports the data into a table (T) of three columns for the X, Y, and Z coordinates.

```
T=
readtable(sprintf('%s',Tname),'Sheet',Soption,'Range','G1:I100000');
```

Due to the removal of coordinates associated with internal defects, some parts of the Excel spreadsheets might be empty. The next step allowed MATLAB to look into Table T and remove any rows with missing or empty cells. In addition, three separate arrays were created for the X, Y, and Z coordinates.

```
T.Properties.VariableNames = ["Var1","Var2","Var3"];
T = rmmissing(T);
x= T.Var1;
x = x(isfinite(x));
y= T.Var2;
y = y(isfinite(y));
z= T.Var3;
z = z(isfinite(z));
```

A.2.2 Initial scatter plot

From the X, Y, and Z coordinates, a 3D point cloud model represents each strut's surface. First, a matrix made of the three arrays x, y, and z was created, and the coordinates were then centered along the geometrical centroid of the model.

```
point=[x y z];
midxy=mean([max(point);min(point)]);
x=(point(:,1)-midxy(1));
y=point(:,2)-midxy(2);
z=point(:,3)-midxy(3);
point=[x y z];
optCloud = pointCloud(point);
figure1 = figure;
axes1 = axes(Parent=figure1);
pcshow(optCloud,Parent=axes1,AxesVisibility='on');
set(gcf,'color','w');
set(gca,'color','w','XColor','black','YColor','black',
'ZColor','black');
xlabel('X');
ylabel('Y');
zlabel('Z');
title('3-D Point Cloud',FontSize=14)
```

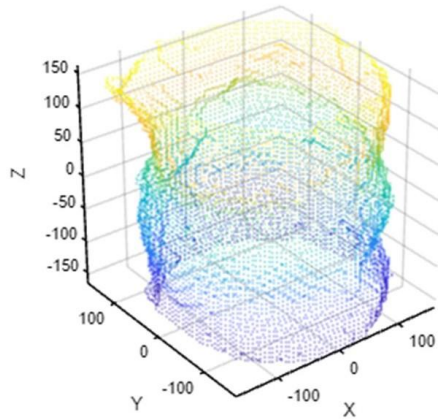


Figure A-9: The strut surface vertices shown in cartesian coordinates.

A.2.3 Rotation of the strut (only for perpendicular struts)

Given that the rest of the code only works if the struts were standing upright along the Z-axis, the next step involved rotating perpendicular struts to have their length axis parallel to the Z-axis.

```

if Soption=='XY')
Rotaxis=input('Enter axis of rotation\n','s');
Rotaxis=upper(Rotaxis);
if Rotaxis == ('X')
rotationAngles = [90 0 0];
translation = [0 0 0];
tform = rigidtransform3d(rotationAngles,translation);
elseif Rotaxis ==('Y')
rotationAngles = [0 90 0];
translation = [0 0 0];
tform = rigidtransform3d(rotationAngles,translation);
end
ptCloud = pctransform(optCloud,tform);
else
ptCloud=optCloud;
end
figure3 = figure;
axes2 = axes(Parent=figure3);
fig(1)=pcshow(ptCloud,Parent=axes2,AxesVisibility='on');
set(gcf,'color','w');
set(gca,'color','w','XColor','black','YColor','black',
'ZColor','black');
xlabel('X');

```

```
ylabel('Y');
xlabel('Z');
title({'Rotation of 3-D Point Cloud'},FontSize=14)
hold off;
```

A.2.4 Strut thickness measurement

The strut thickness values were measured through ellipses that fit the cross-section of the struts. First, the x, y and z coordinates were reassigned from the point cloud into three arrays: *xf*, *yf*, and *zf*.

```
xf=ptCloud.Location(:,1);
yf=ptCloud.Location(:,2);
zf=ptCloud.Location(:,3);
```

An ellipse was then fit into the plot of the *xf-yf*. The fit was done using an imported function, written by Gal (2023), which fits an ellipse using least square estimation. The output is an ellipse's fit equation corresponding to the strut's vertices points.

```
ellipse_t = fit_ellipse(xf,yf);
Nb=numel(zf)-1;
```

From the ellipse fits, a set of cartesian points were extracted in three arrays, *eX*, *eY* and *eZ*, each representing the X-coordinates, Y-coordinates, and Z-coordinates of the ellipse, respectively. This was done using an imported function written by Long (2023). The code converted the ellipse and strut cartesian coordinates into polar coordinates. The ellipse polar coordinates were then used to measure the major and minor lengths of the ellipse. The strut thickness is calculated as the average of the major and minor lengths of the ellipse. Both the ellipse and the strut polar coordinates were then plotted.

```
[radm,the,co,si,radn,xpos]=ellipse(ellipse_t.a,ellipse_t.b,ellipse_
t.phi,ellipse_t.X0,ellipse_t.Y0,'',Nb);
eX=radm*cos(the)*co-si*radn*sin(the)+xpos;
eY=radm*cos(the)*si+co*radn*sin(the)+xpos;
eX=eX(:);
eY=eY(:);
eZ=zf;
[eth,eh,espan]=cart2pol(eX,eY,eZ);
ellipsemajor=max(eh)*2;
ellipseminor=min(eh)*2;
strutthickness = (ellipsemajor+ellipseminor)/2;
lam=(ellipse_t.a-ellipse_t.b)/(ellipse_t.a+ellipse_t.b);
```

```

perimeter=pi*((ellipse_t.a+ellipse_t.b))*(1+((3*lam*lam)/(10+sqrt(4-
(3*lam*lam)))));
[fth,fh,fspan]=cart2pol(xf,yf,zf);
Figure
fig(2)=polarscatter(fth,fh,"green",".");
hold on;
fig(3)=polarscatter(eth,eh,"m",".");
hold off;

```

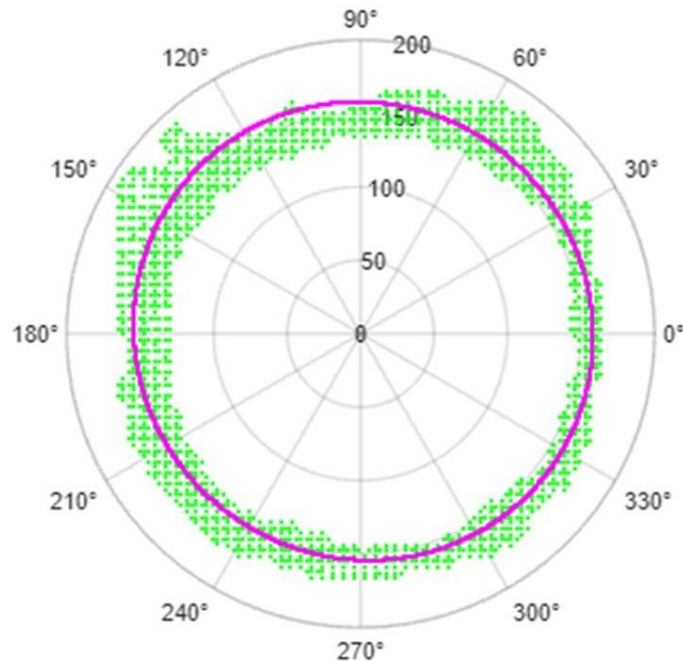


Figure A-10: The vertices of the strut surface shown on a polar plot (green) and the best fit ellipse formed from the polar plot vertices (pink).

A.2.5 Defining the height, span and radial angle of the vertices of the surface profile

The polar coordinates consist of the span length (span), radial angle (th) and height (h). These values were defined into independent variables as they were used in the surface roughness analysis.

The height is the distance between the point (0,0) and the vertices. The unit of measurement is μm . The span length is the location of each vertex along the length of the strut, defined as the z-axis. The span length has a minimum value of 0 and a maximum value equal to the length of the measured strut. The unit of measurement is μm . Finally, the radial angle

(normally defined as θ but written as th in the script) is the arc measured between the horizontal surface and the vertices. The radial angle ranges between 0 and 2π and is measured in radians.

```
h=fh;
span=fspan;
span=span-min(span);
th=fth+pi;
```

A.2.6 Creating gridded data

Ideally, the surface mesh profile is taken directly from the STL's vertices and faces when doing the surface roughness analysis. However, the surface profiles extracted in this study were highly irregular, with many defects and intersections of vertices in the mesh profile. Hence, the mesh required a rearrangement along the vertices. This was done by applying a linear square fit on the vertices, creating three 500×500 matrices, each representing either the height (Gh), span (Gspan) or radial angle (Gth). By stacking these matrices together, a 3D surface mesh represents the struts' surface profile. When plotted, this surface represented the 'rolled out' strut surface profile.

```
Separation=500;
minth=min(th);
maxth=max(th);
minspan=min(span);
maxspan=max(span);
thlin=linspace(minth,maxth,Separation);
spanlin=linspace(minspan,maxspan,Separation);
[Gth,Gspan]=meshgrid(thlin,spanlin);
Gh=griddata(th,span,h,Gth,Gspan);
```

All further steps in this analysis required that no gaps or missing data exist. In surface contour analysis, missing data normally existed around the edges of the surface profile. First, the missing data points were identified.

```
TFth1=isnan(Rawhth);
nTFth1=numel(find(TFth1(:)==1));
```

If any data points were found to be missing, a 2×2 mean filter was used over the whole surface profile. A second check was done to ensure no missing information remained within the surface profile.

```

if nTFth1>0
Rawhth1=fillmissing(Rawhth, 'movmean', 2, 1);
Rawhth=fillmissing(Rawhth1, 'movmean', 2, 2);
end
TFth2=isnan(Rawhth);
nTFth2=numel(find(TFth2(:)==1));

```

If any further missing data existed after the previous checks. The edges were trimmed to get rid of these missing data points. This step would remove 10 cells from all sides of the surface profile. If that does not fix the missing data, then a second 20 cells trim occurs. Note that the second step was used as a last resort measure and might have caused loss of viable data points.

```

if nTFth2>0
[NaNrows, NaNcolumns] = find(isnan(Rawhth));
NaNrows=numel(unique(NaNrows));
NaNcolumns=numel(unique(NaNcolumns));
removalthresh=10;
Separationmax=Separation-removalthresh;
Separationmin=removalthresh;
Gth=Gth(Separationmin:Separationmax, Separationmin:Separationmax);
Gspan=Gspan(Separationmin:Separationmax, Separationmin:Separationmax);
Rawhth=Rawhth(Separationmin:Separationmax, Separationmin:Separationmax);
TFth3=isnan(Rawhth);
nTFth3=numel(find(TFth3(:)==1));
if nTFth3>0
[NaNrows, NaNcolumns] = find(isnan(Rawhth));
NaNrows=numel(unique(NaNrows));
NaNcolumns=numel(unique(NaNcolumns));
removalthresh=20;
Separationmax=Separation-removalthresh;
Separationmin=removalthresh;
Gth=Gth(Separationmin:Separationmax, Separationmin:Separationmax);
Gspan=Gspan(Separationmin:Separationmax, Separationmin:Separationmax);
Rawhth=Rawhth(Separationmin:Separationmax, Separationmin:Separationmax);

```

A final check of any missing data was done to ensure no missing data existed.

```

TFth4=isnan(Rawhth);
nTFth4=numel(find(TFth3(:)==1));

```

```
end
end
```

While several measures were taken to remove outliers, it might be inevitable to have some outliers or displaced mesh elements. A 3D (2×2×2) median filter was applied to remove these outliers.

```
Gh = medfilt3(Rawhth);
```

Reference span and radial angle arrays were created using linear spacing according to the number of vertices. This was done because some values were taken out during the filtering process, and no filtering process can proceed without having a value of the span length and radial angle for each height value.

```
nx=height(Gh);
thref = unique(Gth');
thref = thref(:)';
thref=linspace(min(thref),max(thref),nx);
spanref = unique(Gspan');
spanref = spanref(:)';
spanref=linspace(min(spanref),max(spanref),nx);
```

A.2.7 Generating the surface profile for roughness analysis

At this point, the surface profile was in its raw form when plotted.

```
figure
fig(4)=mesh(Gth,Gspan,Gth);
hold on;
view([-48 66])
xlabel('Radial Angle (radians)', 'Interpreter', 'none');
ylabel('Axial Length (microns)', 'Interpreter', 'none');
zlabel('Height (microns)', 'Interpreter', 'none');
title('Raw Surface with the arc ');
hold off;
```

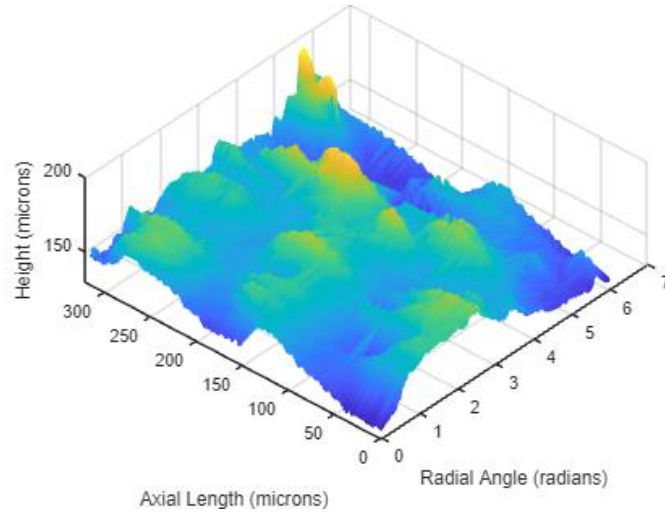



Figure A-11: The surface of the strut with the polar coordinates shown in rectangular form.

The next step was to filter out the surface features that are irrelevant in the roughness analysis. This includes the form shape (also known as nominal shape) of the struts and the features smaller than the overall voxel size. The filtering process starts with a high-pass Gaussian filter that takes off the small features of the surface profile. This filter was applied over each 10 data points along the span length and the minimum difference between two consecutive points along the radial angle. The outcome was called the S-surface, and the script generates both this surface and the removed surface.

```
mindth=min(nonzeros(unique(abs(th(:)))));
mindspan=min(nonzeros(unique(abs(span(:)))));
differenceth=nonzeros(abs(th(:))-(mindth));
differencespan=nonzeros(abs(span(:))-(mindspan));
maxdiffth=abs(max(differenceth));
mindiffth=abs(min(differenceth));
maxdiffspan=abs(max(differencespan));
mindiffspan=abs(min(differencespan));
S1 = smoothdata(Gh,"gaussian",mindiffth,"SamplePoints",thref);
S= smoothdata(Gh,"gaussian",10,"SamplePoints",spanref);
RemovedS=R-S;
SSurface=S;
figure
fig(5)=mesh(Gth,Gspan,SSurface);
hold on;
view([-48 66])
xlabel('Radial Angle (radians)', 'Interpreter', 'none');
```

```
ylabel( 'Axial Length (microns)', 'Interpreter', 'none' );  
zlabel( 'Height (microns)', 'Interpreter', 'none' );  
title('S-Surface');  
hold off;  
figure  
fig(6)=mesh(Gth,Gspan,RemovedS);  
hold on;  
view([-48 66])  
xlabel( 'Radial Angle (radians)', 'Interpreter', 'none' );  
ylabel( 'Axial Length (microns)', 'Interpreter', 'none' );  
zlabel( 'Height (microns)', 'Interpreter', 'none' );  
title('Removed-S-Surface');  
hold off;
```

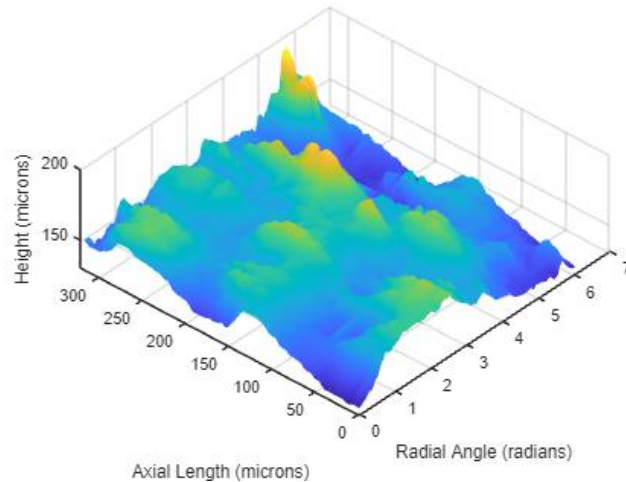


Figure A-12: The surface plot after the gaussian filter (S-filter) is applied to the raw surface.

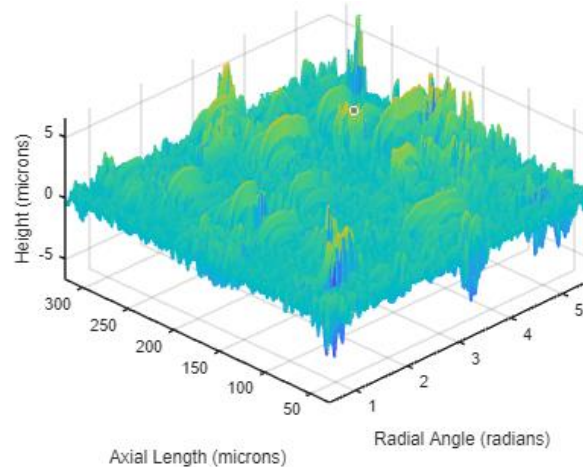


Figure A-13: The removed part of the surface plot after applying the S-filter.

The form shape was removed using the detrend function in MATLAB. This function detected the form shape and subtracted it from the S-surface. The resulting surface is called the primary surface profile and was given the variable name 'P'.

```
SF1= detrend(S,"SamplePoints",thref);
P= detrend(SF1,"SamplePoints",spanref);
F=R-P;
figure
fig(7)=mesh(Gth,Gspan,F);
hold on;
view([-48 66])
xlabel('Radial Angle (radians)', 'Interpreter', 'none');
ylabel('Axial Length (microns)', 'Interpreter', 'none');
zlabel('Height (microns)', 'Interpreter', 'none');
```

```
title('RemovedF-Surface');
hold off;
```

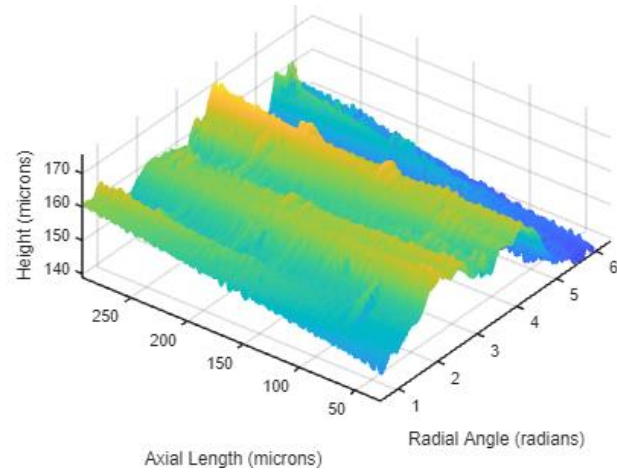


Figure A-14: The removed form surface from the plot. This surface represents the curvature of the strut shape.

```
figure
fig(8)=mesh(Gth,Gspan,P);
hold on;
view([-49.8 35.9])
colorbar
xlabel('Radial Angle (radians)', 'Interpreter', 'none');
ylabel('Axial Length (microns)', 'Interpreter', 'none');
zlabel('Height (microns)', 'Interpreter', 'none');
title('SF-Surface');
hold off;
```

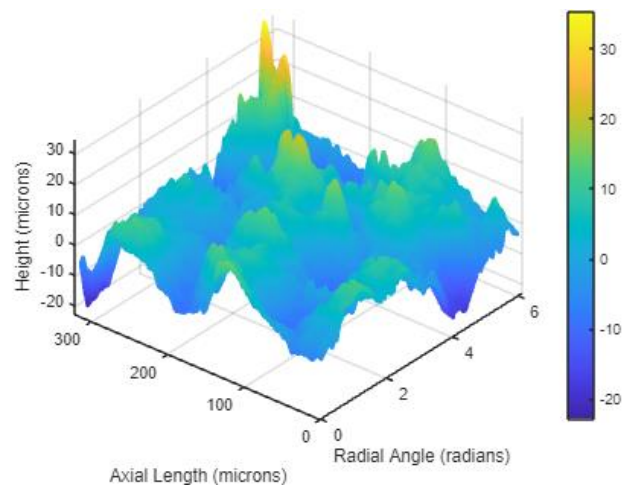


Figure A-15: The SF-surface plot. This is the primary surface plot that is used in the surface texture measurements.

A.2.8 Analysis of the surface texture parameters

The next step was to detect the locations of the peaks and valleys and coordinate locations along the primary surface.

```
iPPeak=imregionalmax(P);
iPValley=imregionalmin(P);
PPeakh=P(iPPeak);
PPeakth=Gth(iPPeak);
PPeakSpan=Gspan(iPPeak);
PValleyh=P(iPValley);
PValleyth=Gth(iPValley);
PValleySpan=Gspan(iPValley);
```

Then an analysis of the surface texture was done to find the arithmetic mean height (P_a), and maximum peak-to-valley height (P_z). Finally, the results were exported into a spreadsheet table, and the figures were automatically saved.

```
AP=abs(P);
area=eSpan*perimeter;
SumP=sum(AP(:));
Pa=SumP/area;
Pp=max(PPeakh);
Pv=abs(min(PValleyh));
Pz=Pp+Pv;
```

A.2.9 Roughness analysis of the non-porous constructs

The MATLAB script used to analyze the surface texture and roughness of the non-porous constructs was similar to that used in the porous constructs. However, several script sections were not used (A.2.3, A.2.4, and A.2.5). The variables used to plot the surface profile were the profile height, x-length, and y-length. The surfaces analyzed in the non-porous constructs were oriented perpendicularly to the x-axis and y-axis. Hence, the surface needed to be laid down on the X-Y plane to allow the rest of the code to be operable.

```
Points=[x y z];
Points=unique(Points,'rows');
xp=Points(:,1);
yp=Points(:,2);
```

```

zp=Points(:,3);
midxy=mean([max(point);min(point)]);
cx=(point(:,1)-midxy(1));
cy=point(:,2)-midxy(2);
cz=point(:,3)-midxy(3);
axis=input('Enter axis of rotation\n','s');
axis=upper(axis);
if axis == ('X')
AxisMes=sprintf('X');
Points=[cz cy cx];
x=cz;
y=cy;
h=cx;
elseif axis ==('Y')
AxisMes=sprintf('Y');
Points=[cz cx cy];
x=cz;
y=cx;
h=cy;
end
figure
fig(2)=scatter3(x,y,h, '.');
xlabel('x (microns)', 'Interpreter', 'none' );
ylabel('Y (microns)', 'Interpreter', 'none' );
zlabel('Height (microns)', 'Interpreter', 'none' );
hold off;

```

A.3 The material properties of Ti6Al4V for use in FEA analysis

The material properties used in the FEA analysis of Ti6Al4V are summarized in Table A-. The detailed process of determining the material properties is provided in this section.

Table A-2: Material properties used in FEA models.

Density	4.42 g/cm ³
Young's modulus	102.763 GPa
Poisson's Ratio	0.342
Plastic properties	Interpolation from the plastic region of TSolid
Damage Initiation	Fracture Strain = 0.077; Stress Triaxiality = 0.33; Strain Rate= 0
Damage Evolution	Type: Displacement; Softening: Linear; Degradation: Maximum; Displacement at Failure: 0.067

A.3.1 Density and Poisson's ratio

The density of the Ti6Al4V was taken from the provider of the Ti6Al4V powder (Renishaw PLC, 2017). Poisson's ratio was derived from data found in the literature (Peng et al., 2020).

A.3.2 Young's modulus

The Young's modulus value used in the FEA analysis was derived from the results of mechanical tests done on 10 non-porous Ti6Al4V tensile tests (Table A-3). The mean Young's modulus of these tests was 102.76 ± 12.0 GPa.

Table A-3: The Young's modulus (E_T) values obtained from mechanical tests on non-porous Ti6Al4V specimens.

	1	2	3	4	5	6	7	8	9	10
E_T (GPa)	86.53	110.52	104.36	112.68	93.82	113.86	88.91	121.75	104.92	90.28

A.3.3 Plastic properties

The plastic properties were introduced to ABAQUS to simulate the proportionality limit point, yield point (0.2% offset) and peak point (the point where the ultimate tensile strength was recorded). These values were derived from the mechanical tests on nonporous Ti6Al4V constructs. The proportionality limit is the point at which the curve switches from elastic to plastic loading region. The elastic limit (Table A-4) was found to occur on average stress of 512.16 ± 220 MPa and a strain level of 0.005 ± 0.003 . It should be noted that this value had a high level of variation between the different specimens. The yield point (Table A-5) was found to occur on average at a stress of 866.42 ± 33.71 MPa and a strain level of about 0.0103 ± 0.001 . The peak point (Table A-6) was found to occur on average at a stress of 1038.98 ± 28.89 MPa and a strain level of about 0.077 ± 0.010 .

Table A-4: The elastic limit strength (σ_{PT}) and strain (ϵ_{PT}) values obtained from mechanical tests on non-porous Ti6Al4V specimens.

	1	2	3	4	5	6	7	8	9	10
ϵ_{PT}	0.008 8	0.003 7	0.00 3	0.002 9	0.009	0.003 1	0.009 1	0.001 7	0.004 7	0.007 8
σ_{PT} (GPa)	735.3 2	392.7 7	303	315.8 1	816.0 4	339.6 8	789.3 4	267.2 8	475.5 6	686.8 4

Table A-5: The yield point strength (σ_{TY}) and strain (ϵ_{TY}) values obtained from mechanical tests on non-porous Ti6Al4V specimens.

	1	2	3	4	5	6	7	8	9	10
ϵ_{TY}	0.0112	0.0096	0.0101	0.0095	0.0114	0.0099	0.0117	0.0081	0.0102	0.0119
σ_{TY} (MPa)	804.93	849.09	856.74	859.79	891.55	910.34	877.79	828.06	878.21	907.71

Table A-6: The peak strength (σ_{UTS}) and strain (ϵ_{UTS}) values obtained from mechanical tests on non-porous Ti6Al4V specimens.

	1	2	3	4	5	6	7	8	9	10
ϵ_{UTS}	0.093 6	0.0615	0.075	0.0813	0.0799	0.0709	0.0782	0.0808	0.0863	0.0634
σ_{UTS} (MPa)	973.0 5	1023.8 6	1050.5 6	1036.7 4	1047.0 2	1087.6 1	1046.0 4	1027.6 2	1049.4 2	1047.9 1

The calibration tool in Abaqus was used to interpolate the plastic region expected for Ti6Al4V. The estimated plastic region is plotted into a stress-plastic strain curve (Figure A-16). Plastic strain is found by subtracting the elastic strain from the total strain value. In this case, the strain at the elastic limit is subtracted from the strain values.

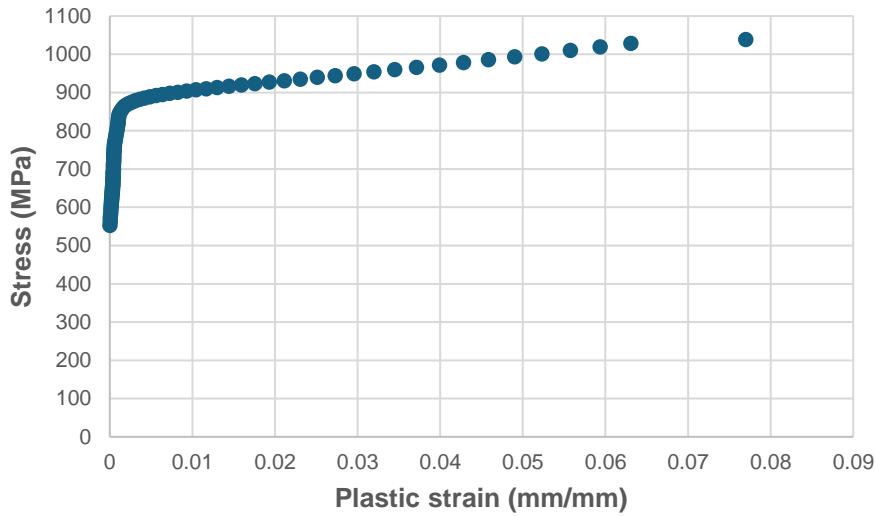


Figure A-16: The stress-plastic strain plastic behaviour of Ti6Al4V used in the FEA analysis.

A.3.4 Damage simulation

The ductile damage settings consist of the ductile damage initiation and the evolution of the ductile damage. The fracture strain, the stress triaxiality, and the damage evolution were determined using the methods described by Wagner (2021). The failure strain is normally calculated at the x-intercept of a line parallel to the elastic region of the stress-strain curve. However, given that failure was seen to occur almost instantaneously in the mechanical tests, the strain at failure was used in setting up this simulation. In this study, the failure strain was about 0.077. Stress triaxiality is the ratio of hydrostatic stress to the von Mises equivalent stress. The hydrostatic stress (p) can be calculated as one-third of the sum of principal stresses at the three different axes (σ_x , σ_y , and σ_z). Von Mises stress (σ_v) is a scalar value of stress, which is defined as the uniaxial tensile stress that would create the same distortion levels as that created by the combined applied stresses (Logan, 2012). The von Mises stress is calculated using Equation equation 3-1. The stress triaxiality (η) is normally calculated using the following equation:

$$\eta = \frac{-p}{\sigma_v} = \frac{-\frac{1}{3}(\sigma_x + \sigma_y + \sigma_z)}{\sigma_x} \quad (\text{A-1})$$

Since the loading process used here was uniaxial tensile loading, the σ_v was approximately equivalent to σ_x . At the same time, the σ_y and σ_z as well as all shear stresses were close to zero. Thus, the stress triaxiality value was set to 0.33. In this study, it is presumed that the Ti6Al4V behaviour is not affected by the strain rate under room temperature conditions. This stress triaxiality value has been used in several previous works of modelling Ti6Al4V in FEA, such as the work done by Yáñez et al. (2020).

Simplified damage evolution settings were established since fractures in SLM constructs were seen to happen almost instantaneously in SLM-built constructs. Damage evolution was defined to have a linear softening, meaning that damage evolution from damage initiation to complete failure is linear. The displacement was used to define the damage evolution, with the displacement at failure at 0.067 mm, which was found through trial and error. The following equation defines damage evolution:

$$d = -1\left(\frac{\sigma_{\text{failure}}}{\bar{\sigma}_{\text{failure}}} - 1\right) \quad (\text{A-2})$$

Where d is the damage evolution ranging between 0 and 1, with 1 meaning that the element failed. σ_{failure} is the true stress while $\bar{\sigma}_{\text{failure}}$ is the stress had the model maintained perfect plastic behaviour. As damage evolution occurred, d increases within the elements. In this study, the value of d was limited to a range between 0 and 0.1 to simulate a rapid failure.

Given all these properties, the results of the FEA model of the tensile loading of a non-porous model showed mechanical properties close to those seen in the mechanical tests done on 3D-printed constructs. The plot below (Figure A-17) compares the non-porous tensile model (blue) to the results of tensile loading of non-porous constructs.

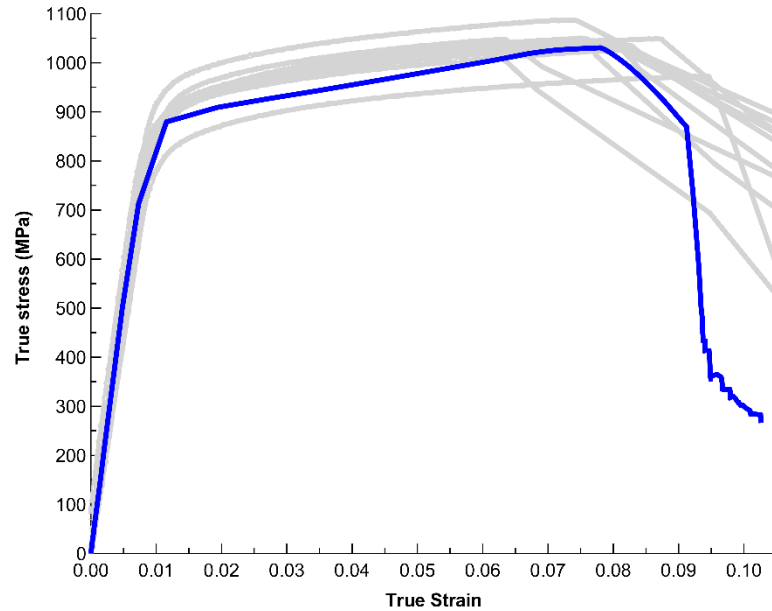


Figure A-17: The FEA simulation of tensile loading of a non-porous Ti6Al4V model (blue) compared to the results of the tensile tests done on SLM-printed constructs (n=10) (grey).

A.4 Determining the appropriate lattice properties for mandibular reconstruction

Using the regression fits obtained from the mechanical tests (Table A-7), the optimal pore geometry could be determined for use in mandibular reconstruction.

Table A-7: Equations of the fits of the mechanical properties depending on strut thickness (t).

	SLM	FEA S-Section	FEA C-section
Young's Modulus (E_T)	$E_T = e^{-5.93+1.53 \ln t}$	$E_T = e^{-4.04+1.26 \ln t}$	$E_T = e^{-6.63+1.63 \ln t}$
Yield Stress (σ_{TY})	$\sigma_{TY} = e^{-5.38+1.76 \ln t}$	$\sigma_{TY} = e^{-2.46+1.33 \ln t}$	$\sigma_{TY} = e^{-4.96+1.69 \ln t}$
Ultimate Tensile Strength (σ_{UTS})	$\sigma_{UTS} = e^{-5.46+1.79 \ln t}$	$\sigma_{UTS} = e^{-2.96+1.43 \ln t}$	$\sigma_{UTS} = e^{-5.86+1.85 \ln t}$
Tensile Toughness (T_T)	$T_T = 0.2e^{0.006t}$	$T_T = 1.2e^{0.004t}$	$T_T = 0.7e^{0.005t}$
Flexural Modulus (E_F)	$E_F = e^{-6.60+1.62 \ln t}$	$E_F = e^{-4.56+1.34 \ln t}$	$E_F = e^{-7.22+1.72 \ln t}$
Flexural yield stress (σ_{FY})	$\sigma_{FY} = e^{-6.07+1.93 \ln t}$	$\sigma_{FY} = e^{-3.12+1.49 \ln t}$	$\sigma_{FY} = e^{-5.82+1.87 \ln t}$
Flexural strength (σ_F)	$\sigma_F = e^{-6.79+2.07 \ln t}$	$\sigma_F = e^{-3.92+1.64 \ln t}$	$\sigma_F = e^{-6.94+2.08 \ln t}$
Flexural Toughness (T_F)	$T_F = e^{-9.28+1.56 \ln t}$	$T_F = e^{-7.80+1.37 \ln t}$	$T_F = e^{-10.21+1.72 \ln t}$

The mechanical properties for mandibles were established as per previous literature. Table A-8 shows the material properties of cortical bones for the comparative analysis.

Table A-8: Mechanical properties of mandibular cortical bones

Mechanical Property	Minimum	Maximum	References
E_Y - Young's Modulus (GPa)	10	31	(Bujtár et al., 2010; Nagasao et al., 2009; Seong et al., 2009)
σ_{UTS} - Ultimate Tensile Strength (MPa)	-	130	(Nagasao et al., 2009; van Eijden, 2000)
E_F - Flexural Modulus (GPa)	5	21	(Hara et al., 1998; Lettry et al., 2003; Odin et al., 2010; Tamatsu et al., 1996)
σ_F - Flexural Strength (MPa)	-	120	(Vitins et al., 2003)

From these fits, along with information from the literature and observations from the preliminary studies, criteria were set to determine the optimal pore geometry that could be used in mandibular implants (Table A-9). These criteria considered the reproducibility of the struts and the optimal pore sizes for bone ingrowth.

Table A-9: The optimal design criteria and limitations for the lattice constructs.

Objective	Design Criteria
Countering Stress Shielding	$16 \text{ GPa} \leq E_T \leq 31 \text{ GPa}$
Maintaining Tensile Strength	$\sigma_{UTS} \geq 135 \text{ MPa}$
Maintaining Yield Strength	$\sigma_{FY} \geq 80 \text{ MPa}$
Disallow localized yielding	$\sigma_v \leq 866 \text{ MPa}$
Reproducible struts	$350 \mu\text{m} \leq \text{Strut Thickness} \leq 1000 \mu\text{m}$
Allowing Healthy Bone Ingrowth	$\text{Pore Size} \geq 300 \mu\text{m}$

The strut thicknesses that would fit the stiffness criteria to avoid stress shielding ranged between 324 and 432 μm (Table A-10).

Table A-10: The optimal strut thickness of lattice constructs at different mandible bone parts, according to Young's modulus values of cortical bones.

Mandible Part	Young's Modulus of Cortical Bone Part (GPa)	Range of Optimal Strut Thickness (μm)	Mean Optimized Strut Thickness (μm)
Symphysis	18.9 – 22.23	329 – 366	348
Body	16.1 – 20.5	296 – 347	322
Angle	21.3 – 25.7	356 – 403	380
Ramus	20.78 – 28.7	350 – 433	392
Coronoid	25.6 – 31.2	401 – 457	429

To confirm the matching of the mechanical strength criteria, the other fits are used with the given range of strut thicknesses (Table A-11). Strut thicknesses between 350 and 450 μm satisfied both the reproducibility and bone growth criteria.

Table A-11: The strength properties of the constructs built with the optimized strut thicknesses as well as the standard strut thicknesses used in the mechanical tests. All the values provided are calculated from the previously found fits (Table A-1). The strut thicknesses that were tested in this study are marked with an Asterix (*).

Strut Thickness (μm)	Young's Modulus (GPa)	Tensile Yield Strength (MPa)	UTS (MPa)	Flexural Modulus (GPa)	Flexural Yield Strength (MPa)	Flexural Strength (MPa)	Pore Size (μm)
324	18.3	117.5	134.0	15.9	161.9	177.0	676
350*	20.5	134.5	153.8	18.0	187.9	207.7	650
382	23.5	156.7	179.9	20.7	222.4	248.9	618
395	24.7	166.2	191.0	21.9	237.3	266.7	605
432	28.4	194.4	224.2	25.3	282.0	321.1	568
450*	30.2	208.8	241.2	27.0	305.2	349.4	550
460	31.2	216.9	250.9	28.0	318.4	365.6	540

A.5 Comparison between the FEA models with and without structural imperfections

The FEA models were designed without reflecting structural imperfections, such as internal defects and surface roughness. This was done to ensure the detailed flexural and tensile models, especially models with struts, which are in the range of 1.2×10^5 and 7.0×10^5 elements, could be solved using our computational power. Inspired by the comments, a numerical test was performed to understand the effect of lack of structural imperfections on the prediction of mechanical properties. All models in this new numerical test were created using nTop CAD software (nTop Inc., New York, NY, USA). A series of four tensile porous CAD models were built with three pores, each with strut thickness of $350 \mu\text{m}$ and pore size of $650 \mu\text{m}$ (Figure A-18). By using 3-pore segments, we can use extremely small elements to represent internal defect and rough surfaces. These models either had no structural defects (model nRnD), internal defects only (model nRD), surface roughness only (model RnD), or both internal defects and surface roughness (model RD).

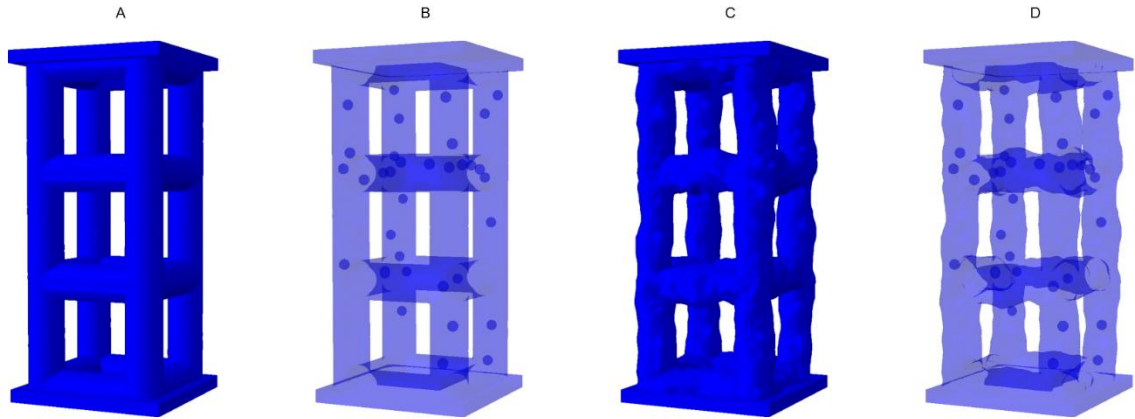


Figure A-18: Schematic diagrams showing the FEA models used to compare the tensile mechanical properties with and without structural imperfections.

The models either had no structural defects (A, model nRnD), internal defects only (B, model nRD), surface roughness only (C, model RnD), or both internal defects and surface roughness (D, model RD).

These CAD models were then used to create FEA models using Simulia Abaqus 2020 (Dassault Systèmes Simulia Corp, Providence, RI, United States). All the models were exposed to tensile loading simulation up to 1000 N. The models were discretized into tetrahedral quadratic mesh elements of a maximum size of 75 μm . The internal defects were allocated randomly within the FEA models, with the internal defects modelled as spheres of a diameter of 200 μm , which made up $\approx 0.8\%$ of the total volume of the models. Surface roughness was modelled to match the maximum peak to valley height ($\approx 100 \mu\text{m}$). While attempts were made to model the arithmetic surface roughness ($\approx 5 \mu\text{m}$), the limitation of the computational power did not allow for the modelling of the features that were less than 20 μm . All the elements were assigned the same Ti6Al4V material properties described in Appendix C. Tensile mechanical properties predictions in all four models were found, and deviations between the individual mechanical properties were calculated with the model nRnD as the benchmark model. The number of elements for these FE models ranged from 6.6×10^5 and 1.3×10^6 elements.

The results of the FEA modelling revealed that the surface roughness and internal defects did decrease the predicted values of all the mechanical properties (Figure A-19). However, the effect of these structural imperfections was limited to the plastic region of loading, as evident from the lack of difference in the results of the Young's modulus (E_T) and the proportionality limits point stress (σ_{PS}) and strain (ϵ_{PS}) between the different models

(deviation <10%). The strain at the yield point (ϵ_y) was found to have little difference in all the models from the nRnD model (deviation <10%), while the yield stress (σ_y) was found to have the highest deviation of $\approx 12\%$, with the other models showing deviations <10%. At the maximum stress (σ_{UTS}), and right before failure occurred, the deviations of the models from the nRnD models was found to be $\approx 6\%$ in the nRD model, $\approx 13\%$ in the RnD model and $\approx 17\%$ in the RD model, Furthermore, the strain at the maximum stress point (ϵ_{UTS}) was found to be highest in both models with surface roughness, with the deviation of the RnD model reaching to $\approx 56\%$ from the nRnD model, and the deviation of the RD model reaching up to $\approx 57\%$. The nRD with only internal defects had a smaller deviation of $\approx 38\%$. Consequently, the tensile toughness (T_T) results showed a deviation of $\approx 38\%$ in the nRD model, $\approx 66\%$ in the RnD model, and $\approx 68\%$ in the RD model.

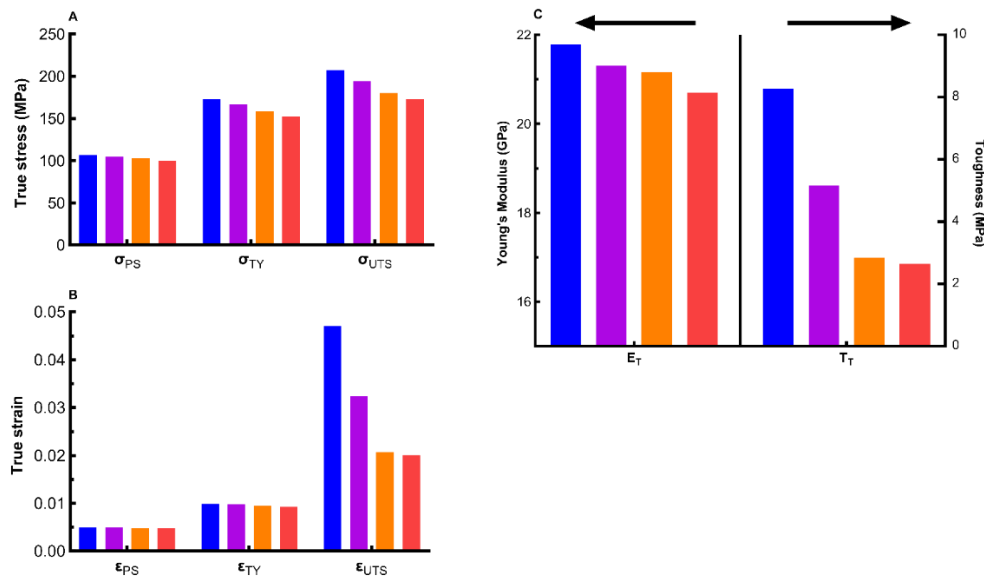


Figure A-19: The mechanical properties predictions from the FEA models of exposed to tensile loading simulations.

The graphs show the results of the measurements of the stress parameters (A), the strain parameters (B), Young's modulus and tensile toughness (C). The models shown in the graphs are as follows: model nRnD (■), model nRD (■), model RnD (■), and model RD (■). The results suggest that surface roughness and internal defects can affect the plastic mechanical behaviour of the porous SLM-built constructs, with the surface roughness causing the largest drop in the plastic strain, stress, and tensile toughness values. The elastic mechanical behaviour was found to be identical in all the models. The arrows in the part C represents the axis of measurement.

When looking at the von Mises contour maps, it was found that the models with internal defects (nRD) tend to fail at locations where the defects are closest to the loading side of the model, as opposed to the models without structural imperfections (nRnD), where

failures occurred at the middle of the gauge length of the model (Figure A-20). High von Mises stress concentrations were detected along the internal defects, indicating that they acted as stress risers, which might explain why failures were located close to them.

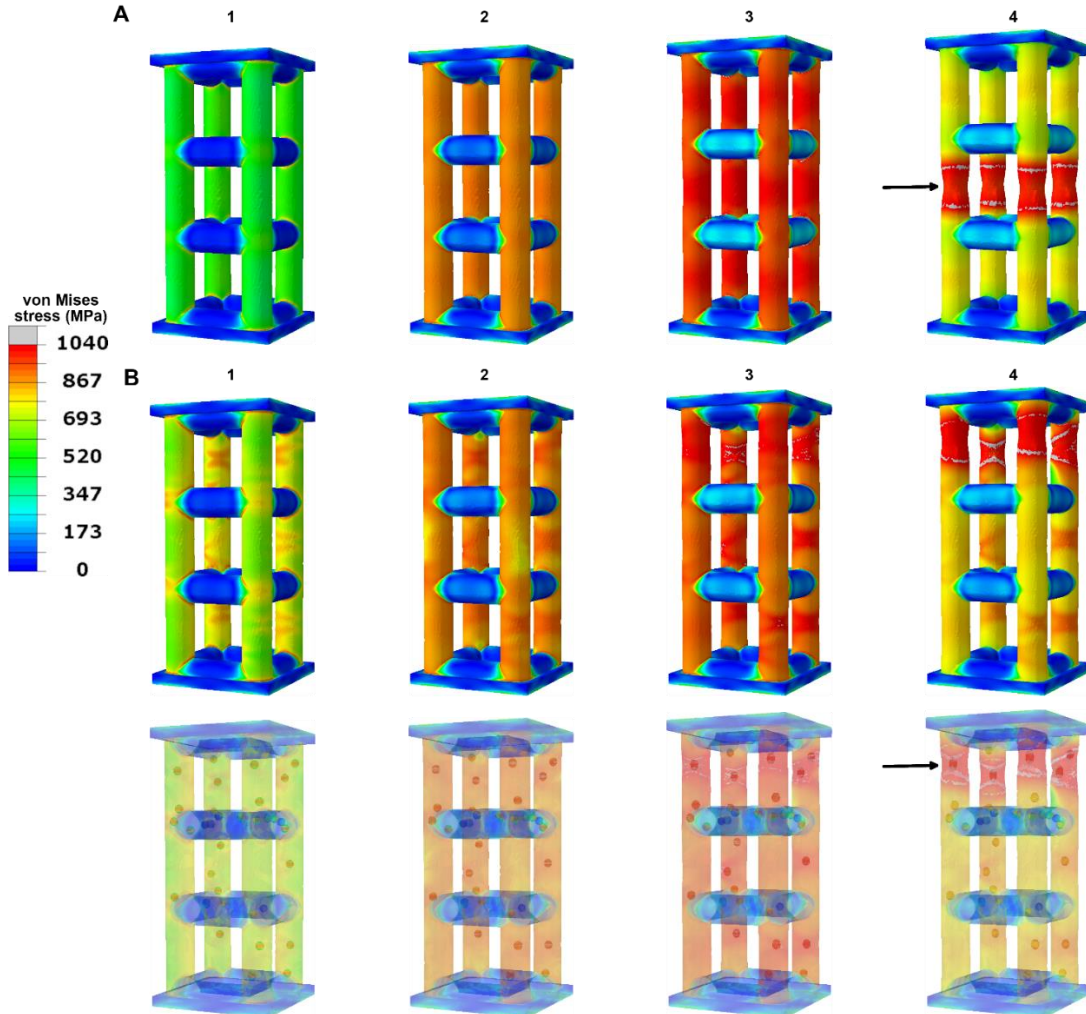


Figure A-20: von Mises stress contour maps of the nRnD model (A) and nRD model (B).

In addition, figures with transparent views were added to show the location of the defects. The models are shown at different points during the tensile loading process: these are the proportionality point (1), yield point (2), point of maximum stress (3), and failure point (4). Unlike the model nRnD which had not structural imperfections, the nRD model had high concentration of von Mises stress, which might have influenced the failure at that location. The arrows in the figures show the location of failure within the FEA models.

In the models with surface roughness (Figure A-21), the valleys on the surface of the models acted as stress risers, as evident by the von Mises concentrations forming along the valleys. However, the location of failure of the constructs appeared to be determined by the internal defects. This can be seen when comparing the RD model, where failure

occurred at locations where internal defects were present (Figure A-21 B), as opposed to the RnD model which (Figure A-21 A) where failure occurred at the center of the gauge length, similar to that seen in the nRnD model (Figure A-20 A).

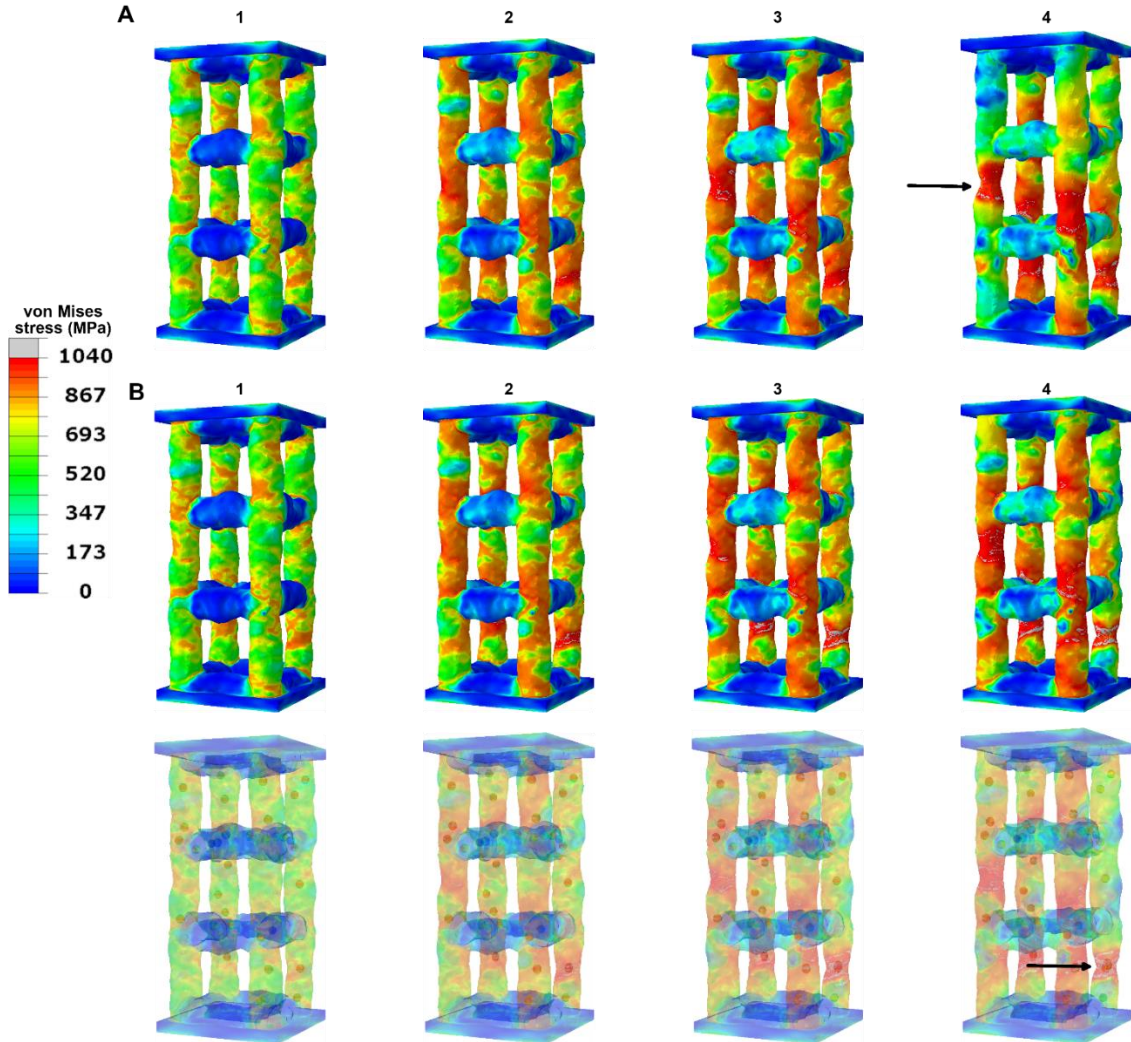


Figure A-21: von Mises stress contour maps of the RnD model (A) RD model and (B) RD model.

In addition, figures with transparent views were added to show the location of the defects. The models are shown at different points during the tensile loading process: these are the proportionality point (1), yield point (2), point of maximum stress (3), and failure point (4). While surface roughness is shown to cause stress concentration along the ridges of the surface, acting as stress-risers, the internal defects appear to affect the location of failure. The arrows in the figures show the location of failure within the FEA models.

In summary, while models without structural imperfections can differ from those with structural imperfections, the stress and strain values within the elastic region and until the yield point of loading remain to be similar in all the models tested in this section. In addition, it is unfeasible to use our available computational power to build large construct

models with complex structural features such as internal defects or surface roughness. It can thus be concluded that, before computational power has been drastically increased to handle these extreme small elements in the complete bending or tension models, the use of models without structural imperfections is a viable option despite the disadvantages in deviations within the plastic region of loading.

A.6 Supplementary tables for Chapter 3

Table A-12: Tensile testing porous CAD models' geometrical properties.

	Model Code	Pore Size (μm)	Strut Thickness (μm)	Gauge Length (mm)	Width (mm)	Thickness (mm)
S-Section	TS250	750	250	8.00	3.25	1.25
	TS350	650	350	8.00	3.35	1.35
	TS450	550	450	8.00	3.45	1.45
	TS550	450	550	8.00	3.55	1.55
	TS650	350	650	8.00	3.65	1.65
C-section	TC250	750	250	8.00	3.25	1.25
	TC350	650	350	8.00	3.35	1.35
	TC450	550	450	8.00	3.45	1.45
	TC550	450	550	8.00	3.55	1.55
	TC650	350	650	8.00	3.65	1.65
Nonporous	TSolid	0	1000	8.00	3.15	1.15

Table A-13: Flexural testing porous CAD models' geometrical properties.

	Model Code	Pore Size (μm)	Strut Thickness (μm)	Gauge Length (mm)	Width (mm)	Thickness (mm)
S-Section	FS250	750	250	80	4.25	4.25
	FS350	650	350	80	4.35	4.35
	FS450	550	450	80	4.45	4.45
	FS550	450	550	80	4.55	4.55
	FS650	350	650	80	4.65	4.65
C-section	FC250	750	250	76.5	4.25	4.25
	FC350	650	350	78.3	4.35	4.35
	FC450	550	450	80.1	4.45	4.45
	FC550	450	550	81.9	4.55	4.55
	FC650	350	650	83.7	4.65	4.65
Nonporous	FSolid	0	1000	80	5	5

Table A-14: The geometrical dimensions of the CAD models used to build the CT-scanned specimens.

Model Code	Pore Size (μm)	Strut Thickness (μm)	Length (mm)	Width (mm)	Thickness (mm)
S250	750	250	10.25	5.25	5.25
S350	650	350	10.35	5.35	5.35
S450	550	450	10.45	5.45	5.45
S550	450	550	10.55	5.55	5.55
S650	350	650	10.65	5.65	5.65
Nonporous	0	1000	11	6	6

Table A-15: The deviation of the SLM-built strut thickness values from the nominal values in porous constructs and models.

Nominal strut thickness	Strut thickness (μm)		Deviation	
	Parallel struts	Perpendicular struts	Parallel struts	Perpendicular struts
650	680.52	817.08	5%	26%
550	562.23	680.31	2%	24%
450	448.53	575.47	0%	28%
350	313.16	429.90	11%	23%
250	226.45	302.24	9%	21%
Average deviation			5%	24%

Table A-16: The deviation of the SLM-built major axis length values from the nominal values in porous constructs and models.

Nominal strut thickness	Major axis length (μm)		Deviation	
	Parallel struts	Perpendicular struts	Parallel struts	Perpendicular struts
650	734.01	956.08	13%	47%
550	594.30	838.82	8%	53%
450	465.49	737.61	3%	64%
350	332.51	562.52	5%	61%
250	248.11	429.34	1%	72%
Average deviation			6%	59%

Table A-17: The deviation of the SLM-built minor axis length values from the nominal values in porous constructs and models.

Nominal strut thickness	Minor axis length (μm)		Deviation	
	Parallel struts	Perpendicular struts	Parallel struts	Perpendicular struts
650	627.03	678.09	4%	4%
550	530.15	521.80	4%	5%
450	431.56	413.32	4%	8%
350	293.81	297.28	16%	15%
250	204.78	175.14	18%	30%
Average deviation			9%	13%

Table A-18: The deviation of the Young's modulus values of FEA models from the SLM-built constructs.

Nominal strut thickness	Young's modulus (GPa)			Deviation	
	SLM-built constructs	S-section FEA model	C-section FEA model	Deviation of S-section FEA models	Deviation of C-section FEA models
Nonporous	103.43	106.04	102.48	3%	1%
650	53.50	61.62	50.78	15%	5%
550	41.44	49.92	38.67	20%	7%
450	30.48	38.77	27.88	27%	9%
350	20.75	28.25	18.51	36%	11%
250	12.40	18.49	10.70	49%	14%
Average deviation				25%	8%

Table A-19: The deviation of the tensile yield strength values of FEA models from the SLM-built constructs.

Nominal strut thickness	Tensile yield strength (MPa)			Deviation	
	SLM-built constructs	S-section FEA model	C-section FEA model	Deviation of S-section FEA models	Deviation of C-section FEA models
Nonporous	878.00	834.90	823.95	5%	6%
650	411.36	470.77	397.85	14%	3%
550	306.57	376.98	299.99	23%	2%
450	215.35	288.67	213.71	34%	1%
350	138.37	206.66	139.76	49%	1%
250	76.54	132.10	79.14	73%	3%
Average deviation				33%	3%

Table A-20: The deviation of the ultimate tensile strength values of FEA models from the SLM-built constructs.

Nominal strut thickness	Ultimate tensile strength (MPa)			Deviation	
	SLM-built constructs	S-section FEA model	C-section FEA model	Deviation of S-section FEA models	Deviation of C-section FEA models
Nonporous	997.13	1010.39	1011.66	1%	1%
650	461.18	545.70	455.96	18%	1%
550	341.98	429.74	334.74	26%	2%
450	238.78	322.54	230.93	35%	3%
350	152.28	225.17	145.06	48%	5%
250	83.38	139.17	77.84	67%	7%
Average deviation				33%	3%

Table A-21: The deviation of the tensile toughness values of FEA models from the SLM-built constructs.

Nominal strut thickness	Tensile toughness (MPa)			Deviation	
	SLM-built constructs	S-section FEA model	C-section FEA model	Deviation of S-section FEA models	Deviation of C-section FEA models
Nonporous	73.37	70.54	66.70	4%	9%
650	9.30	16.80	13.81	81%	48%
550	5.16	11.15	8.80	116%	71%
450	2.86	7.40	5.61	159%	96%
350	1.58	4.91	3.58	210%	126%
250	0.88	3.26	2.28	271%	160%
Average deviation				140%	85%

Table A-22: The deviation of the flexural modulus values of FEA models from the SLM-built constructs.

Nominal strut thickness	Flexural modulus (GPa)			Deviation	
	SLM-built constructs	S-section FEA model	C-section FEA model	Deviation of S-section FEA models	Deviation of C-section FEA models
Nonporous	98.55	109.55	104.73	11%	6%
650	49.04	61.51	49.92	25%	2%
550	37.41	49.17	37.45	31%	0%
450	27.03	37.58	26.52	39%	2%
350	17.99	26.83	17.21	49%	4%
250	10.43	17.09	9.65	64%	7%
Average deviation				37%	4%

Table A-23: The deviation of the flexural yield strength values of FEA models from the SLM-built constructs.

Nominal strut thickness	Flexural yield strength (MPa)			Deviation	
	SLM-built constructs	S-section FEA model	C-section FEA model	Deviation of S-section FEA models	Deviation of C-section FEA models
Nonporous	1425.06	1337.91	1265.08	6%	11%
650	620.52	692.13	553.24	12%	11%
550	449.50	536.02	401.43	19%	11%
450	305.16	394.31	273.08	29%	11%
350	187.88	268.44	168.55	43%	10%
250	98.14	160.43	88.34	63%	10%
Average deviation				29%	11%

Table A-24: The deviation of the flexural strength values of FEA models from the SLM-built constructs.

Nominal strut thickness	Flexural strength (MPa)			Deviation	
	SLM-built constructs	S-section FEA model	C-section FEA model	Deviation of S-section FEA models	Deviation of C-section FEA models
Nonporous	1824.49	1730.13	1711.91	5%	6%
650	747.95	842.64	689.81	13%	8%
550	529.29	637.51	484.89	20%	8%
450	349.37	455.98	317.51	31%	9%
350	207.66	299.69	186.84	44%	10%
250	103.48	170.86	91.86	65%	11%
Average deviation				30%	9%

Table A-25: The deviation of the relative flexural toughness values of FEA models from the SLM-built constructs.

Nominal strut thickness	Relative flexural toughness (MPa)			Deviation	
	SLM-built constructs	S-section FEA model	C-section FEA model	Deviation of S-section FEA models	Deviation of C-section FEA models
Nonporous	4.86	5.43	5.31	12%	9%
650	2.42	2.98	2.51	23%	4%
550	1.84	2.37	1.88	28%	2%
450	1.33	1.79	1.32	34%	1%
350	0.89	1.26	0.85	42%	4%
250	0.51	0.79	0.48	54%	7%
Average deviation				32%	4%

A.7 Mesh convergence analysis results

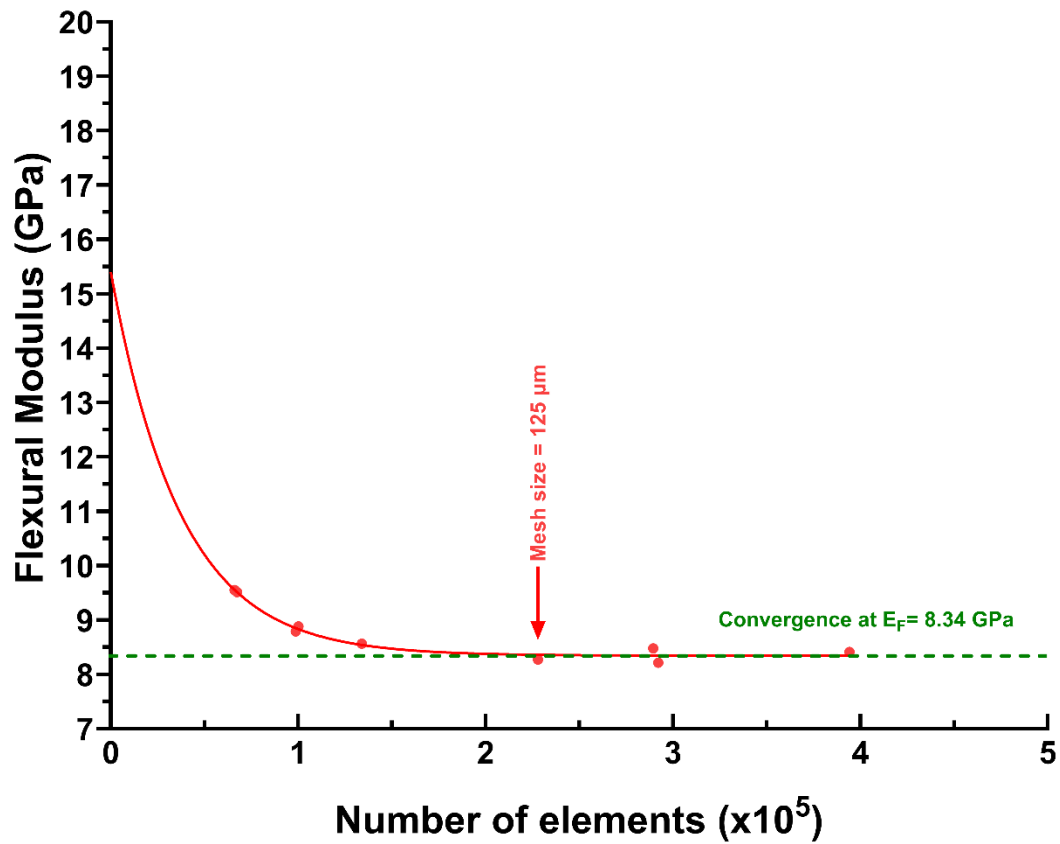


Figure A-22: Mesh convergence analysis performed on the flexural FEA models with strut thickness of 250 μm .

Flexural modulus plotted against the number of elements in FEA models with different mesh element sizes ($R^2 = 0.97$). The larger mesh element size models had smaller number of elements. The results showed that the flexural modulus value converged at 8.34 GPa, and the mesh element size of 125 μm (shown with the red arrow) produced a flexural modulus that is located at the start of the convergence.

Appendix B

B Additional information for Chapter 4

B.1 MATLAB: Dynamic flexural loading analysis

The MATLAB code described in this section was used to analyze the fatigue testing data. Each part of the code is presented along with an explanation of the operation of the MATLAB code.

B.1.1 Read Data

The user is first prompted to enter the code of each sample to be analyzed, along with the number of cycles to failure, the number of runs done to complete each test, and the static flexural yield stress of the sample.

```
close all;
clearvars;
SName=input(sprintf('Enter the Sample Code \n'),'s');
failure=upper(input(sprintf('Enter the failure \n'),'s'));
FileNumber = input(sprintf('Enter the number of loops \n'));
W = input(sprintf('Enter Width (mm) \n'));
Th = input(sprintf('Enter Thickness (mm) \n'));
L = input(sprintf('Enter Length (mm) \n'));
Yield = input(sprintf('Enter Yield Stress (MPa) \n'));
iC=0;
iT=0;
N1 = zeros(100000,5);
```

The force, position, time and cycle count are then extracted from each spreadsheet containing the raw data from cyclic loading tests. Remove the first 100 cycles from each of the tables, this is the enveloping wave and is not considered part of the fluctuating cyclic loading. This step is done within a loop that ends with the creation of a matrix containing the leftover raw data obtained from all the runs applied on each sample.

```
for x=1:FileNumber
    F= 0;
    P=0;
```



```

C=0;
Ti=0;
S=0;
Name= input('Enter file name Code \n','s');
filecheck=isfile(sprintf('%s', Name,'stepstracking.csv'));
    if (filecheck==1)
        T= readtable(sprintf('%s', Name,'stepstracking.csv'));
    elseif (filecheck==0)
        T= readtable(sprintf('%s',
Name, '.steps.tracking.csv'));
    end
F= abs(T.Force_8800_0_3_Load_N);
P=abs(T.Position_8800_0_3_Position_mm);
C=T.TotalCycleCount_8800_0_3_Waveform;
Ti=T.TotalTime_s;
S=T.Step;
iC100=find(C<100);
S(iC100)=[];
F(iC100)=[];
C(iC100)=[];
P(iC100)=[];
Ti(iC100)=[];
C=iC+C;
iC=C(end,:);
Ti=iTi+Ti;
iT=Ti(end,:);
M=[S Ti C P F];
N1=[N1;M];
end
clearvars -except N1 SName W Th L Yield minF maxF iC

```

B.1.2 Process and cleaning up of data

Now that the data is read and compiled for all the spreadsheets, a follow up process is needed to clip and clean up the data from the tests. This is done by limiting the data to the step when fluctuating loading (cyclic loading with constant forces were applied).

```

clear xlabel ylabel;
N=N1;
Ti=N(:,2);
C=N(:,3);
P=N(:,4);
F=N(:,5);

```

```

fig(1)=figure;
plot(C,F);
xlabel('Number of Cycles')
ylabel('Force (N)')
title(sprintf('Initial Force - Number of Cycles of %s',SName));
hold off;
TF1 = N(:,1)==1;
N(TF1,:)=[];
TF2 = N(:,1)==0;
N(TF2,:)=[];
TF3 = N(:,1)==3;
N(TF3,:)=[];
Ti=N(:,2);
C=N(:,3);
P=N(:,4);
F=N(:,5);

```

Find the displacement readings by finding the starting position (at C=0) and then use it as the reference point for all upcoming position points. The time is also reset so the first point is set as 0 seconds.

```

minP=min(P);
D=P-minP;
minTi=Ti(1,1);
Ti=Ti-minTi;
fig(2)=figure;
plot(C,F);
xlabel('Number of Cycles')
ylabel('Force (N)')
title(sprintf('Force - Number of Cycles of %s',SName));
hold off;
fig(3)=figure;
plot(C,D);
xlabel('Number of Cycles')
ylabel('Displacement (mm)')
title(sprintf('Displacement - Number of Cycles of %s',SName));
hold off;

```

B.1.3 Convert to Stress-Strain

A simple conversion of the force readings into flexural stress and displacement into flexural strain readings. Three different matrices were then created, one for force-displacement

readings, another for the stress-strain readings and a third having the initial geometrical properties of the sample.

```
Strain= = (6*Th*Disp)/(L^2);
Stress = (3*F*L)/(2*W*Th^2);
fig(4)=figure;
plot(C,Strain);
xlabel('Number of Cycles')
ylabel('Strain (mm/mm)')
title(sprintf('Strain - Number of Cycles of %s',SName));
hold off;
fig(5)=figure;
plot(C,Stress);
xlabel('Number of Cycles')
ylabel('Stress (MPa)')
title(sprintf('Stress - Number of Cycles of %s',SName));
hold off;
N=[Ti C D F];
O=[Ti C Strain Stress];
G=[L W Th];
```

B.1.4 Find Extremes

This step involves finding the peaks and valleys of the signal. Given that outliers would exist within the extracted peak and valley points, the script was adjusted to remove these arbitrary points on the curve. The extreme points' stress, strain, time, and number of cycles are then combined as the union between the peaks and valleys.

```
[peak, iPeaks, width, p] = findpeaks(Stress,
'MinPeakDistance',100);
meanStress = mean(Stress);
ioutlier = peak < meanStress;
peak(ioutlier) = [];
iPeaks(ioutlier) = [];
[valley, iValleys] = findpeaks(-Stress, 'MinPeakDistance', 100);
valley = -valley;
ioutlier = valley > meanStress;
valley(ioutlier) = [];
iValleys(ioutlier) = [];
maxF=F(iPeaks);
minF=F(iValleys);
maxDisp=D(iPeaks);
```

```

minDisp=D(iValleys);
maxStress=Stress(iPeaks);
minStress=Stress(iValleys);
maxTi=Ti(iPeaks);
minTi=Ti(iValleys);
maxStrain=Strain(iPeaks);
minStrain=Strain(iValleys);
maxC=C(iPeaks);
minC=C(iValleys);
iext= union(iValleys,iPeaks);
extStress=Stress(iext);
extStrain=Strain(iext);
extTi=Ti(iext);
extC=C(iext);

```

B.1.5 Analyze the Fatigue Data

This part of the script is used to determine the ‘stable’ phase of the cyclic loading, which is where mean, amplitude, and range values of the stress and strain were measured.

```

History=[extC extStress];
window = (max(C)/max(Ti))*100;
PextTi = linspace(0,max(extTi),window);
PextC = linspace(0,max(extC),window);
PmaxC=linspace(0,max(maxC),window);
PminC=linspace(0,max(minC),window);
umaxC=unique(maxC);
uminC=unique(minC);
numberofmaxsamples=numel(umaxC);
numberofminsamples=numel(uminC);
if numberofmaxsamples<numel(maxC) || numberofminsamples<numel(minC)
    maxC=maxC(1:numberofmaxsamples);
    minC=minC(1:numberofminsamples);
    maxStress=maxStress(1:numberofmaxsamples);
    minStress=minStress(1:numberofminsamples);
    maxStrain=maxStrain(1:numberofmaxsamples);
    minStrain=minStrain(1:numberofminsamples);
end
PmaxStress = GaussianSmoothing(window, maxStress, maxC,PextC);
PminStress= GaussianSmoothing(window, minStress, minC,PextC);
PmaxStrain= GaussianSmoothing(window, maxStrain, maxC,PextC);
PminStrain= GaussianSmoothing(window, minStrain, minC,PextC);

```

```

meanStress=(PmaxStress+PminStress)/2;
meanStrain=(PmaxStrain+PminStrain)/2;
ampStress=(PmaxStress-PminStress)/2;
ampStrain=(PmaxStrain-PminStrain)/2;
diffStress=PmaxStress-PminStress;
diffStrain=PmaxStrain-PminStrain;
fig(6)=figure;
scatter(PmaxC,PmaxStress,'x');
hold on;
scatter(PminC,PminStress,'x');
hold on;
xlabel('Number of Cycles')
ylabel('Stress (MPa)')
title(sprintf('Extreme Stresses - Number of Cycles of %s',SName));
legend('Max Stress','Min Stress');
legend("Position", [0.38438,0.48241,0.2,0.082143])
hold off;
fig(7)=figure;
scatter(PmaxC,PmaxStrain,'x');
hold on;
scatter(PminC,PminStrain,'x');
xlabel('Number of Cycles')
ylabel('Strain (mm/mm)')
title(sprintf('Extreme Strain - Number of Cycles of %s',SName));
legend('Max Strain','Min Strain');
legend("Position", [0.74018,0.22586,0.20714,0.11905])
hold off;
fig(8)=figure;
scatter(PextC,ampStress,'x');
xlabel('Number of Cycles')
ylabel('Amplitude Stress (MPa)')
title(sprintf('Amplitude Stress - Number of Cycles of %s',SName));
hold off;
fig(9)=figure;
scatter(PextC,ampStrain,'x');
xlabel('Number of Cycles')
ylabel('Amplitude Strain (mm/mm)')
title(sprintf('Amplitude Strain - Number of Cycles of %s',SName));
hold off;
fig(10)=figure;
scatter(PextC,diffStress,'x');
xlabel('Number of Cycles')

```

```

ylabel('Stress Difference (MPa)')
title(sprintf('Stress Difference - Number of Cycles of %s',SName));
hold off;
fig(11)=figure;
scatter(PextC,diffStrain,'x');
xlabel('Number of Cycles')
ylabel('Strain Difference (mm/mm)')
title(sprintf('Strain Difference- Number of Cycles of %s',SName));
hold off;

fig(12)=figure;
scatter(PextC,meanStress,'x');
xlabel('Number of Cycles')
ylabel('Mean Stress (MPa)')
title(sprintf('Mean Stress- Number of Cycles of %s',SName));
hold off;

fig(13)=figure;
scatter(PextC,meanStrain,'x');
xlabel('Number of Cycles')
ylabel('Mean Strain (mm/mm)')
title(sprintf('Mean Strain- Number of Cycles of %s',SName));
hold off;
qCh1=1;
TiLim=[PextTi(1) PextTi(imaxMod)];
TiLimMax=max(TiLim);
TiLimMin= min(TiLim);
CLim=[PextC(1) PextC(imaxMod)];
CLimMax=max(CLim);
CLimMin=min(CLim);
%Mean Fit of Max and Minimum Stress
[f1,gof1,output1] =
fit(transpose(PextC(1:imaxMod)),transpose(PmaxStress(1:imaxMod)), 'p
oly1');
[f2,gof2,output2] =
fit(transpose(PextC(1:imaxMod)),transpose(PminStress(1:imaxMod)), 'p
oly1');
O1=coeffvalues(f1);
O2=coeffvalues(f2);
meanMaxStress = O1(1,2);
meanMinStress = O2(1,2);

%Mean Fit of Max and Minimum Strain

```

```

[f3,gof3,output3] =
fit(transpose(PextC(1:imaxMod)),transpose(PmaxStrain(1:imaxMod)), 'p
oly1');
[f4,gof4,output4] =
fit(transpose(PextC(1:imaxMod)),transpose(PminStrain(1:imaxMod)), 'p
oly1');

O3=coeffvalues(f3);
O4=coeffvalues(f4);
meanMaxStrain = O3(1,2);
meanMinStrain = O4(1,2);

meanMaxF=StresstoForce(meanMaxStress, L, W, Th);
meanMinF=StresstoForce(meanMinStress,L, W, Th);
meanMaxDisp=StraintoDisp(Th,meanMaxStrain,L);
meanMinDisp=StraintoDisp(Th,meanMinStrain,L);

meanAllStress=(meanMaxStress+meanMinStress)/2;
rangeStress=meanMaxStress-meanMinStress;
altAllStress=rangeStress/2;
StressRatio=meanMinStress/meanMaxStress;
PercentYield=meanMaxStress/Yield;

```

B.1.6 Plot final curves and table of results

```

%Plots
fig(19)=figure;
maxStressSc=scatter(maxC,maxStress,'magenta','.');
hold on;
maxStressFit=plot(PextC,PmaxStress,'Red','LineWidth',2);
hold on;
minStressSc=scatter(minC,minStress,'Cyan','.');
hold on;
minStressFit=plot(PextC,PminStress,'Blue','LineWidth',2);
hold on;
plot(f1,'-.');
hold on
plot(f2,'-.');
hold on
xline(CLimMin);
hold on
xline(CLimMax);
hold on
% title(sprintf('Stress Trend Plot of %s', Name));

```

```

xlim([0 max(PextC)+100])
ylim([0 max(maxStress)+5])
xlabel('Cycles (N)');
ylabel('Stress (MPa)');
legend(["Mean Max Stress","Mean Min Stress","Beginning of Linear
Part","End of Linear Part"]);
hold off;
legend off;

fig(20)=figure;
maxStressSc=scatter(maxC,maxStrain,'magenta','.');
hold on;
maxStressFit=plot(PextC,PmaxStrain,'Red','LineWidth',2);
hold on;
minStressSc=scatter(minC,minStrain,'Cyan','.');
hold on;
minStressFit=plot(PextC,PminStrain,'Blue','LineWidth',2);
hold on;
plot(f3,'-.');
hold on
plot(f4,'-.');
hold on
xline(CLimMin);
hold on
xline(CLimMax);
hold off;

% title(sprintf('Strain Cycle Plot of %s', Name));
xlim([0 max(PextC)+100])
ylim([0 max(maxStrain)+1e-3])
xlabel('Cycles (N)');
ylabel('Strain (mm/mm)');
legend(["Mean Max Stress","Mean Min Stress","Beginning of Linear
Part","End of Linear Part"]);
hold off;
legend off;
markersize=100;
markershape='X';

newcolors = {'#F00','#F80','#FF0','#0B0','#00F','#50F','#A0F'};

colororder(newcolors);

```



```
PropertiesArray=({'Starting Position (mm)';'Minimum Displacement  
(mm)';'Maximum Displacement (mm)';'Minimum Force (N)';'Maximum  
Force (N)'; 'Minimum Strain (mm/mm)';'Maximum Strain  
(mm/mm)';'Minimum Stress (MPa)';'Maximum Stress (MPa)'; 'Modulus  
after 100 Cycles (GPa)';      'Stress Ratio';'Stress to Yield  
Ratio'});
```

```
ResultsArray=({minP;meanMinDisp;meanMaxDisp;meanMinF;meanMaxF;meanM  
inStrain;meanMaxStrain;meanMinStress;meanMaxStress;StressRatio;Perc  
entYields});
```

```
Results = [PropertiesArray ResultsArray];
```

B.2 Supplementary tables for Chapter 4

B.2.1 Models and constructs nominal geometrical measurements.

Table B-1: Geometrical dimensions of the constructs and models.

	Width unit cells × Thickness unit cells	Strut thickness (μm)	Computer (CAD) models			SLM-built constructs		
			Width (mm)	Thickness (mm)	Gauge length (mm)	Width (mm)	Thickness (mm)	Gauge length (mm)
ST350-2×2	2×2	350	2.35	2.35	42.3	2.36 ± 0.01	2.36 ± 0.01	43.11 ± 1.30
ST350-3×3	3×3	350	3.35	3.35	60.3	3.39 ± 0.01	3.39 ± 0.01	60.73 ± 0.36
ST450-2×2	2×2	450	2.45	2.45	44.1	2.47 ± 0.01	2.46 ± 0.02	44.44 ± 0.33
ST450-3×3	3×3	450	3.45	3.45	62.1	3.47 ± 0.01	3.47 ± 0.01	62.10 ± 0.00

B.2.2 Fatigue tests and model fits

Table B-2: ($\sigma_{fmax} - N_f$) and ($\sigma_{fmax}/\sigma_{FY} - N_f$) curve fits found for each of the tests and simulations conducted in this experiment. Information here was used to determine the average deviations.

	ST350-3×3	ST450-2×2
Maximum flexural fatigue stress		
SLM-built constructs	$\sigma_{fmax} = 424.1 (N_f)^{-0.166}$	$\sigma_{fmax} = 714.5 (N_f)^{-0.156}$
Normalized fatigue strength		
SLM-built constructs	$\sigma_{fmax}/\sigma_{FY} = 3.103 (N_f)^{-0.166}$	$\sigma_{fmax}/\sigma_{FY} = 2.285 (N_f)^{-0.156}$
Numerical models	$\sigma_{fmax}/\sigma_{FY} = 4.498 (N_f)^{-0.193}$	$\sigma_{fmax}/\sigma_{FY} = 3.686 (N_f)^{-0.187}$

Table B-3: Deviation of yield-normalized fatigue stress ratio ($\sigma_{fmax}/\sigma_{FY}$) between the fits from ST350 numerical models and the cyclic flexural loading of SLM-built ST350 constructs.

Number of cycles	SLM	Numerical model	Deviation
100	1.445	1.851	28%
200	1.288	1.619	26%
300	1.204	1.497	24%
400	1.148	1.416	23%
500	1.106	1.357	23%
600	1.073	1.310	22%
700	1.046	1.271	22%

800	1.023	1.239	21%
900	1.003	1.211	21%
1000	0.986	1.187	20%
2000	0.879	1.038	18%
3000	0.821	0.960	17%
4000	0.783	0.908	16%
5000	0.755	0.870	15%
6000	0.732	0.840	15%
7000	0.714	0.815	14%
8000	0.698	0.795	14%
9000	0.685	0.777	13%
10000	0.673	0.761	13%
20000	0.600	0.666	11%
30000	0.561	0.616	10%
40000	0.534	0.582	9%
50000	0.515	0.558	8%
60000	0.500	0.539	8%
70000	0.487	0.523	7%
80000	0.476	0.509	7%
90000	0.467	0.498	7%
100000	0.459	0.488	6%
200000	0.409	0.427	4%
300000	0.382	0.395	3%
400000	0.365	0.373	2%
500000	0.351	0.358	2%
600000	0.341	0.345	1%
700000	0.332	0.335	1%
800000	0.325	0.327	1%
900000	0.319	0.319	0%
1000000	0.313	0.313	0%
2000000	0.279	0.274	2%
3000000	0.261	0.253	3%
4000000	0.249	0.239	4%
5000000	0.240	0.229	4%

6000000	0.233	0.221	5%
7000000	0.227	0.215	5%
8000000	0.222	0.209	6%
9000000	0.217	0.205	6%
10000000	0.214	0.201	6%

Table B-4: Deviation of yield-normalized fatigue stress ratio ($\sigma_{\text{fmax}}/\sigma_{\text{FY}}$) between the fits from ST450 numerical models and the cyclic flexural loading of SLM-built ST450 constructs.

Number of cycles	SLM	Numerical model	Deviation
100	1.114	1.560	40%
200	1.000	1.370	37%
300	0.939	1.270	35%
400	0.897	1.203	34%
500	0.867	1.154	33%
600	0.842	1.116	32%
700	0.822	1.084	32%
800	0.805	1.057	31%
900	0.791	1.034	31%
1000	0.778	1.014	30%
2000	0.698	0.891	28%
3000	0.655	0.826	26%
4000	0.627	0.782	25%
5000	0.605	0.750	24%
6000	0.588	0.725	23%
7000	0.574	0.705	23%
8000	0.562	0.687	22%
9000	0.552	0.672	22%
10000	0.543	0.659	21%
20000	0.487	0.579	19%
30000	0.458	0.537	17%
40000	0.437	0.509	16%
50000	0.423	0.488	15%
60000	0.411	0.472	15%
70000	0.401	0.458	14%
80000	0.393	0.447	14%

90000	0.385	0.437	13%
100000	0.379	0.429	13%
200000	0.340	0.376	11%
300000	0.319	0.349	9%
400000	0.305	0.331	8%
500000	0.295	0.317	8%
600000	0.287	0.307	7%
700000	0.280	0.298	6%
800000	0.274	0.291	6%
900000	0.269	0.284	6%
1000000	0.265	0.279	5%
2000000	0.238	0.245	3%
3000000	0.223	0.227	2%
4000000	0.213	0.215	1%
5000000	0.206	0.206	0%
6000000	0.200	0.199	0%
7000000	0.195	0.194	1%
8000000	0.191	0.189	1%
9000000	0.188	0.185	2%
10000000	0.185	0.181	2%

Table B-5: The overall average deviation for both models, calculated from the results presented in Table B-3 and B-4. The models exhibited smaller deviation from the fatigue strength at higher number of cycles.

Overall average deviation (range 10^2 to 10^7 cycles)	14%
Overall average deviation (range 10^3 to 10^7 cycles)	10%

B.3 Determining the optimal K_t factor for use in fatigue modelling

The original surface roughness factor (K_t) was initially chosen as per the surface roughness readings found in Chapter 3. The deviation of $\sigma_{fmax}/\sigma_{FY} - N_f$ curves from the models from those from real-life curves was about 14%. It was noted that the deviation was highest in the low-cycle and high-stress region of the $\sigma_{fmax}/\sigma_{FY} - N_f$ curves. The stresses reached when N_f was between 10^2 and 10^3 cycles was either close to or greater than the yield stress. These stress levels were irrelevant within the context of mandibular implant designs, which are not supposed to reach those stress levels. In addition, these stress levels were not tested

in real-life, hence the SLM-built construct curves did not extend to these low cycle ranges. Instead, all the deviations were concentrated on the range between 10^3 to 10^7 cycles.

It is thought that internal defects could have caused drops in the fatigue strength of the real-life SLM-built constructs. However, stress concentration from the internal defects were not accounted for in the original models. Hence, a set of models was tested with K_t ranging from 1.3 to 1.8. The fatigue simulations were run as described in the methodology (section 4.3.3.2). $\sigma_{fmax} - N_f$ and $\sigma_{fmax}/\sigma_{FY} - N_f$ curves were then generated and plotted (Figure B-1).

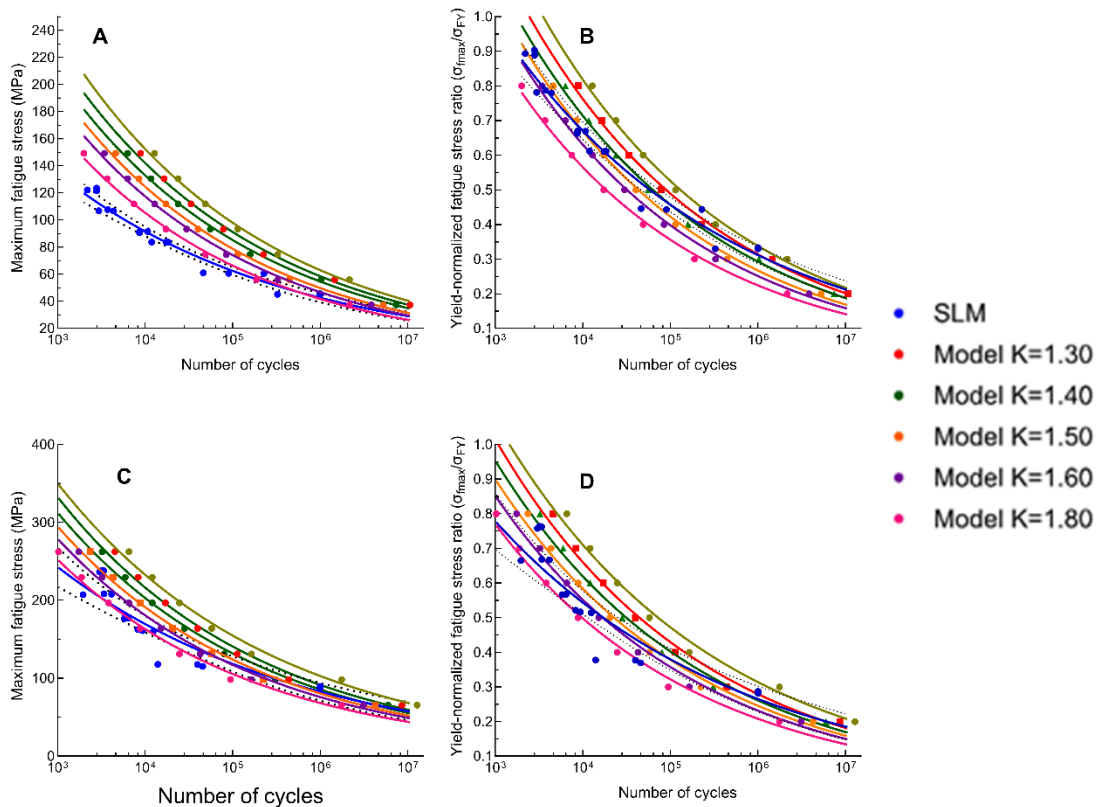


Figure B-1: $\sigma_{fmax} - N_f$ (A and C) and $\sigma_{fmax}/\sigma_{FY} - N_f$ (B and D) curves for (A and B) ST350 models and (C and D) ST450 models with different K_t values.

The overall average deviation (range 10^3 to 10^7 cycles) was calculated for each of the models tested in this test and the deviations were plotted against the K_t values (Figure B-2). The optimal K_t value sits at $K_t = 1.4$. However, the difference in the deviations seen in the $K_t = 1.3$ and $K_t = 1.4$ models is not large. The results indicated that with increasing K_t value,

the deviation at higher cyclic stresses decreased while increasing the deviation at lower cyclic stresses, which is disadvantageous given that the applied stresses in mandibular implants are expected to be on the lower end of the $\sigma_{fmax}/\sigma_{FY} - N_f$ curve. Hence, it was concluded that the original model is sufficient for predicting the fatigue strength of the porous constructs.

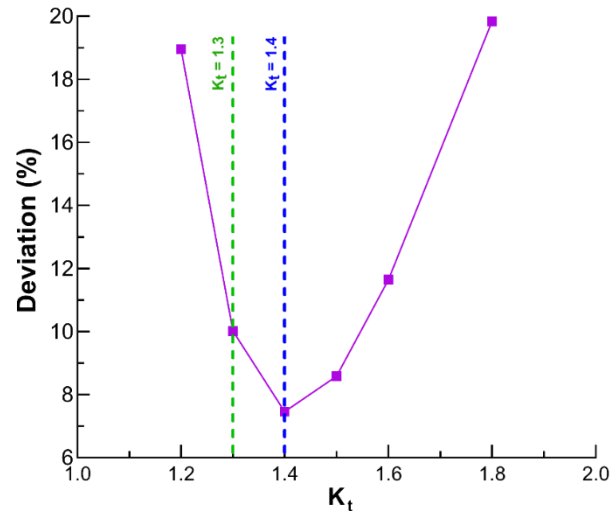


Figure B-2: The deviation of the $\sigma_{fmax}/\sigma_{FY} - N_f$ from the fatigue models when compared to the real-life fatigue tests.

While the $K_t = 1.3$ model remains accurate at 10% deviation, the optimal $K_t = 1.4$ achieves a lower level of overall deviation is at 8%.

B.4 Multiple K_t values used in the same model

An improvement to the model would be considering different K_t at different applied stress levels. This model assumes that the K_t is higher when the applied stress is increased due to the increased prominence of the effect of internal defects on fatigue failure within the constructs. To build this model, we plotted the deviation against the real-life yield-normalized stress ratio ($\sigma_{fmax}/\sigma_{FY}$) for both the ST350 and ST450 models (Figure B-33).

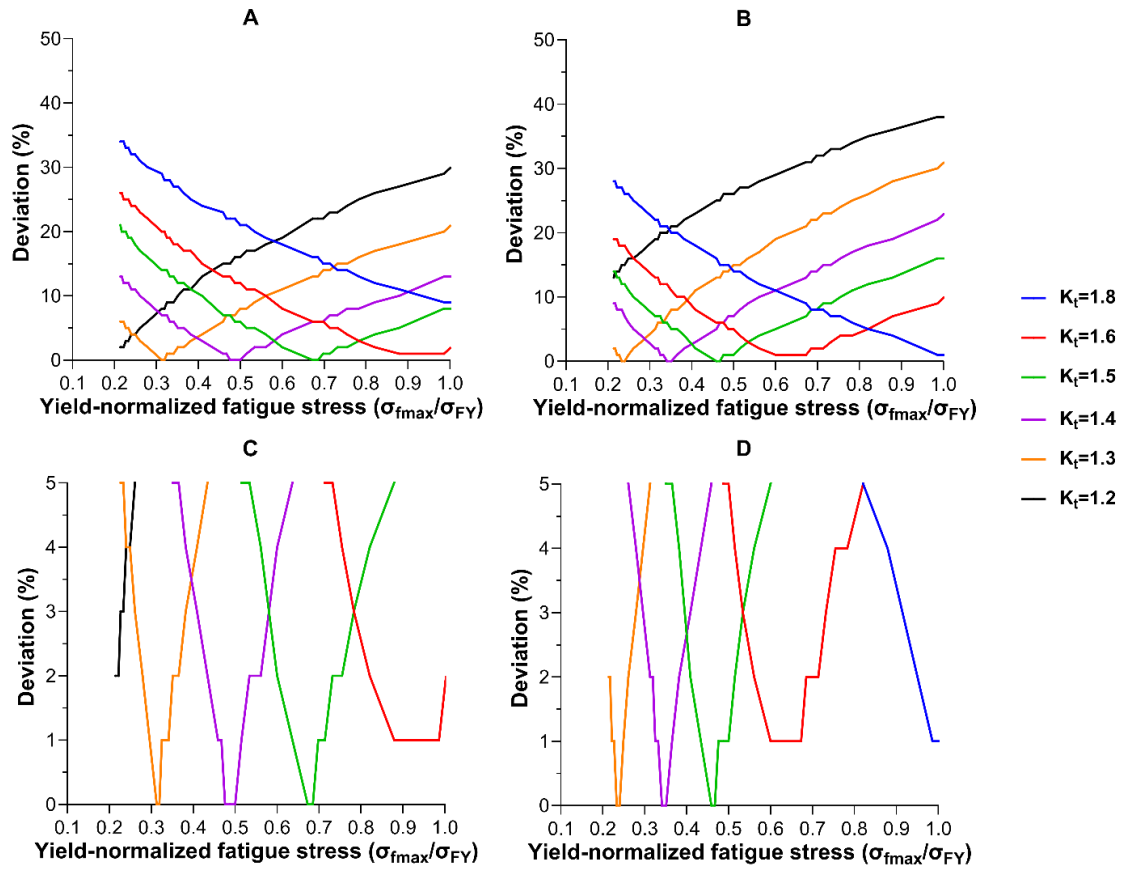


Figure B-3: The comparisons of the deviation of (A) ST350 and (B) ST450 models against the real-life $\sigma_{fmax}/\sigma_{FY} - N_f$ curves.

The bottom plots show the same plots by concentrating on deviations < 5% for (C) ST350 and (D) ST450 models. These plots show the differences in the deviations between the different K_t factors also depend on the models' applied stress.

Following the plots in Figure B-3, the optimal $\sigma_{fmax}/\sigma_{FY}$ ranges for each K_t factor were determined (Table B-6). Within these ranges, the deviations remained < 5% if the matching K_t factor was chosen. The range intersection between the ST350 and the ST450 models was then determined for each K_t value.

Table B-6: Matching of the K_t factor with the best fitting $\sigma_{fmax}/\sigma_{FY}$ ranges.

K_t	ST350 models	ST450 models	Best fitting $\sigma_{fmax}/\sigma_{FY}$ range
1.2	0-0.24	N/a	N/a
1.3	0.25 - 0.4	0-0.3	0-0.3
1.4	0.41-0.6	0.31-0.4	0.31-0.4
1.5	0.61-0.8	0.41-0.55	0.41-0.6
1.6	0.8-1	0.551-0.8	0.61-1
1.8	N/a	0.8-1	N/a

When using multiple K_t factors according to the matching $\sigma_{fmax}/\sigma_{FY}$ range, the deviation between the fatigue models and real-life $\sigma_{fmax}/\sigma_{FY}$ curves are diminished to 3% in both the ST350 and ST450 models, compared to the 10% seen in the original $K_t=1.3$ models (Figure B-4).

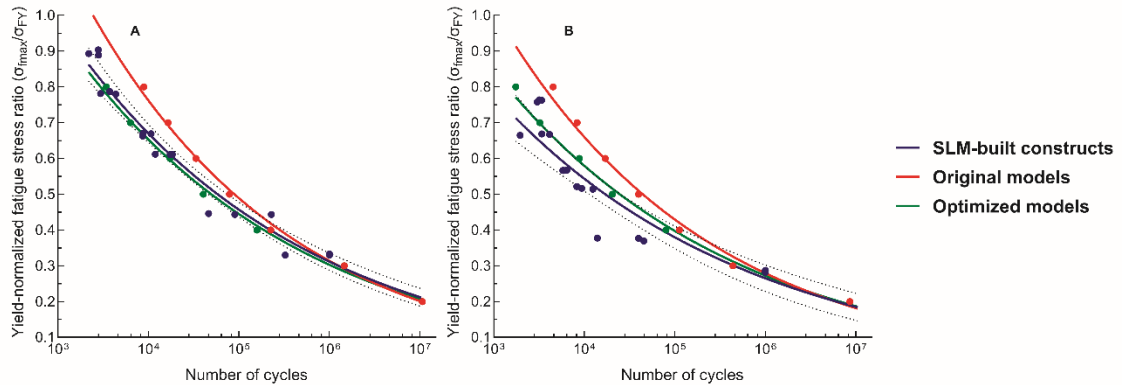


Figure B-4: The $\sigma_{fmax}/\sigma_{FY} - N_f$ curves of (A) ST350 and (B) ST450 real-life tests, original models and optimized models.

The number of cycles is placed on a logarithmic scale. All the curves fit into power series ($R^2 > 0.89$). The optimized models deviation from the real-life results is about 3%, which is significantly lower than the original models with constant $K_t = 1.3$.

This optimized model, while highly accurate, requires further investigation into how internal defects affect the fatigue strength of porous constructs at different stress levels to justify its use. While internal defects are known to decrease the fatigue strength of SLM-built constructs (Ahmadi et al., 2019, Wickmann et al., 2021, Leuders et al., 2013, Hu et al., 2020), the effect of internal defects on the constructs at higher stress levels, as opposed to lower stress levels, in cyclic loading remains unclear. Ahmadi et al. (2018) suggested that internal defects have a higher effect on the fatigue strength at high stresses and a lower

number of cycles, which aligns with the observations seen in this study. In addition, it should be noted that the effect of internal defects is highly dependent on the size and volume percentage of the internal defects, as seen in studies done by Wickmann et al. (2021) and du Plessis et al. (2020).

B.5 Additional SEM and light microscopy images

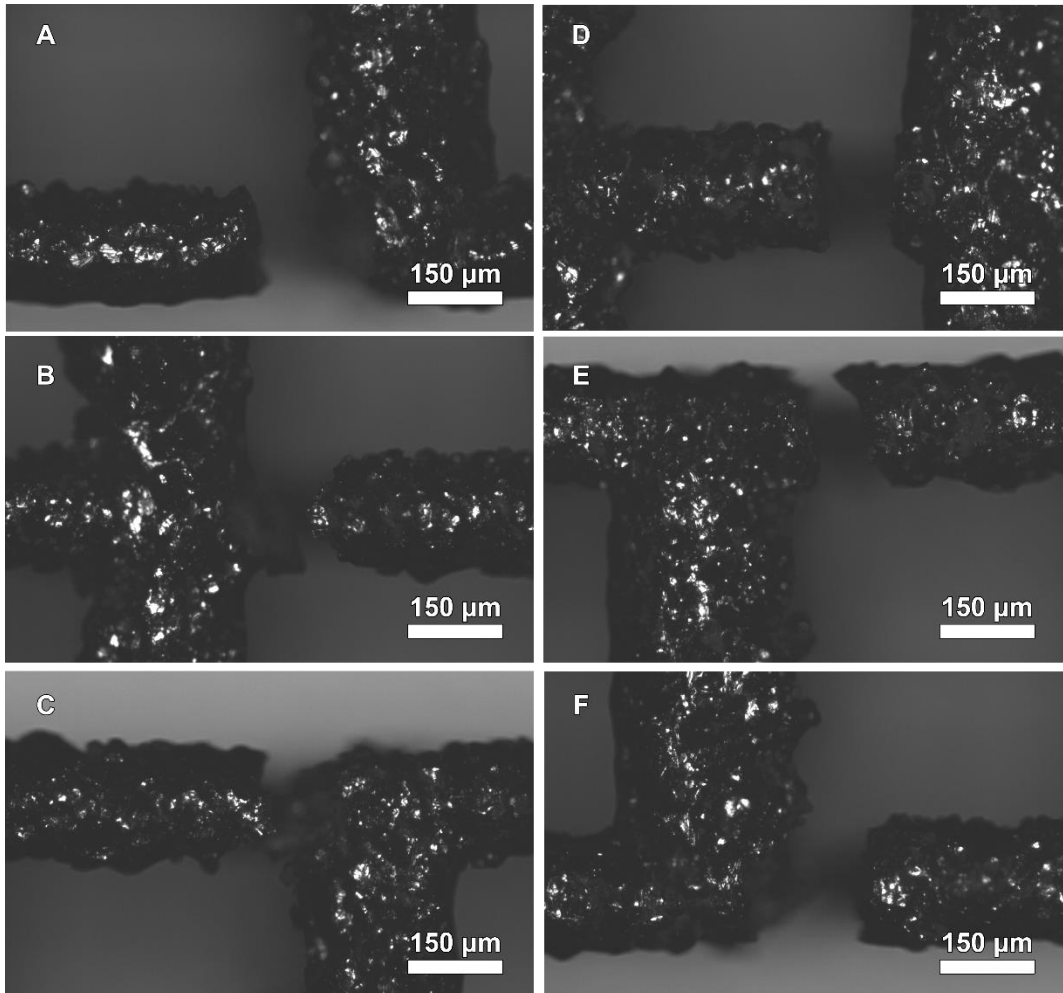


Figure B-5: Representative light microscopy images of the ST350 constructs that underwent cyclic loading at $\sigma_{fmax}/\sigma_{FY} = 0.4$ (A-C) and $\sigma_{fmax}/\sigma_{FY} = 0.8$ (D-F). All the fractures in these constructs occurred at the junction of struts.

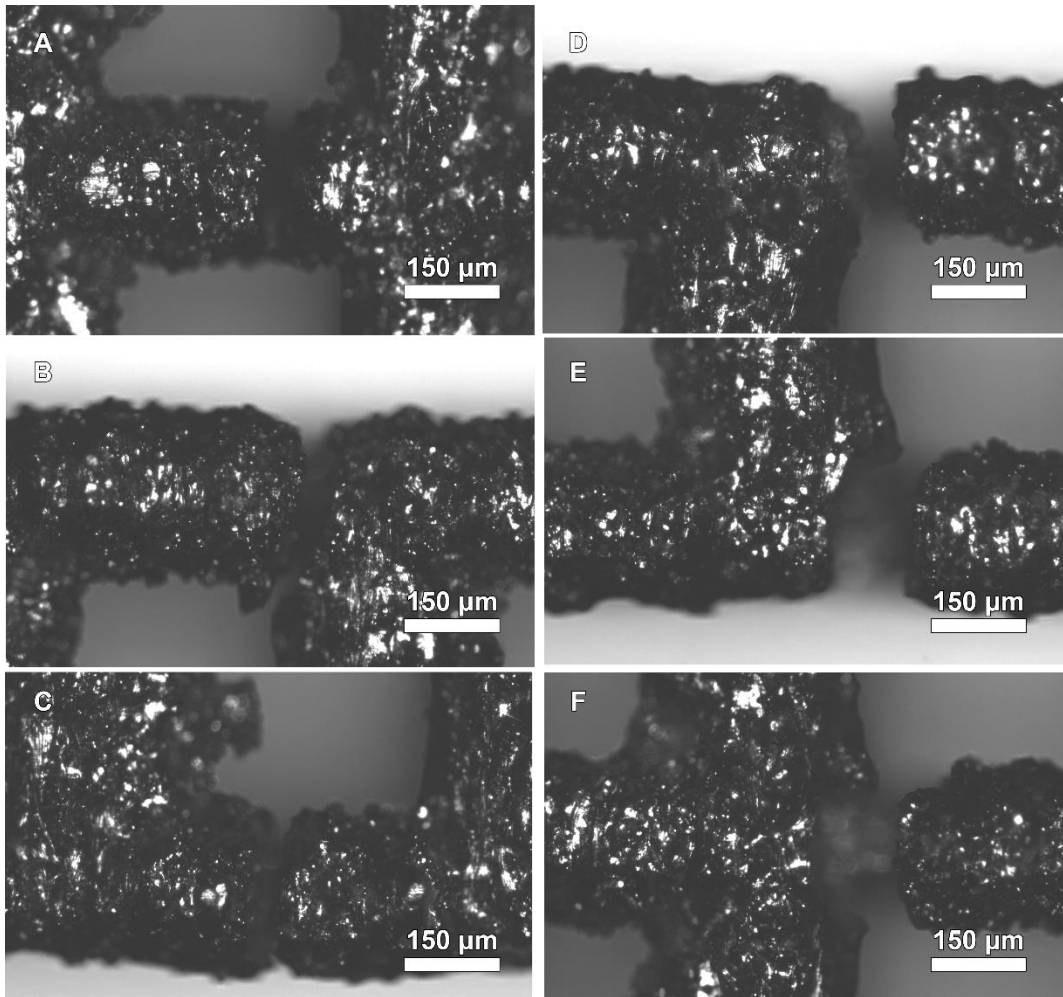


Figure B-6: Representative light microscopy images of the ST450 constructs that underwent cyclic loading at $\sigma_{fmax}/\sigma_{FY} = 0.4$ (A-C) and $\sigma_{fmax}/\sigma_{FY} = 0.8$ (D-F). All the fractures in these constructs occurred at the junction of struts.

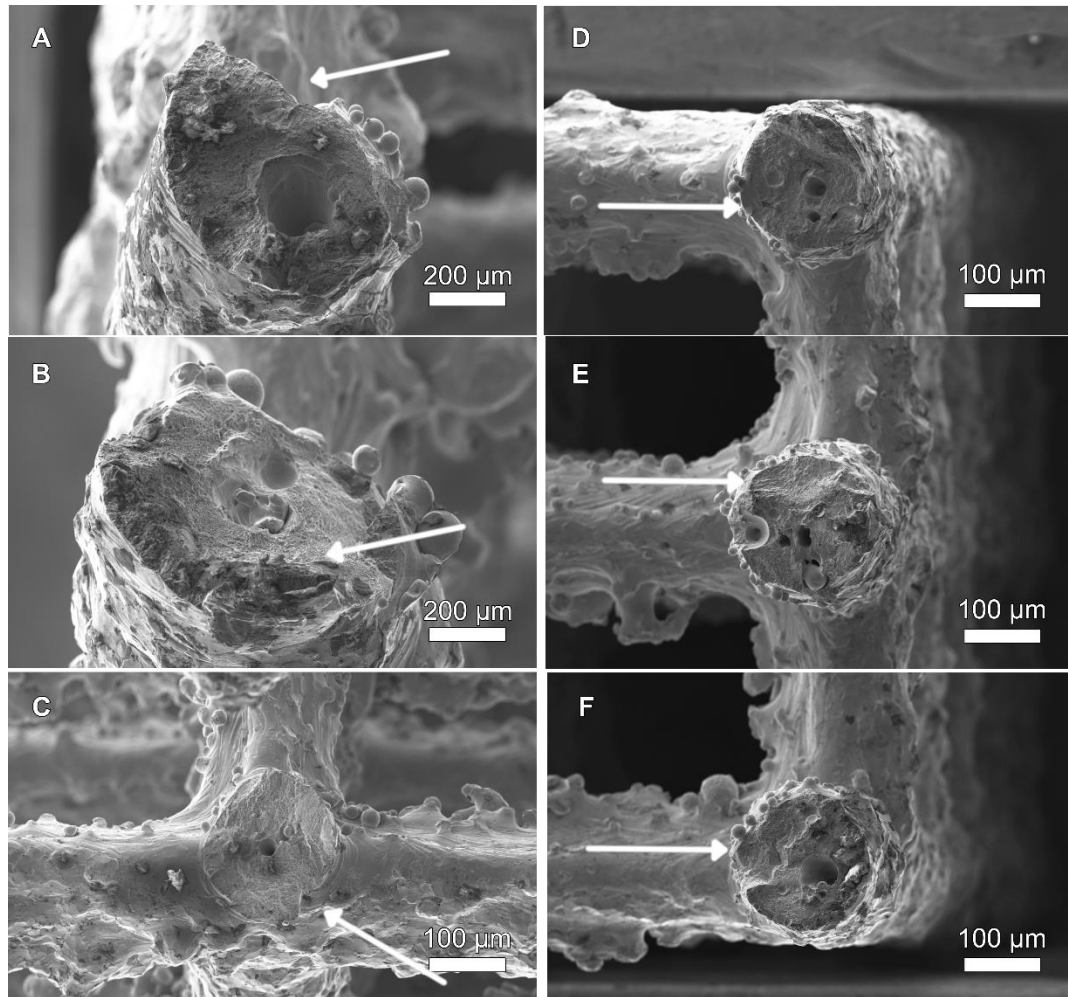


Figure B-7: Representative SEM images of the ST350 constructs that underwent cyclic loading at $\sigma_{fmax}/\sigma_{FY} = 0.4$ (A-C) and $\sigma_{fmax}/\sigma_{FY} = 0.8$ (D-F).

In all the fracture surfaces, fracture site appears to have occurred starting either from the surface, as evidenced by the chipping from close to the surface of the strut (A, B, C, D, F), or from a defect along the surface of the strut, as seen in some cases (E). In almost all the scans of the fracture surface, internal defects were almost always present, which might have caused the general weakening of the strut. However, no evidence of cracking occurring from the internal defects were seen in the scans. Note that some of the struts did have contamination due to inadequate storage (such as the case with A and F).

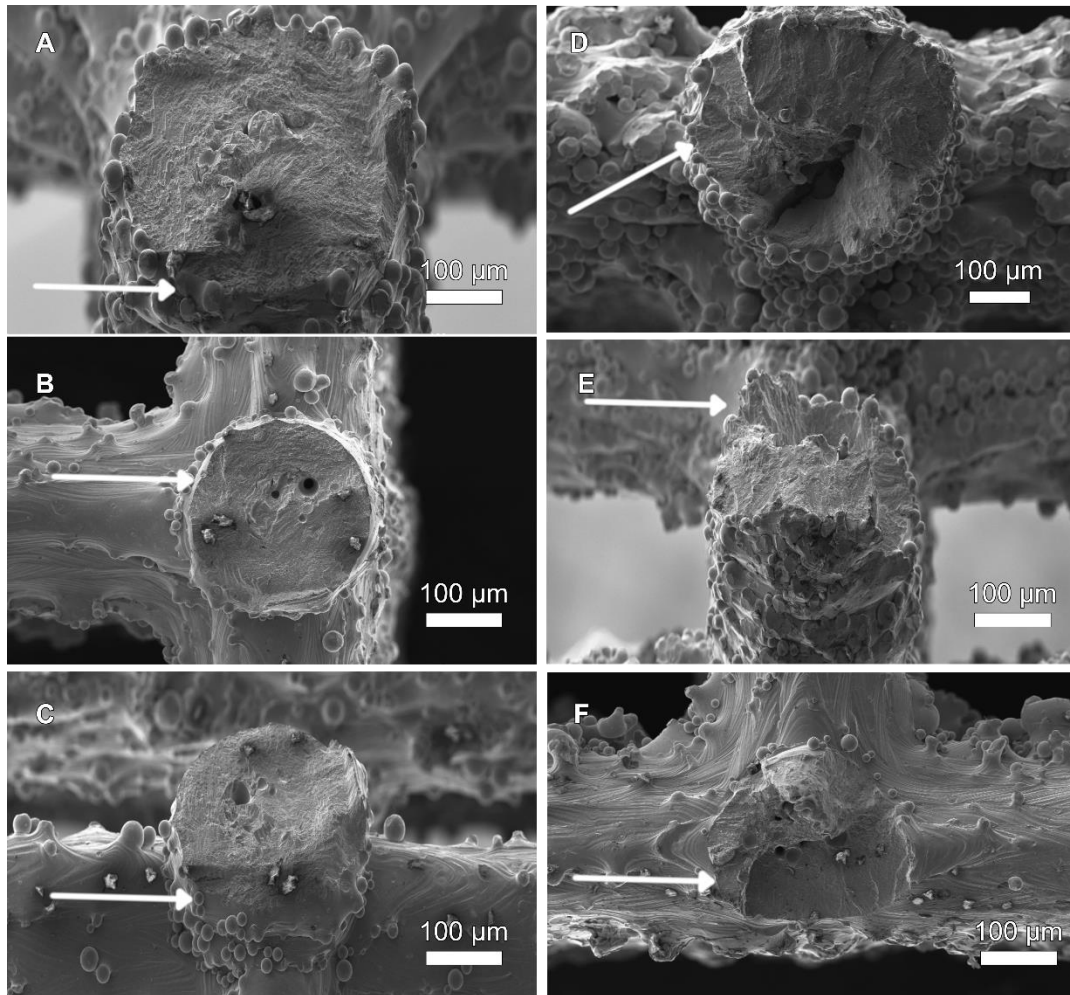


Figure B-8: Representative SEM images of the ST450 constructs that underwent cyclic loading at $\sigma_{fmax}/\sigma_{FY} = 0.4$ (A-C) and $\sigma_{fmax}/\sigma_{FY} = 0.8$ (D-F).

Appendix C

C Permissions

The following are the details on the permissions of reuse of published materials and articles from the thesis. This is pertinent to Chapters 1, 3, 4, and 5 as well as the supplementary materials provided in Appendices A and B.

C.1 Chapters and figures reused from publications in MDPI

C.1.1 Relevant parts of the thesis: Chapter 1, Figure 1-3 and Figure 1-5

Chapter 1 was adapted from a review article written by the author of the thesis.

HIJAZI, K. M., DIXON, S. J., ARMSTRONG, J. E. & RIZKALLA, A. S. 2024. Titanium Alloy Implants with Lattice Structures for Mandibular Reconstruction. *Materials (Basel)*, 17, 140. doi: [10.3390/ma17010140](https://doi.org/10.3390/ma17010140)

Figure 1-3 was reprinted from previous work by Jahadakbar et al. (2016). The citation for this work can be seen below:

JAHADAKBAR, A., SHAYESTEHE MOGHADDAM, N., AMERINATANZI, A., DEAN, D., KARACA, H. E. & ELAHINIA, M. 2016. Finite Element Simulation and Additive Manufacturing of Stiffness-Matched NiTi Fixation Hardware for Mandibular Reconstruction Surgery. *Bioengineering (Basel)*, 3, 36. doi: [10.3390/bioengineering3040036](https://doi.org/10.3390/bioengineering3040036)

Figure 1-5 was reprinted from a previous work by Shen et al (2022). The citation for this work can be seen below:

SHEN, Y. W., TSAI, Y. S., HSU, J. T., SHIE, M. Y., HUANG, H. L. & FUH, L. J. 2022. Biomechanical Analyses of Porous Designs of 3D-Printed Titanium Implant for Mandibular Segmental Osteotomy Defects. *Materials (Basel)*, 15, 576. doi: [10.3390/ma15020576](https://doi.org/10.3390/ma15020576)

Both of these works were published by MDPI. Hence, they follow the rules and regulations set by the publisher.

C.1.2 MDPI Open Access information and Policy

As per MDPI Open Access Policy, laid out in this [link](#). No special permission is required to reuse all, or part of article published by MDPI, including figures and tables. A snippet from MDPI's open access information and policy is shown below:

MDPI Open Access Information and Policy


All articles published by MDPI are made immediately available worldwide under an open access license. This means:

- everyone has free and unlimited access to the full-text of *all* articles published in MDPI journals;
- everyone is free to re-use the published material if proper accreditation/citation of the original publication is given;
- open access publication is supported by the authors' institutes or research funding agencies by payment of a comparatively low Article Processing Charge (APC) for accepted articles.

Permissions

No special permission is required to reuse all or part of article published by MDPI, including figures and tables. For articles published under an open access Creative Common CC BY license, any part of the article may be reused without permission provided that the original article is clearly cited. Reuse of an article does not imply endorsement by the authors or MDPI.

All MDPI publications were licensed under the Creative Commons Attribution 4.0 (CC-by-4.0) International License. The details of the license can be seen in this [link](#). The deed of the license can be seen below:



CC BY 4.0 DEED
Attribution 4.0 International

Canonical URL: <https://creativecommons.org/licenses/by/4.0/> [See the legal code](#)

You are free to:

Share — copy and redistribute the material in any medium or format for any purpose, even commercially.

Adapt — remix, transform, and build upon the material for any purpose, even commercially.

The licensor cannot revoke these freedoms as long as you follow the license terms.

Under the following terms:

Attribution — You must give appropriate credit, provide a link to the license, and indicate if changes were made. You may do so in any reasonable manner, but not in any way that suggests the licensor endorses you or your use.

No additional restrictions — You may not apply legal terms or technological measures that legally restrict others from doing anything the license permits.

Notices:

You do not have to comply with the license for elements of the material in the public domain or where your use is permitted by an applicable exception or limitation.

No warranties are given. The license may not give you all of the permissions necessary for your intended use. For example, other rights such as publicity, privacy, or moral rights may limit how you use the material.

The copyright permission is provided by MDPI on their website, with the link shown here: <https://www.mdpi.com/authors/rights>. The following screenshot details the permissions afforded to authors in regard to use of the article in this thesis:

MDPI Journals Topics Information Author Services Initiatives About Mobile Layout Sign In / Sign Up Submit

Search for Articles: Title / Keyword Author / Affiliation / Email All Journals All Article Types Search Advanced

Copyrights

Copyright and Licensing

For all articles published in MDPI journals, copyright is retained by the authors. Articles are licensed under an open access Creative Commons CC BY 4.0 license, meaning that anyone may download and read the paper for free. In addition, the article may be reused and quoted provided that the original published version is cited. These conditions allow for maximum use and exposure of the work, while ensuring that the authors receive proper credit.

In exceptional circumstances articles may be licensed differently. If you have specific condition (such as one linked to funding) that does not allow this license, please mention this to the editorial office of the journal at submission. Exceptions will be granted at the discretion of the publisher.

C.2 Chapters and figures reused from publications in Elsevier

C.2.1 Relevant parts of the thesis: Chapter 4 and Appendix B

Chapter 4 and Appendix B were adapted from a journal article written by the author of the thesis.

HIJAZI, K. M., MAO, H., HOLDSWORTH, D. W., DIXON, S. J. & RIZKALLA, A. S. 2024. Cyclic flexural fatigue of porous Ti6Al4V constructs for use in mandibular reconstruction. *International Journal of Fatigue*, 185, 108329. <https://doi.org/10.1016/j.ijfatigue.2024.108329>

The copyright permission is provided by Elsevier on their website ([link for more details](#)). The following screenshot details the rights afforded to reuse the article as the original author:

Cyclic flexural fatigue of porous Ti6Al4V constructs for use in mandibular reconstruction
 Author: Khaled M. Hijazi, Haojie Mao, David W. Holdsworth, S. Jeffrey Dixon, Amin S. Rizkalla
 Publication: International Journal of Fatigue
 Publisher: Elsevier
 Date: Available online 11 April 2024
 © 2024 Published by Elsevier Ltd.

Journal Author Rights

Please note that, as the author of this Elsevier article, you retain the right to include it in a thesis or dissertation, provided it is not published commercially. Permission is not required, but please ensure that you reference the journal as the original source. For more information on this and on your other retained rights, please visit: <https://www.elsevier.com/about/our-business/policies/copyright#Author-rights>

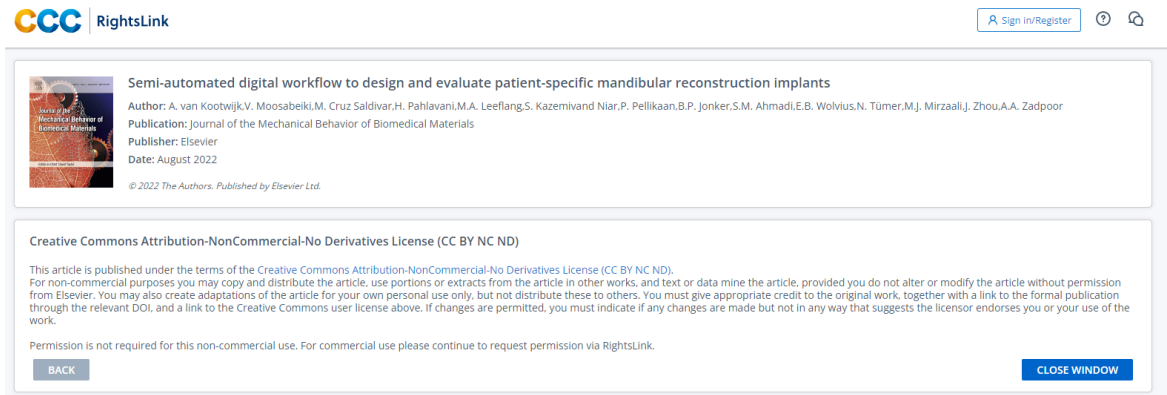
BACK CLOSE WINDOW

C.2.2 Relevant parts of the thesis: Figure 1-6

Figure 1-6 was reprinted from previous work by van Kootwijk et al. (2016). The citation for this work can be seen below:

VAN KOOTWIJK, A., MOOSABEIKI, V., SALDIVAR, M. C., PAHLAVANI, H., LEEFLANG, M. A., KAZEMIVAND NIAR, S., PELLIKAAN, P., JONKER, B. P., AHMADI, S. M., WOLVIUS, E. B., TUMER, N., MIRZAALI, M. J., ZHOU, J. & ZADPOOR, A. A. 2022. Semi-automated digital workflow to design and evaluate patient-specific mandibular reconstruction implants. *J Mech Behav Biomed Mater*, 132, 105291. doi: [10.1016/j.jmbbm.2022.105291](https://doi.org/10.1016/j.jmbbm.2022.105291)

This article was published under the terms of Creative Commons Attribution-Noncommercial-No Derivatives License (CC BY NC ND). The link to the license deed and details can be found through this [link](#). The following is the screenshot showing that no permission is required to reuse the figure from the article as per provided information by RightsLinks, and permitted by Elsevier:



The screenshot displays the RightsLink interface for the article "Semi-automated digital workflow to design and evaluate patient-specific mandibular reconstruction implants". At the top left, the "CCC RightsLink" logo is visible. On the top right, there is a "Sign in/Register" button and icons for help and search. The article information includes the title, author list (A. van Kootwijk, V. Moosabeiki, M. Cruz Saldivar, H. Pahlavani, M.A. Leeftang, S. Kazemivand Niar, P. Pellikaan, B.P. Jonker, S.M. Ahmadi, E.B. Wolvius, N. Tümer, M.J. Mirzaali, J. Zhou, A.A. Zadpoor), publication details (Journal of the Mechanical Behavior of Biomedical Materials, Elsevier, August 2022), and a copyright notice (© 2022 The Authors. Published by Elsevier Ltd.). Below this, a Creative Commons Attribution-NonCommercial-No Derivatives License (CC BY NC ND) is displayed, explaining that the article is published under these terms and that non-commercial use is permitted with appropriate credit. A "BACK" button is located at the bottom left, and a "CLOSE WINDOW" button is at the bottom right.

Appendix D

D References used in the Appendices

- AHMADI, S. M., HEDAYATI, R., LI, Y., LIETAERT, K., TÜMER, N., FATEMI, A., RANS, C. D., POURAN, B., WEINANS, H. & ZADPOOR, A. A. 2018. Fatigue performance of additively manufactured meta-biomaterials: The effects of topology and material type. *Acta Biomaterialia*, 65, 292--304.
- AHMADI, S. M., KUMAR, R., BORISOV, E. V., PETROV, R., LEEFLANG, S., LI, Y., TUMER, N., HUIZENGA, R., AYAS, C., ZADPOOR, A. A. & POPOVICH, V. A. 2019. From microstructural design to surface engineering: A tailored approach for improving fatigue life of additively manufactured meta-biomaterials. *Acta Biomaterialia*, 83, 153-166.
- BARRETT, J. F. & KEAT, N. 2004. Artifacts in CT: recognition and avoidance. *Radiographics*, 24, 1679-91.
- DU PLESSIS, A., RAZAVI, N. & BERTO, F. 2020. The effects of microporosity in struts of gyroid lattice structures produced by laser powder bed fusion. *Materials & Design*, 194, 108899.
- HU, Y. N., WU, S. C., WITHERS, P. J., ZHANG, J., BAO, H. Y. X., FU, Y. N. & KANG, G. Z. 2020. The effect of manufacturing defects on the fatigue life of selective laser melted Ti-6Al-4V structures. *Materials & Design*, 192.
- LEUDERS, S., THÖNE, M., RIEMER, A., NIENDORF, T., TRÖSTER, T., RICHARD, H. A. & MAIER, H. J. 2013. On the mechanical behaviour of titanium alloy TiAl6V4 manufactured by selective laser melting: Fatigue resistance and crack growth performance. *International Journal of Fatigue*, 48, 300--307.
- WICKMANN, C., BENZ, C., HEYER, H., WITTE-BODNAR, K., SCHAFFER, J. & SANDER, M. 2021. Internal Crack Initiation and Growth Starting from Artificially Generated Defects in Additively Manufactured Ti6Al4V Specimen in the VHCF Regime. *Materials (Basel)*, 14.

Curriculum Vitae

Name: Khaled Marwan Anis Hijazi

Post-secondary Education and Degrees:

German Jordanian University
Amman, Jordan
2009-2014 B.Sc. in Biomedical Engineering

Saint Mary's University
Halifax, NS, Canada
2014-2017 Master of Applied Science

The University of Western Ontario
London, Ontario, Canada
2017-2024 Ph.D. in Biomedical Engineering

Honors and Awards:

Finalist IADR IRG Young Investigator Award Competition
2021

Second Place Poster Presentation in Bone Basic Science
Presentations at CBJC 2020

Related Work Experience:

Teaching Assistant
Saint Mary's University
2014-2017

Teaching Assistant
The University of Western Ontario
2017-2021

Publications:

HIJAZI, K. M., MAO, H., HOLDSWORTH, D. W., DIXON, S. J. & RIZKALLA, A. S. 2024. Cyclic flexural fatigue of porous Ti6Al4V constructs for use in mandibular reconstruction. *Int J Fatigue*, 184, 108329.

HIJAZI, K. M., DIXON, S. J., ARMSTRONG, J. E. & RIZKALLA, A. S. 2024. Titanium Alloy Implants with Lattice Structures for Mandibular Reconstruction. *Materials (Basel)*, 17, 140.

HIJAZI, K. M., SINGFIELD, K. L. & VERES, S. P. 2019. Ultrastructural response of tendon to excessive level or duration of tensile load supports that collagen fibrils are mechanically continuous. *J Mech Behav Biomed Mater*, 97, 30-40.